Mechanisms of Tropical Pacific Climate Change During the Holocene

Alyssa Regine Atwood

A dissertation

submitted in partial fulfillment of the

requirements for the degree of

Doctor of Philosophy

University of Washington

2015

Reading Committee:

Julian P. Sachs, Chair

David S. Battisti

LuAnne Thompson

Program Authorized to Offer Degree:

School of Oceanography

University of Washington

Abstract

Mechanisms of Tropical Pacific Climate Change During the Holocene

Alyssa Regine Atwood

Chairs of the Supervisory Committee:
Professor Julian P. Sachs
School of Oceanography
Professor David S. Battisti
Dept. of Atmospheric Sciences

A novel set of hydroclimate reconstructions is presented from the eastern equatorial Pacific that spans the last 9100 years. Past changes in total climatological rainfall and rainfall associated with El Niño events were reconstructed using the sedimentary distribution, accumulation rate, and hydrogen isotope composition of four lipid biomarkers in the sediment of El Junco Lake, San Cristóbal Island. Possible mechanisms of the multi-decadal to millennial scale rainfall variations inferred at El Junco Lake are evaluated in light of tropical hydroclimate and global climate reconstructions through the Holocene.

Tropical hydroclimate changes are further investigated during the so-called "8.2 ka event" and the Little Ice Age (LIA) using climate model simulations. We propose that rainfall changes

at El Junco Lake ca. 8500-8000 yr BP were produced by a large meltwater pulse in the North Atlantic that caused a southward shift of the ITCZ (via reduced northward ocean heat transport and expanded Arctic sea ice) and weakened El Niño/Southern Oscillation (ENSO) variability (via tropical Pacific mean state changes that increased the stability of the coupled ocean-atmosphere system). We provide support for this concept using simulations with a fully coupled global climate model (CESM) and a linearized ocean-atmosphere model of the tropical Pacific (LOAM),

Tropical hydroclimate changes and their mechanisms during the LIA were investigated in the CMIP5/PMIP3 last millennium simulations. Climate forcings and feedbacks were quantified using the Approximate Partial Radiative Perturbation and radiative kernel methods, highlighting the role of volcanic forcing and the water vapor, lapse rate, and surface albedo feedbacks during the LIA. A weak southward shift in zonally averaged tropical precipitation was found during the LIA in the model simulations in association with anomalous northward cross-equatorial atmospheric energy transport that was driven by greater volcanic forcing and greater snow and sea ice response in the Northern (versus Southern) Hemisphere.

A second theme of this dissertation is the influence of tropical Pacific mean state changes on ENSO variability. This concept is explored through simulations of the 8.2 ka event, as well as through analysis of the large, unforced, multi-decadal changes in ENSO variability in the General Circulation Model GFDL CM2.1. Experiments using LOAM suggest that a two-way feedback operates between ENSO and the mean state of the tropical Pacific in CM2.1, whereby random forcing and nonlinear dynamics produce low frequency changes in ENSO variance that are then counteracted by mean state feedbacks.

TABLE OF CONTENTS

LIST OF FIGURES

LIST OF TABLES

ACKNOWLEDGEMENTS

I owe many thanks to an enormous team of colleagues, friends, and family that have made this work possible. I extend special thanks to Julian Sachs and David Battisti for their incredible mentorship and for their steadfast support and enthusiasm of my somewhat diverse research program. Their creative and expansive, yet rigorous and directed, scientific approach has been a constant source of inspiration.

Others that contributed immensely to this work include LuAnne Thompson, Dargan Frierson, and Paul Quay who kindly served on my PhD committee. Dargan also provided critical support and insight into the energy budget analyses in Chapters 7 and 8. Orest Kawka provided tremendous support and mentorship in the lab. Thanks go to Will Roberts and Dan Vimont for their on-going assistance with LOAM and to Andrew Wittenberg who provided invaluable insight into the ENSO/GFDL CM2.1 analyses in Chapter 6. I gratefully acknowledge DOE GCEP and NSF for their fellowship awards.

I extend thanks to all of my colleagues at the University of Washington who contributed to its uniquely creative, collaborative, and supportive environment, especially to Andrea, Kirsten, Liz, Jesse, Dan, Seth, Nemiah, Stu, Steve, Kelly and the many others that walked this path with me. Their friendship over the years has smoothed out the bumps in the road.

Finally, I thank my family and friends for their tireless support and unwavering belief in me.

DEDICATION

I dedicate this work to my mother- her tenacity, selflessness, and lightness of being give me something to aspire to every day. To my sisters, for their inspirational passion, idealism, and drive for the greater good. And to Joel, whose incredible partnership I have been blessed with along this journey.

Chapter 1. INTRODUCTION

I climb because I thirst to throw back the margins of my world.
There remains so much that I do not know.

Gregory Crouch, *Enduring Patagonia*

Constraining the evolution of the Earth's climate system through the present interglacial period (i.e. the last 11,700 years, known as the Holocene epoch) is critical for understanding natural variations in the climate system and for placing recent climate change into a broader context. The dominant drivers of climate change during the Holocene include orbital forcing (as the Earth undergoes precession around its rotational axis with a period of ca. 26,000 years), volcanic forcing (as large volcanic eruptions catapult light-scattering aerosols into the stratosphere which then spread across the globe), changes in solar irradiance, and changes in the concentration of atmospheric greenhouse gases. However, the evolution of the Holocene climate remains poorly understood. This is exemplified by the large disparities that exist between proxy reconstructions and climate model simulations of temperature trends over the Holocene (Liu et al., 2014; Marcott and Shakun, 2015).

One component of past climate variations that warrants particular attention is the tropical Pacific climate due to its unique ability to dramatically and rapidly reorganize and to project its changes across the globe. The global impact of changes in tropical Pacific climate is apparent on interannual timescales in the El Niño-Southern Oscillation (ENSO), a tropical Pacific coupled atmosphere-ocean phenomenon that drives the single largest pattern of natural climate variability on a global scale, affecting precipitation and temperature patterns across more than half of the globe every 3-7 years (e.g. Alexander et al., 2002; Rasmusson and Carpenter, 1982; Trenberth et al., 1998). It is also thought to have played a fundamental role in driving global climate change on much longer (i.e. orbital and millennial) timescales (e.g. Chiang, 2009). Developing a firm understanding of past climate change (at any timescale) thus necessitates a firm understanding of changes in the tropical Pacific. However, robust reconstructions of tropical Pacific climate over the Holocene are hampered by a paucity of continuous, high-resolution paleoclimate archives from this region.

The goals of this dissertation are to develop a new set of hydroclimate reconstructions from the eastern equatorial Pacific that span the current interglacial period and to examine mechanisms of tropical Pacific climate change during this time through a combination of proxy- and climate model-based approaches. In Chapters 2-4, a set of Holocene hydroclimate reconstructions from the Galápagos Islands is presented, based on the accumulation rate and isotopic composition of sedimentary lipid biomarkers in El Junco Lake. These reconstructions offer insight into rainfall changes associated with ENSO and the climatological position of the Intertropical Convergence Zone (ITCZ; the region of convergence of the northern and southern trade winds that produces a band of convection and heavy rainfall just north of the equator). In Chapter 2, we present the method and analysis techniques used to interpret the proxy records and develop the rainfall reconstructions. In Chapter 3, we present the 9100 yr hydroclimate record from El Junco Lake and evaluate the inferred tropical Pacific hydroclimate changes in the context of global climate changes through the Holocene. In Chapter 4, which concludes the geochemistry portion of this dissertation, we present evidence from these records suggesting that large hydroclimate changes occurred in the eastern equatorial Pacific during the time that large glacial lakes discharged into the North Atlantic ca. 8300 yr BP. Mechanisms of a dynamical link between a climatological southward shift of the ITCZ and weakened ENSO variability (as inferred from the El Junco Lake hydroclimate reconstructions) are explored using a intermediate complexity model of the tropical Pacific.

In Chapters 5-8 of this dissertation, we focus on dynamical mechanisms of tropical Pacific climate change during the Holocene, with an emphasis on the North Atlantic freshwater event ca. 8300 yr BP and the Little Ice Age (LIA). The so-called "8.2 kyr event" is thought to have been the most abrupt climate change event of the Holocene, with proxy records indicating cooling across the North Atlantic, including a precipitous drop of 3-7 °C in the surface temperature of central Greenland in less than 20 years (Alley et al., 1997; Kobashi et al., 2007; Leuenberger et al., 1999; Morrill et al., 2013; Thomas et al., 2007). More recently in Earth's history, widespread cooling is thought to have occurred across much of the globe during the LIA, ca. 700-100 yr BP (1250-1850 AD), with average Northern Hemisphere cooling of ca. 0.5 °C over the second half of this period (Mann, 2009; Pages 2k Consortium, 2013). We argue that during both the 8.2 kyr event and the LIA, proxy records provide evidence for large changes in tropical Pacific hydroclimate, but the mechanisms of these changes are not well understood. In Chapter 5, we

investigate the influence of a large North Atlantic freshwater perturbation on the mean state and variability of the tropical Pacific by performing a set of experiments with a fully coupled global climate model in tandem with a highly idealized model of the tropical Pacific. A particular focus of this work is to evaluate the influence of tropical Pacific mean state changes on ENSO dynamics. In Chapter 6 we further explore the interactions between tropical Pacific mean state changes and ENSO by investigating mechanisms of unforced ENSO variability in the General Circulation Model (GCM) GFDL CM2.1. In the final two chapters of this dissertation (Chapters 7 and 8), we investigate mechanisms of tropical hydroclimate changes during the LIA, looking to a suite of simulations performed as a part of the Coupled Model Intercomparison Project phase 5/Paleoclimate Model Intercomparison Project phase 3. In Chapter 7 we evaluate the climate forcings and feedbacks responsible for global cooling during the LIA and in Chapter 8 we evaluate the simulated changes in tropical precipitation during the LIA and their association with hemispheric asymmetries in the forcings and feedbacks.

Chapter 2. RECONSTRUCTING RAINFALL CHANGES IN THE GALÁPAGOS ISLANDS OVER THE LAST 3 KYR USING D/H RATIOS OF MULTIPLE LIPID BIOMARKERS

This prelude is to alert readers who have read Atwood and Sachs (2014) of several important differences between that paper and the results herein. While this chapter closely follows Atwood and Sachs (2014), presenting some of the same data and drawing on some of the same analyses, new data has been added and the interpretation of the data has been revised based on recent advances in our understanding of the proxy records and their climatic implications. An overview of the important updates to the biomarker data and their interpretations is provided in Chapter 2.4.4. Readers who are not familiar with Atwood and Sachs (2014) should proceed to Chapter 2.1.

2.1 INTRODUCTION

The climate dynamics of the tropical Pacific play a fundamental role in climate variability across the globe. The Intertropical Convergence Zone (ITCZ) and the El Niño/Southern Oscillation (ENSO) are two primary features of the tropical Pacific that influence climate on a global scale. The ITCZ demarks the ascending branch of the Hadley cell, the major meridional overturning cell in the tropical atmosphere that is responsible for transporting energy poleward out of the deep tropics. The ITCZ is characterized by the convergence of the northern and southern trade winds that produce a nearly zonal band of convection and heavy rainfall near the equator over the Pacific and Atlantic oceans. The ITCZ(s) change latitude seasonally, shifting north and south concomitant with the changing tropical SST and latitude of maximum insolation, lagging the insolation changes by ca. two months, largely due to the thermal inertia associated with the portion of the upper ocean that participates in the seasonal cycle. While well defined over the Atlantic and central/eastern Pacific Oceans, the ITCZ has little structure over landmasses and the warm western Pacific Ocean where widespread convection occurs as well as over the Indian Ocean where convection is predominantly set by monsoon circulations. The seasonal migration of the ITCZ drives the wet and dry seasons in the tropics that sculpt the natural environment and provide access to freshwater for 40% of the world's population (http://daac.ornl.gov).

ENSO is another fundamental feature of the tropical Pacific that represents the leading source of interannual climate (temperature and precipitation) variability on a global scale. The ENSO phenomenon refers to the irregular warming and cooling of the eastern equatorial Pacific sea surface that typically lasts 1-1.5 years and reoccurs approximately every 3-7 years (Rasmusson and Carpenter, 1982; Trenberth et al., 2002). During ENSO events, changes in atmospheric circulation patterns in the tropics result in numerous climate perturbations that stretch across the globe (Alexander et al., 2002; Trenberth et al., 1998). Impacts from the associated tropical and midlatitude temperature and precipitation anomalies can be dramatic and widespread. Terrestrial impacts include drought, flooding, crop failure, and disease; while changes in ocean temperature and upwelling have substantial impacts on marine ecosystems through changes in primary productivity, fish stocks, and coral health. These impacts affect the natural environment and the lives of billions of people across the globe.

Some paleoclimate evidence suggests that ENSO and the mean annual position of the ITCZ have changed dramatically over the Holocene, however these changes are poorly constrained due to the low temporal and spatial coverage of paleoclimate records from regions where the fundamental dynamics of ENSO and the ITCZ operate. Paleo-rainfall records from the tropical Pacific can aid in these reconstructions, provided that the various climate features that influence local rainfall can be distinguished. El Junco Lake (Fig. 2.1) is located on San Cristóbal Island, Galápagos (1° S, 89° W) in the heart of the eastern equatorial Pacific (EEP) cold tongue with a climate highly sensitive to movements of the ITCZ and to ENSO. In this study we present a unique method of disentangling the ITCZ and ENSO rainfall signals from algal and plant lipid biomarkers and their hydrogen isotope ratios in this lake to infer changes in ENSO and the position of the ITCZ over the late Holocene.

Located at the southern edge of the ITCZ, seasonality at El Junco Lake is characterized by the annual migration of the ITCZ, which produces a wet season from January-May and a dry season from June-December (Fig. 2.2). The wet season occurs when the ITCZ is shifted southward- weakened trade winds and reduced ocean upwelling cause the EEP cold tongue to recede, sea surface temperature (SST) and air temperatures to increase, and the resultant convection results in increased rainfall. Conversely, the dry season occurs as the ITCZ shifts northward– stronger trade winds and upwelling result in lower SST and air temperatures and minimal convection. At elevations higher than approximately 250 m (including El Junco Lake at

670 m), the dry season is characterized by significantly higher annual rainfall than lower elevations as strong upwelling and cool SSTs result in cooler air at the surface than aloft, which creates a temperature inversion that produces persistent stratus clouds (called *garúa*) that blanket the highlands (Trueman and d'Ozouville, 2010). It is estimated that approximately 25% of rainfall in the Galápagos highlands comes from *garúa* (Pryet et al., 2012).

Rainfall in the Galápagos Islands also varies in response to SST anomalies (SSTAs) associated with ENSO. Annual rainfall is correlated to warm Niño 3.4 SSTAs ($r = 0.73$, $p < 0.05$), with the highest rainfall amounts observed during moderate-to-strong El Niño events (Niño 3.4 SSTAs ≥ 1.0 °C; Fig. 2.3). The historical record of station rainfall from the Galápagos demonstrates that strong El Niño events are marked by annual rainfall that is 4–7 times as large as rainfall during non-El Niño years, while La Niña events have little influence on local rainfall (Fig. 2.4). The historical rainfall record also demonstrates that year-to-year variations in wet season rainfall in the Galápagos generally reflect the large-scale pattern of rainfall in the eastern Pacific along the equator (1°S to 1°N, 110°E to 85°E), irrespective of the ENSO phase, which suggests that the changes in the ITCZ (that are not related to ENSO) influence Galápagos rainfall on interannual timescales, in addition to driving the wet/dry seasons. Because rainfall in this region is highly dependent on both the presence of El Niño conditions and on the position of the ITCZ (independent of ENSO), rainfall reconstructions from this region should take into account possible changes in both of these climate phenomena.

In this study we use algal biomarker distributions and hydrogen isotope ratios from El Junco Lake sediment to infer past changes in local rainfall. Hydrogen isotope ratios of lipid biomarkers from algae are a valuable tool with which to investigate past climate changes (Pahnke et al., 2007; Sachs et al., 2009; Sachse et al., 2012; Smittenberg et al., 2011; van der Meer et al., 2008). In closed (endorheic) lakes, lake water δD is driven by the ratio of precipitation to evaporation (Craig, 1961) and the isotopic value of the precipitation which, in the tropics, is strongly negatively correlated with the amount of precipitation on monthly or longer timescales (Dansgaard, 1964; Risi et al., 2008). The combination of these processes amplifies the response of lake water δD to changes in rainfall with lower (higher) δD values occurring during periods of wetter (drier) conditions. Changes in rainfall can therefore be reconstructed from δD values of sedimentary algal lipids, due to the near perfect correlation between water δD and algal lipid δD values (Englebrecht and Sachs, 2005; Sachse et al., 2004; Sauer et al., 2001; Schouten et al.,

2006; Zhang and Sachs, 2007) and the preservation of hydrogen isotope ratios of lipid biomarkers over geologic timescales (Yang and Huang, 2003).

In regions where multiple climate phenomena influence local rainfall, paleo-rainfall records can be difficult to interpret. In this study we present a novel method to distinguish changes in mean rainfall from changes in El Niño-related rainfall from the Galápagos Islands using a suite of molecular and isotopic records from El Junco Lake. δD profiles of dinosterol, a lipid biomarker produced by dinoflagellates (Structure I, Fig. 2.5), are compared to accumulation rate and δD profiles of C_{34} botryococcene, a biomarker produced by the B Race of the green algae, *Botryococcus braunii* (Structure II, Fig. 2.5). In addition, abundances of C_{30} ω20-keto-1-ol (Structure V, Fig. 2.5) produced by ferns are compared to abundances of the algal C_{30} ω16-keto-1-ol (Structure III, Fig. 2.5) in the sediment record. Biomarker data derived from the same sediment samples are compared, thus eliminating potential age differences in the derived climate signals. These biomarker records are used to reconstruct changes in mean rainfall and El Niño-related rainfall for the past 3,000 years.

2.2 METHODS

2.2.1 *Study Site*

El Junco Lake is located atop a caldera in the highlands of San Cristóbal Island, Galápagos (1° S, 89° W) at 670 m elevation. With the exception of possible overflow conditions and seepage, it is an endorheic lake whose hydrologic fluxes are dominated by precipitation and evaporation. A channel cuts through the lowest point of the crater rim that was located approximately 2–3 m above the lake level during the field outing in Sept. 2004. El Junco Lake is the only permanent freshwater lake in the Galápagos Islands and during our 2004 field outing, the lake had a diameter of 280 m, maximum depth of 6 m, and temperature of 19 °C. The lake chemistry is characterized by a conductivity of 20–27 μS/cm, pH ca. 5.5 and is mesotrophic (Colinvaux, 1968; Ferrington and Pehofer, 1996). The presence of strong easterly trade winds combined with the relatively shallow depth result in the lake being well mixed, as indicated by nearly constant temperature, O_2, and δD depth profiles.

2.2.2 *Field Methods, Age Model, Biomarker Measurements, and Idealized Lake Model*

Details of the field methods, dating methods, and age model can be found in Appendix A (Table A1, Table A2) and (Zhang et al., 2014)). The age model was constructed in OxCal 4.0.1 (Bronk Ramsey, 2009) using 15 ^{210}Pb measurements with a constant rate of supply model and 21 ^{14}C measurements with linear interpolation between data points and the SHCa104 calibration curve. The age model predicts a basal age of the sediment cores of 9.1 kyr BP and a sedimentation rate that ranges from 2.3 mm/yr (1 cm ≈ 5 years) in the top 5 cm and declines to 0.2 mm/yr (1 cm ≈ 50 years) for the lower 1 m. No significant reservoir effect is thought to exist in El Junco Lake, an assertion supported by the presence of nuclear bomb-derived ^{14}C in the upper 8 cm of sediment and the smooth transition from ^{210}Pb-derived- to ^{14}C-derived-age models (Table A1, and Fig. 2.5 in Zhang et al., 2014). Estimates of age model uncertainty can be found in Appendix A and Tables A1 and A2.

Purification, quantification, and δD measurement methods for dinosterol can be found in Appendix A and for C_{34} botryococcene can be found in Zhang et al. (2007), Zhang and Sachs (2007), and Zhang et al. (2014). Details of the idealized model of El Junco Lake can be found in Appendix B.

2.3 RESULTS

2.3.1 *Dinosterol as a Recorder of Climatological Conditions in El Junco Lake*

Dinosterol is a source-specific biomarker that exists in abundance throughout the El Junco Lake sedimentary profile. The sterol composition of the sediment indicates that a dinoflagellate of the genus *Peridinium* has been the source of dinosterol in El Junco Lake throughout the sedimentary record (Atwood et al., 2014). Dinoflagellates of this genus have been found to thrive in a wide range of nutrient conditions (Domingues et al., 2011; Trigueros et al., 2000; Umaña-Villalobos, 2001; Viner-Mozzini et al., 2003).

The concentration of dinosterol is fairly uniform through the 3 kyr sediment record (Fig. 2.7A), suggesting that the dinoflagellate thrives in a wide variety environmental conditions. Furthermore, its concentration is weakly correlated to its δD value ($R = 0.51$, $p < 0.05$; Fig. 2.6), from which we infer that the dinoflagellate has somewhat of a preference for drier conditions,

and by inference, more nutrient rich conditions as solutes become concentrated in a smaller lake volume.

As the available evidence suggests that the dinoflagellate population persists throughout the varying hydrologic conditions experienced by El Junco Lake, we assume that the dinoflagellate grows continuously in El Junco Lake. In the subsequent analyses, we thus interpret the sedimentary dinosterol δD as a record of the climatological (decadal-to-centennial) lake conditions (which includes the impact of El Niño events). The decadal-to-centennial averaging comes from the sample resolution, which increases with depth through the sedimentary record. Further support for our interpretation of dinosterol δD is provided by an independent proxy of mean lake level changes, outlined in Chapter 2.4.2.

2.3.2 *Botryococcenes as a Recorder of El Niño Conditions in El Junco Lake*

Botryococcenes (dominated by C_{34} botryococcene) represent some of the most abundant lipids in El Junco Lake sediment and are produced by a single race of the green alga, *Botryococcus braunii* (Metzger et al., 1985; Zhang et al., 2007). Although the growth conditions of *B. braunii* have not been documented in El Junco Lake, this algae has been found to thrive in oligotrophic conditions (e.g. in oligotrophic lakes and during summer stratification of meso-eutrophic temperate lakes), while its abundance has been found to decrease with increasing NH_4 and total nutrient concentration (Huszar et al., 2003; Huszar and Caraco, 1998; Smittenberg et al., 2005). This evidence suggests that *B. braunii* blooms during periods of oligotrophic conditions in El Junco Lake.

The sedimentary botryococcene profile further supports this theory. The log of C_{34} botryococcene concentration is anti-correlated to its δD value ($R = -0.62$, $p < 0.05$) and is highly variable, with a concentration range that spans five orders of magnitude and falls below the detection limit of 0.1 μg/g in several intervals in the sedimentary record (Fig. 2.6, Fig. 2.8A). These characteristics suggest that *B. braunii* thrives during periods of high rainfall and that blooms are highly sensitive to changing environmental conditions.

Variations in nutrient concentration and water column stability are the most probable sources of the dissimilar relationships between the concentrations and δD values of C_{34} botryococcene and dinosterol in El Junco Lake. In particular, conditions favorable for *B. braunii* blooms are thought to occur during El Niño events in association with three distinct processes

that promote oligotrophic conditions and lake stratification. Firstly, the heavy rains associated with moderate-to-strong El Niño events are thought to dilute the nutrient solutes, causing oligotrophic conditions. El Junco Lake is an endorheic lake (with the exception of occasional overflow conditions and possibly seepage) located within a caldera with a small catchment area consisting only of the narrow crater rim (Conroy et al., 2008). In such lakes the concentration of nutrients tend to decrease as lake levels increase through dilution of the incoming nutrients (Magyari et al., 2009; Smol et al., 2001). Because monthly rainfall in this area can be an order of magnitude higher during strong El Niño events as compared to non-El Niño periods (c.f., Fig. 2.4) and the lake has been reported to overflow during strong El Niño events, considerable dilution and flushing of nutrients likely occur during these times. Secondly, reduced nutrient input to the lake exacerbates oligotrophic conditions during strong El Niño events. A major source of nutrients to the lake is thought to be guano deposited directly into the lake by the large number of seabirds that frequent it (Colinvaux, 1968). Such a predominance of avian-derived nutrients has been documented in a number of lake systems (Manny et al., 1994; Marion et al., 1994). However, during strong El Niño events, this nutrient source is diminished as the Galápagos seabird population plummets in response to the massive fish die-offs associated with a deep thermocline and low ocean productivity in the EEP (Gibbs et al., 1987). Finally, El Niño events in the EEP are associated with conditions that increase water column stability and lake stratification, including warmer air temperatures, reduced cloud cover, and reduced trade wind strength (Cózar et al., 2012; Lewis Jr., 1983; Ndebele-Murisa et al., 2010; O'Reilly et al., 2003), conditions which have been shown to exacerbate nutrient depletion in the surface of oligotrophic lakes (O'Reilly et al., 2003).

Increases in water column stability during El Niño events should further promote favorable conditions for the lipid-rich, colony-forming *B. braunii* due to their buoyancy. In various locations across the globe, *B. braunii* blooms have been strongly linked to increases in water column stability due to both their tolerance of oligotrophic conditions and their anti-sinking strategy (Kebede and Belay, 1994; Souza et al., 2008; Winder and Hunter, 2008). In particular, in a Columbian lake with conditions (including depth, pH, conductivity, and nutrient concentration) comparable to El Junco Lake, *B. braunii* blooms have been found to occur during the annual flood stage in association with nutrient flushing, oligotrophic conditions, and lake

stratification (Pinilla, 2006), conditions that closely mimic moderate to strong El Niño events in El Junco Lake.

These lines of evidence strongly suggest that conditions favorable for *B. braunii* growth occur during moderate-to-strong El Niño events. In the subsequent analyses, we assume that *B. braunii* blooms exclusively during El Niño events and thus that C_{34} botryococcene δD records the hydrologic conditions of the lake *exclusively* during El Niño events. Based on the arguments outlined thus far, the possibility can't be ruled out that oligotrophic conditions that accompany a substantially wetter mean climate (unassociated with El Niño events) are sufficient to drive *B. braunii* blooms. However, if this were the case, during such periods we would expect to see botryococcene accumulation rates increase in association with decreased dinosterol δD (due to wetter mean lake conditions). However, the wettest mean conditions of 9.1 kyr record, as inferred from dinosterol δD, are marked by anomalously low botryococcene accumulation rates (e.g. see Fig. 4.1), suggesting that *B. braunii* blooms occur only during El Niño events, not in association with low frequency climate variations.

2.3.3 *Inferring Climatological Rainfall Changes and El Niño Rainfall Changes from El Junco Lake Biomarker Records*

From the available evidence, we infer that sedimentary dinosterol δD reflects the long-term mean (climatological) lake δD and thus changes in the climatology of mean annual rainfall owing to the "amount effect" (e.g. Fig. 2.7B). From the C_{34} botryococcene data, we infer that botryococcene δD reflects the mean isotopic composition of El Junco Lake during El Niño events, and that to first order, changes in lake δD during El Niño events are driven by changes in the mean monthly rainfall during those events. Changes in botryococcene δD thus provide a measure of changes in the average amplitude of El Niño rainfall events (e.g. Fig. 2.7H). Finally, we infer that the sedimentary accumulation rate of C_{34} botryococcene scales with the climatological rainfall associated with El Niño events (i.e. the total rain that fell during El Niño events divided by the total amount of time in the sedimentary interval; e.g. Fig. 2.7E). This inference is equivalent to assuming that, during a given interval, the total accumulation of botryococcenes in the sediment scales with the total rain that fell during El Niño events. Under this assumption, changes in the botryococcene accumulation rate reflect changes in

climatological rainfall due to changes in El Niño rainfall. Our interpretation of the botryococcene accumulation rate (i.e. climatological rainfall associated with El Niño events) differs from that of the botryococcene δD (i.e. El Niño mean monthly rainfall), as changes in the climatological rainfall associated with El Niño events (and therefore botryococcene accumulation rate) should be sensitive to changes in the frequency, amplitude, and/or duration of El Niño rainfall events, while changes in El Niño mean monthly rainfall (and therefore botryococcene δD) should only be sensitive to changes in the average *amplitude* of El Niño rainfall events. The botryococcene accumulation rate thus provides a broader (statistical) measure of the variability of El Niño rainfall events. Due to the temporal resolution of the biomarker data, all rainfall reconstructions represent averages over decadal and longer timescales.

Based on these inferences, we propose that rainfall at El Junco Lake can be reconstructed in the following way:

$$\Delta P^*_E = -\alpha \cdot \Delta(botryococcene\ \delta D) \quad (2.1)$$

$$\Delta \overline{P_T} = -\beta \cdot \Delta(dinosterol\ \delta D) \quad (2.2)$$

$$\Delta \overline{P_E} = \gamma \cdot \Delta(log(F_{bot})) \quad (2.3)$$

where ΔP^*_E is the change in mean monthly rainfall during El Niño events, $\Delta \overline{P_T}$ is the total change in climatological rainfall, $\Delta \overline{P_E}$ is the change in climatological rainfall attributable to El Niño events (i.e. the change in El Niño mean annual rainfall), and F_{bot} is the sedimentary botryococcene accumulation rate (in μg $cm^{-2}yr^{-1}$). The botryococcene accumulation rate is related to the botryococcene concentration in the following way:

$$F_{botryo} = ([botryo] * DBD * d)/t \quad (2.4)$$

where [botryo] is the botryococcene concentration (in μg/g), DBD is the dry bulk density of the sediment (in g/cm^3), d is the thickness of the sediment sample (in cm), and t is the duration of time represented by the sediment sample (in yr). In this study, an average DBD has been estimated from the top 15 cm of sediment. Future work will include incorporating improved estimates of DBD based on down-core gamma ray density measurements.

The El Junco Lake biomarker records are shown in Fig. 2.8A-C. Positive (negative) values of $\Delta \overline{P_T}$ indicate an increase (decrease) in climatological rainfall. Positive (negative) values of ΔP^*_E indicate an increase (decrease) in the average amplitude of El Niño rainfall events. Positive

(negative) values of $\Delta\overline{P_E}$ indicate an increase (decrease) in climatological rainfall due to an increase (decrease) in El Niño rainfall. It is important to note the distinction between El Niño rainfall reconstructions (as presented here) and El Niño SSTA reconstructions, since it has been suggested that the frequency and amplitude of rainfall anomalies in the eastern Pacific during El Niño events can change without a corresponding change in the amplitude of SSTAs. For instance, (Cai et al., 2014) demonstrated, using future climate simulations from the Coupled Model Intercomparison Project phase 3 and phase 5, that extreme rainfall in the Niño 3 region increases in response to a weakened mean zonal SST gradient in the tropical Pacific due to enhanced probability of anomalous deep convection in the eastern Pacific under a given SSTA. Possible mechanisms of increased (decreased) El Niño rainfall as recorded by the botryococcene records therefore include: (1) decreased (increased) mean zonal SST gradient in the tropical Pacific, (2) increased (decreased) variance of ENSO SSTAs, and/or (3) a shift in the distribution of ENSO SSTAs to more eastern Pacific (central Pacific) El Niño events. $\Delta\overline{P_E}$ and $\Delta P^*{}_E$ should be more sensitive to changes in Eastern Pacific (EP) El Niño events as compared to Central Pacific (CP) events due to the location of El Junco Lake in the eastern equatorial Pacific (Ashok et al., 2007; Murphy et al., 2015).

2.3.4 *Modern Biomarker Records*

We compare the El Junco Lake biomarker records to Galápagos rainfall data over the period for which meteorological measurements are available (Fig. 2.7). 10-year averages of rainfall were taken to coincide with the average time slice represented by our sediment samples. While the short observational record, combined with low sampling resolution in the biomarker data, and large errors relative to trends in the data prohibit a robust test of the proxy data, the behavior of the rainfall indices is broadly consistent with our interpretation. In particular, the correspondence between (1) dinosterol δD and $\Delta\overline{P_T}$ (Fig. 2.7A,B), (2) log of the botryococcene accumulation rate and. $\Delta\overline{P_E}$ (mean annual rainfall associated with El Niño events based on Niño 3 SSTAs; Fig. 2.7E), and (3) botryococcene δD and $\Delta P^*{}_E$ (mean monthly rainfall during El Niño events based on Niño 3 SSTAs; Fig. 2.7G,H), is broadly consistent with our interpretation. The small variations in the biomarker data over the 20th century relative to those over the 3 kyr record suggest that large hydrologic changes occurred at El Junco Lake in the late Holocene in comparison to those that occurred in the 20th century.

2.3.5 *Inferring changes in residual rainfall from El Junco Lake biomarker records*

Due to the sensitivity of rainfall at El Junco Lake to the climatological position of the eastern Pacific ITCZ, we propose that further climatic information gain be gained by comparing the changes in inferred total climatological rainfall to the changes in climatological rainfall associated with El Niño events. We first assume that changes in climatological rainfall ($\Delta\overline{P_T}$) at El Junco Lake is comprised of two contributions: (1) changes in climatological rainfall associated with changes in El Niño rainfall ($\Delta\overline{P_E}$) and (2) changes in (residual) climatological rainfall due to processes *unassociated* with El Niño ($\Delta\overline{P_R}$; i.e. changes in the climatological position of the ITCZ, changes in the Hadley circulation, or changes in localized convective processes). This is represented in the following equation:

$$\Delta\overline{P_T} = \Delta\overline{P_E} + \Delta\overline{P_R} \quad . \tag{2.4}$$

We therefore propose that changes in residual rainfall (i.e. changes in climatological rainfall unassociated with changes in El Niño rainfall) can be inferred in the following way. From Eq. (2.4), we have:

$$\Delta\overline{P_R} = \Delta\overline{P_T} - \Delta\overline{P_E} \quad .$$

Substituting Eq. (2.2) and (2.3) into (2.4), we therefore obtain

$$\Delta\overline{P_R} = -\beta \cdot \Delta(dinosterol\ \delta D) - \gamma \cdot \Delta(log(F_{botryo})) \quad . \tag{2.5}$$

Since the proportionality constants β and γ are unknown (although both are greater than zero), $\Delta\overline{P_R}$ cannot be fully reconstructed. However, the sign of $\Delta\overline{P_R}$ is constrained for periods in which $-\Delta$(dinosterol δD) and $\Delta(log(F_{botryo}))$ are of opposite sign – that is, for periods in which the inferred change in total climatological rainfall opposes the change in climatological rainfall associated with El Niño events. We thus limit our interpretation of $\Delta\overline{P_R}$ to its sign during such periods. Positive (negative) values of $\Delta\overline{P_R}$ indicate an increase (decrease) in climatological rainfall due to processes unassociated with El Niño.

The primary utility of the $\Delta\overline{P_R}$ reconstructions is to help interpret the source of the most prominent mean rainfall changes at El Junco Lake. E.g. a positive value of $\Delta\overline{P_R}$ indicates that the increase in $\Delta\overline{P_T}$ was due an increase in $\Delta\overline{P_R}$ that was greater than the decrease in $\Delta\overline{P_E}$ (i.e. that the source of the increased climatological rainfall was from non-El Niño contributions). For instance, a positive $\Delta\overline{P_R}$ would result if the increase in climatological rainfall associated with a

southward shifted ITCZ in the eastern Pacific was greater than a coincident decrease in El Niño contributions to climatological rainfall. In contrast, a negative value of $\Delta\overline{P_R}$ indicates that the decrease in $\Delta\overline{P_T}$ was due a decrease in $\Delta\overline{P_R}$ that was greater than the increase in $\Delta\overline{P_E}$ (i.e. that the source of the decreased climatological rainfall was from non-El Niño contributions, such as a northward shift of the ITCZ). The El Junco Lake rainfall reconstructions are shown in Fig. 2.9 for the last 3,000 years.

By design, the periods of inferred $\Delta\overline{P_R}$ highlight periods in which $\Delta\overline{P_T}$ was opposed by $\Delta\overline{P_E}$ (or, equivalently, $\Delta\overline{P_E}$ opposed $\Delta\overline{P_R}$). Such opposing changes in $\Delta\overline{P_E}$ and $\Delta\overline{P_R}$ appear to account for several of the largest hydrologic changes in El Junco Lake over the last 3,000 years (Fig. 2.9).

As previously noted, one interpretation of $\Delta\overline{P_R}$ is in terms of meridional shifts of the climatological position of the ITCZ in the eastern Pacific. This interpretation is supported by the fact that such meridional ITCZ shifts drive the largest rainfall changes on seasonal time scales in the modern environment and that the zonally averaged position of the ITCZ is known to be sensitive to changes in the climate system that affect the energy budget of the atmosphere (Donohoe et al., 2013; Frierson and Hwang, 2012). However, other sources of $\Delta\overline{P_R}$ are possible that are unrelated to meridional displacements of the ITCZ, such as changes in the strength of the annual cycle in the Walker Circulation and changes in local convection.

We provide further support for the interpretation of the El Junco Lake proxy records in terms of changes in El Niño and non-El Niño rainfall contributions through development of an idealized isotope model of El Junco Lake in the next section (Chapter 2.4.1).

2.4 DISCUSSION

2.4.1 *Lake Responses to Climate Change in an Idealized Model*

To facilitate our interpretation of the El Junco Lake biomarker records, we developed an idealized model of the isotope hydrology of El Junco Lake forced with idealized changes in rainfall. This model was originally presented in Atwood and Sachs (2014) and is implemented again in this study in conjunction with our updated interpretation of the rainfall reconstructions. Using this model, we simulated the response of lake δD to a wide range of climate conditions by varying the amount of monthly El Niño and ITCZ rainfall. Because a comprehensive sensitivity

analysis of the model is outside the scope of this study, we present this model solely as a tool to aid in the illustration of our proxy interpretations outlined in the preceding sections. Three representative simulations of the lake model are shown in Fig. 2.10; the details of these simulations can be found in Appendix B.

Analysis of the full suite of model simulations with imposed changes in El Niño and ITCZ rainfall indicates that changes in mean lake δD scale linearly with the prescribed changes in (total) climatological rainfall ($\Delta\overline{P_T}$; Fig. 2.11A). In addition, changes in mean lake δD during El Niño events scale linearly with the prescribed changes in mean monthly El Niño rainfall (ΔP^*_E; Fig. 2.11B). Interestingly, while the presence of strong non-linearities cannot be ruled out in the real world, simulations with the idealized lake model suggest that the relationship between rainfall changes and lake δD may be fairly linear over a wide range of climate perturbations-even in the presence of overflowing lake conditions.

As noted in Chapter 2.3.1, an alternative interpretation of the dinosterol data is that dinoflagellates grow only under non-El Niño conditions in the lake and thus that dinosterol δD reflects the lake δD exclusively during non-El Niño conditions. If this is indeed the case, the model results indicate that changes in lake δD during non-El Niño conditions still roughly scale linearly with $\Delta\overline{P_T}$ ($R^2 = 0.83$, $p < 0.01$; Fig. 2.11D), suggesting that dinosterol δD should still reflect changes in climatological rainfall. However, the lake δD during non-El Niño conditions is more closely related to changes in climatological rainfall associated with processes other than El Niño ($\Delta\overline{P_R}$; $R^2 = 0.93$, $p < 0.01$; Fig. 2.11C), suggesting that if dinoflagellates only grow under non-El Niño conditions in the lake, dinosterol δD could be used directly as a proxy for $\Delta\overline{P_R}$. We prefer to adopt the more conservative approach outlined in Chapter 2.3.4 in which dinosterol δD is interpreted as a proxy for $\Delta\overline{P_T}$ and $\Delta\overline{P_R}$ is only inferred during periods in which $\Delta\overline{P_T}$ opposes $\Delta\overline{P_E}$.

2.4.2 *Changing Hydrologic Conditions in El Junco Lake from Keto-ols*

As an independent assessment of past hydrologic changes of El Junco Lake, a record of mean lake level changes was developed based on the ratio of sedimentary keto-ol isomers derived from algae and ferns. Long chain keto-ols are abundant in El Junco Lake sediment and present additional indicators of paleo-environmental change due to their source-specificity (Atwood et al., 2014). C_{30} ω16-keto-1-ol (structure III, Fig. 2.5) is produced by algae of the class

Eustigmatophyceae (Méjanelle et al., 2003; Volkman et al., 1999; Volkman et al., 1992), while C_{30} ω20-keto-1-ol (structure V, Fig. 2.5) is produced by *Cyathea weatherbyana,* an abundant tree fern around El Junco Lake (Atwood et al., 2014).

Because C_{30} 1,ω20-diols and keto-ols are produced by terrestrial and shoreline ferns, while C_{30} 1,ω16-diols and keto-ols are produced by aquatic algae, it is expected that as the lake level increases (decreases), the input of C_{30} ω20-keto-1-ol relative to C_{30} ω16-keto-1-ol would decrease (increase) due to both an increase (decrease) in the ratio of surface area to circumference of the lake and to an increase (decrease) in the ratio of lake area to catchment area (see Appendix B for more details).

In support of our interpretation of dinosterol δD as a proxy of total mean annual rainfall changes, the ratio of C_{30} ω16-keto-1-ol/ω20-keto-1-ol is anti-correlated to the dinosterol δD values over the last 3 kyr ($R = -0.54$, $p < 0.05$; Fig. 2.8D,E). Of note, however, are the large differences in dinosterol δD and keto-ol records in the near-surface sediment. In particular, the ω16-keto-1-ol/ω20-keto-1-ol ratio decreases to near zero in the upper 5 cm of sediment while the dinosterol δD values are constant or decrease slightly. We hypothesize that these differences are due to a lower degree of diagenetic transformation of diols to keto-ols in the surface sediment relative to deeper sediment (see Appendix C).

Although we place more weight on the dinosterol δD record than on the keto-ol record as a record of climatological rainfall changes (Appendix C), the ratio of C_{30} ω16-keto-1-ol/ω20-keto-1-ol provides an independent record of past lake hydrologic conditions that supports many of the prominent trends in the dinosterol δD record and thus strengthens the paleoclimate interpretations of the biomarker records.

2.4.3 *Comparison with Other El Junco Lake Paleohydrologic Records*

Although we defer an in-depth analysis of the rainfall reconstructions presented here to Chapters 3 and 4, we include a basic comparison between our rainfall reconstructions and those based on El Junco Lake sediment grain size from Conroy et al. (2008). Variations in the volume ratio of silt to clay (where silt and clay are defined based on particle diameters of 3.9–62.5 μm and < 3.9 μm, respectively) were interpreted by Conroy et al. (2008) as a proxy for mean rainfall. We thus compare dinosterol δD from this study to the ratio of silt to clay in Fig. 2.9B. A visual

comparison suggests general coherency in several of the major features present in the two records from ca. 1700 years BP–present. For instance, the minima in dinosterol δD ca. 650–600 years BP (1300–1350 AD), indicative of wet mean conditions, corresponds to a period when the silt/clay ratio was also high. The dinosterol δD and the silt/clay ratio also show agreement ca. 1200–1000 years BP (750–950 AD), when the driest mean conditions inferred from dinosterol δD correspond to a low ratio of silt/clay. The inferred decrease in residual climatological rainfall during this time (Fig. 2.9A), suggests that the decrease in climatological rainfall was due to processes unrelated to El Niño. Poorer agreement between the two records is observed prior to ca. 1700 years BP (250 AD).

Variations in percent sand were interpreted by Conroy et al. (2008) as a proxy for changes in the number and/or magnitude of intense rainfall events associated with El Niño conditions. A comparison between the Conroy et al. (2008) sand record and the El Junco botryococcene records suggests several coherent features, including extrema in these records (indicating a minimum in the amplitude and perhaps frequency of El Niño rainfall events) ca. 1400–1200 years BP (550–750 AD). Leading up to this minimum, El Niño rainfall appears to have declined in this region from ca. 1900–1400 years BP (50–550 AD). Following the period of lowest inferred El Niño rainfall, the records suggest that the amplitude and perhaps frequency of El Niño rainfall events began increasing ca. 1200 years BP (750 AD) and culminating ca. 700 years BP (1250 AD). The records show less agreement over the last 600-700 years; while the El Niño rainfall reconstructions from this study suggest that climatological rainfall associated with El Niño events and El Niño rainfall amplitude remained higher from ca. 700–100 years BP (1250–1850 AD), the sand record suggests that the El Niño rainfall amplitude and/or frequency was similar to, or lower than, modern conditions between ca. 600–100 years BP (1350–1850 AD). Another notable dissimilarity between the records is the maximum in sand abundance ca. 2000–1600 years BP (50 BC–350 AD), which is not mirrored in the El Niño rainfall indices from El Junco Lake.

Any lack of co-variation between our biomarker-derived rainfall reconstructions and the sediment grain size records from Conroy et al. (2008) may result in part from complexities in the relationship between the biomarker records and rainfall on the one hand, and complexities in the relationship between sediment grain size and rainfall on the other. The grain size of sediment in El Junco Lake will be influenced by weathering, which is a complex function of rainfall,

temperature, vegetation type and cover, tectonics, among other things. Therefore, rainfall is just one of several factors that will influence the grain size parameters, and any relationship between rainfall and grain size could be non-stationary in time. Furthermore, the grain size of sediment is likely to be insensitive to the source of the rain, and unable to distinguish between ITCZ rainfall and El Niño rainfall, both of which impact rainfall intensity. Nevertheless, climate changes that are inferred from both the organic geochemical and grain size records should be more robust than interpretations from either data set alone.

Though we believe that our interpretation of the biomarker data is the most straightforward interpretation, we acknowledge that other interpretations are possible. Because the modern-day ecology of El Junco Lake is not well studied, it is possible that the *B. braunii* and dinoflagellate communities vary in different or more complex ways than what is presented in our hypotheses. Further research on the ecology and limnology of El Junco Lake should aid in the evaluation of these hypotheses. In addition, δD values of lipid biomarkers can be influenced by factors other than the δD values of the environmental water, such as the growth rate of the organism, temperature, and salinity (Sachs and Schwab, 2011; Schouten et al., 2006; Wolhowe et al., 2009; Zhang et al., 2009). Due to the extremely low conductivity of El Junco Lake (20 μS/cm; Colinvaux, 1968) and its tropical location, salinity and temperature are unlikely to have varied significantly over the sedimentary record. Growth rate changes are difficult to constrain in the paleo-environment but could have varied due to changes in nutrient concentrations and/or light levels (associated with changes in cloud cover). However, field studies of modern freshwater lake systems indicate that the primary determinant of lipid δD values is water δD values (Huang et al., 2004; Sachse et al., 2004; Sauer et al., 2001). Thirdly, we interpret changes in the hydrologic conditions of the lake to result from changes in rainfall, while changes in the stratus cloud cover (*garúa*), through its impact on evaporation, could also play an important role.

2.4.4 *Revisions to Previous Biomarker-Based El Junco Lake Rainfall Reconstructions*

Interpretation of the biomarker data presented here are consistent with that presented in Atwood and Sachs (2014) and Zhang et al. (2014) with the following exceptions:

1. Atwood and Sachs (2014) use the botryococcene concentration data to fill in missing values of botryococcene δD during periods in which the concentration was too low for isotopic analysis, while Zhang et al. (2014) propose that changes in botryococcene

concentration scale with changes in the frequency of El Niño events. In this study, we acknowledge the value of independent interpretations of the botryococcene δD and concentration data as performed by Zhang et al. (2014), but adopt what we believe to be a more conservative interpretation of the data than that used in their study. Here, we infer that the sedimentary botryococcene accumulation rate is proportional to climatological rainfall associated with El Niño events. In adopting this interpretation, we allow for the possibility that the sedimentary botryococcene accumulation rate is sensitive to changes in the frequency, amplitude, and duration of El Niño rainfall events (as determined through their combined influence on climatological rainfall associated with El Niño events).

2. Due to the revised interpretation of the botryococcene data, another distinction between the results presented in Atwood and Sachs (2014) and this work is the construction and interpretation of changes in residual climatological rainfall (i.e. climatological rainfall that is unassociated with El Niño). Here, we reconstruct changes in residual climatological rainfall ($\Delta\overline{P_R}$) based on differences in the dinosterol δD and botryococcene accumulation rate data (versus the dinosterol δD and botryococcene δD data as in Atwood and Sachs (2014). However, due to the correlation between the down-core botryococcene δD and concentration, our conclusions concerning changes in residual climatological rainfall have not been substantially modified.
3. In an effort to adopt a more conservative approach to the reconstruction of $\Delta\overline{P_R}$ (as compared to that presented in Atwood and Sachs (2014), in this study we define only the sign of $\Delta\overline{P_R}$ (as relative changes in its magnitude are dependent on the proportionality constants β and γ in Eq. 2.5, which are not empirically constrained).

2.5 SUMMARY

Past changes in (total) climatological rainfall and rainfall associated with El Niño events were reconstructed from the Galápagos Islands over the last 3000 years using the sedimentary distribution, accumulation rate, and hydrogen isotope composition of four lipid biomarkers in the sediment of El Junco Lake, San Cristóbal Island. Sedimentary dinosterol δD is interpreted as a proxy for changes in (total) climatological rainfall, while the accumulation rate of C_{34} botryococcene is interpreted as a proxy for changes in climatological rainfall associated with El

Niño events. Botryococcene δD is interpreted as a proxy for changes in the average amplitude of El Niño rainfall events. A fourth hydrologic proxy was developed from the sedimentary ratio of C_{30} ω16-keto-1-ol (produced by aquatic algae) to C_{30} ω20-keto-1-ol (produced by terrestrial and shoreline ferns) that provides a record of past changes in mean lake level. Its co-variation with the dinosterol δD record bolsters the utility of the latter as a record of climatological rainfall changes. These proxy records are further used to reconstruct changes in climatological rainfall associated with processes other than El Niño during periods in which the inferred change in total climatological rainfall opposed the change in climatological rainfall associated with El Niño. An idealized isotope hydrology model of El Junco Lake facilitates the interpretation of these rainfall reconstructions.

A comparison between the biomarker records presented in this study and previously published sedimentary grain size record from El Junco Lake suggests that many of the prominent features in the biomarker records have counterparts in the grain size records, enabling more robust interpretation of rainfall changes in the Galápagos Islands over the past 3000 years. That these records come from the core of the eastern equatorial Pacific where the fundamental dynamics of ENSO and the ITCZ operate and where few such records exist, represents an important contribution toward furthering our understanding of past climate change in this region.

Figure 2.1. A) Map of the Galápagos Islands with location of El Junco Lake represented by the red dot; B) Photo of El Junco Lake taken in Aug. 2011. (Photo credit: Margaret Johnson).

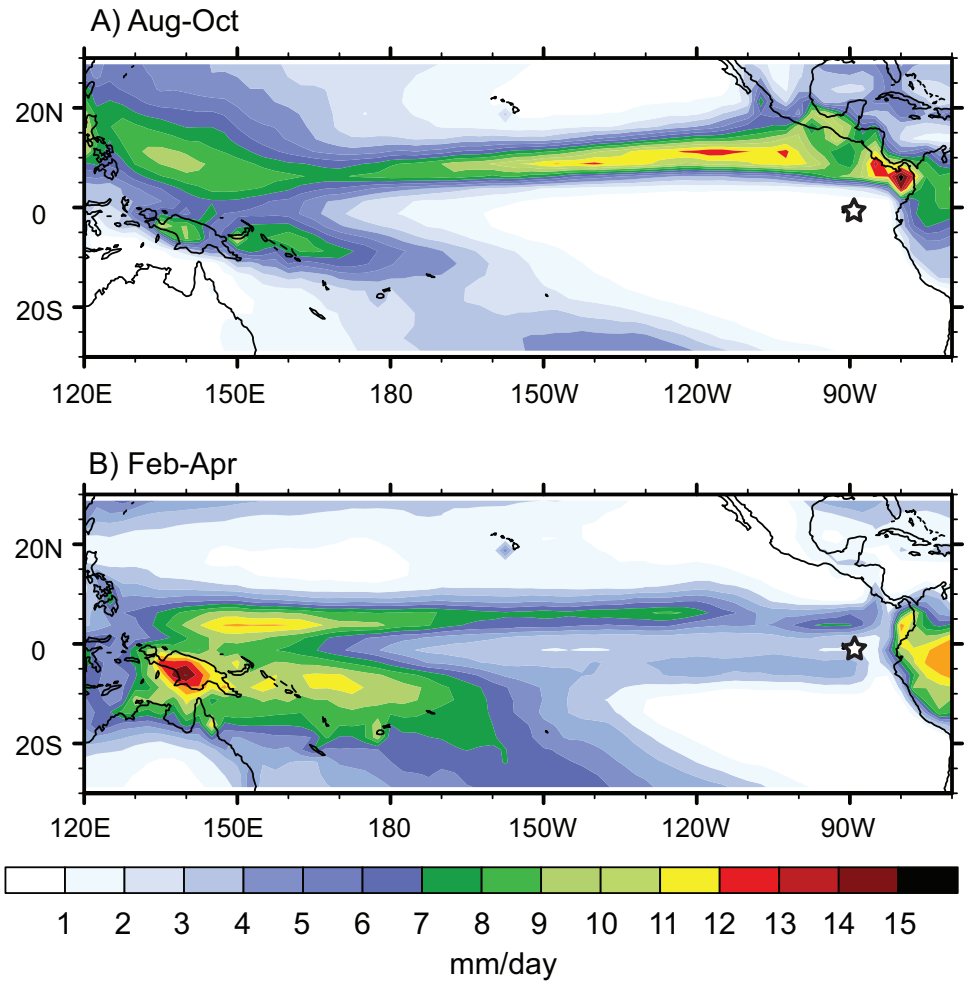

Figure 2.2. Seasonal cycle of the ITCZ in the tropical Pacific. Climatological rainfall from 1980–2010 AD averaged over the peak of the A) dry season (Aug-Oct) and B) wet season (Feb-April). The star indicates the location of San Cristóbal Island, Galápagos. Rainfall

data is from GPCP Version 2.2 Combined Precipitation Data Set (http://www.esrl.noaa.gov).

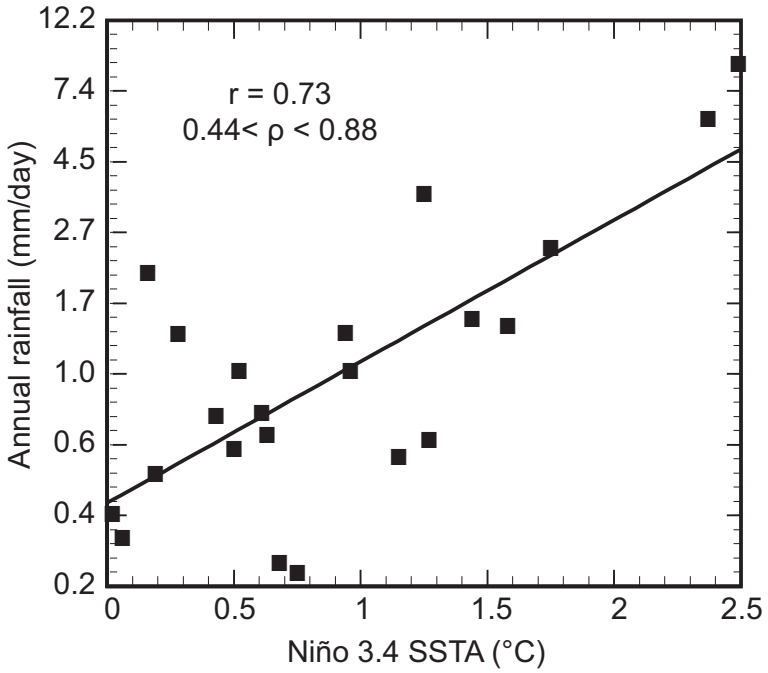

Figure 2.3. Galápagos annually-averaged rainfall (averaged from Aug–July and plotted on a natural log scale) versus positive Niño 3.4 SSTAs averaged over Dec-Feb. The 95% confidence interval for the true correlation coefficient (ρ) is $0.44 < \rho < 0.88$ for a sample size of N = 22. No significant correlation was observed between annual rainfall and negative SSTAs (r = 0.30, N = 23). Rainfall data is from the Puerto Ayora weather station on Santa Cruz Island (http://www.darwinfoundation.org) and spans the period from 1964–2011 AD.

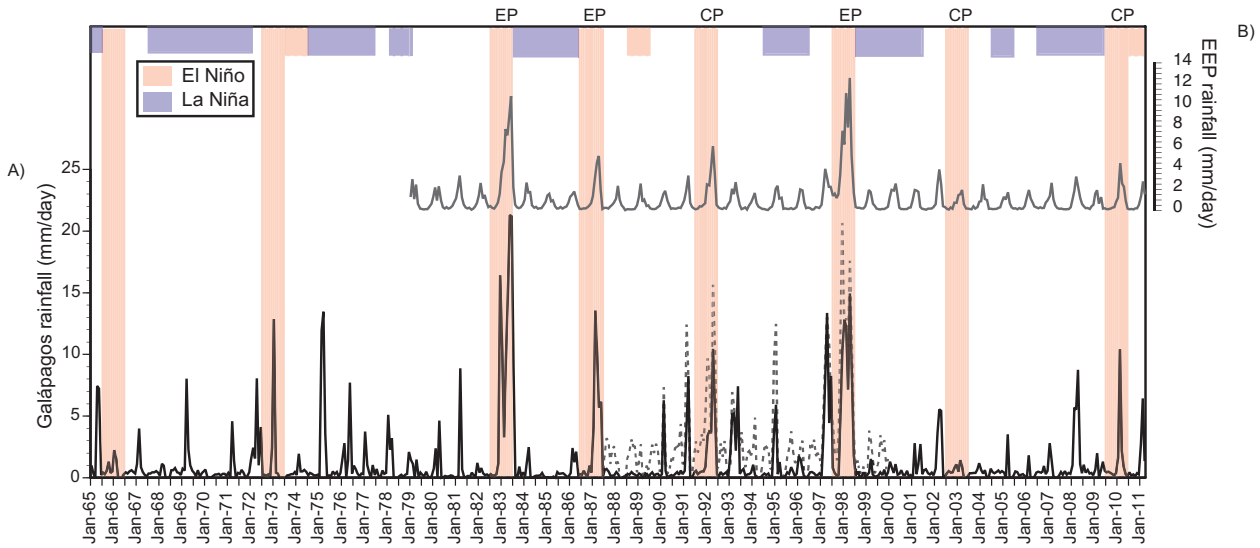

Figure 2.4. Time series of Galápagos rainfall. A) Galápagos lowland rainfall (solid; from the Puerto Ayora weather station at 2 m a.s.l.) and highland rainfall (dashed; from the Bellavista weather station at 194 m a.s.l.) from 1964–2011 AD in comparison with El Niño and La Niña events and B) satellite-based rainfall data averaged over the eastern Pacific along the equator (1 °S to 1 °N, 110 °W to 85°W). Blue shaded bars at the top of the plot indicate La Niña events, while red shaded bars indicate El Niño events. Moderate to strong El Niño events are indicated by full-length bars. El Niño and La Niña events are defined by 3-month running mean Niño 3.4 SSTAs where El Niño (La Niña) events are defined as SSTAs ≥ 0.5 °C (≤ - 0.5 °C) and moderate-to-strong El Niño events are defined as SSTAs ≥ 1.0 °C for three or more consecutive months. SST data was obtained from NOAA ERSST v3b. Rainfall data from Puerto Ayora and Bellavista weather stations on Santa Cruz Island was obtained from the Charles Darwin Research Station (http://www.darwinfoundation.org). Satellite rainfall data was obtained from GPCP Version 2.2 Combined Precipitation Data Set (http://www.esrl.noaa.gov). Designations of EP and CP El Niño events are from Kidwell et al. (2014).

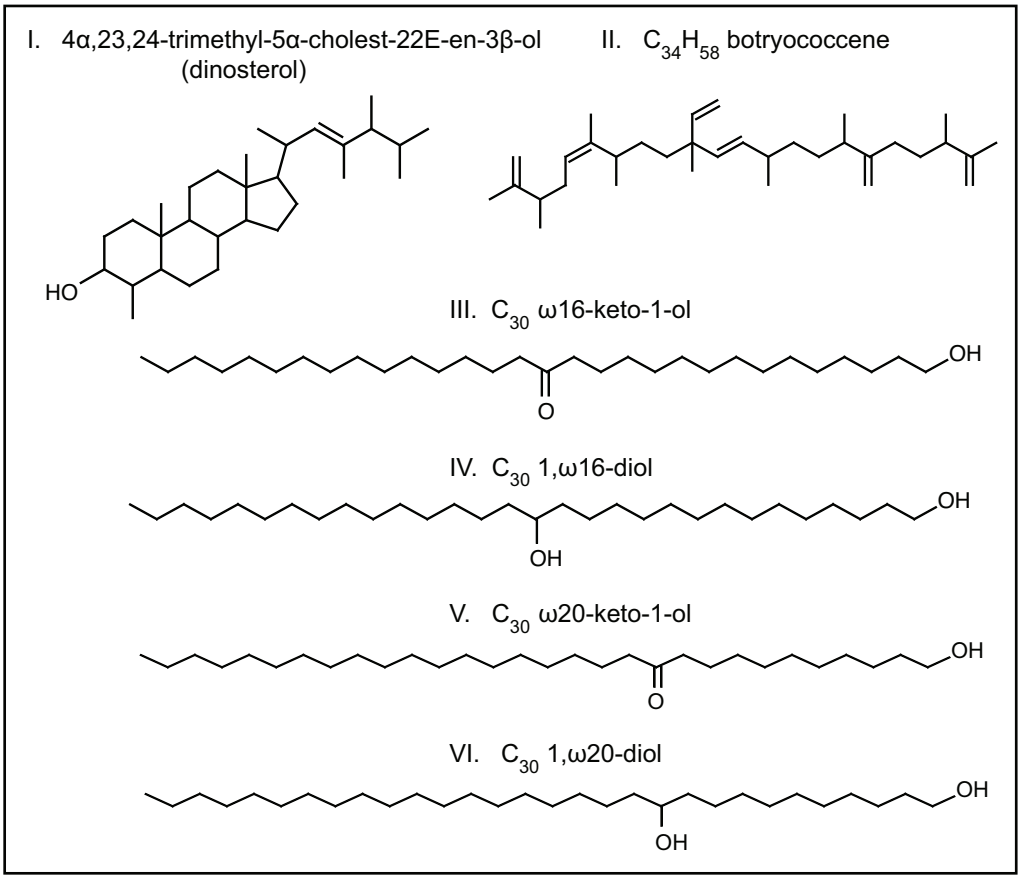

Figure 2.5. Structures of the biomarkers in this study.

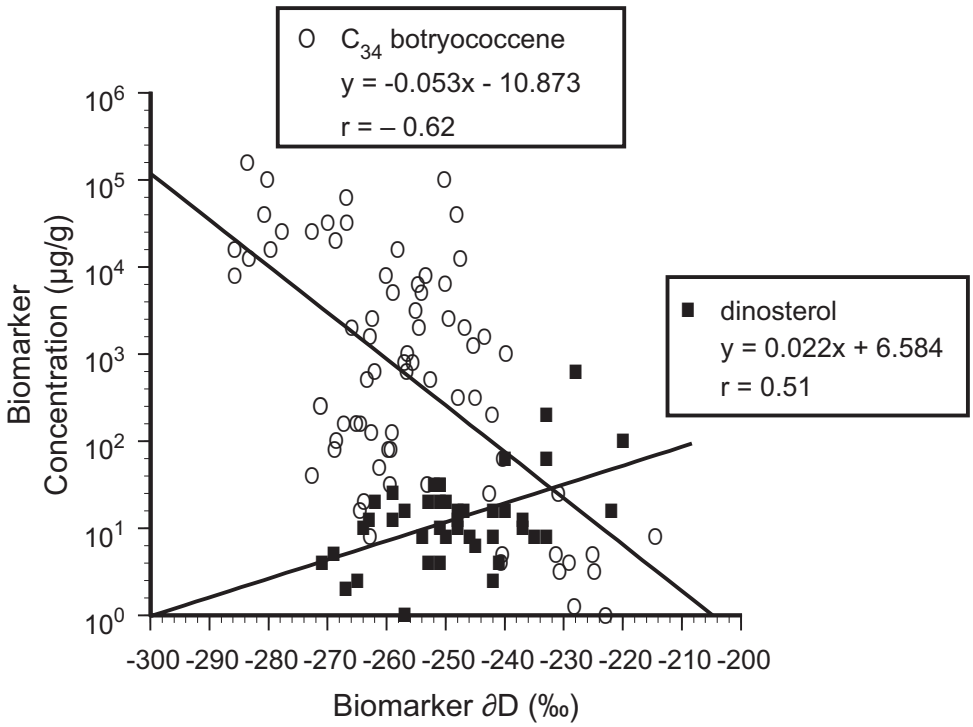

Figure 2.6. C_{34} botryococcene and dinosterol concentration versus δD values for the full 9.1 kyr record (with concentration plotted on a log scale). The 95% confidence interval for the true correlation coefficient (ρ) is $0.47 < \rho < 0.74$; N = 85 for the C_{34} botryococcene data and $0.24 < \rho < 0.71$; N = 41 for the dinosterol data.

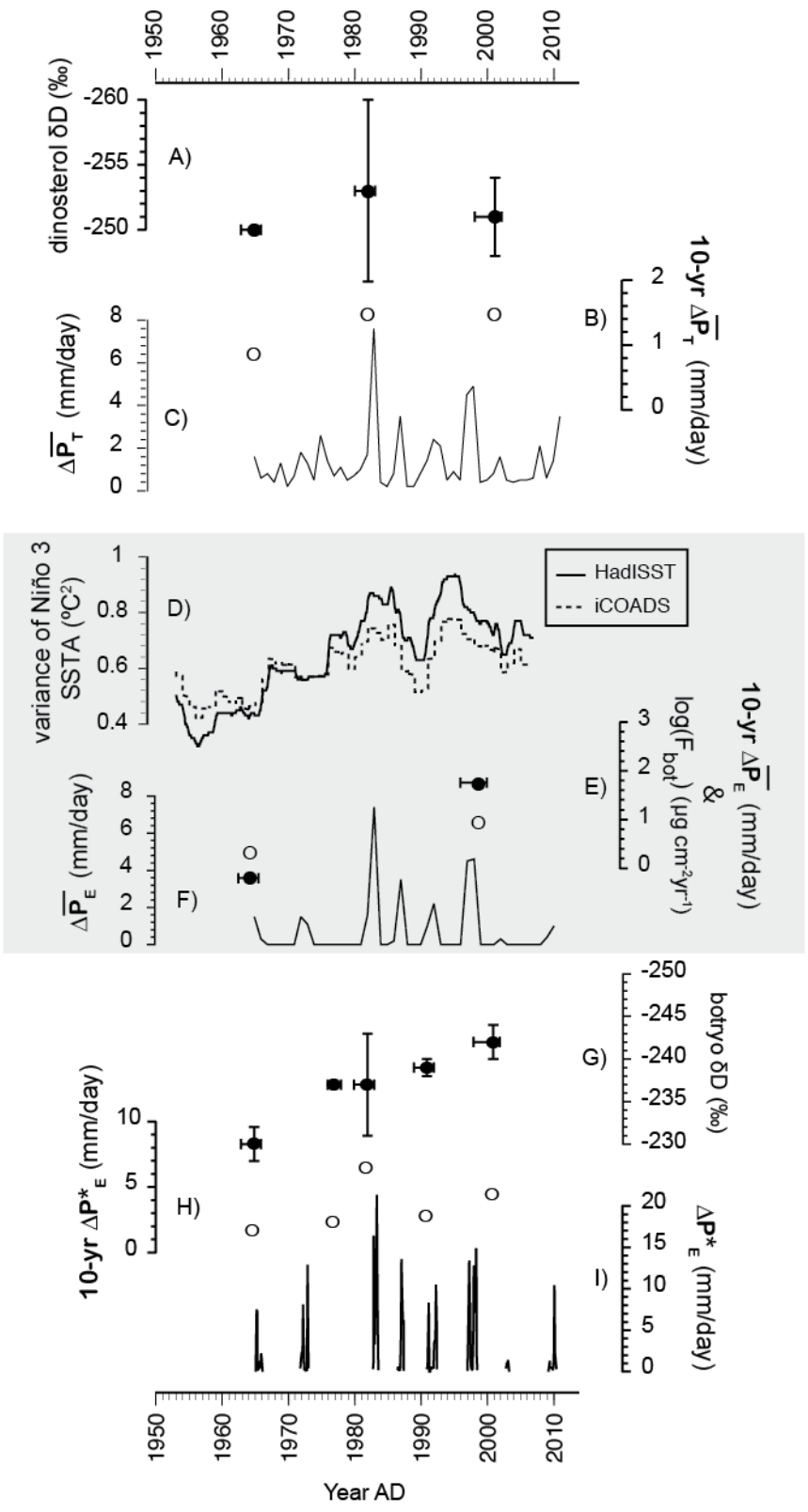

Figure 2.7. El Junco Lake biomarker records plotted with instrumental rainfall and SST data. A) dinosterol δD; B) 10-year average of total mean annual rainfall (10-yr $\Delta\overline{P_T}$)

centered at the dinosterol δD time points; C) total mean annual rainfall ($\Delta\overline{P_T}$); D) variance of Niño 3 SSTAs (20-year sliding window); E) log of the botryococcene accumulation rate (closed circles) and 10-year average of El Niño mean annual rainfall (10-yr $\Delta\overline{P_E}$) centered at the botryococcene time points (open circles); F) mean annual rainfall associated with moderate-to-large El Niño events as determined from Niño 3 SSTAs ($\Delta\overline{P_E}$); G) botryococcene δD; H) 10-year average of El Niño mean monthly rainfall centered at the botryococcene δD time points (10-yr ΔP^*_E); I) monthly rainfall during moderate-to-large El Niño events as determined from Niño 3 SSTAs (ΔP^*_E). Rainfall data is from the Puerto Ayora weather station on Santa Cruz Island (http://www.darwinfoundation.org), SST data is from the iCOADS (http://icoads.noaa.gov/) and HadISST (http://www.metoffice.gov.uk/hadobs/hadisst/) data sets.

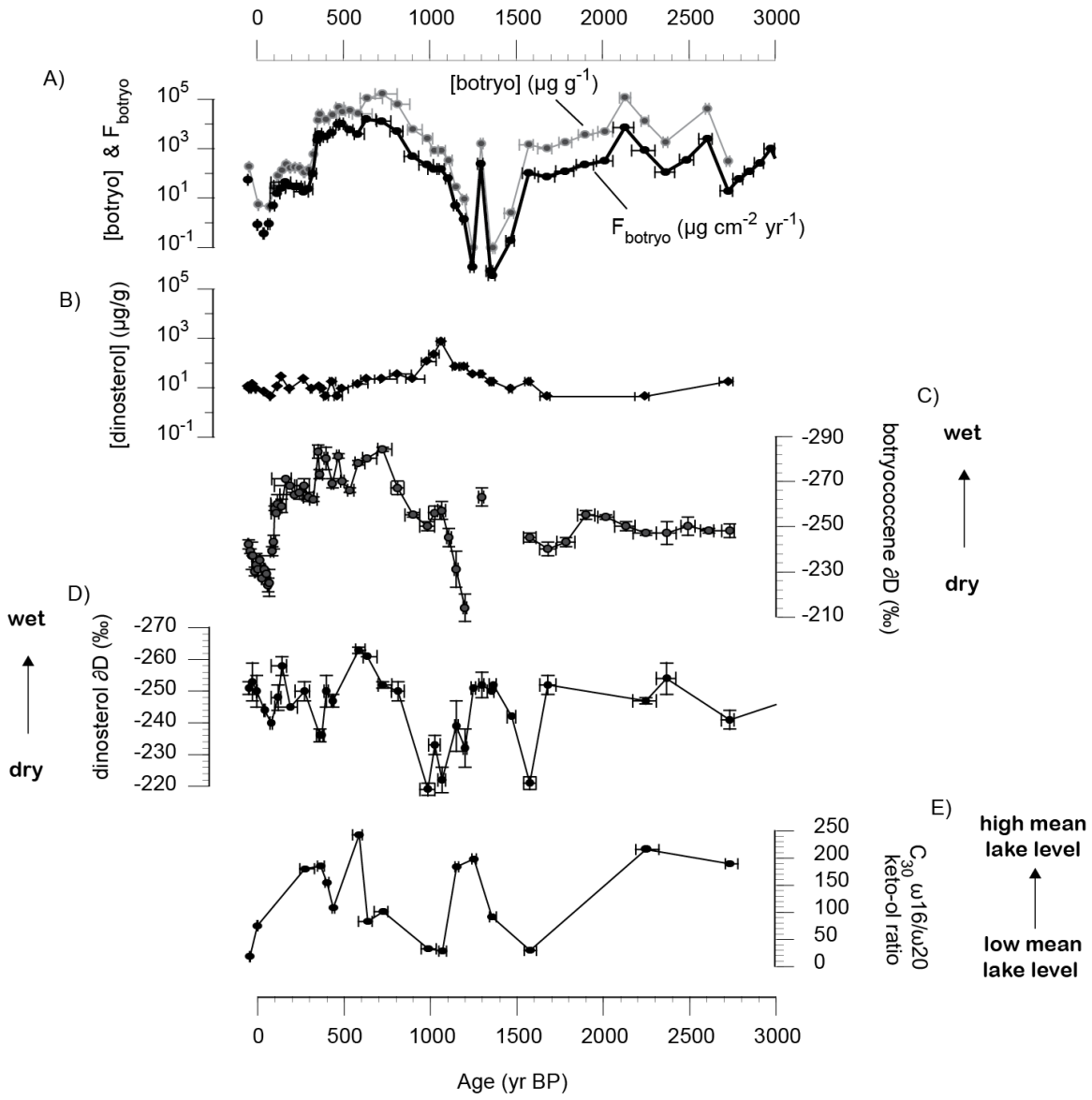

Figure 2.8. Biomarker records from El Junco Lake over the last 3 kyr. A) C_{34} botryococcene concentration and accumulation rate; B) dinosterol concentration; C) C_{34} botryococcene δD; D) dinosterol δD; E) C_{30} ω16-keto-1-ol/ω20-keto-1-ol ratio. The y-error bars represent ±1σ of the triplicate δD measurements and the x-error bars represent the age model uncertainty.

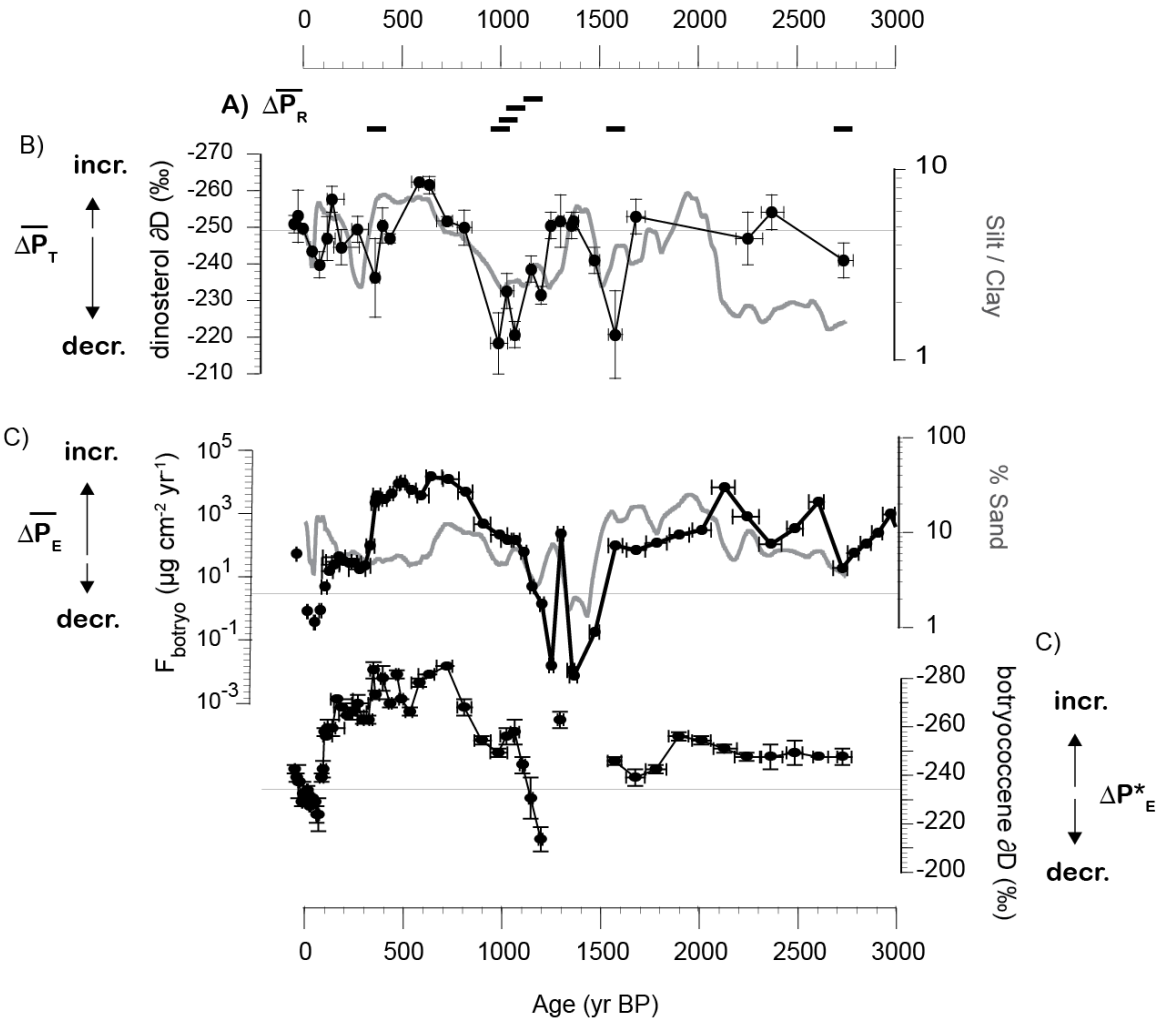

Figure 2.9. El Junco rainfall proxy records plotted with smoothed (70-year running mean) El Junco Lake grain size records from Conroy et al. (2008). A) The sign of the inferred change in climatological rainfall due to processes unassociated with El Niño ($\Delta\overline{P_R}$); B) dinosterol δD (black) plotted with the silt/clay ratio (grey) from Conroy et al. (2008); B) botryococcene accumulation rate (black) plotted on a log scale with percent sand (grey) from Conroy et al. (2008); C) botryococcene δD. The y-error bars are derived from the 1σ error of the triplicate δD measurements and the x-error bars represent the age model uncertainty.

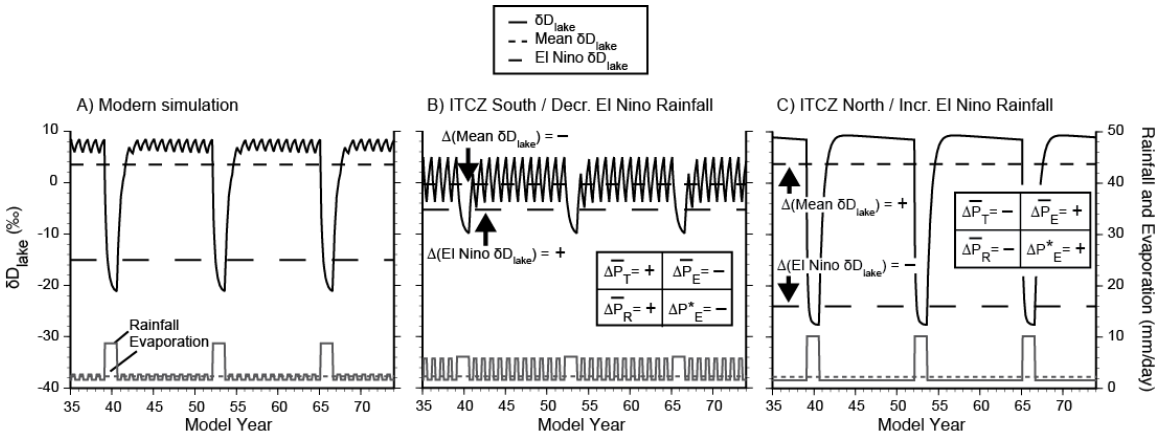

Figure 2.10. Response of climatological mean δD_{lake} and El Niño δD_{lake} (i.e. the mean lake δD during El Niño events) to prescribed changes in ITCZ and El Niño rainfall in the idealized model of El Junco Lake. A) Modern simulation of El Junco Lake; B) simulation in which El Niño rainfall was decreased and ITCZ rainfall was increased; C) simulation in which El Niño rainfall was increased and ITCZ rainfall was decreased (see Appendix B for more details).

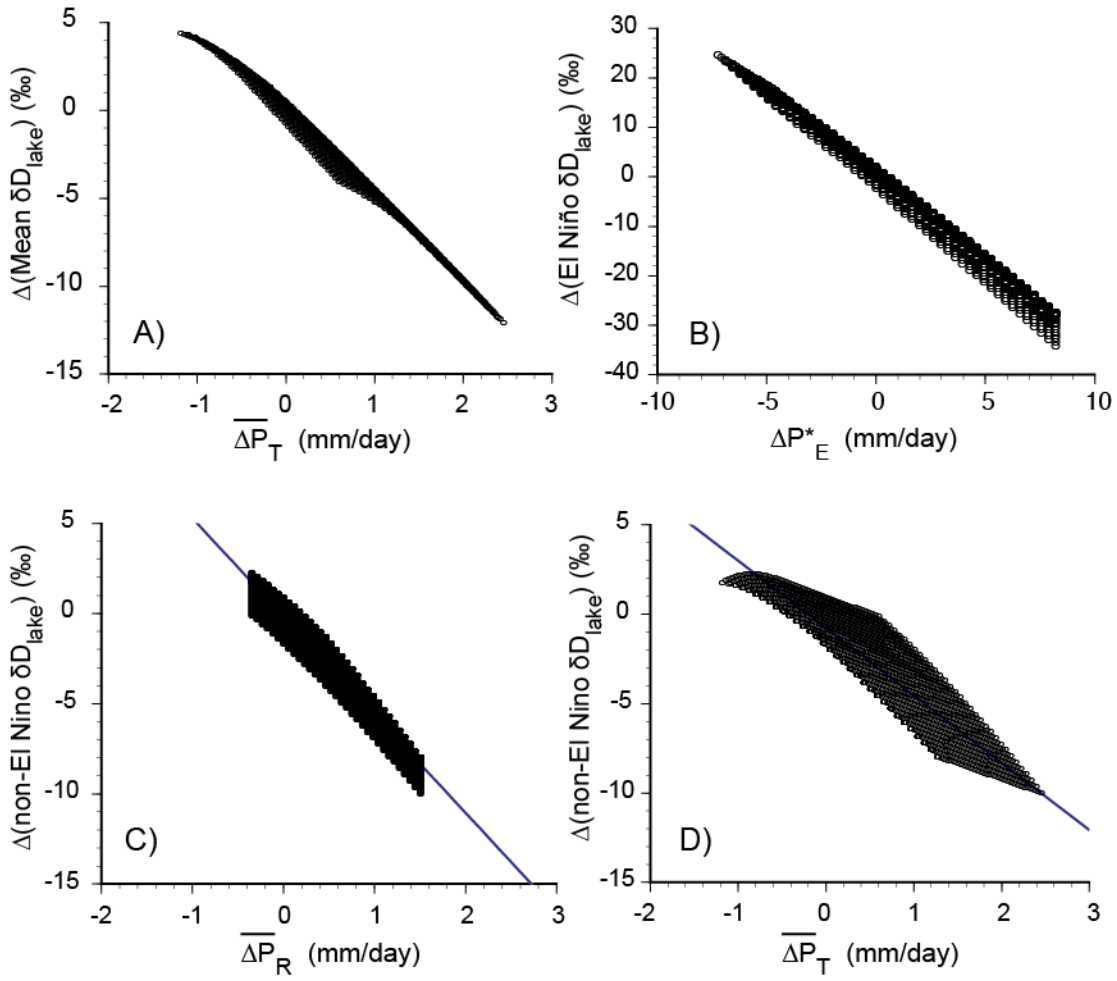

Figure 2.11. Rainfall changes versus lake δD as simulated by an idealized model of El Junco Lake (where changes are defined relative to the modern simulation). A) The change in climatological lake δD versus the change in climatological rainfall ($\Delta\overline{P_T}$); B) the change in mean lake δD during El Niño events (El Niño δDlake) versus change in mean monthly rainfall during El Niño events (ΔP^*_E); C) the change in mean lake δD during non-El Niño conditions versus the change in climatological rainfall not associated with El Niño events ($\Delta\overline{P_R}$); D) the change in mean lake δD during non-El Niño conditions versus the change in total climatological rainfall ($\Delta\overline{P_T}$). Each data point represents output from a simulation with a uniquely prescribed set of El Niño and ITCZ monthly rainfall values.

Chapter 3. EASTERN EQUATORIAL PACIFIC HYDROCLIMATE CHANGES THROUGH THE HOLOCENE

3.1 INTRODUCTION

The tropical Pacific is thought to have played a fundamental role in orbital and millennial scale climate variability due to its ability to dramatically and rapidly reorganize and to project changes across the globe (Chiang, 2009). Because of these characteristics, understanding past climate change necessitates a firm understanding of changes in tropical Pacific climate.

One of the fundamental components of the tropical climate system is the Hadley cell and its ascending branch, the Intertropical Convergence Zone (ITCZ), due to its role in transporting energy out of the deep tropics. Its sensitivity to change is evidenced by the fact that its latitude changes seasonally in response to solar forcing in the tropics and subtropics. Another example of the ability of the tropical Pacific climate to rapidly reorganize and project changes across the globe is the El Niño/Southern Oscillation (ENSO), which governs variations in the global climate on interannual time scales.

Despite the importance of understanding natural variations of the tropical climate, robust reconstructions of the Pacific ITCZ and ENSO spanning the present interglacial period do not currently exist. Such robust reconstructions require proxy records from regions where the fundamental dynamics of ENSO and the Pacific ITCZ operate, but where these signals can be distinguished from one another, and are not obscured by phenomena such as monsoons. Open ocean locations provide a direct signal of tropical Pacific climate variability but proxy indicators of tropical rainfall in open ocean regions are scarce because changes in ocean chemistry associated with rainfall are subtle and marine sediments accumulate slowly.

Expanding upon the method presented in Chapter 2, here we reconstruct past rainfall changes in the Galápagos Islands over the Holocene from the abundance and hydrogen isotope composition of lipid biomarkers in the sediments of El Junco Lake, San Cristóbal Island. Located in the heart of the eastern equatorial Pacific (EEP), with a hydroclimate highly sensitive to movements of the ITCZ and to variations in ENSO (Fig. 3.1) but unaffected by monsoons, these reconstructions offer valuable insight into past tropical Pacific climate change.

3.2 METHODS

Based on the findings presented in Chapter 2, a novel set of proxies are used to infer changes in (total) climatological mean annual rainfall and climatological rainfall associated with El Niño events at El Junco Lake based on paired sedimentary biomarkers. As outlined in Chapter 2, the El Junco Lake rainfall records are constructed from the following:

1. Dinosterol δD, produced by a dinoflagellate of the genus *Peridinium* that is assumed to grow continuously in El Junco Lake, is interpreted as a proxy for climatological mean annual rainfall ($\Delta\overline{P_T}$; Fig. 2.7B).
2. C_{34} botryococcene δD, produced by a single race of the green algae Botryococcus braunii that is assumed to bloom exclusively during El Niño events, is interpreted as a proxy for mean monthly rainfall during El Niño events ($\Delta {P^*}_E$; Fig. 2.7H).
3. The accumulation rate of C_{34} botryococcene (F_{botryo}) is interpreted as a proxy for climatological rainfall associated with El Niño events ($\Delta\overline{P_E}$; Fig. 2.7F; i.e. the total rain that fell during El Niño events divided by the total amount of time in the sedimentary interval).
4. Changes in climatological rainfall unassociated with El Niño events ($\Delta\overline{P_R}$) can be constrained for periods in which the inferred change in total climatological rainfall opposes the change in climatological rainfall associated with El Niño events – that is, for periods in which $-\Delta(dinosterol\ \delta D)$ and $\Delta(log(F_{botryo}))$ are of opposite sign.

While both botryococcene δD and F_{botryo} provide a measure of El Niño rainfall, botryococcene δD should only be sensitive to changes in the amplitude of El Niño rainfall events, while F_{botryo} should be sensitive to changes in the amplitude, frequency, and/or duration of El Niño rainfall events (as determined through their combined influence on climatological El Niño rainfall).

As rainfall at El Junco Lake is highly sensitive to El Niño events, as well as to large-scale climate phenomena unassociated with ENSO, such as the climatological position of the eastern Pacific ITCZ, we propose that $\Delta\overline{P_R}$ is a useful indicator of changes in these (non-El

Niño) climate processes. An in-depth description of the proxies and their climatic interpretations can be found in Chapter 2.3.

3.3 RESULTS

3.3.1 *Hydroclimate Changes in the Eastern Equatorial Pacific Over the Holocene*

The 9,100-year biomarker records and the rainfall indices derived from those records are shown in Fig. 3.1. Multi-century oscillations of total mean annual rainfall ($\Delta\overline{P_T}$) appear to have occurred at El Junco Lake over the Holocene (Fig. 3.1B). While low sampling resolution limits our interpretation of the data in much of the early Holocene, some of the highest mean annual rainfall is inferred at El Junco Lake is ca. 8500-8200 yr BP, followed by reduced mean annual rainfall (relative to present) ca. 7800 and 7100 yr BP. The mid-Holocene is generally characterized by increased mean annual rainfall at El Junco Lake, with local maxima ca. 5400-5000 and 4000 yr BP. Large changes in $\Delta\overline{P_T}$ also appear to have occurred during the late Holocene. The lowest values of $\Delta\overline{P_T}$ (i.e. the driest mean conditions) of the entire Holocene are inferred during the onset of the Medieval Warm Period, ca. 1200-950 yr BP (750-1000 AD) and ca. 1600 yr BP, followed by the highest values (i.e. the wettest mean conditions) of the late Holocene during the onset of the Little Ice Age (LIA), ca. 700-500 yr BP (1250-1450 AD).

Large, multi-centennial oscillations in the amplitude and variability of El Niño rainfall ($\Delta\overline{P_E}$ and ΔP^*_E) also appear to have occurred in this region throughout the Holocene, as inferred from the botryococcene δD and accumulation rate records (Fig. 3.1C,D; Zhang et al., 2014). The early Holocene (9100-5600 yr BP) is characterized by highly variable El Niño rainfall at the multi-centennial time scale, while the mid-Holocene (5600-4000 yr BP) is generally characterized by decreased amplitude and possibly frequency of El Niño rainfall events. The late Holocene is generally characterized by increased El Niño rainfall relative to present (ca. 3300-350 yr BP), aside from the dramatic reduction in El Niño rainfall that occurred ca. 1350 -1250 yr BP. Step-wise decreases in El Niño rainfall occurred ca. 350 and 100 yr BP, followed by small but persistent increases over the last 100 years.

Increased climatological rainfall due with processes unassociated with El Niño (i.e. positive values of $\Delta\overline{P_R}$) is inferred ca. 8500-8200, 5400-5000 and 4000 yr BP, while decreased rainfall (negative values of $\Delta\overline{P_R}$) is inferred ca. 7800 yr BP, 2700 yr BP, and in a number of intervals

over the last two millennia, including ca. 1600 yr BP, 1200-950 yr BP (750-1000 AD), and 350 yr BP (1600 AD; Fig. 3.1A).

3.4 DISCUSSION

3.4.1 *Global Context of Eastern Pacific Mean Rainfall Changes During the Holocene*

Many of the most pronounced changes in total mean annual rainfall inferred from the El Junco biomarker records coincide with similar hydroclimate changes in central-eastern Brazil as inferred from oxygen isotope ratios in cave deposits (Fig. 3.2B-D; Novello et al., 2012; Strikis et al., 2011). Both sets of hydroclimate reconstructions indicate that some of the wettest conditions of the Holocene occurred ca. 8500-8000 and 5500-5000 yr BP, while a wet event of lower amplitude occurred ca. 4000 yr BP. In addition, the wet conditions ca. 8400-8100 yr BP recorded in the Brazilian stalagmite were followed by a dry event ca. 7800 yr BP of similar amplitude and duration (300 years; Strikis et al., 2011); similarly dry conditions during this time are also observed in the El Junco Lake dinosterol δD record. Finally, the driest mean conditions of the Holocene are inferred at El Junco Lake ca. 1200-950 yr BP (750 AD-1000 AD), overlapping with the early Medieval Warm Period (MWP; e.g. Diaz et al., 2011; Graham et al., 2011; Seager et al., 2007). While the Lapa Grande speleothem record terminates ca. 1300 yr BP, a speleothem record from nearby Diva de Maura Cave, 380 km NE of Lapa Grande Cave, also indicates anomalously dry conditions in central-eastern Brazil during this time (Fig. 3.2C; Novello et al., 2012). These periods of pronounced changes in (total) climatological rainfall at El Junco Lake are coeval with opposing changes in climatological rainfall associated with El Niño events (Fig. 3.1). Thus, these prominent changes in climatological rainfall appear to be driven by processes other than El Niño, e.g. changes in climatological rainfall associated with movements of the ITCZ.

During the period of extreme aridity at El Junco Lake (ca. 1200-950 yr BP; 750-1000 AD), widespread aridity is a prominent feature of tropical hydroclimate records that span South America (Fig. 3.2D; Apaestegui et al., 2014; Bird et al., 2011b; Haug et al., 2003) to Saharan Africa (Shanahan et al., 2009; Street-Perrott et al., 2000). Aridity is also found in Mesoamerica during this time, where it is suggested to have played a role in the collapse of the Maya civilization during the Terminal Classic Period (Fig. 3.2E,F; Bhattacharya et al., 2015; Curtis et

al., 1996; Hodell et al., 2001). Runoff records from the Cariaco Basin suggest that extended regional aridity in the Terminal Classic Period (ca. 1250-1050 yr BP; 700-900 AD) was punctuated by intense, multiyear droughts in Venezuela (Haug et al., 2003). In contrast, during the second half of this interval (ca. 1050-900 yr BP; 900-1050 AD), wet conditions prevailed in this region. While a common forcing mechanism of these widespread tropical hydroclimate changes has not been identified, evidence of increased SSTs in the northern tropical Atlantic (Apaestegui et al., 2014; Feng et al., 2008; Keigwin, 1996; Wurtzel et al., 2013) possibly related to a strengthening of the AMOC during this time (Wurtzel et al., 2013), suggest a shared mechanism for the aridity in the Galápagos Islands, Brazil, and Peru and for the wet event in northern South America via a northward migration of the ITCZ (in the eastern Pacific and western Atlantic basins) and a weakening of the South American summer monsoon. Mechanisms of Mesoamerican and Saharan aridity during this time are unclear, but may have involved teleconnections from the tropical Atlantic and/or Pacific (Bhattacharya et al., 2015; Feng et al., 2008).

Concerning the periods of highest total mean annual rainfall at El Junco Lake (inferred ca. 8500-8200, 5400-5000, and 4000 yr BP and during the onset of the LIA (ca. 700 – 500 years BP; 1250-1450 AD), there is evidence to suggest that these events broadly correspond to periods of notable changes in tropical hydroclimate and high latitude climate. We discuss the global signature of each of these intervals below.

The period ca. 8500-8000 yr BP marked the largest and most abrupt climate event of the Holocene. During this period, proglacial Lake Agassiz is thought to have catastrophically drained into the North Atlantic, causing a dramatic slowdown of the AMOC and pronounced cooling in the North Atlantic, Europe, and Greenland (Fig. 3.2I; e.g. Barber et al., 1999; Ellison et al., 2006; Kleiven et al., 2008; Kobashi et al., 2007; LeGrande et al., 2006; Lewis et al., 2012). Evidence of weakened summer monsoons in East Asia (Fig. 3.2G) and India (Fig. 3.2H), and an intensified South American summer monsoon (Fig. 3.2D) during this time suggest that the associated climate perturbations extended to the tropics. This anti-phased behavior of weakened NH and strengthened SH monsoon systems indicates that a large-scale southward shift in tropical continental precipitation occurred during this time. Further, the El Junco Lake hydroclimate records suggest that the southward shift in tropical precipitation may have extended into the tropical Pacific, as the inferred increase in non-El Niño climatological rainfall is consistent with

a southward shifted ITCZ in the eastern equatorial Pacific ca. 8500-8200 yr BP (Fig. 3.2A). The climate event ca. 8200 yr BP and its signature in the tropical Pacific is the focus of Chapter 4.

While not linked to a similarly well-constrained climate event, the wet conditions at El Junco Lake and central-eastern Brazil ca. 5400-5000 and 4000 yr BP also broadly coincide with high latitude climate changes, including glacial advances in Asia, North America and Scandinavia (Fig. 3.2K; Mayewski et al., 2004; Stuiver and Grootes, 2000) and an influx of cold, fresh, ice-bearing water from the Nordic and Labrador Seas into the North Atlantic (as indicated by ice-rafted debris records; Fig. 3.2J; Bond et al., 2001). A combination of orbital and solar forcing, and variability in the AMOC have been invoked to explain the cooling and ice rafting during these times (e.g. Wanner and Butikofer, 2008). Further evidence of high latitude climate change ca. 6000-5000 yr BP includes changes in high latitude atmospheric circulation patterns (inferred from large variations in aerosol concentrations in Greenland and Antarctic ice (Mayewski and Maasch, 2006; O'Brien et al., 1995), and substantially reduced North Atlantic Deep Water production (inferred from carbon isotope ratios of benthic forams; Oppo et al., 2003), suggesting that this period constituted one of the most severe climate events of the Holocene interval. Increased aridity throughout parts of the northern tropics coincided with these high latitude climate changes (Magny and Haas, 2004 and references therein), including aridity in the Middle East (Fig. 3.3H; Fleitmann et al., 2003), and Africa (Chalie and Gasse, 2002; Itambi et al., 2010; Russell et al., 2003) ca. 5600-5000 yr BP and the abrupt end to the African Humid Period ca. 5500 yr BP (deMenocal et al., 2000).

The wet conditions at El Junco Lake and central-eastern Brazil ca. 4000 yr BP, while corresponding with a weaker high latitude climate signal, is widely recognized as a time of extreme drought in the Northern Hemisphere tropics and extratropics, including regions of the Asian, North American, and North African summer monsoons (Booth et al., 2005; Cosford et al., 2008; Gupta et al., 2005; Itambi et al., 2010; Shanahan et al., 2006; Staubwasser et al., 2003; Thompson et al., 2002; Wang et al., 2005a). Indeed, the collapse of major civilizations in India, Egypt, Mesopotamia, and China have been attributed to aridity during this time (Liu and Feng, 2012 and references therein).

Finally, the wettest mean conditions of the late Holocene (ca. 700-500 yr BP; 1250-1450 AD) are inferred at El Junco Lake during onset of the Little Ice Age, encompassing one of the most volcanically active centuries of the last 1500 years (ca. 1200-1300 AD; Gao et al., 2008)

and characterized by high latitude cooling and expanded Arctic sea ice (Miller et al., 2012). Hydroclimate records indicate widespread changes in monsoon systems during the early LIA, including megadroughts in India (Sinha et al., 2011) ca. 650-500 yr BP (1300-1450 AD), a weakened East Asian summer monsoon ca. 500 yr BP (1450 AD; Fig. 3.2F; Wang et al., 2005a) and the onset of a strengthened South American summer monsoon (Vuille et al., 2012).

In contrast to the widespread aridity in the northern tropics during these four periods (8500-8200, 5400-5000, 4000, and 700-500 yr BP), the Galápagos Islands and parts of South America appear to have experienced anomalously wet conditions during these intervals; in the case of El Junco Lake, these periods correspond to the wettest mean conditions of the Holocene. Taken together, these hydroclimate records suggest that tropical rainfall patterns may have been shifted southward during these intervals, possibly in association with high latitude climate changes. Any inferred connection between the tropical and high latitude climate could have involved a two-way interaction—for instance, while shifts of the zonally averaged ITCZ have been shown to occur in direct response to high latitude cooling (e.g. Chiang and Bitz, 2005), externally-forced tropical hydroclimate changes can contribute to high latitude climate changes, e.g. through the influence of changes in moisture transport on the circulation of the atmosphere and ocean (Cane, 1998; Chiang, 2009; Gupta et al., 2005; Mignot and Frankignoul, 2005; Schmittner and Clement, 2002; Yuan, 2004). Through this and other mechanisms, the tropics may have played a central role in determining the character of global climate change during the Holocene.

3.4.2 *Changes in Eastern Pacific El Niño Rainfall Through the Holocene*

The El Junco Lake botryococcene records indicate three distinct periods of El Niño rainfall during the Holocene (Fig. 3.1), as also described in Zhang et al. (2014). The early Holocene (9100-5600 yr BP) is characterized by highly variable El Niño rainfall at the multi-centennial time scale (as inferred from large oscillations in both $\Delta\overline{P_E}$ and ΔP^*_E; Fig. 3.1C,D). The mid-Holocene (5600-4000 yr BP) is generally characterized by decreased climatological rainfall associated with El Niño events (Fig. 3.1C), perhaps driven by decreased amplitude of El Niño rainfall events (Fig. 3.1D). In contrast, the late Holocene is generally characterized by increased El Niño rainfall (positive $\Delta\overline{P_E}$ and ΔP^*_E) relative to present ca. 3300-350 yr BP, aside from the dramatic reduction in El Niño rainfall that occurred ca. 1350-1250 yr BP.

Notable similarities between the El Niño rainfall reconstructions from El Junco Lake and other Holocene ENSO records include evidence for a persistently weak ENSO during the mid-Holocene, as supported by a number of hydroclimate and sea surface temperature records from the tropical Pacific (Conroy et al., 2008; Donders et al., 2008; Koutavas et al., 2006; Koutavas and Joanides, 2012; Riedinger et al., 2002). In addition, evidence of variable ENSO during the early Holocene, as inferred from the El Junco Lake biomarker records, has also been documented from coral records in the tropical Pacific (Cobb et al., 2013).

However, other features of the El Niño rainfall reconstructions from El Junco Lake during the Holocene do not appear to have counterparts in coral-based ENSO reconstructions. For instance, the El Junco Lake biomarker records suggest that the amplitude and possibly frequency of El Niño rainfall events was increased throughout most of the last three millennia relative to the 20th century. In contrast, western and central Pacific coral records indicate that ENSO variance (as measured through coral δ18O, which records both changes in SST and rainfall) was higher during the 20th century than almost any other period through the Holocene (Cobb et al., 2013; Tudhope et al., 2001). We propose that these differences may be due to disparate processes driving changes in El Niño rainfall versus ENSO SST anomalies and/or the disparate location of the proxy reconstructions. As outlined in Chapter 2.3.2, modeling studies have demonstrated that the frequency and amplitude of rainfall anomalies in the eastern Pacific during El Niño events can change without a corresponding change in the amplitude of SSTAs associated with ENSO (Cai et al., 2014). Possible mechanisms of the inferred increase in eastern Pacific El Niño rainfall during the late Holocene therefore include: (1) a decreased zonal SST gradient in the tropical Pacific (e.g. Cai et al., 2014), (2) increased variance of ENSO SSTAs, and/or (3) a shift in the distribution of ENSO SST anomalies to more eastern Pacific (versus central Pacific) El Niño events. SST reconstructions based on Mg/Ca ratios in planktonic forams provide evidence for higher mean eastern equatorial Pacific SSTs in the late Holocene (ca. 4000-1500 yr BP) as compared to the mid-Holocene (6000-4000 yr BP; Koutavas et al., 2006). It is therefore possible that the increase in El Niño rainfall from the mid- to late Holocene occurred in response to surface warming in the eastern equatorial Pacific. Reconstructions of central Pacific SST anomalies that span the last millennium (Cobb et al., 2003; Cobb et al., 2013; Emile-Geay et al., 2013) provide no indication of higher than modern ENSO variance ca. 900-350 yr BP, however, mean SSTs and interannual SST anomalies in the eastern equatorial Pacific are poorly

constrained during this time (e.g. Emile-Geay et al., 2013). Therefore, we propose that increased mean SSTs in the eastern Pacific and/or a shift in the distribution of ENSO SSTAs to more eastern Pacific events may have been responsible for the higher than modern El Niño rainfall in the Galápagos Islands over most of the late Holocene.

3.4.3 *Alternating Holocene Changes in ENSO and the ITCZ Versus Persistent Trends*

The Holocene-scale trends in eastern equatorial Pacific rainfall inferred from the El Junco Lake biomarker records differ markedly from most continental hydroclimate records from the tropics. For instance, a monotonic southward shift in the position of the ITCZ through the Holocene in association with changes in orbital precession has been inferred from a number of iconic continental-based hydroclimate records, including runoff records from the Cariaco Basin off the north coast of Venezuela (Fig. 3.3B; Haug et al., 2001), speleothem and authigenic lacustrine calcite oxygen isotope records from the Peruvian and Venezuelan Andes (Fig. 3.3C; Bird et al., 2011a), and speleothem records from the Asian and Australasian monsoon regions (Fig. 3.2F,G; Cosford et al., 2008; Fleitmann et al., 2003; Partin et al., 2007; Wang et al., 2005a).

In contrast to these studies, we find no evidence for monotonic trends in rainfall associated with the eastern Pacific ITCZ from the biomarkers records in El Junco Lake. A shift of the eastern Pacific ITCZ even slightly northward from its modern position would be expected to bring substantially drier conditions to El Junco Lake; such drier than modern conditions are not reflected in the reconstructions of either $\Delta\overline{P_T}$ or $\Delta\overline{P_R}$ through the Holocene. Instead, the proxy records indicate alternating changes in total climatological rainfall and climatological rainfall associated with processes other than El Niño in the eastern equatorial Pacific throughout the Holocene (Fig. 3.3A).

Further, while the El Junco Lake biomarker records support of the long-standing paradigm of a persistently weak ENSO during the mid-Holocene, they do not provide evidence for an increasing trend in El Niño activity through the Holocene, as inferred from reflectance data in Peruvian lake sediment on the eastern flank of the Andes (Fig. 3.3D-F; Moy et al., 2002).

The El Junco Lake biomarker records thus seem to suggest that, unlike monsoons, ENSO and the position of the Pacific maritime ITCZ do not respond linearly to precessional forcing. This finding highlights that the conventional use of the term ITCZ for all tropical rainfall zones can be misleading, as tropical rainfall is comprised of a number of disparate regions governed by

distinct processes. We argue that the El Junco Lake biomarker records are distinct from the continental-based proxy records mentioned above in that they directly reflect changes in the eastern equatorial Pacific climate, thereby providing unique insight into the dynamics of ENSO and the well-defined maritime ITCZ in this region.

3.5 SUMMARY

The El Junco Lake biomarker records presented here provide a novel record of past hydroclimate changes in the eastern equatorial Pacific through the Holocene. Multi-decadal to millennial oscillations of (total) climatological rainfall and rainfall associated with El Niño events are inferred over the Holocene. Mechanisms of El Niño rainfall variations recorded at El Junco Lake over the Holocene could include basin-wide changes in the variance of ENSO SST anomalies, a shift in the distribution of ENSO SST anomalies to eastern Pacific versus central Pacific El Niño events, and/or changes in the mean tropical Pacific SST gradient. Most of the large (total) climatological rainfall changes that occurred at El Junco Lake during the Holocene were opposed by changes in climatological rainfall associated with El Niño events, from which we infer that the changes in total climatological rainfall were driven by non-El Niño processes (e.g. meridional displacements of the eastern Pacific ITCZ).

Most of the pronounced changes in total mean annual rainfall inferred from the El Junco biomarker records have counterparts in hydroclimate reconstructions from central-eastern Brazil and coincide with periods of notable tropical hydroclimate and high latitude climate changes. For example, the driest conditions of the Holocene are inferred at El Junco Lake ca. 1200-950 yr BP (750 AD-1000 AD), at a time when widespread aridity was recorded in tropical hydroclimate records that span Mesoamerica, South America and Saharan Africa. Anomalously wet conditions at El Junco Lake and central-eastern Brazil ca. 8500-8000, 5500-5000, and 4000 yr BP appear to have broadly coincided with widespread northern tropical aridity, suggesting that tropical rainfall patterns may have been shifted southward during these intervals, possibly in association with high latitude climate changes.

In contrast to several well-cited continental hydroclimate records from the tropics, the El Junco Lake biomarker records do not provide support for monotonic trends in ENSO variability or the position of the ITCZ in the eastern equatorial Pacific through the Holocene. Instead, the data indicate alternating changes in El Niño and non-El Niño climatological rainfall in the

eastern equatorial Pacific throughout the Holocene. These records thus seem to suggest that, unlike monsoons, ENSO and the position of the eastern Pacific ITCZ do not respond linearly to precessional forcing. We argue that the hydroclimate records presented here provide unique insight to the evolution of the eastern equatorial Pacific climate system through the Holocene.

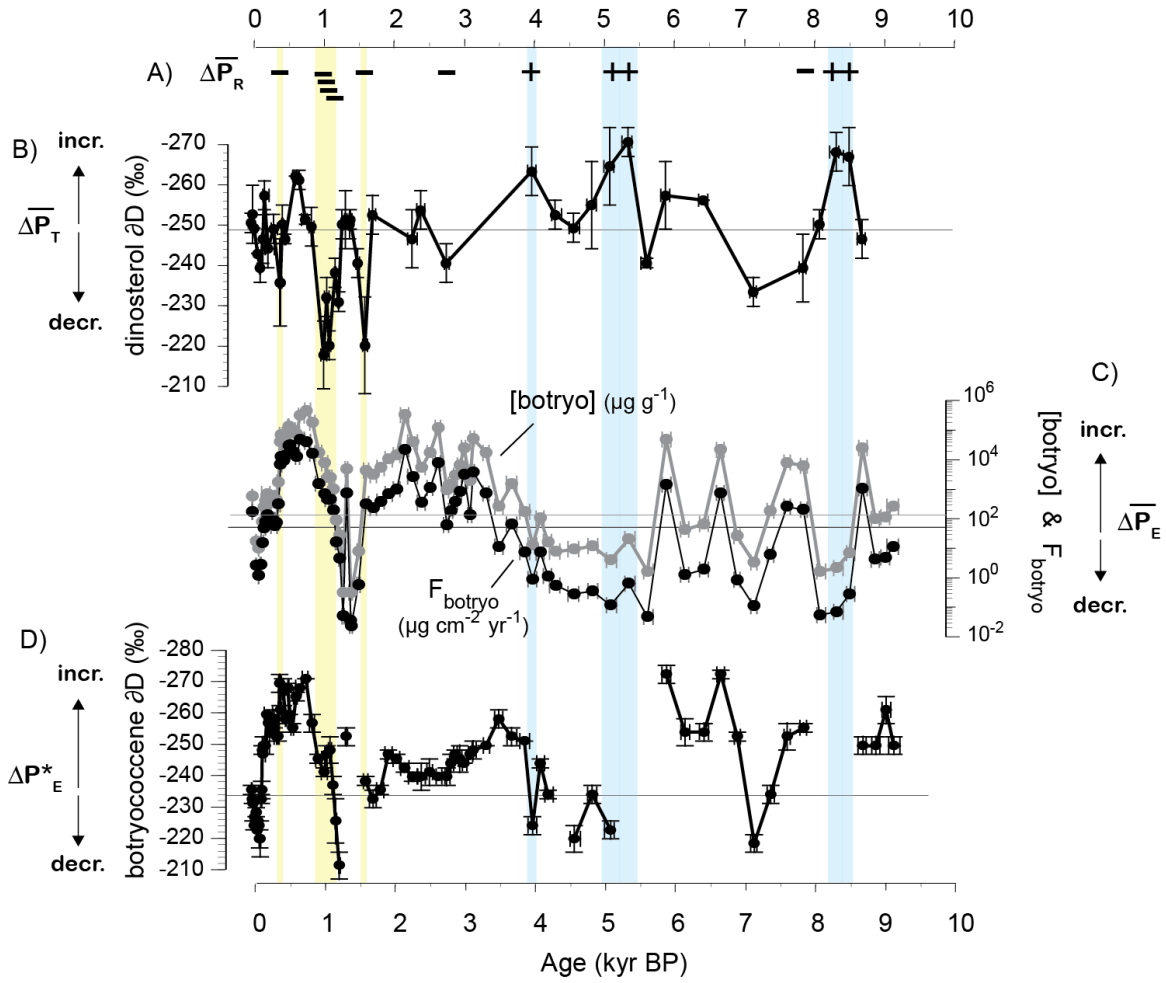

Figure 3.1. El Junco Lake biomarker records over the last 9.1 kyr. A) The sign of the inferred change in climatological rainfall due to processes unassociated with El Niño ($\Delta\overline{P_R}$); B) dinosterol δD; C) botryococcene concentration and accumulation rate (plotted on a log scale); D) botryococcene δD. The y-error bars represent ±1σ of the triplicate δD measurements and the x-error bars represent the age model uncertainty. The horizontal lines represent the average values over the last 100 years. Colored bars highlight the periods for which changes in processes unassociated with El Niño appear to have driven the largest anomalies in climatological rainfall at El Junco Lake- blue bars highlight where anomalously wet conditions ($\Delta\overline{P_T}$ > 1σ) coincide with periods of increased residual rainfall ($\Delta\overline{P_R} = +$), yellow bars indicate where anomalously dry conditions ($\overline{P_T} < -1\sigma$) coincide with periods of decreased residual rainfall ($\Delta\overline{P_R} = -$).

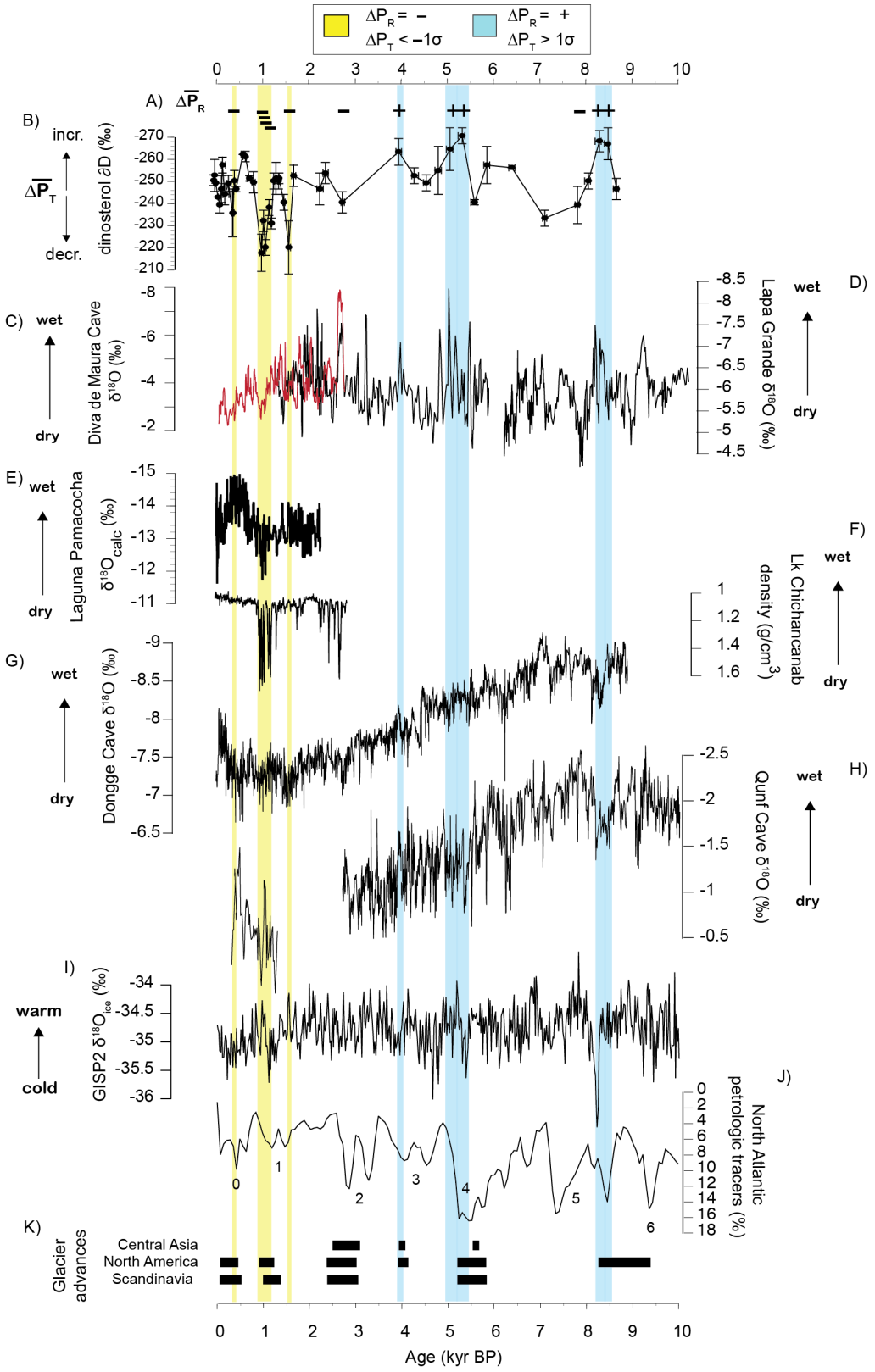

Figure 3.2. El Junco Lake biomarker records from 9.1 kyr BP to the present in comparison to global climate records. A) The sign of the inferred change in

climatological rainfall due to processes unassociated with El Niño ($\Delta\overline{P_R}$); B) dinosterol δD from this study; C) speleothem δ18O from Diva de Maura Cave, Brazil (Novello et al., 2012); D) speleothem δ18O from Lapa Grande, Brazil (Strikis et al., 2011); E) authigenic calcite $\delta^{18}O$ from Laguna Pumacocha in the eastern Peruvian Andes (Bird et al., 2011b); F) bulk density in Lake Chichancanab sediment, in the Yucatan Peninsula of Mexico (Hodell et al., 2005); G) $\delta^{18}O$ record from Dongge Cave, China (Wang et al., 2005a); H) speleothem $\delta^{18}O$ from Qunf Cave, Oman (Fleitmann et al., 2003); I) bidecadal $\delta^{18}O_{ice}$ from the GISP2 ice core (Stuiver and Grootes, 2000); J) North Atlantic drift ice record (Bond et al., 2001); K) NH glacier advances (Mayewski et al., 2004). Colored bars highlight the periods for which changes in processes unassociated with El Niño appear to have driven the largest anomalies in climatological rainfall at El Junco Lake- blue bars highlight where anomalously wet conditions ($\Delta\overline{P_T} > 1\sigma$) coincide with periods of increased residual rainfall ($\Delta\overline{P_R} = +$), yellow bars indicate where anomalously dry conditions ($\overline{P_T} < -1\sigma$) coincide with periods of decreased residual rainfall ($\Delta\overline{P_R} = -$).

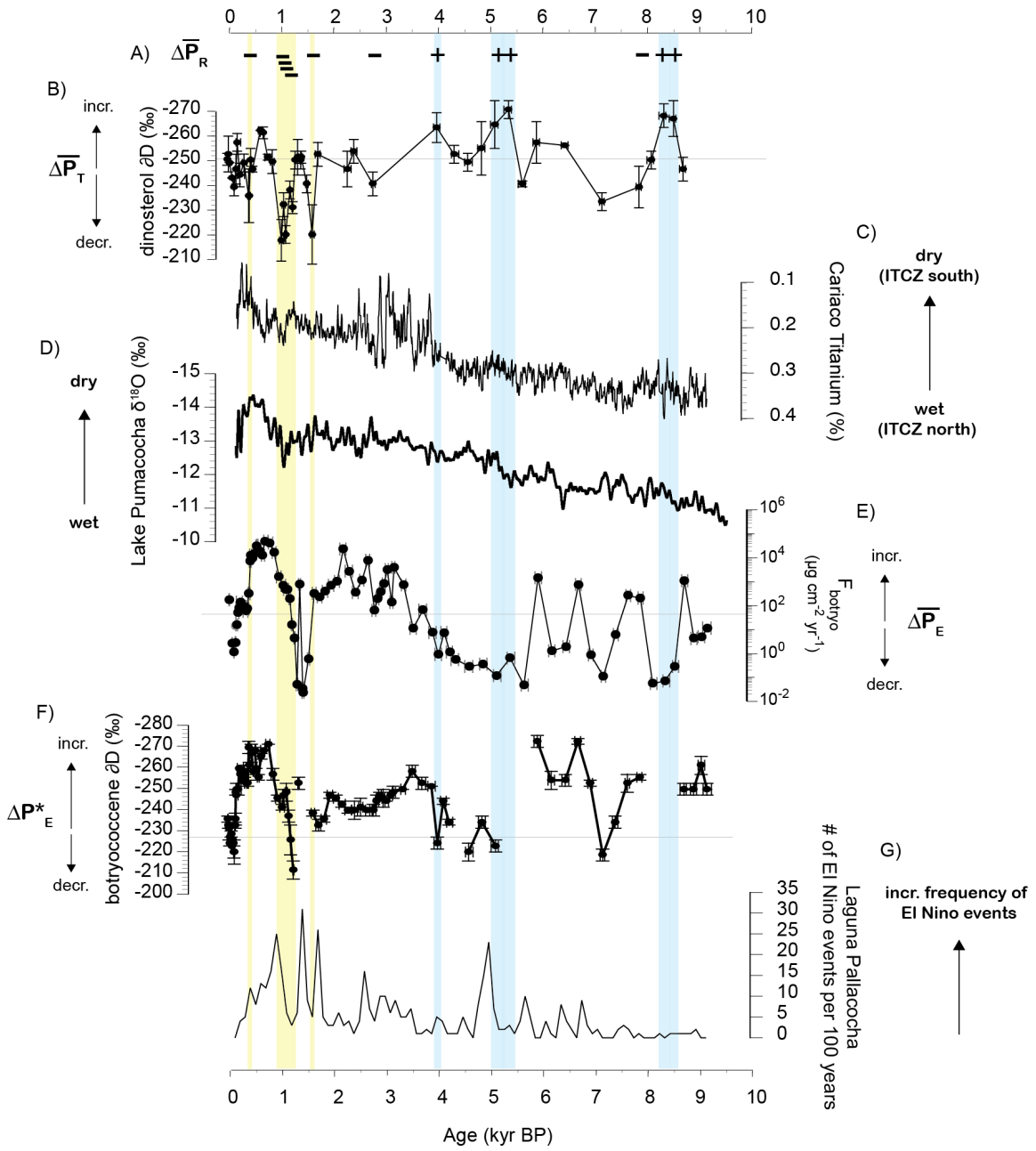

Figure 3.3. El Junco Lake biomarker records from 9.1 kyr BP to present in comparison to other tropical hydroclimate reconstructions. A) The sign of the inferred change in climatological rainfall due to processes unassociated with El Niño ($\Delta\overline{P_R}$); B) dinosterol δD from this study; C) titanium concentration in Cariaco Basin sediments (Haug et al., 2001); D) authigenic calcite δ18O from Lake Pumacocha in in the eastern Peruvian Andes (Bird et al., 2011a); E) botryococcene accumulation rate (plotted on a log scale); F) botryococcene δD; G) reconstruction of El Niño event frequency based on reflectance of Laguna Pallacocha sediment in the eastern Peruvian Andes (Moy et al., 2002). Colored

bars highlight the periods for which changes in processes unassociated with El Niño appear to have driven the largest anomalies in climatological rainfall at El Junco Lake- blue bars highlight where anomalously wet conditions ($\Delta\overline{P_T} > 1\sigma$) coincide with periods of increased residual rainfall ($\Delta\overline{P_R} = +$), yellow bars indicate where anomalously dry conditions ($\overline{P_T} < -1\sigma$) coincide with periods of decreased residual rainfall ($\Delta\overline{P_R} = -$).

Chapter 4. THE 8.2 KYR EVENT IN THE TROPICAL PACIFIC

4.1 INTRODUCTION

The relatively stable climate of the Holocene epoch (11,700 yr BP-present) was punctuated by a period of large and abrupt climate change during the so-called "8.2 kyr event". Paleoclimate data and modeling studies suggest that this event was caused by the catastrophic drainage of glacial lakes formed by the retreating North American ice sheet into the North Atlantic Ocean, which weakened the Atlantic Meridional Overturning Circulation (AMOC) and caused dramatic cooling in Greenland and the Labrador Sea (Alley et al., 1997; Barber et al., 1999; LeGrande et al., 2006; Rohling and Palike, 2005). The timing of the final Lake Agassiz drainage is estimated at ca. 8300 yr BP, with an error range of 8000–8500 yr BP (Lewis et al., 2012). A concomitant decrease in methane concentration in the Greenland ice record (Blunier et al., 1995) provides evidence that the associated climate perturbations reached the tropics, through the influence of changes in tropical precipitation on tropical wetland dynamics (Mitsch et al., 2010; Prigent et al., 2001). However, while paleoclimate records indicate that monsoon systems across the globe were altered (Cheng et al., 2009; Gupta et al., 2005; Shanahan et al., 2006; Thompson et al., 2002), little is known about the behavior of the tropical Pacific climate during this time.

A novel set of proxy records, based on the accumulation rate and hydrogen isotopic composition of sedimentary biomarkers, was developed from El Junco Lake in the Galápagos Islands in Chapter 2 to reconstruct changes in climatological rainfall, and to decompose the changes in total climatological rainfall into contributions from El Niño and non-El Niño processes. Rainfall at El Junco Lake, located in the eastern equatorial Pacific, is highly sensitive to both El Niño events and to movements of the eastern Pacific ITCZ (Fig. 4.1). In Chapter 3, we presented the El Junco Lake rainfall reconstructions over the last 9100 years and noted the evidence for large perturbations to the tropical Pacific hydroclimate around the time of the 8.2 kyr event. Here we investigate these rainfall changes in greater detail and supplement the proxy records with a dynamical model of the tropical Pacific coupled atmosphere-ocean system to explore the influence of tropical

Pacific mean state changes possibly associated with the 8.2 kyr event on the variability of ENSO.

4.2 Tropical Pacific Climate Changes During the 8.2 kyr event

Around 8500–8000 yr BP, the El Junco Lake biomarker records demonstrate large hydroclimate anomalies (relative to the modern period) in the Galápagos Islands. Increased total climatological rainfall (positive $\Delta\overline{P_T}$) and decreased climatological rainfall associated with El Niño events (negative $\Delta\overline{P_E}$) provide evidence for increased climatological rainfall associated with processes other than El Niño (positive $\Delta\overline{P_R}$). These reconstructions are consistent with a climatological southward shift of the eastern Pacific ITCZ) and decreased amplitude, frequency, and/or duration of El Niño rainfall events during this time (Fig 4.2). This period coincides within dating uncertainties to the final discharge of the proglacial Lake Agassiz into the North Atlantic.

Proxy records indicate that ca. 8300 yr BP an estimated 163,000 km^3 of glacial meltwater was released through the Hudson Bay (in one or two pulses) that produced a sufficient salinity anomaly to weaken the Atlantic Meridional Overturning Circulation (Fig. 4.3; Barber et al., 1999; Ellison et al., 2006; Kleiven et al., 2008; Lewis et al., 2012; Teller et al., 2002). The largest climate anomalies of the Holocene in Greenland ice (Fig. 4.3D) (Alley et al., 1997; Stuiver and Grootes, 2000) and North Atlantic sediment records (Ellison et al., 2006; Kleiven et al., 2008) are inferred during this time. Proxy records indicate that surface temperatures in central Greenland dropped by 3-8 °C (Fig. 4.3B; Barber et al., 1999; Kobashi et al., 2007) while those in the North Atlantic and Europe dropped by 2-3 °C (Fig. 4.3E; Ellison et al., 2006; Hoffman et al., 2012; Kleiven et al., 2008; Morrill and Jacobsen, 2005). While ice core records and some sediment records indicate that the associated climate perturbations only lasted 100-150 years (Daley et al., 2011; Kleiven et al., 2008; Kobashi et al., 2007), other sediment records suggest that multi-step SST anomalies (SSTAs) and prolonged changes in ocean circulation may have occurred over several centuries (Ellison et al., 2006).

It has been well established from theory and climate model simulations that a weakened AMOC associated with freshwater forcing in the North Atlantic produces a southward shift of the zonally-averaged climatological position of the ITCZ. Climate theory demonstrates

that the position of the ITCZ is fundamentally linked to the atmospheric energy budget and that shifts of the ITCZ accompany changes in the amount of heat transported across the equator by the atmosphere (Donohoe et al., 2013; Frierson and Hwang, 2012; Kang et al., 2008). Because atmospheric heat transport is fundamentally tied to ocean heat transport, much of which is accomplished through the AMOC, changes in the strength of the AMOC would be expected to produce meridional shifts of the ITCZ. Indeed, a variety of modeling studies have demonstrated that a meltwater pulse in the North Atlantic and the associated reduction in the AMOC produce a southward shift of the ITCZ. A southward shifted ITCZ acts to balance the deficit in energy fluxes into the atmosphere in the northern hemisphere caused by the reduced ocean energy transport from the South Atlantic to North Atlantic (Otto-Bliesner and Brady, 2010; Timmermann et al., 2007; Zhang and Delworth, 2005).

Numerous proxy data support the model results for a southward displacement of the zonally averaged ITCZ during the 8.2 kyr event. For example, a decrease in atmospheric methane concentration is observed in Greenland ice records concomitant with the 8.2 kyr event (Fig. 4.3D; Alley et al., 1997; Blunier et al., 1995; Kobashi et al., 2007; Stuiver and Grootes, 2000). Decreased atmospheric methane concentrations are expected in association with a southward shift of the zonally averaged ITCZ due to decreased tropical wetland area and methane emissions (Chappellaz et al., 1993; Lea et al., 2003; Loulergue et al., 2008; Tzedakis et al., 2009). On a more regional level, proxy evidence suggests that the ITCZ in the western Atlantic Ocean was shifted southward during this time as inferred from reconstructions of reduced rainfall over Central America (Fig. 4.4G; Lachniet et al., 2004) and increased upwelling in the Cariaco Basin (indicating strengthened trade winds off the north coast of Venezuela; Fig. 4.4I; Hughen et al., 1996). In addition, proxy evidence points to a weakened Indian (and possibly Asian) summer monsoon (Fig. 4.4E,F; Cheng et al., 2009; Fleitmann et al., 2007; Hong et al., 2003; Pausata et al., 2011; Wang et al., 2005a) and an intensified South American summer monsoon (Fig. 4.4H; Cheng et al., 2009; Strikis et al., 2011) based on cave stalagmite records, while evidence for arid conditions in the North Africa monsoon region comes from lake sediment and tropical ice core records (Gasse, 2000; Shanahan et al., 2006; Thompson et al., 2002). Such paleoclimate records from the western Atlantic Ocean, Central America, and the monsoon regions of Asia, Africa, and South America, in conjunction with the eastern Pacific rainfall reconstructions from this

study, indicate that a global southward shift of tropical precipitation likely occurred during the 8.2 kyr event.

4.3 Response of ENSO to an Equatorward ITCZ Shift in the Tropical Pacific

While theory and modeling studies support the proxy evidence for a southward shifted ITCZ during the 8.2. ka event, a theoretical basis for the concomitant reduction in the variability of El Niño rainfall events (as inferred from the El Junco Lake biomarker records) is less clear. A substantial body of literature indicates that ENSO variability is modulated by changes in the mean state of the tropical Pacific, including changes in the strength of the equatorial trade winds, thermocline depth, and zonal SST gradient (e.g. An et al., 2008; Battisti and Hirst, 1989; Clement et al., 1996; Fedorov and Philander, 2001; Sun, 2003; Watanabe et al., 2012). Thus, one plausible hypothesis is that the inferred reduction in climatological rainfall associated with El Niño events in the eastern Pacific was due to changes in the tropical Pacific mean state through its associated impacts on the variability of ENSO.

In fact, theory presented by Battisti (1988) and Battisti and Hirst (1989), suggest that a reduction in ENSO variability would be expected in association with a climatological southward shift of the Pacific ITCZ (such as inferred from proxy records during this time) through the influence of the tropical Pacific background state on the stability of the coupled ocean-atmosphere system. Such a relationship between the long-term mean position of the ITCZ and ENSO variability should not be confused with their relationship on interannual timescales. For instance, during El Niño events, the ITCZ in the central and eastern equatorial Pacific shifts southward onto the equator in response to warm SSTAs there. In contrast, climatological shifts of the mean annual position of the ITCZ would be accompanied by substantial changes in the mean state of the tropical Pacific that would be expected to drive changes in ENSO variability through changes in the stability of the coupled ocean-atmosphere system.

The theory presented in Battisti (1988) and Battisti and Hirst (1989) relates changes in the background state of the tropical Pacific through the annual cycle to changes in the stability of the coupled ocean-atmosphere system. In boreal fall the ITCZ is located at its

northern-most position, and the tropical Pacific is characterized by strong equatorial trade winds, strong equatorial upwelling, a shallow eastern equatorial Pacific (EEP) thermocline and a large zonal SST gradient. The combination of stronger upwelling and a shallower thermocline causes enhanced coupling between the subsurface and surface temperature anomalies in the EEP, a feature that is critical for the growth of ENSO events. During this time the coupled ocean-atmosphere system is least stable, and therefore more susceptible to the growth of ENSO events. Conversely, the coupled system is most stable, and least conducive to the growth of ENSO events during boreal spring, when the ITCZ lies closest to the equator and the tropical Pacific is characterized by weak equatorial trades and upwelling, a deep EEP thermocline and a weak zonal SST gradient. This influence of the background state on the stability of the coupled system is thought to be responsible the phase locking of ENSO to the seasonal cycle (Ham et al., 2013; Stein et al., 2010; Thompson and Battisti, 2001; Tziperman et al., 1998).

The influence of changes in the background tropical Pacific climate on coupled ocean-atmosphere stability that exists on seasonal timescales also applies to mean state changes, as demonstrated by Battisti and Hirst (1989). A climatological northward (southward) shift of the mean annual position of the Pacific ITCZ would be expected to be associated with stronger (weaker) equatorial trade winds and upwelling, a shallower (deeper) thermocline in the EEP, and an increased (decreased) zonal SST gradient in the tropical Pacific. Modeling studies using a variety of coupled atmosphere-ocean models have demonstrated that mean climate conditions characterized by stronger equatorial trade winds, larger zonal SST gradient in the tropical Pacific, and/or a shallower EEP thermocline increase the instability of the coupled system (Battisti and Hirst, 1989; Galanti et al., 2002; Hirst, 1986; Sun, 2003).

In order to further evaluate the mechanism by which ENSO variability could be dynamically linked to the climatological position of the ITCZ, we ran a set of idealized experiments with an intermediate complexity model of the tropical Pacific. The Linearized Ocean Atmosphere Model (LOAM; Thompson and Battisti, 2000) is an intermediate complexity of the tropical Pacific. LOAM is linearized variant of the Zebiak and Cane (1987) coupled model, updated to include observationally constrained parameter values and observed climatological mean state fields, including ocean currents and vertical thermal structure. Briefly, LOAM is comprised of a 1.5 layer ocean model and a two-layer model of

the atmosphere, in which heating is a function of SST and surface wind convergence (Gill, 1980). The atmosphere is modeled as a single baroclinic mode on an equatorial β plane and is linear with mechanical and thermodynamic damping. As compared to the Zebiak Cane model and the Battisti (1988) model, the atmospheric convergence feedback has been linearized as in Battisti and Hirst (1989). The ocean model consists of an upper layer governed by the linear shallow water equations on an equatorial β plane and a motionless lower layer. An Ekman layer of fixed 50 m depth is imbedded in the upper layer and is in steady state with the surface winds. The linearized prognostic equation for sea surface temperature (SST) includes three-dimensional advection of temperature anomalies by the climatological currents, anomalous advection of the climatological temperature, vertical mixing and a simple parameterization of surface heat flux (see Roberts and Battisti, 2011; Thompson, 1998). The dependent variables for the ocean are: meridional and zonal surface wind anomalies and the thermocline perturbation. The ocean equations are discretized spectrally in y by projecting them onto Rossby waves space and discretized in x using finite differences. The atmosphere and SST equations are projected onto Hermite function space in y and also discretized in x using finite differences.

We performed a simple set of three idealized experiments with LOAM to simulate changes in the mean state of the tropical Pacific associated with meridional shifts of the ITCZ and determine their influence on ENSO. Observed mean fields of SST, surface ocean currents, and the vertical structure of ocean temperature along the equator were obtained from the Simple Ocean Data Assimilation (SODA) data set (Carton et al., 2000a; Carton et al., 2000b; http://www.atmos.umd.edu/~ocean/). Observed surface winds were taken from NCEP reanalysis (Kalnay et al., 1996; http://www.cdc. noaa.gov/). In the first experiment (the control run), ENSO variability around the observed mean state was simulated by constructing the annual propagator matrix (R) from the full suite of observed monthly mean fields (i.e. $R_{year} = R_{12}R_{11}R_{10}R_9R_8R_7R_6R_5R_4R_3R_2R_1$), where 1-12 represent months Jan – Dec. The model was then run for 2,000 years and the characteristics of ENSO evaluated. In the second experiment (the boreal spring run), a mean state governed by a southward shifted ITCZ was simulated by building the annual propagator matrix from the observed mean fields from only March to June (i.e. $R_{year} = R_3R_3R_4R_4R_5R_5R_6R_6R_5R_5R_4R_4$). In the final experiment (the boreal fall run), a mean state governed by a northward shifted ITCZ was

simulated by building the propagator matrix from the observed mean fields in September to December (i.e. $R_{year} = R_9R_9R_{10}R_{10}R_{11}R_{11}R_{12}R_{12}R_{11}R_{11}R_{10}R_{10}$).

In the control run, the stochastic forcing of LOAM was adjusted to obtain a variance of Niño 3 SSTAs that matches observations ($\sigma^2 = 0.7\ °C^2$). As shown in Roberts and Battisti (2011), when the propagator matrix is built from the full annual cycle and the model is stochastically forced, the essential physics of ENSO are captured by LOAM. While the center of action is located farther west in LOAM than in observations, the structure, period, and damping rate of the ENSO mode in LOAM is similar to that found from a linear inverse model fit to the observations (Fig. 4.5A,B; Table 1). In addition, the structure and variance explained by the first two EOFs of tropical Pacific SSTAs are similar to those from observations (Fig. 4.6A,B).

The annually averaged fields and annual cycle of SST, surface winds, and thermocline depth from the three LOAM simulations are shown in Fig. 4.7-9. It should be noted that in both the boreal spring and fall simulations, the annual cycle is reduced as compared to the control run (Fig. 4.6). When the annual cycle was restricted to boreal spring conditions (i.e. southward shifted ITCZ) the mean state of the tropical Pacific was characterized by weaker equatorial trade winds, a flatter central Pacific to east Pacific thermocline slope, and a reduced zonal SST gradient. In this simulation the growth rate of the ENSO mode decreased by 50% (representing an increase in the stability of the ENSO mode) and the modal period increased by 20% (Table 1). When the model was stochastically forced the variance of Niño 3 SSTAs decreased by >80% (Fig. 4.10C). In contrast, when the annual cycle was restricted to boreal fall conditions (i.e. a northward shifted ITCZ) the mean state of the tropical Pacific was characterized by stronger equatorial trade winds, a steeper thermocline slope, and a larger zonal SST gradient. In this simulation the growth rate of the ENSO mode increased by 20% (representing a decrease in the stability of the ENSO mode) and the period decreased by 20%. When LOAM was stochastically forced, the variance of Niño 3 SSTA increased by 20% and ENSO variability shifted to shorter periods (Fig. 4.11). Though the amplitude and period of ENSO events were modified in this simulation, the structure of ENSO was little affected (Fig. 4.5B,D; Fig. 4.6B,D).

These idealized model simulations provide a set of causal mechanisms by which an equatorward shift of the ITCZ could give rise to reduced ENSO variability, in support the

rainfall reconstructions from El Junco Lake, indicating reduced El Niño rainfall variability coeval with increased climatological rainfall associated with non-El Niño processes (consistent with an equatorward shift of the eastern Pacific ITCZ) ca. 8500-8200 yr BP. An equatorward (poleward) shift of the climatological position of the Pacific ITCZ as simulated through perpetual boreal spring (fall) conditions in the tropical Pacific gives rise to decreased (increased) ENSO variability through an increase (decrease) in the stability of the coupled ocean-atmosphere system.

4.4 SUMMARY

The large freshwater pulse to the North Atlantic during the so-called "8.2 kyr event" resulted in climate perturbations that stretched across the globe. Here we present the first evidence for large perturbations to the tropical Pacific climate, based on paired sedimentary biomarker records from El Junco Lake. Rainfall reconstructions from these biomarker records indicate that El Niño rainfall variability was weak while climatological rainfall unassociated with El Niño events increased. In light of other tropical hydroclimate reconstructions from this time, we infer that the southward shift in tropical precipitation that is well documented in continental regions, also extended to an equatorward shift of the climatological position of the eastern Pacific ITCZ. We demonstrate using a simple set of idealized simulations with a coupled climate model of intermediate complexity that such a connection between the climatological position of the Pacific ITCZ and ENSO variability is found under prescribed modifications to the seasonal cycle of the tropical Pacific background state. Perpetual boreal spring (fall) conditions in the tropical Pacific are characterized by an equatorward (poleward) shift of the mean annual position of the ITCZ, weakened (strengthened) equatorial trade winds, a deeper (shallower) EEP thermocline, and a decreased (increased) tropical Pacific zonal SST gradient, which give rise to increased (decreased) stability of the coupled ocean-atmosphere system. Taken in conjunction with reconstructions from monsoon regions and the tropical Atlantic, the data presented here suggest that the large meltwater pulse to the North Atlantic produced a global southward shift of tropical rainfall, from which the associated southward shift of the Pacific ITCZ may have given rise to reduced ENSO variability. In Chapter 5 we further evaluate the

connection between North Atlantic freshwater forcing, tropical Pacific mean state changes, and ENSO variability using simulations with a fully coupled global climate model.

Table 4.1. Characteristics of the ENSO mode

Model	Growth rate (yr-1)	Period (yr)
Obs (NOAA ERSST v3b)	0.37	4.0
LOAM Control Run	0.31	2.8
LOAM Boreal Spring Run	0.15	3.3
LOAM Boreal Fall Run	0.38	2.2

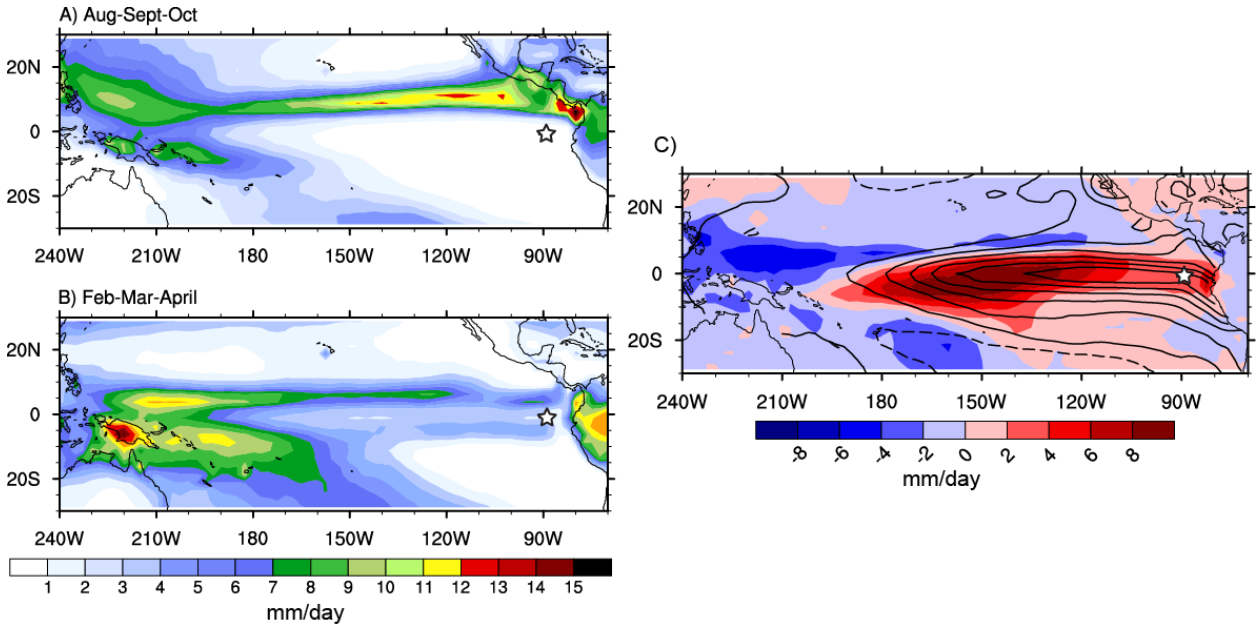

Figure 4.1. Tropical Pacific rainfall patterns associated with the ITCZ and ENSO. A) Seasonal cycle of the Pacific ITCZ from GPCP precipitation averaged over A) Aug–Oct and B) Feb–April for the period 1980–2010; C) GPCP precipitation anomalies (colors) and SST anomalies (contours) composited from the peak of the 1972–73, 1982–83, and 1997–98 El Niño events (Oct–Mar). Data taken from NCEP/NCAR Reanalysis (http://www.esrl.noaa.gov). The location of the Galápagos Islands is indicated by the white star.

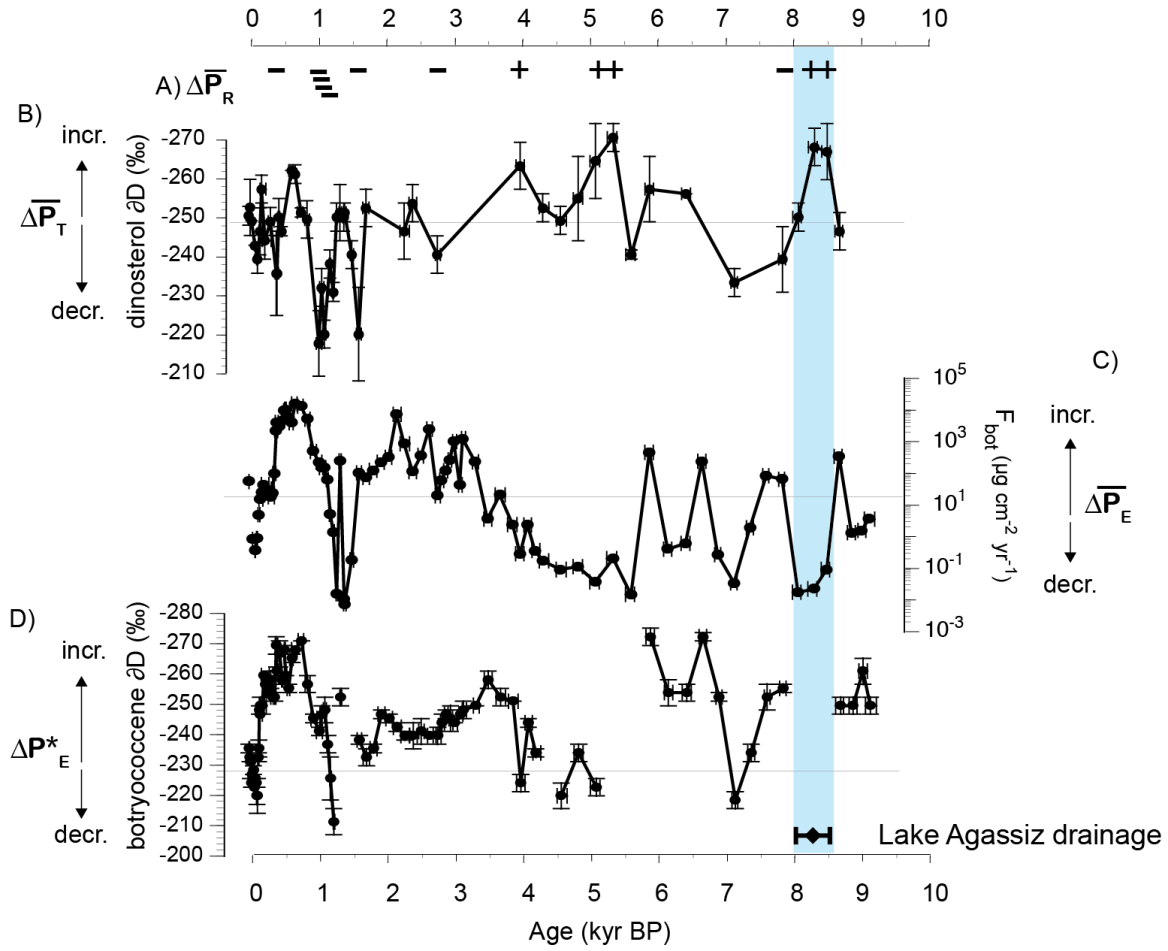

Figure 4.2. El Junco Lake biomarker records with the timing of Lake Agassiz drainage highlighted. A) The sign of the inferred change in climatological rainfall due to processes unassociated with El Niño ($\Delta\overline{P_R}$); B) dinosterol δD; C) botryococcene accumulation rate (plotted on a log scale); D) botryococcene δD. The highlighted color bar and the diamond with error bars at the bottom of the figure represent the timing of the terminal Lake Agassiz outburst at 8.33 kyr with error ranges from 8.04–8.49 kyr (Lewis et al., 2012).

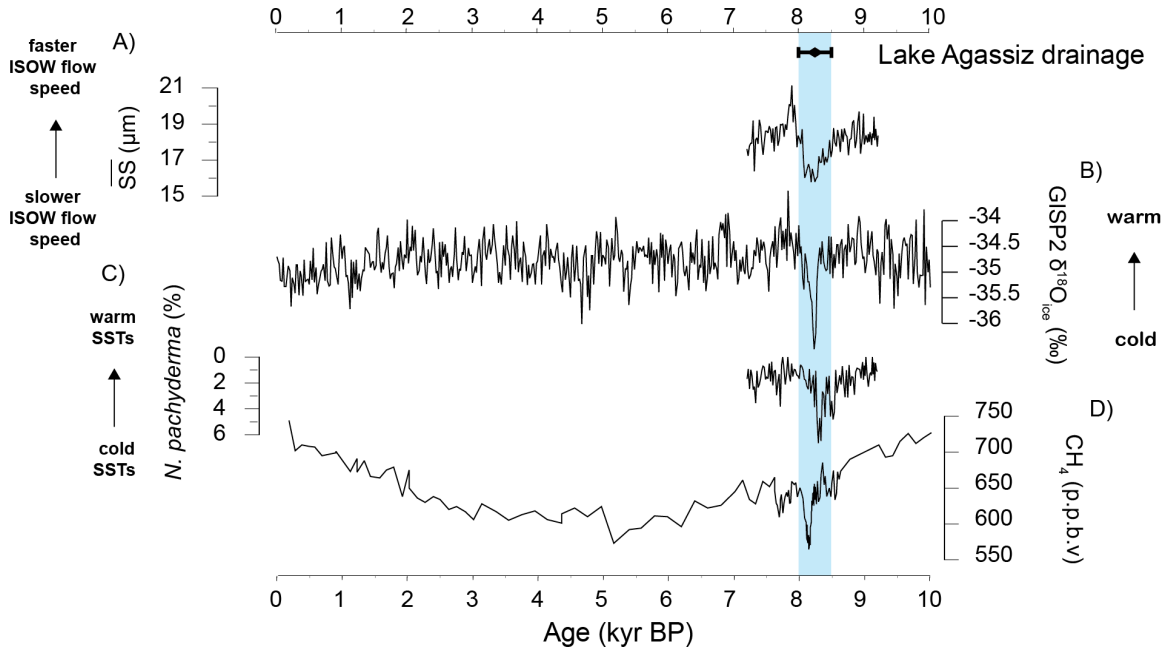

Figure 4.3. North Atlantic and Greenland proxy records of the 8.2 kyr event. A) Mean sortable silt size from a deep-sea sediment core in the subpolar North Atlantic (core MD99-2251) indicating flow speed of the Iceland Scotland Overflow Water (ISOW; Ellison et al., 2006); B) bidecadal $\delta^{18}O$ values of ice from the GISP2 ice core (Stuiver and Grootes, 2000); C) subpolar North Atlantic SST reconstruction based on the relative abundance of the polar foraminifer *Neogloboquadrina pachyderma* sinistral coiling from core MD99-2251 (Ellison et al., 2006); D) mean atmospheric CH_4 concentrations from the Greenland ice core GRIP (Blunier et al., 1995). The highlighted color bar and the diamond with error bars at the bottom of the figure represent the timing of the terminal Lake Agassiz outburst at 8.33 kyr with error ranges from 8.04–8.49 kyr (Lewis et al., 2012).

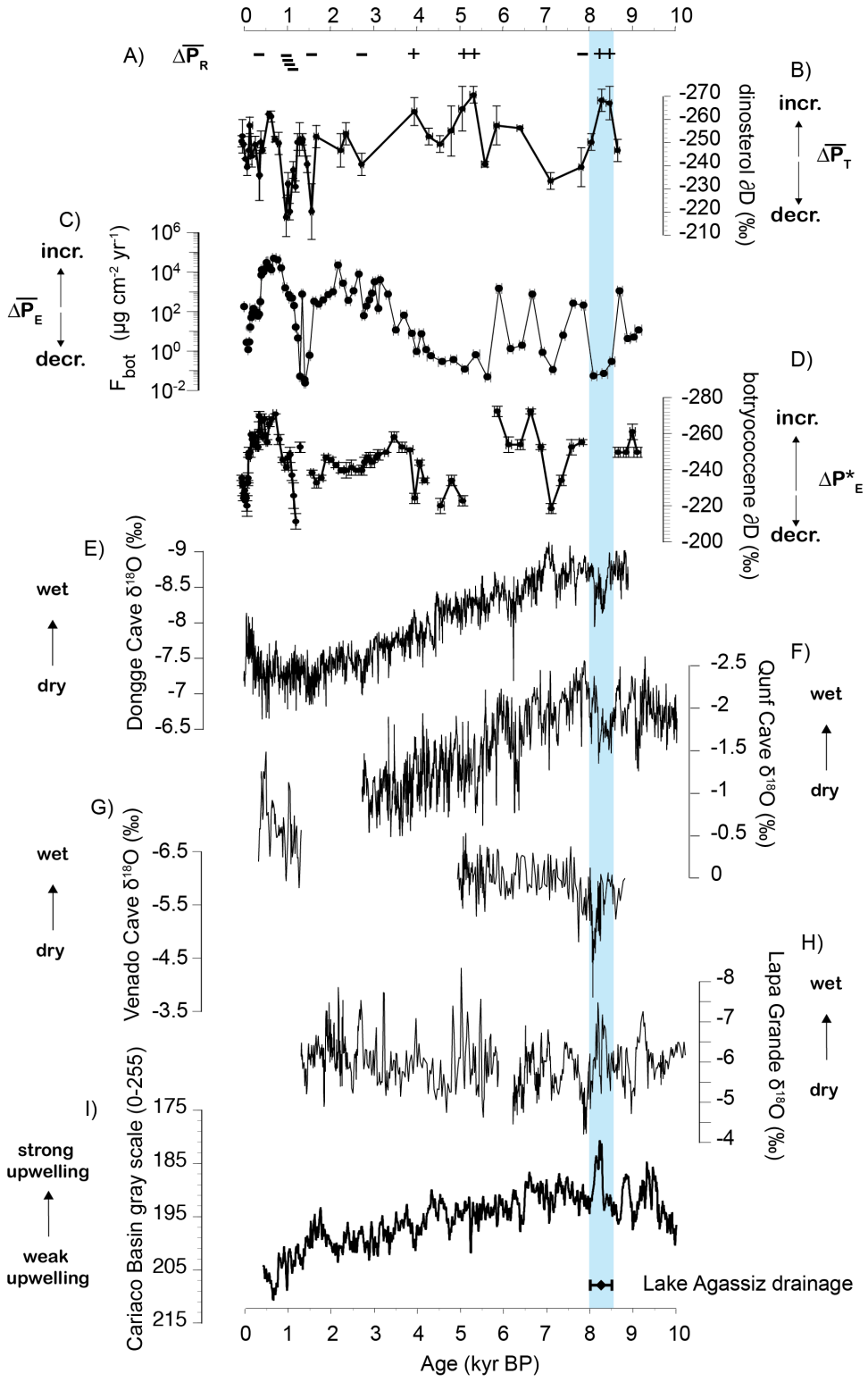

Figure 4.4. El Junco Lake biomarker records in comparison to tropical hydroclimate records. A) The sign of the inferred change in climatological rainfall due to processes unassociated with El Niño ($\Delta\overline{P_R}$); B) dinosterol δD from this study; C) botryococcene

accumulation rate from this study (plotted on a log scale); D) botryococcene δD from this study; E) δ18O record from Dongge Cave, China (Wang et al., 2005a); F) δ18O record from Qunf Cave, Oman (Fleitmann et al., 2003); G) δ18O record from Venado Cave, Costa Rica (Lachniet et al., 2004); H) δ18O record from Lapa Grande, Brazil (Strikis et al., 2011); I) Cariaco Basin grey scale record (Hughen et al., 1996). The highlighted color bar and the diamond with error bars at the bottom of the figure represent the timing of the terminal Lake Agassiz outburst at 8.33 kyr with error ranges from 8.04 – 8.49 kyr (Lewis et al., 2012).

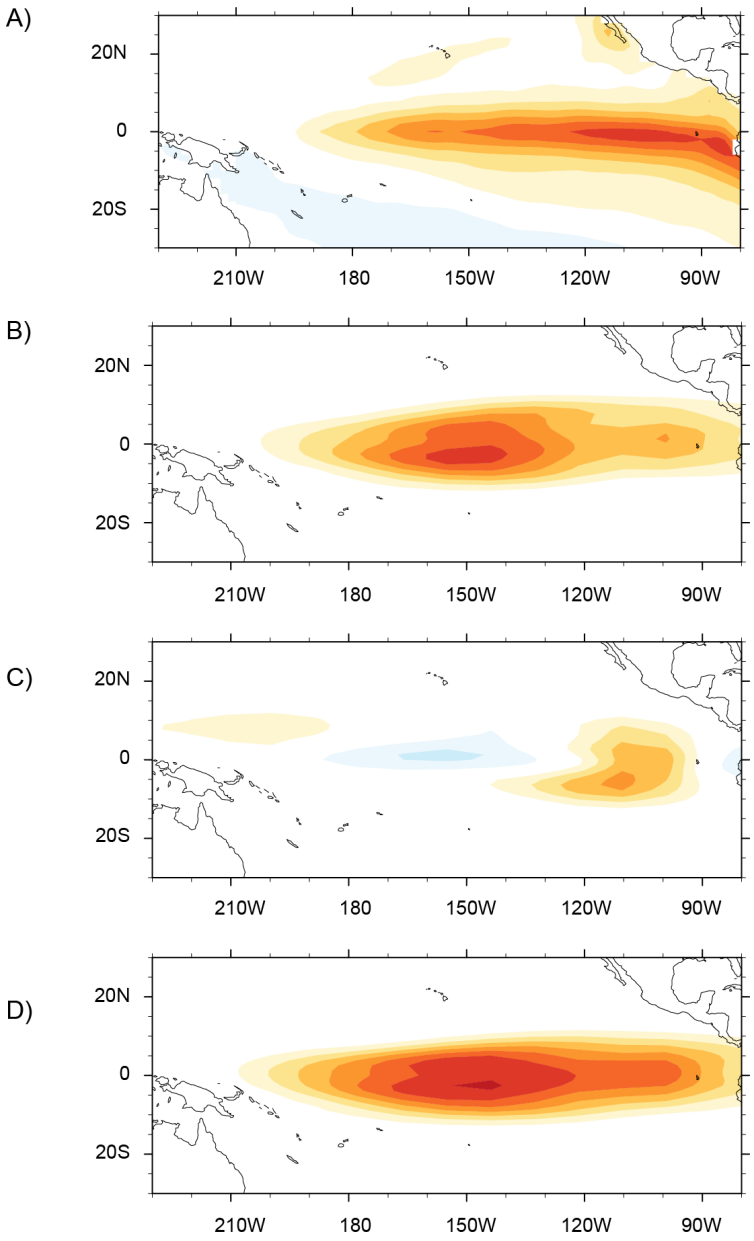

Figure 4.5. The SST component of the ENSO mode in observations and the LOAM simulations. A) The structure of the ENSO mode in a linear inverse model fit to observations (NOAA ERSST v3b); B) the LOAM control run; C) the LOAM boreal spring simulation; D) the LOAM boreal fall simulation.

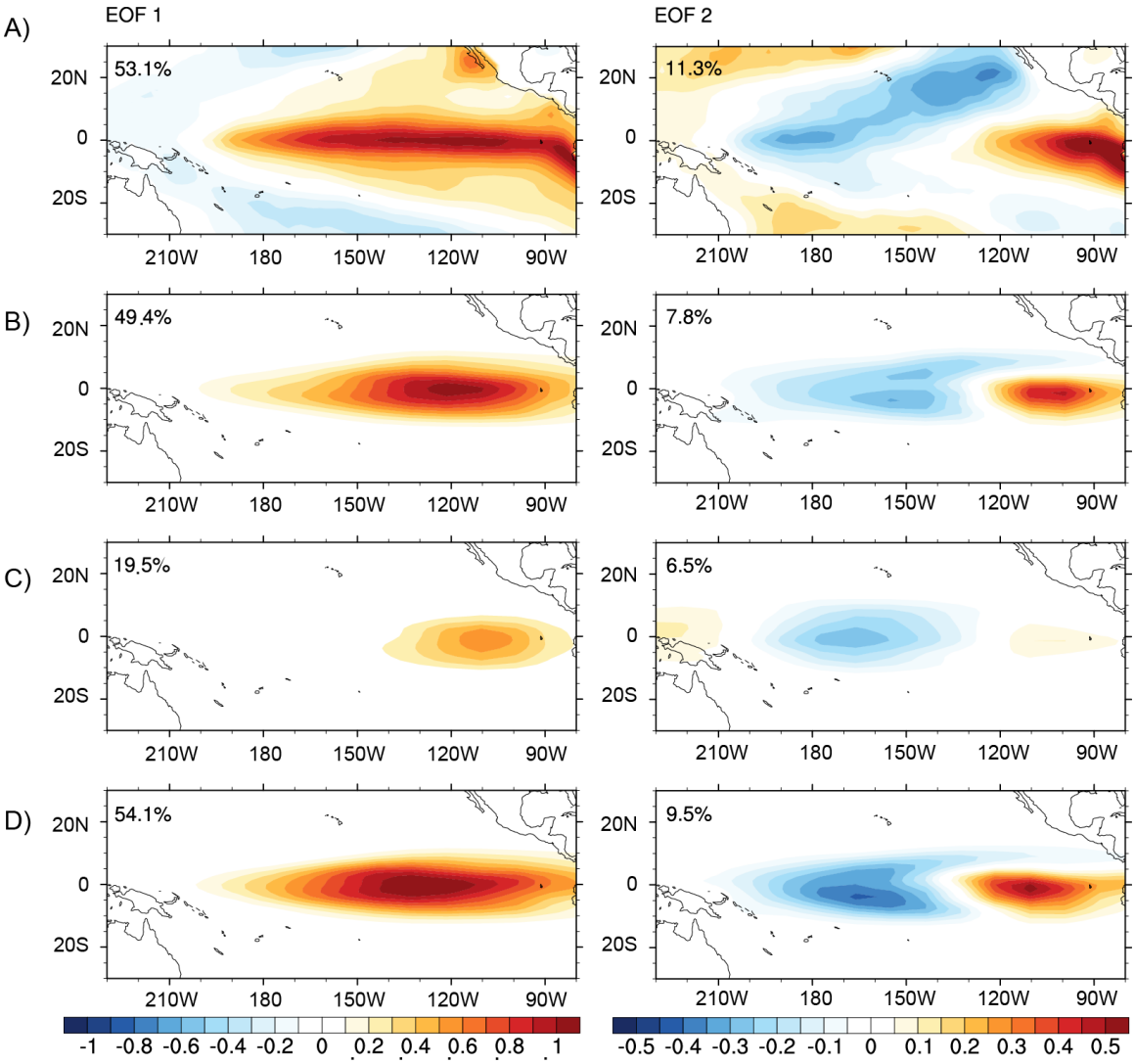

Figure 4.6. Structure of SSTAs associated with ENSO in observations and the LOAM simulations. EOF 1 and 2 of SST anomalies from A) observations (NOAA ERSST v3b); B) the LOAM control run; C) the LOAM boreal spring run; D) the LOAM boreal fall run.

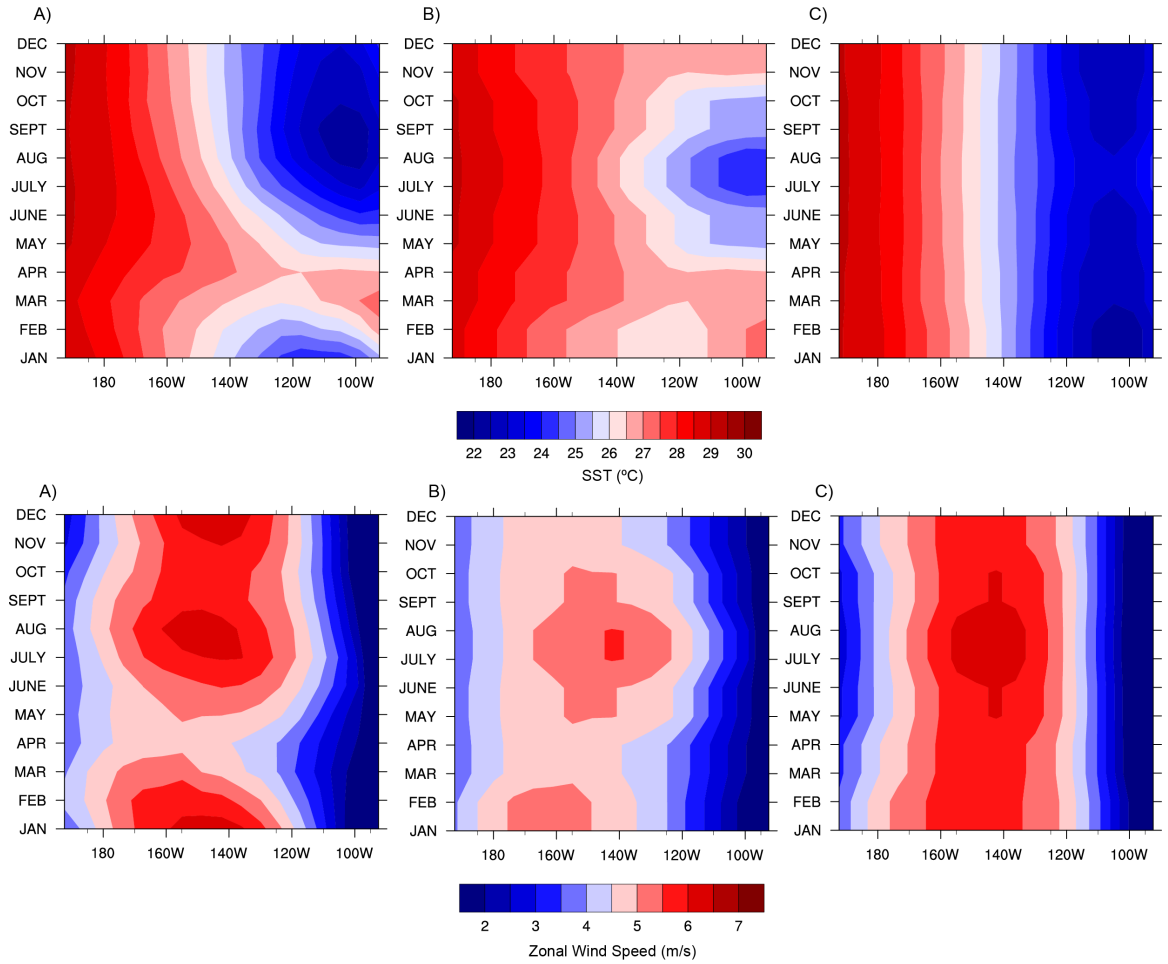

Figure 4.7. Hovmoller plots of climatological SST (top) and zonal wind speed (bottom) across the equatorial central and eastern Pacific (2°S-2°N) for the three LOAM simulations: A) control run; B) boreal spring run; C) boreal fall run.

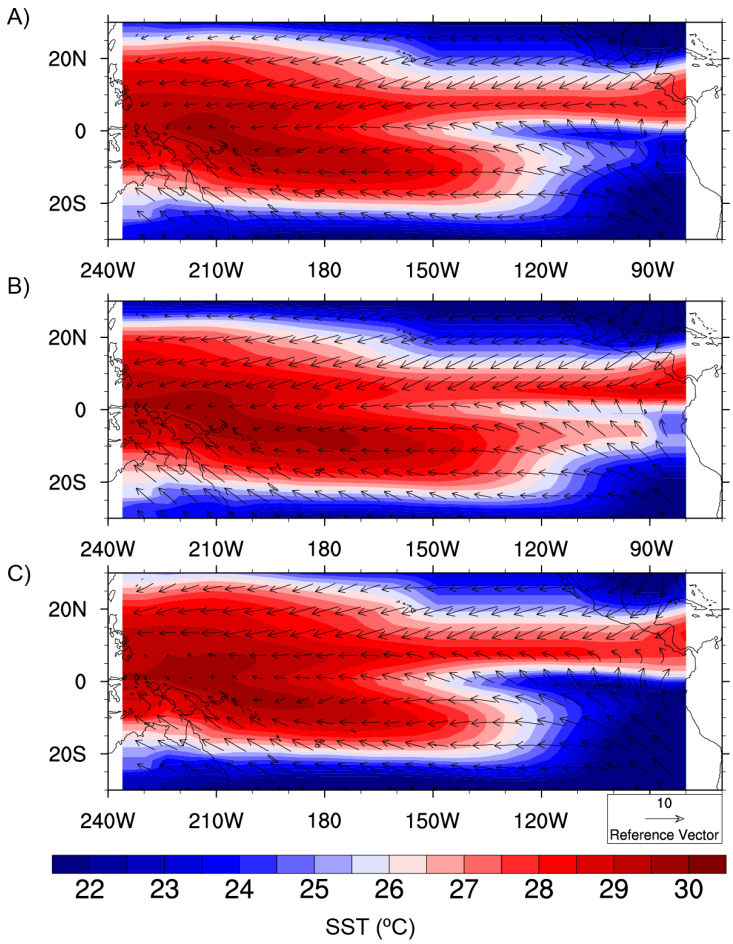

Figure 4.8. Mean SST and surface wind vectors for the three LOAM simulations A) control run; B) boreal spring run; C) boreal fall run.

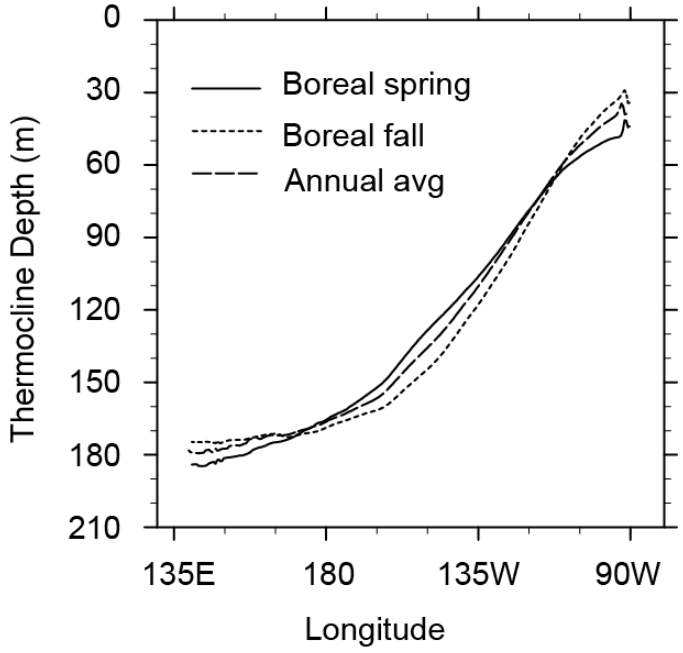

Figure 4.9. Climatological thermocline depth (as represented by the 20 °C isotherm) from SODA data during boreal spring, boreal fall, and the annual average. This data was used to parameterize subsurface temperature for the three LOAM simulations (the boreal spring, boreal fall, and control run, respectively).

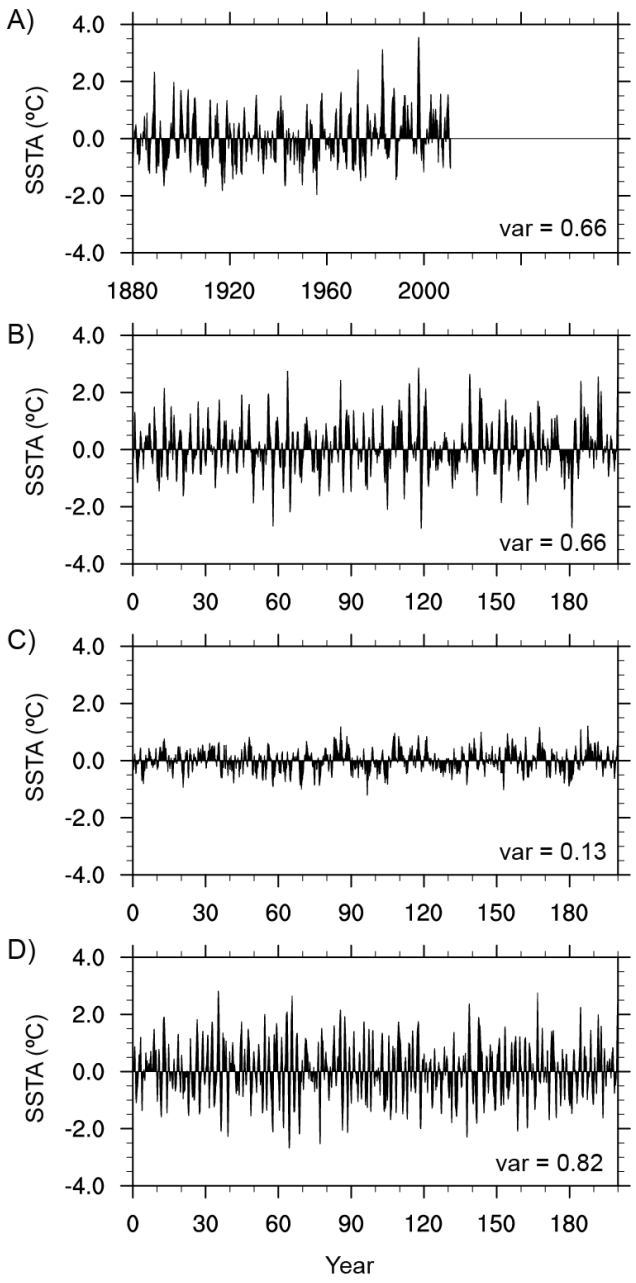

Figure 4.10. Time series of Niño 3 SSTAs in observations and the LOAM simulations. A) Observations (NOAA ERSST v3b); B) LOAM control run; C) LOAM boreal spring run, D) LOAM boreal fall run.

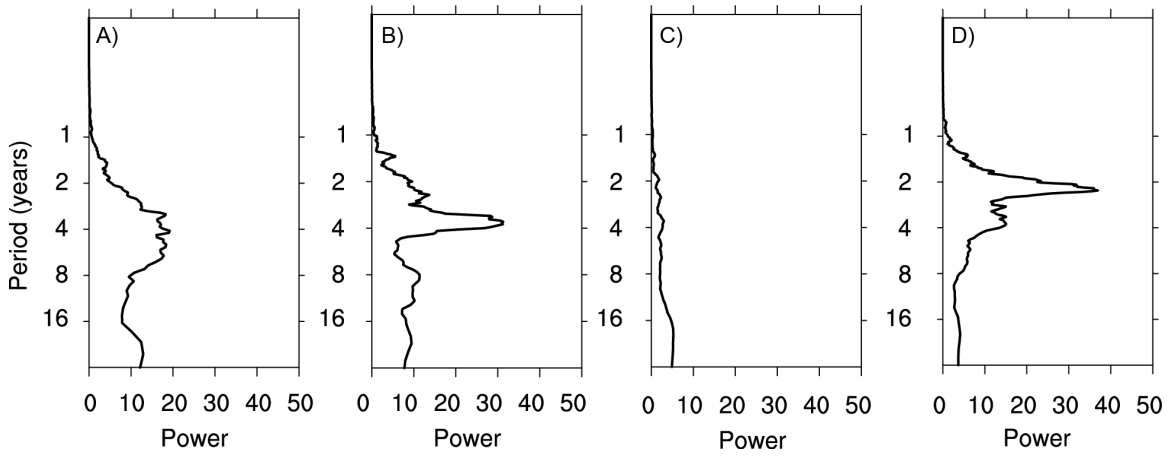

Figure 4.11. Power spectra of Niño 3 SSTAs in observations and the LOAM simulations. A) Observations (NOAA ERSST v3b); B) LOAM control run, C) LOAM boreal spring run; D) LOAM boreal fall run.

Chapter 5. MECHANISMS OF REDUCED ENSO VARIABILITY IN RESPONSE TO NORTH ATLANTIC FRESHWATER DISCHARGE IN CESM

5.1 INTRODUCTION

Paleoclimate evidence suggests that ca. 8300 ± 200 yr BP, a large freshwater anomaly in the North Atlantic produced a slowdown of the Atlantic Meridional Overturning Circulation (AMOC), widespread cooling across the North Atlantic, Europe, and Greenland, and a global southward shift in tropical precipitation. In addition, a new set of rainfall reconstructions from the Galápagos Islands was presented in Chapters 2-4 that provides evidence for large perturbations to the eastern equatorial Pacific hydroclimate during this period. During the period ca. 8500-8200 yr BP, these biomarker records provide evidence for increased total climatological rainfall coeval with decreased climatological rainfall associated with El Niño events, from which we infer that climatological rainfall associated with processes other than El Niño increased. In light of other tropical hydroclimate reconstructions from this time, we infer that the well-documented southward shift in tropical precipitation that occurred in continental regions was also manifested through an equatorward shift of the eastern Pacific ITCZ.

While climate theory supports the proxy evidence for a climatological southward shift of the ITCZ in association with a weakened AMOC, a theoretical basis to support a concomitant reduction in ENSO variability, also suggested by the El Junco Lake records, is less well developed. Although a substantial body of literature indicates that ENSO variability is modulated by changes in the mean state of the tropical Pacific (e.g. Battisti and Hirst, 1989; Clement et al., 1996; Fedorov and Philander, 2001; Roberts et al., 2014), little agreement exists as to the manner and mechanisms by which mean state changes affect ENSO (Guilyardi et al., 2012a; Timmermann et al., 2007). This is likely due in part, if not in full, to the large tropical mean state biases that exist in General Circulation Models (GCMs). While GCMs represent the most comprehensive tools available for describing the climate system, they exhibit a wide range of biases in their simulation of

tropical Pacific climatology as well as in their representation of ENSO variability (Bellenger et al., 2014; de Szoeke et al., 2010; Li et al., 2014; Lin et al., 2014). Such biases present a fundamental obstacle in the ability of these models to provide robust projections of past (and future) ENSO changes, as ENSO is known to be highly sensitive to the mean state of the tropical Pacific. For instance, simulations of future climate change with the latest generation of GCMs show no consistent response of ENSO to changes in the mean climate (Guilyardi et al., 2012a).

In order to further evaluate the response of the tropical Pacific to a freshwater perturbation in the North Atlantic and thereby provide a more robust interpretation of the El Junco Lake hydroclimate reconstructions, we performed simulations with a state-of-the-art GCM in tandem with an intermediate complexity model of the tropical Pacific, that explicitly evaluates the influence of tropical Pacific mean state changes on the coupled system. Such highly simplified intermediate models of the coupled tropical ocean- atmosphere system are useful in illuminating the fundamental dynamics of ENSO and evaluating how ENSO might respond to changes in the mean state of the tropical Pacific (see e.g. Battisti, 1988; Clement et al., 1996; Roberts, 2007; Zebiak and Cane, 1987). We use these tools to evaluate the response of the tropical Pacific to a large North Atlantic freshwater perturbation.

5.2 METHODS

5.2.1 *CESM Configuration*

We perform simulations with the CESM global atmosphere/ocean/land/ice model (CESM 1.0.5 B1850CN 0.9x1.25_gx1v6), which employs the CAM4 atmospheric model (resolution of 0.9° latitude and 1.25° longitude) and the POP2 ocean model (resolution is approximately uniform in longitude at 1.13° and varies in latitude from 0.27°-0.65°). The model configuration matches the 1,000-year CCSM4 preindustrial control run, which has been well studied and existing biases of the tropical Pacific climatology and variability are well known (Deser et al., 2012). While some ENSO characteristics in CESM compare well with observations, substantial ENSO biases in CESM exist, including overly strong variance and periodicity in CESM relative to observations. However, mean state biases

and ENSO biases are substantially smaller in CESM at 1° resolution (employed here) as compared to 2° resolution (Deser et al., 2012).

The hosing runs are branched from the 1,000-year pre-industrial control run of CCSM4. In these runs, a prescribed freshwater flux of 1.0 Sv was applied for a period of 100 years across the surface of the northern North Atlantic (50°-70°N). This freshwater flux was used in the PMIP2 hosing simulations (https://pmip2.lsce.ipsl.fr/). Although this method likely overestimates the total freshwater flux to the North Atlantic as compared to that during the 8.2 ka event (recent estimates suggest 5.2 Sv over approximately 1 year; Teller et al., 2002), our target is a large reduction in the AMOC over a long enough period of time to obtain robust ENSO statistics. The sensitivity of the ENSO response to the magnitude of hosing is currently being explored. All other boundary conditions are fixed at 1850 AD values. Four ensemble members of hosing runs were run for 100 years in order to evaluate the robustness of the ENSO response to changes in initial conditions and allow for a robust representation of the ensemble mean and spread.

5.2.2 *Description of LOAM*

LOAM is a linearized version of the nonlinear Battisti model (Roberts and Battisti, 2011; Thompson and Battisti, 2000). The coupled atmosphere-ocean system in LOAM is described by:

$$d\boldsymbol{x}/dt = \boldsymbol{M}(t)\boldsymbol{x} + F \qquad (5.1)$$

where **x** is the state of the system (consisting of the oceanic variables T, h (upper layer depth), u1, w1), **M**(t) is the monthly (and spatially) varying dynamical system matrix, and F is a stochastic forcing. The equations that define the dynamical system matrix are linearized around the seasonally-varying climatological mean state of the atmosphere and ocean. The coupled modes of the system are found by decomposing the annual propagator matrix (which is constructed from the dynamical system matrix) into its Floquet modes (eigenmodes of the cyclo-stationary annual propagator matrix). Each mode has an associated period and decay rate that is derived from the eigenvalues of the mode. Roberts and Battisti (2011) demonstrate that the slowest decaying mode

constructed from observed mean states displays similar temporal and spatial characteristics to the observed ENSO- this mode is referred to as the ENSO mode.

The tropical Pacific mean states from the CESM pre-industrial control and hosed simulations are prescribed in LOAM to evaluate the influence of the mean state changes on ENSO dynamics. Further, to determine which of the mean state changes are responsible for the changes in ENSO, sensitivity tests are performed in LOAM by prescribing isolated components of the mean state changes.

5.3 RESULTS

5.3.1 *Response of the AMOC and ITCZ to North Atlantic Hosing in CESM*

In response to the large prescribed freshwater perturbation in the North Atlantic, the AMOC weakens to ca. 15% of its original strength within 20-25 years after the hosing is initiated (Fig. 5.1). In response, the overturning cell in the Southern Ocean extends into the North Atlantic (Fig. 5.2). In response to these dramatic changes in ocean circulation, sea ice extent increases throughout the Arctic (Fig. 5.3A-C) and a hemispheric dipole in SST anomalies form such that the NH cools while the SH warms in step with the weakening of the AMOC (Fig. 5.3D-F). The resultant hemispherically asymmetric changes in surface energy fluxes (initiated by the weakening of the AMOC and intensified by Arctic sea ice growth) produces a southward shift of the ITCZ and a strengthening (weakening) of the NH (SH) Hadley cell. These changes in the Hadley circulation strengthen (weaken) the subtropical anticyclones in the NH (SH), most notably in the Atlantic and Indian Oceans (Fig. 5.3G-I). The increased strength of the subtropical anticyclone in the N. Atlantic drives increased easterly surface trade winds in the tropical Atlantic, which blow across Central America and result in increased easterlies north of the equator in the eastern and central tropical Pacific (Fig. 5.3G-I). The mean change in surface pressure and near surface winds averaged over the last 80 years of the four hosed ensemble members are shown in Fig. 5.4.

5.3.2 *Response of the tropical Pacific to North Atlantic hosing in CESM*

The pattern of SST cooling in the tropical Pacific closely corresponds with the pattern of increased surface wind speed (Fig. 5.5), which suggests that the cooling is driven by increased latent heat fluxes through increased wind speed. In addition the increased surface easterlies in the central and eastern Pacific drive increased zonal wind stress in the tropical Pacific, with maxima centered ca. 10°N and along the equator (Fig. 5.6A). This pattern of zonal wind stress anomaly produces mean wind stress curl changes in the tropical Pacific that are characterized by a north-south dipole of decreased (increased) wind stress curl to the north (south) of the maximum in zonal wind stress at both 10°N and on the equator (Fig. 5.6B). Based on conservation of potential vorticity, theory suggests that the warm water volume above the thermocline of an equatorial box centered on the equator and that spans the tropical Pacific is expected to change when there is a change in the difference in the longitudinal integral of the wind stress curl along the northern and southern boundaries (Clarke et al., 2007): the volume will increases when the change in the difference between the longitudinally integrated wind stress curl along the longitudinal boundaries decreases (i.e., when the south minus north difference in the wind stress curl is positive). The change in the warm water volume in the box is accomplished by divergent meridional flow at the boundaries and vortex stretching (Clarke et al., 2007). Indeed, the pattern of negative (positive) wind stress curl anomaly north (south) of the equator and 10°N produces an increase in the volume of warm water in the equatorial Pacific (ca. 5°S to 5°N) and in the subtropical Pacific (ca. 10°N to 15°N), causing the thermocline to deepen and the subsurface temperature to warm along the equator and subtropical North Pacific (Fig. 5.7A,B). Further, a latitudinal cross section of tropical Pacific temperature along the equator demonstrates that the subsurface warming peaks along the thermocline in the western and central equatorial Pacific, causing the thermocline to deepen and become more diffuse in all but the far eastern equatorial Pacific (Fig. 5.7B). In response to the increase in equatorial zonal wind stress, the E-W slope of the equatorial thermocline steepens, which, combined with the wind stress curl-driven subsurface temperature changes, results in a deepening of the thermocline in the western and central equatorial Pacific and a shoaling of the thermocline in the far eastern equatorial Pacific.

In addition to changes in the annually-averaged mean state of the tropical Pacific, changes in the annual cycle are also very large. Seasonality in the eastern equatorial Pacific decreases dramatically under hosing due to the anomalous easterly trades and resultant SST cooling that peaks in boreal spring, when the climatology of the eastern equatorial Pacific is governed by weak trades and warm SSTs (Fig. 5.8). Importantly, the annual cycle of SST in the eastern equatorial Pacific is reversed in hosing runs as compared to the control run, with SSTs in the hosing runs reaching a minimum (versus maximum) in boreal spring. These changes in the seasonal cycle of tropical Pacific SST and winds are reflected in the tropical Pacific precipitation patterns (Fig. 5.9). Under hosing, the northern branch of the ITCZ shifts slightly south in boreal fall and weakens in the eastern equatorial Pacific due to the anomalous winds and cold SSTs. During boreal spring, the southern branch of the ITCZ (which is already well into the SH in the control run) recedes farther south due to the anomalous winds that spread across the eastern and central Pacific.

5.3.3 *Response of ENSO to the Tropical Pacific Mean State Changes*

The large tropical Pacific mean state changes that occur under North Atlantic hosing (i.e. cooling of ca. 1°C across the tropical Pacific, warming of up to 2°C in the subsurface equatorial Pacific and a 20-70% increase in near surface easterlies along the equator and tropical north Pacific in the annual mean) have a dramatic effect on ENSO variability in CESM. As demonstrated in Fig. 5.10, the variance of Niño 3 SSTAs decreased by more than 20% in the hosed simulations. In addition to the decreased variance of SSTAs, the structure of the SST variability is also changed under hosing. EOF1 of tropical Pacific SSTAs demonstrates that the variability is centered farther in the eastern equatorial Pacific under hosing (Fig. 5.11A,B), perhaps due to an increase in the frequency or amplitude of eastern Pacific El Niño events. Finally, under the weakened seasonal cycle in the tropical Pacific, the seasonality of ENSO is reduced in the hosed simulations (Fig. 5.12B,C).

By prescribing the tropical Pacific mean states from the preindustrial control run and hosed runs of CESM into LOAM, the influence of these mean state changes on the coupled ocean-atmosphere system can be explicitly evaluated. In agreement with the

relative changes in ENSO variance seen in CESM, LOAM simulates decreased ENSO variability when run with mean states from the hosing runs, as compared to LOAM simulations with mean fields from the preindustrial control run of CESM, (Table 5.1). Changes in the structure of the SST variability in LOAM also show broad agreement with CESM, with the center of action shifting farther into the eastern equatorial Pacific under hosing (Fig. 5.11C,D). Evaluation of the eigenmodes of the coupled system in LOAM demonstrate that the decreased ENSO variability under hosing is due to a decrease in the growth rate of the ENSO mode (Table 5.1). The period of this mode also decreases slightly, which leads to a modest shift of the periodicity of ENSO to shorter periods.

In order to determine which components of the tropical Pacific mean state changes are responsible for the decreased growth rate of the ENSO mode under hosing, we performed sensitivity tests in LOAM in which individual components of the mean fields from the CESM hosing runs were prescribed in the LOAM simulation with mean fields from the CESM preindustrial control run. Table 5.1 shows the results of these experiments. To first order, the reduced growth rate of the ENSO mode is due to the deepening and decreased intensity (dT/dz) of the thermocline in the equatorial Pacific. An additional reduction to the growth rate is caused by the tropical Pacific SST changes. Physically, the influence of these mean state changes can be understood in the following way: (1) the equatorial subsurface warming decreases the efficiency with which wind stress anomalies produce SSTAs (as a given thermocline depth anomaly on top of a deeper and more diffuse thermocline yields a weaker change in SST); (2) colder tropical Pacific SSTs decrease in the responsiveness of the atmosphere to a given SSTA (Roberts et al., 2014).

5.3.4 *Application to the 8.2 kyr event*

The CESM hosing simulations demonstrate weakened ENSO variability under hosing, in agreement with the paleohydroclimate records from the Galápagos Islands. In CESM, the large freshwater perturbation in the North Atlantic dramatically weakens the AMOC, which produces a strong north-south SSTA dipole and expanded Arctic sea ice. The large climate changes that occur in the tropical Pacific are communicated from the Atlantic Ocean primarily via the increased easterlies that blow across Central America. From the

LOAM simulations we infer that the increased easterlies in the tropical Pacific under hosing produce an associated increase in zonal wind stress and wind stress curl along the equator, which are central to the decreased SSTs and the deeper/weaker thermocline that decrease the instability of the coupled system.

While these simulations outline a clear set of mechanisms by which a large freshwater flux in the North Atlantic could give rise to reduced ENSO variability, we caution that the simulated response of ENSO to hosing is likely sensitive to tropical Pacific mean state biases in the model. A clear example of the sensitivity of a forced ENSO response to mean state biases can be found in the disagreement among GCMs on the ENSO response to greenhouse gas forcing. Such disagreement among models can also be found in hosing simulations- while ENSO variability decreases under hosing in CESM, other studies using different GCMs have reported increased ENSO variability under hosing (Dong and Sutton, 2007; Timmermann et al., 2007). While CESM with CAM4 is recognized as a top-performing GCM with regard to its simulation of tropical climate variability`, biases in ENSO characteristics are still present`, including simulated ENSO variance that is 30% too large, SST variability that extends too far west, and SST anomalies that are too periodic (Deser et al., 2012). In addition, the phase locking of ENSO to the annual cycle is too weak (Fig. 5.12A,B). Such ENSO biases are common in GCMs and are likely tied to tropical Pacific mean state biases (Ham et al., 2013). Tropical Pacific mean state biases in CESM include a cold SST bias in the NE tropical Pacific that extends along the equator, warm SST biases along the coast of South America and the northern subtropical Pacific, and equatorial easterlies that are too strong across the central Pacific and particularly in the far eastern equatorial Pacific (Fig. 5.13). The surface wind and SST bias in the far eastern equatorial Pacific are related to poorly resolved topography across Central America. This structure of this topography may be of critical importance to determining the tropical Pacific mean state changes and response of ENSO to North Atlantic hosing. Importantly, the LOAM simulations highlighted in Chapter 3 clearly demonstrate the sensitivity of ENSO to changes in the tropical Pacific mean state, suggesting that even small mean state biases in GCMs are likely to result in large biases in ENSO variability. In order to evaluate the sensitivity of the ENSO response to these tropical Pacific mean state and topography biases, further CESM

simulations are currently underway in which surface heat flux corrections and topography modifications in Central America are implemented.

5.4 SUMMARY

Simulations with CESM and a linearized intermediate complexity model of the tropical Pacific demonstrate a mechanistic link between a large freshwater perturbation in the North Atlantic and a southward shift of the ITCZ and reduced ENSO variability, in agreement with a new set of paleoclimate reconstructions from the eastern equatorial Pacific. These simulations indicate that subsurface warming in the tropical Pacific (produced by increased equatorial wind stress through changes in the wind stress curl) decrease the efficiency with which wind stress anomalies produce SSTAs. The coupled ocean-atmosphere system is further stabilized in the models by wind-driven surface cooling throughout the tropical Pacific through a decrease in the responsiveness of the atmosphere to SSTAs.

The increased easterly winds and wind stress in the tropical Pacific are thus central to the reduced ENSO variability in CESM. These strengthened easterlies are brought about under hosing in the following way: hemispherically asymmetric changes in surface energy fluxes (initiated by the weakening of the AMOC intensified by the positive feedback from Arctic sea ice growth) produce a southward shift of the ITCZ and a strengthening (weakening) of the NH (SH) Hadley cell. These changes in the Hadley circulation strengthen (weaken) the subtropical anticyclones in the North Atlantic (South Atlantic), which drive increased easterly trade winds in the tropical Atlantic that are communicated through the eastern and central tropical Pacific via the Panama gap.

While a southward shift of the ITCZ in response to North Atlantic hosing is well supported by theory and is a robust feature of climate model simulations, the response of ENSO to hosing is less established and appears to vary across models. Disagreement across models is likely in part due to large tropical mean state biases in GCMs. Further simulations with CESM in which flux corrections and topography modifications are imposed are currently underway to evaluate the sensitivity of the ENSO response to such mean state biases.

Table 5.1. Period and growth rate of the ENSO mode and variance of Niño 3 SSTAs in LOAM with prescribed mean states from the CESM preindustrial control run (pi) and a CESM hosed run (hosed). CCSM4 pi + X indicates LOAM run with all mean states from the preindustrial control run except X, which is taken from the hosed run. Uvel, vvel and wvel represent the mean ocean currents, U-wind and V-wind represent the zonal and meridional wind fields, Tz2, hdata, cs and p are the four components of "subsfc temp": Tz2 indicates the parameterization of the mean vertical temperature gradient at the base of the thermocline and hdata, cs and p are subsurface parameterizations representing the mean interface depth in the ocean model. In bold are the variances

Model	Mode Period (yr)	Mode Growth (yr-1)	Variance ($°C^2$)
CESM pi			1.11
CESM hosed			0.86
LOAM pi	3.19	0.63	1.11
LOAM hosed	3.07	0.43	0.57
CESM pi + SST	3.05	0.56	0.77
CESM pi + u-vel	3.25	0.58	0.96
CESM pi + v-vel	3.20	0.67	1.55
CESM pi + w-vel	3.68	0.60	1.19
CESM pi + U-wind	3.29	0.85	3.98
CESM pi + V-wind	3.16	0.58	0.83
CESM pi + subsfc temp	3.04	0.38	0.42
CESM pi + Tz2	3.26	0.55	0.80
CESM pi + hdata+cs+p	2.96	0.44	0.54

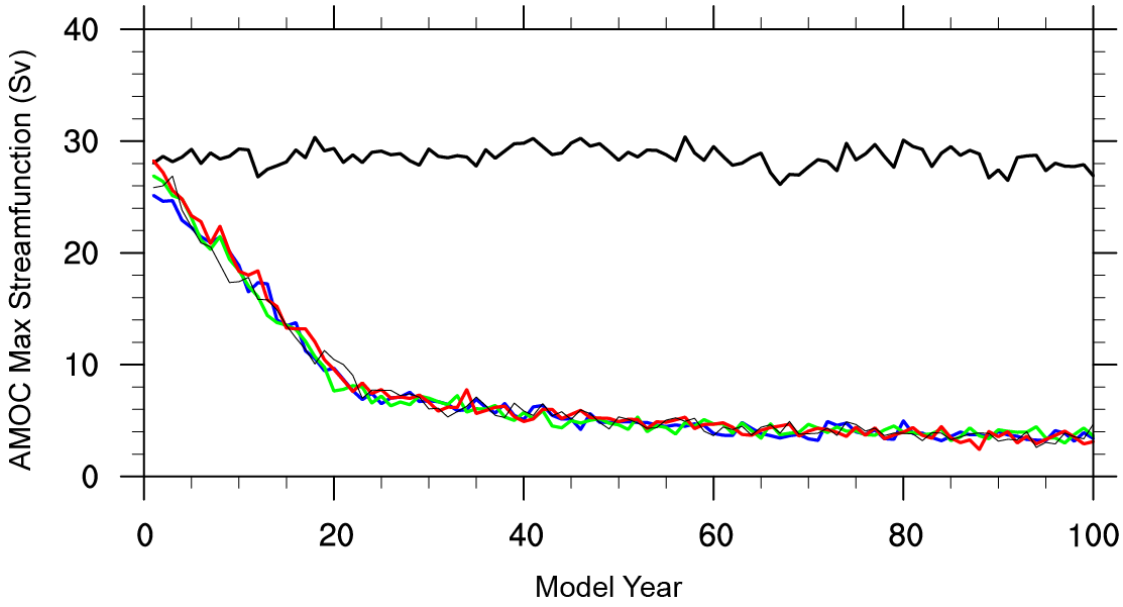

Figure 5.1. Time series of the annually averaged maximum meridional streamfunction in the Atlantic between 28ºN to 90ºN below 500m from 100 years of the CESM preindustrial control simulation (black) and the hosed simulations (colors).

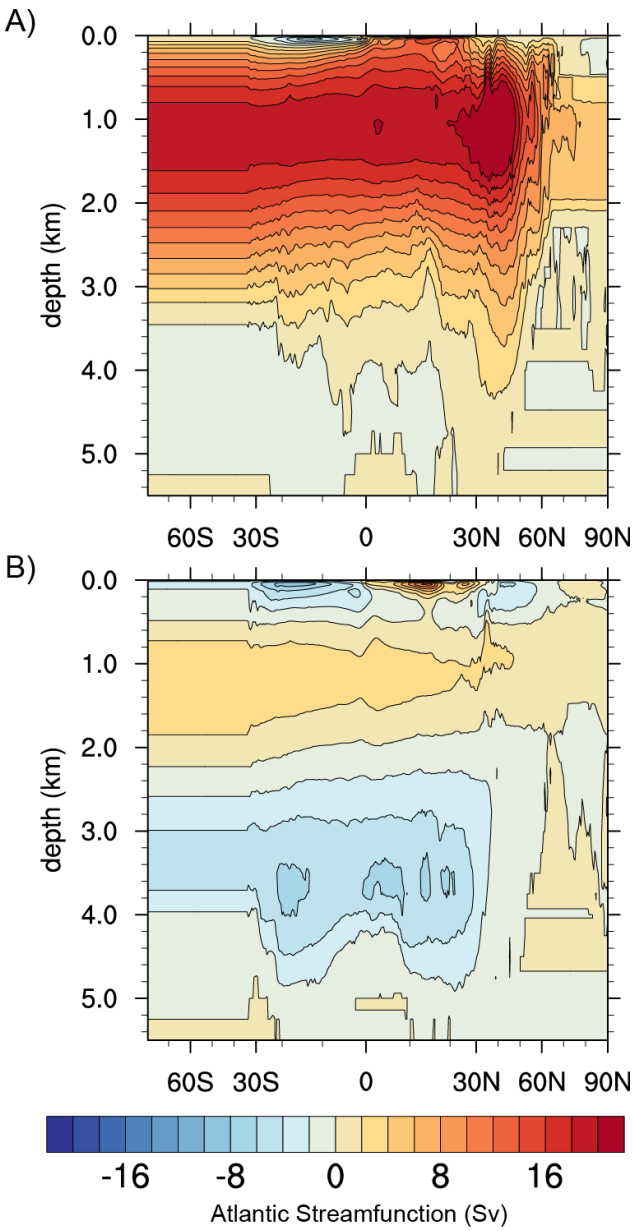

Figure 5.2. Mean meridional streamfunction in the Atlantic in the CESM control and hosed simulations: A) averaged over 320 years of the control simulation; B) averaged over the last 80 years of the four hosed ensemble members.

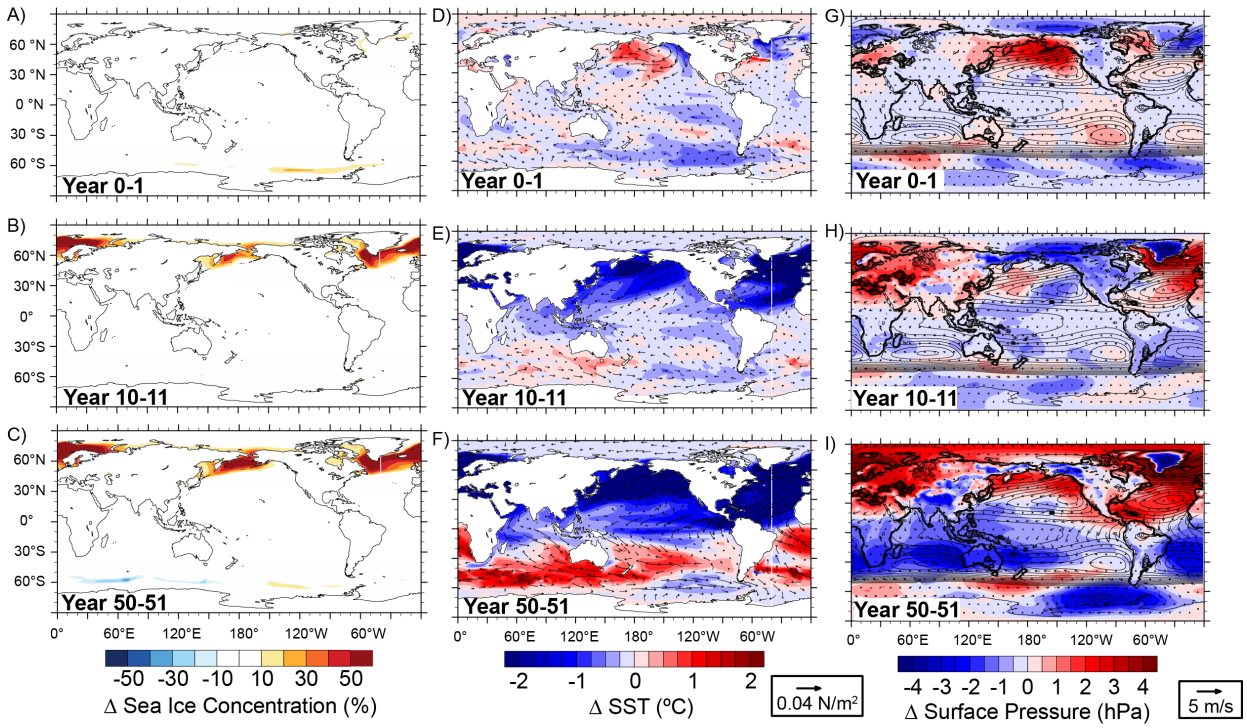

Figure 5.3. Time evolution of the change in: A-C) sea ice concentration; D-F) SST (colors) and wind stress vectors; G-I) surface pressure (colors) and surface wind velocity vectors in the CESM hosed runs with respect to 320 years of the control run. Time snapshots are averages over: Year 0-1 (top), Year 10-11 (middle) and Year 50-51 (bottom).

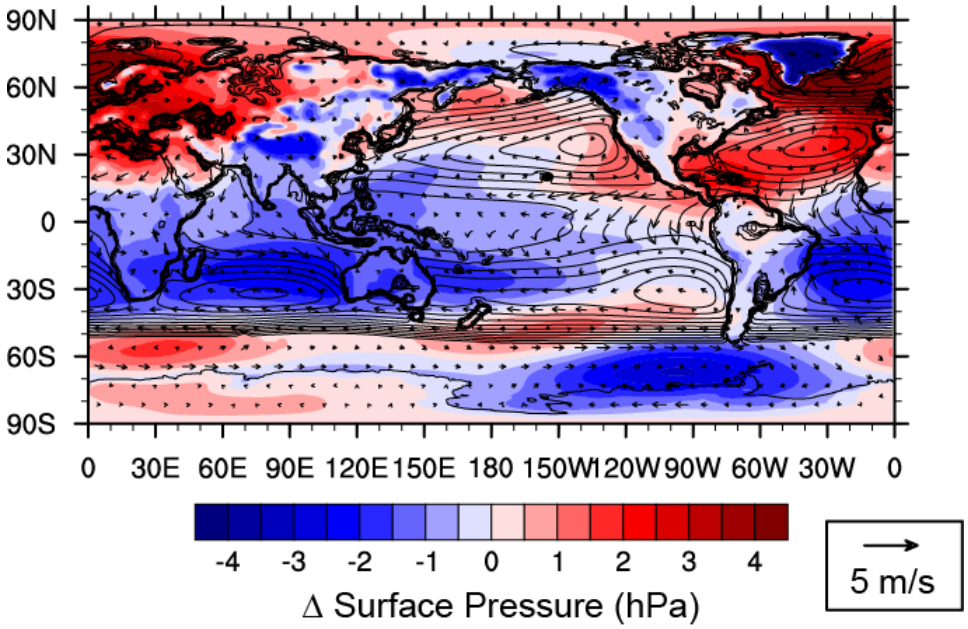

Figure 5.4. Change in surface pressure (colors) and near surface wind velocity (vectors) in the CESM hosed runs. Changes were calculated by subtracting the average over last 80 years of the four hosed ensemble members from the average of 320 years of the preindustrial control run.

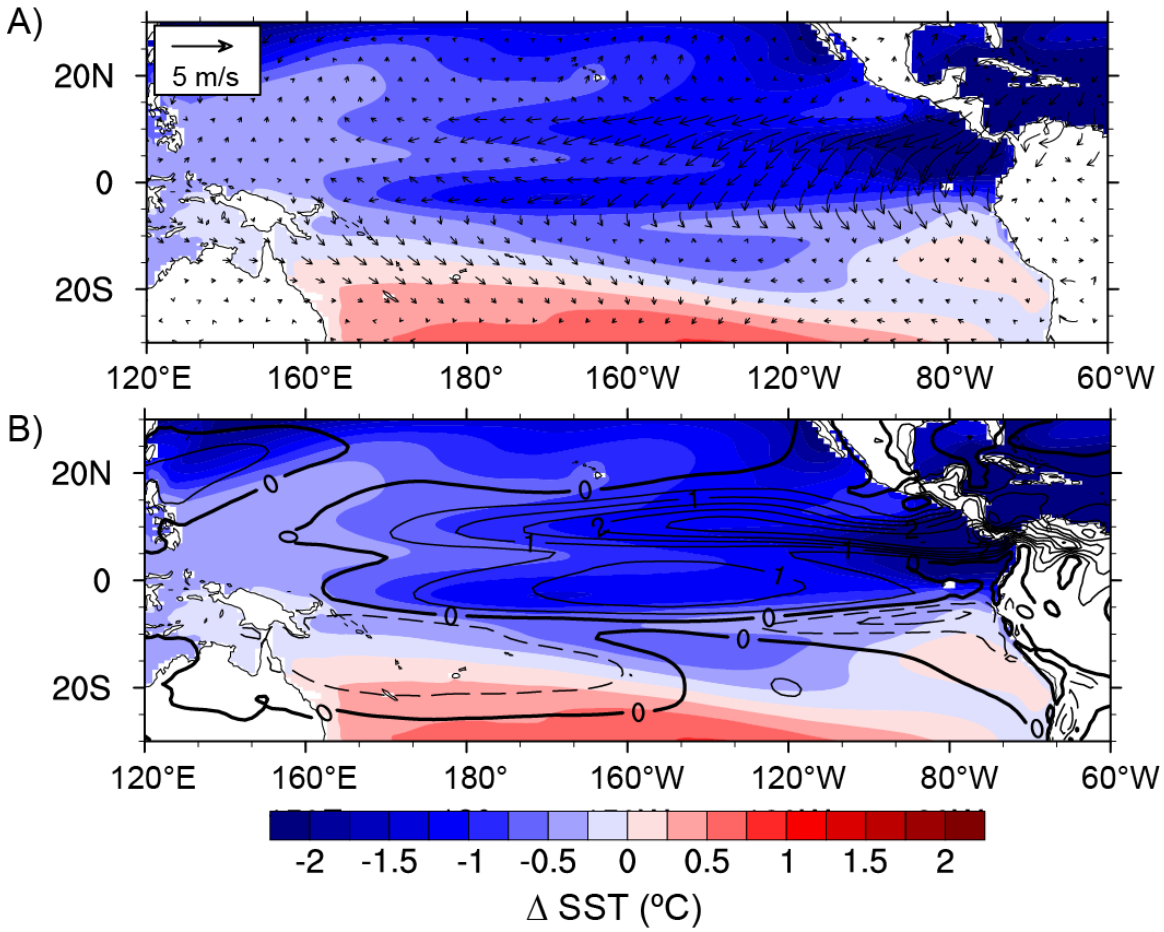

Figure 5.5. Change in tropical Pacific SST and surface wind in the CESM hosed runs. A) SST (colors) and wind velocity (vectors); B) SST (colors) and wind speed (contours). Changes were calculated by subtracting the average over last 80 years of the four hosed ensemble members from the average of 320 years of the preindustrial control run.

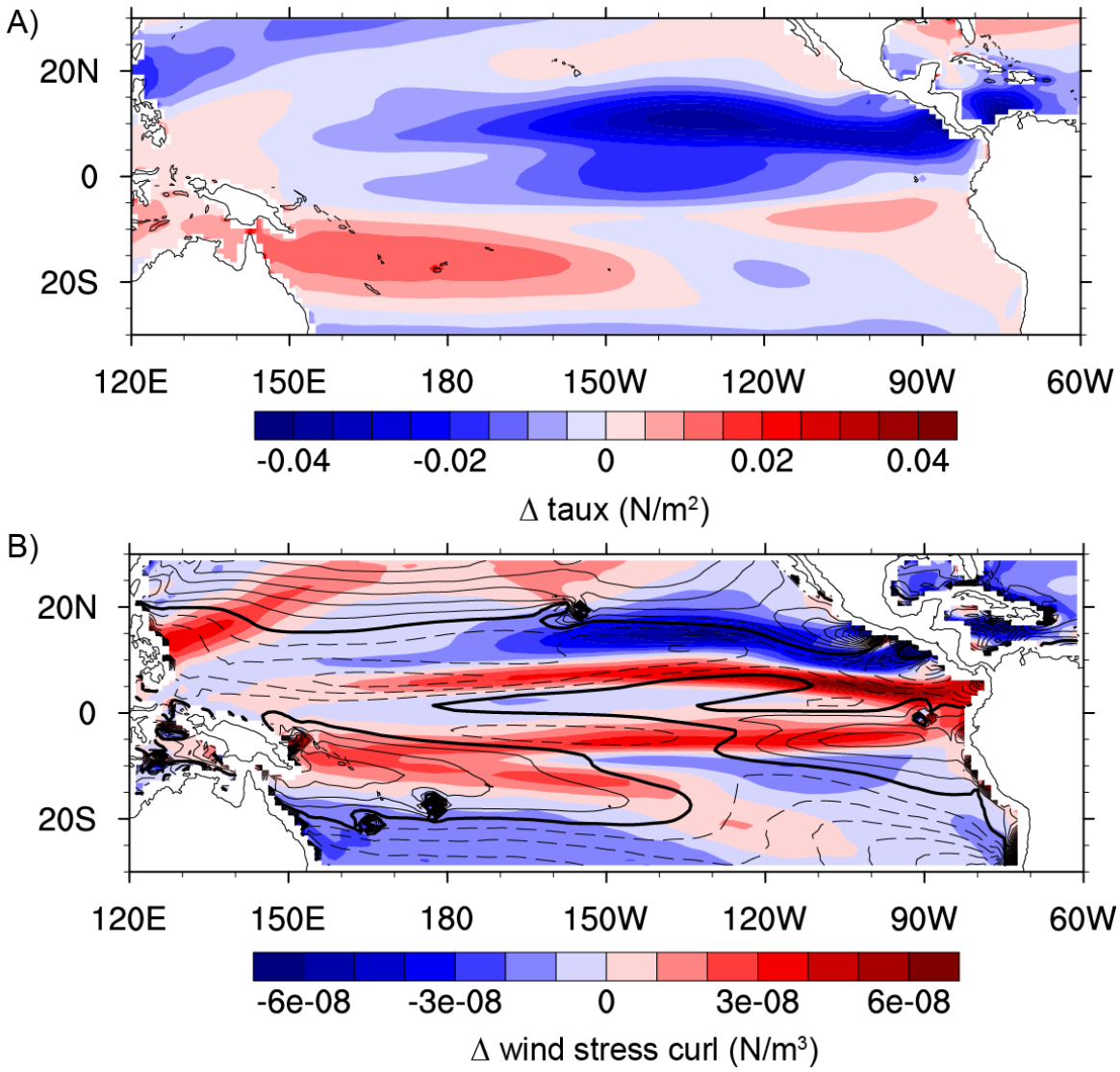

Figure 5.6. Change in tropical Pacific zonal wind stress and wind stress curl in the CESM hosed runs. A) Change in zonal wind stress; B) change in wind stress curl (colors) with the mean wind stress curl from the control run overlaid (unfilled contours). Changes were calculated by subtracting the average over last 80 years of the four hosed ensemble members from the average of 320 years of the preindustrial control run.

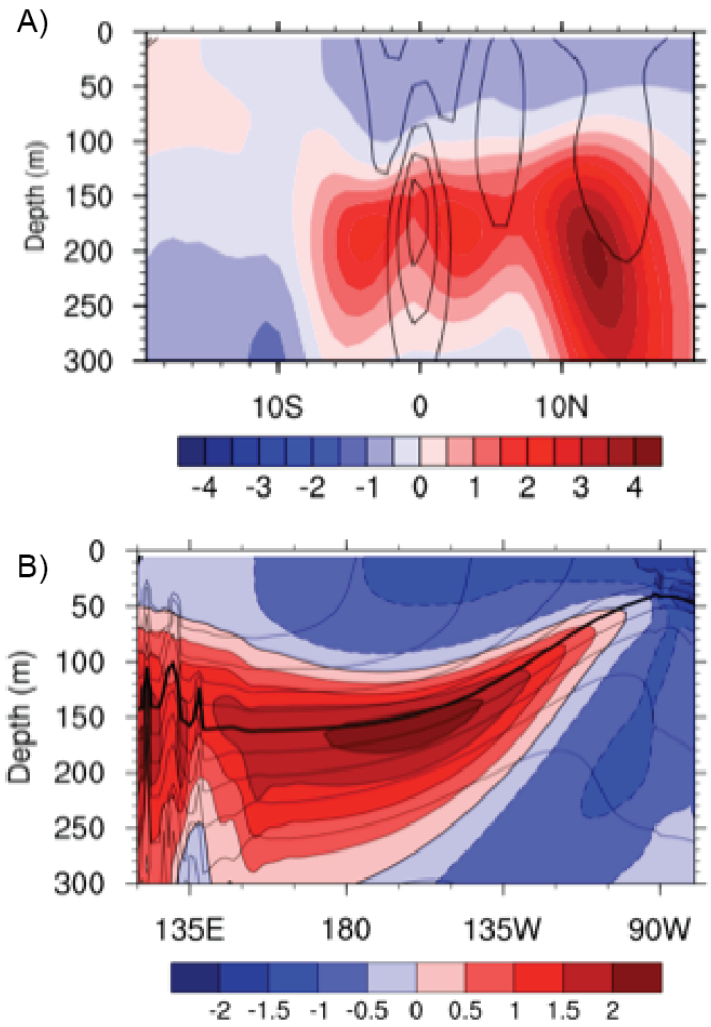

Figure 5.7. Change in tropical Pacific subsurface temperature in the CESM hosed runs. A) Change in mean subsurface temperature (colors; in °C) averaged across the CP (160E:160W), unfilled contours in depict the mean zonal current from the control run; B) change in mean subsurface temperature (colors; in °C) averaged across the equatorial region (5S:5N); unfilled contours depict the mean subsurface temperature from the control run and the bold line represents the 20C isotherm. Changes were calculated by subtracting the average over last 80 years of the four hosed ensemble members from the average of 320 years of the preindustrial control run.

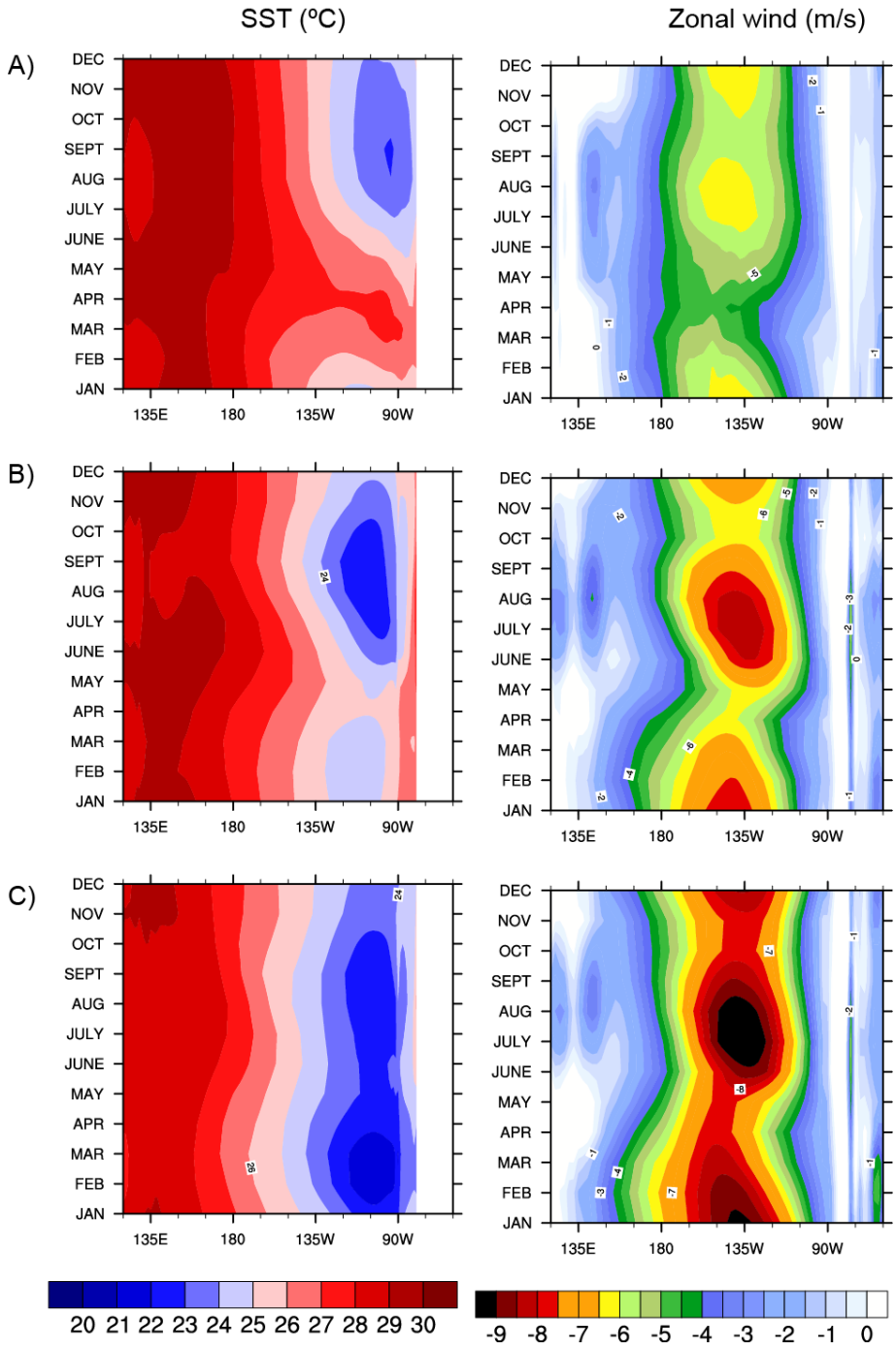

Figure 5.8. Annual cycle of climatological SST and surface winds across the equatorial Pacific (averaged over 5°S to 5°N) in A) observations, B) the CESM preindustrial control run, and C) the CESM hosed runs. Observed SST data is from NOAA ERSST v3b (1971-2010) and observed surface winds are from ERA40 Reanalysis data.

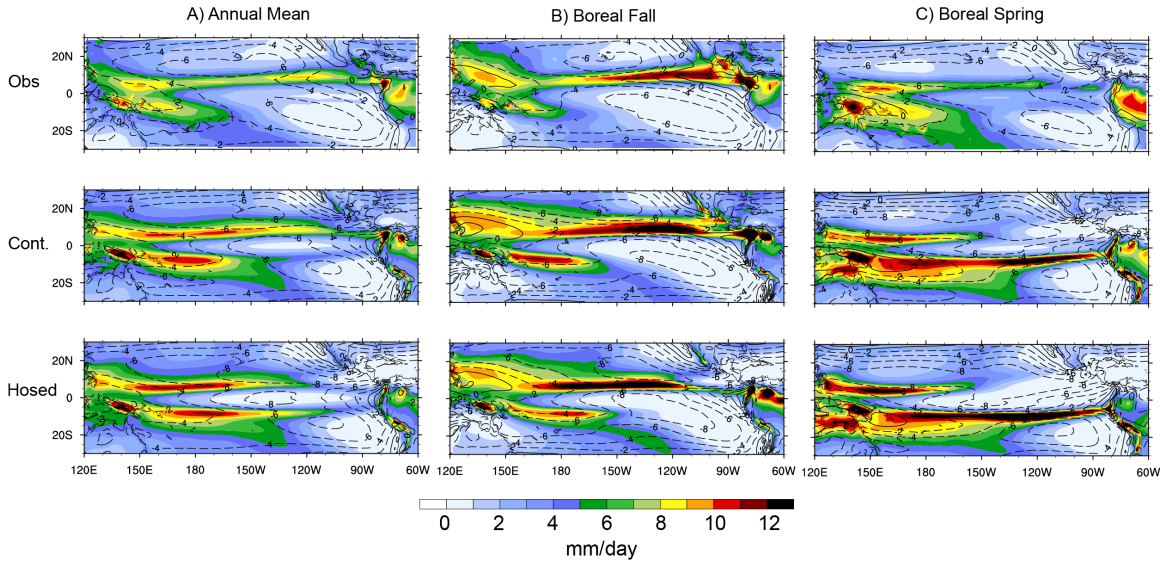

Figure 5.9. Tropical Pacific precipitation (colors) and zonal wind (unfilled contours; m/s) in observations (top), the CESM preindustrial control run (middle) and the hosed runs (bottom) averaged over: A) the annual cycle; B) boreal fall (Aug-Oct); and C) boreal spring (Feb-Apr).

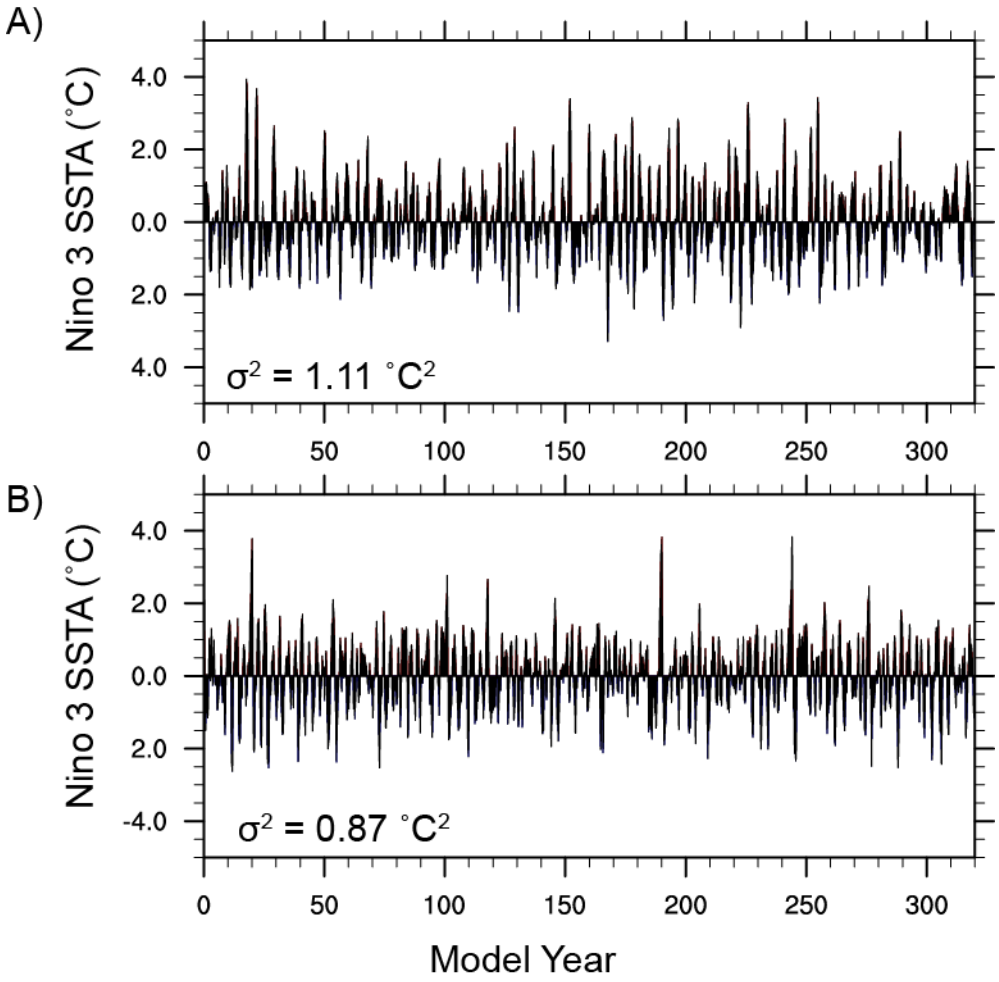

Figure 5.10. Time series of 3-month running mean Niño 3 SSTAs in: A) 320 years of the CESM preindustrial control run; B) the last 80 years of the four CESM hosed ensemble members.

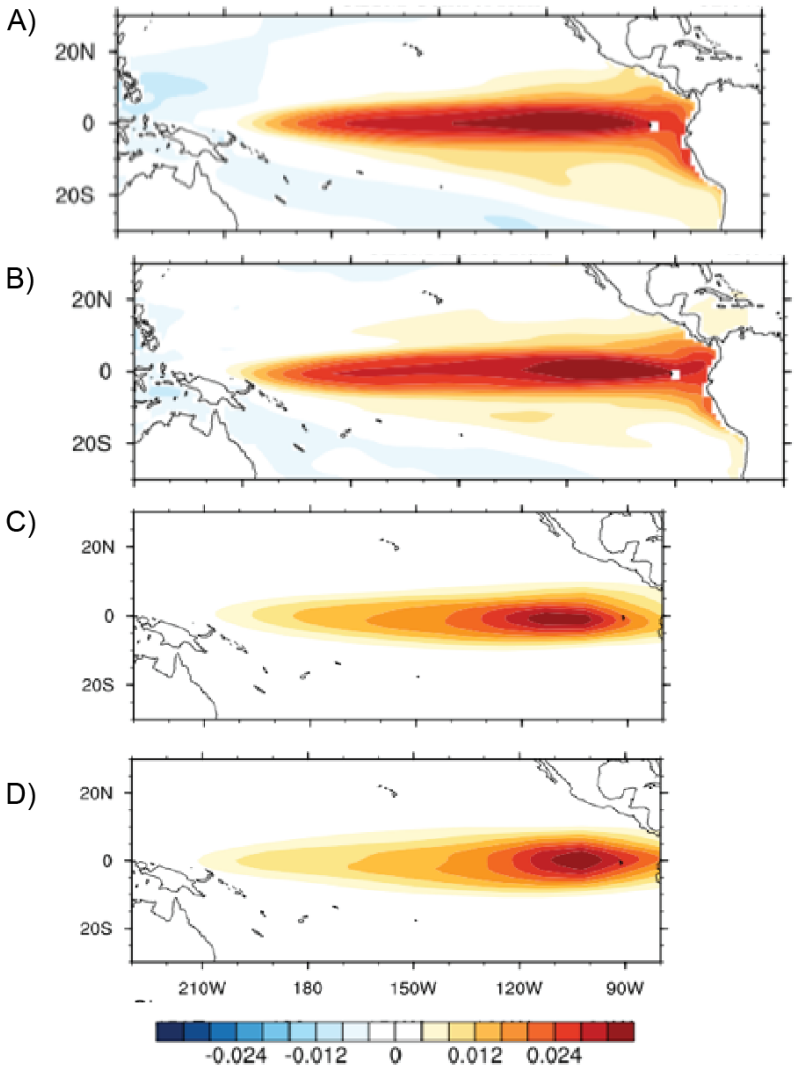

Figure 5.11. EOF1 of tropical Pacific SSTAs in the CESM simulations and LOAM. A) 320 years of the preindustrial control run of CESM; B) the last 80 years of the four hosed ensemble members in CESM; C) LOAM run with mean states from 100 years of the CESM preindustrial control run; D) LOAM run with mean states from 100 years of the CESM hosed runs.

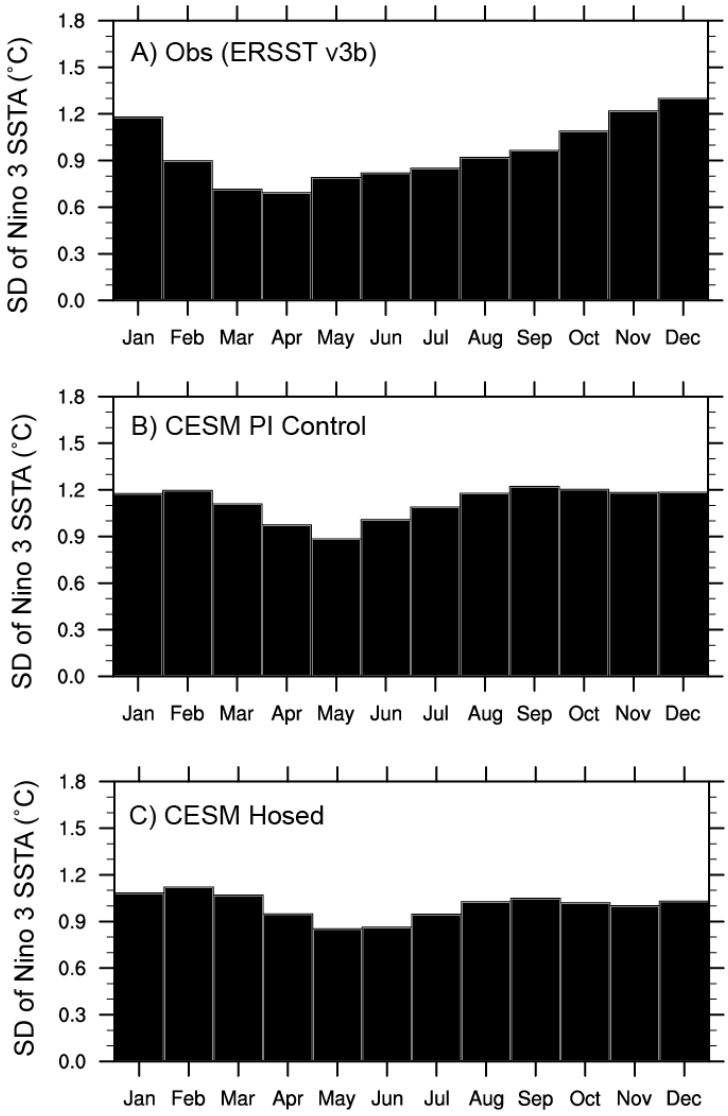

Figure 5.12. Standard deviation of (detrended) Niño 3 SSTAs as a function of month in: A) observations (ERSST v3b, 1971-2010); B) 320 years of the CESM preindustrial control run.

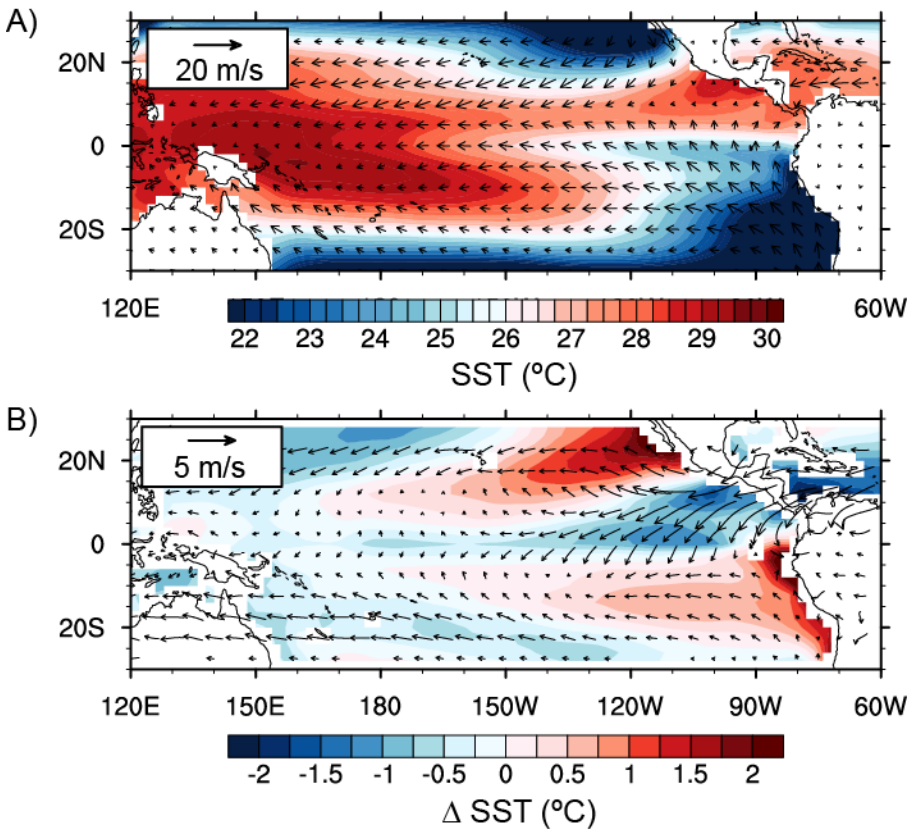

Figure 5.13. Tropical Pacific SST and near surface wind biases in the CESM preindustrial control run. A) Mean annual SST and surface winds in observations; B) SST and surface wind difference in 100 years of the CESM preindustrial control run relative to observations. Observed SST data is from NOAA ERSST v3b (1971-2010) and observed surface winds are from ERA40 Reanalysis data.

Chapter 6. CHARACTERIZING UNFORCED MULTI-DECADAL ENSO VARIABILITY: A CASE STUDY WITH GFDL CM2.1

6.1 INTRODUCTION

Tropical Pacific climate variability on timescales of decades and longer is poorly constrained due to the short observational record but is critical to our understanding of past and future climate change. ENSO variability is thought to have exhibited large changes over the Holocene (Cobb et al., 2013; Koutavas et al., 2006; Tudhope et al., 2001), however, to what degree these variations are forced versus inherent to a noisy coupled ocean-atmosphere system are unknown. This uncertainty arises in part due to the poor constraints on internal ENSO variability on multi-decadal and longer timescales.

Given the short observational record of tropical Pacific climate variability, long, unforced simulations of the climate system with fully coupled General Circulation Models (GCMs) are necessary to constrain ENSO variability on decadal and longer timescales (Russon et al., 2014; Wittenberg, 2009). However, the large ENSO biases prevalent in GCMs undermine the utility of applying empirical constraints of tropical climate variability obtained from GCM simulations to nature. GCMs used in the Fourth and Fifth Assessment Reports of the Intergovernmental Panel on Climate Change exhibit a wide range of biases in their representation of ENSO variability (Guilyardi et al., 2012a; Guilyardi et al., 2012b; Guilyardi et al., 2009), which has resulted little agreement on how ENSO is likely to change in the future (Collins et al., 2010; DiNezio et al., 2012; Vecchi and Wittenberg, 2010; Watanabe et al., 2012). The sources of these ENSO biases are largely unknown, but may likely reflect the sensitivity of ENSO variability to mean state biases in the models.

A 2,000 year-long pre-industrial control run of GFDL CM2.1 (Delworth et al., 2006) was previously shown to exhibit large, unforced, largely unpredictable, multi-decadal changes in ENSO variability (Wittenberg, 2009; Wittenberg et al., 2014), which affect the background climatological state of the tropical Pacific (Ogata et al., 2013). In this

study, we use a linearized intermediate model of the tropical Pacific to investigate the impact of these low frequency, internally-generated mean state changes in the tropical Pacific on the ENSO variability in this model. In addition, we compare the spectrum of ENSO variance in the CM2.1 control run to that from the stochastically forced linear model with prescribed observed mean states to evaluate the influence of nonlinear dynamics and total variance on the distribution of multi-decadal ENSO variability.

6.2 METHODS

In the present study, we run the Linearized Ocean Atmosphere Model (LOAM; Thompson and Battisti, 2000) described in Chapters 4 and 5 with mean fields prescribed from each of three 40-year epochs characterized by extreme ENSO variability in the CM2.1 pre-industrial control simulation and investigate the influence of the changes in tropical Pacific mean state on the coupled system. Stochastic forcing in LOAM is applied as white noise to the SST field. The amplitude of the noise is chosen so that the variance of Niño 3 SST anomalies in LOAM with mean fields from Epoch M is equal to the variance of Niño 3 SST anomalies in Epoch M of the CM2.1. This same amplitude of noise forcing is used in all LOAM runs presented in this study.

LOAM was also run with mean states prescribed from observed mean fields. Ocean temperature, currents, upwelling and wind stress fields are taken from the UMD Simple Ocean Data Assimilation reanalysis (SODA; Carton et al., 2000b) for the period 1958–2001, and wind fields are taken from the European Centre for Medium-Range Weather Forecast ERA-40 reanalysis (http://apps.ecmwf.int/datasets/) for the same period.

6.3 RESULTS AND DISCUSSION

6.3.1 *Characteristics of Tropical Pacific Variability in Extreme ENSO Epochs in CM2.1*

The GFDL CM2.1 global atmosphere/ocean/land/ice model has been widely recognized as a top-performing GCM with regard to its simulation of tropical climate variability and was featured prominently in the third Coupled Model Intercomparison Project and the Intergovernmental Panel on Climate Change Fourth Assessment Report (Reichler and

Kim, 2008; van Oldenborgh et al., 2005; Wittenberg et al., 2006). The 2,000 year-long pre-industrial control run of GFDL CM2.1 exhibits large changes in ENSO variability on multi-decadal time scales, which have been the focus of a number of recent studies (Karamperidou et al., 2014; Wittenberg, 2009; Wittenberg et al., 2014). In the control run of this model, the variance of Niño 3 SSTAs in running mean 40-year periods varies by a factor of more than four (from 0.7 – 3.0 $°C^2$; Fig. 6.1). In this paper we focus on three 40-year periods in the CM2.1 control run that were highlighted in Wittenberg (2009), Karamperidou et al. (2014), and Wittenberg et al. (2014), to represent the diversity of the model's ENSO variability. The time series of Niño 3 SSTAs for each period are shown in Fig. 6.1B-D. Years 1151–1191 (Epoch L) represent a period of extreme low variability (variance of Niño 3 SSTAs = 0.7 $°C^2$). Years 531–571 (Epoch M) are characterized by variability that is similar to the mean of the 2,000 year run (variance of Niño 3 SSTAs = 1.8 $°C^2$), with fairly normally-distributed Niño 3 SSTAs that have a regular periodicity. Years 1711–1751 (Epoch H) are characterized by frequent intense warm events (variance of Niño 3 SSTAs = 3.0 $°C^2$) that last longer and have less regular periodicity than those in Epoch M.

The leading patterns of tropical Pacific SSTAs in each epoch are shown in Fig. 6.2. EOFs 1-3 display roughly similar characteristics in all epochs. Notable differences include a lower fraction of the total variance explained by the first two EOFs in Epoch L relative to the other epochs and variance that is more centered in the eastern equatorial Pacific variability in Epoch H compared to the other epochs.

6.3.2 *ENSO in LOAM versus GFDL CM2.1*

ENSO is known to be highly sensitive to mean state changes in the tropical Pacific (Battisti and Hirst, 1989; Dewitte, 2000; Roberts et al., 2014; Zebiak and Cane, 1987). Because the observed ENSO is well represented by linear dynamics (Penland and Sardeshmukh, 1995; Roberts and Battisti, 2011), we use a linearized anomaly model of the tropical Pacific to evaluate the influence of the tropical Pacific mean state changes highlighted by the extreme ENSO epochs of CM2.1 on ENSO variability. When LOAM is run with mean fields prescribed from the climatology in CM2.1 averaged over all three epochs (120 years of data) and stochastically forced, the spatial pattern of tropical Pacific

SSTA variability is broadly similar between CM2.1 and the CM2.1-tuned LOAM (Fig. 6.3B,C). Notable dissimilarities include that the region of maximum variance doesn't extend as far west in LOAM, is broader meridionally and is weaker in the far eastern equatorial Pacific as compared to CM2.1. In addition, Niño 3 SSTAs in CM2.1 display large asymmetry in the amplitude of warm versus cold events (Fig. 6.4B; Fig. 6.5B), indicating the presence of strong nonlinearities in the coupled ocean-atmosphere system of CM2.1 (Choi, 2013). In contrast, Niño 3 SSTAs in LOAM are by construction linear, which more closely represent the near-normal distribution of observed Niño 3 SSTAs (Fig. 6.5A,C). The periodicity of ENSO also displays notable dissimilarities between CM2.1 and LOAM (Fig. 6.6) - whereas the power spectrum of Niño 3 SSTAs in CM2.1 has a peak at ca. 5 years, the power spectrum in LOAM is more sharply peaked around 3 years. Finally, the phase locking of ENSO to the annual cycle is highly dissimilar between CM2.1 and LOAM (Fig. 6.7). In the real world, ENSO is strongly phase locked to the calendar year, with ENSO events tending to peak in boreal winter (Fig. 6.7A). In contrast, ENSO in CM2.1 displays weak seasonality with the variance of Niño 3 SSTAs peaking in boreal summer (Fig. 6.7B). Given CM2.1 mean states, ENSO in LOAM displays strong seasonality with minimum variance in boreal spring/summer and maximum variance in boreal fall (Fig. 6.7C). The discrepancy in the seasonality in ENSO in CM2.1 and that in LOAM with CM2.1 mean fields may be due to the dependence of surface heat flux on wind speed which is likely to be acting in the western Pacific in CM2.1 but which is absent in LOAM (which could also account for the differences in EOF1 shown in Figs. 3B,C).

6.3.3 *Influence of Mean State Changes on ENSO in LOAM*

In order to evaluate the role of the tropical Pacific mean state changes on ENSO variability in the three CM2.1 epochs, we prescribe the annual cycle of tropical Pacific climatology averaged over each of the three epochs in LOAM. The differences in annually-averaged tropical Pacific climatology among these epochs are shown in Figs. 8-10. Progressing from Epoch L to Epoch H, the mean states are characterized by weakening of the surface easterly trade winds in the western and central equatorial

Pacific, warming of the ocean surface and subsurface in the eastern equatorial Pacific and cooling in the western equatorial Pacific (Fig. 6.9; Fig. 6.10).

When the mean states of the CM2.1 epochs are prescribed in LOAM, the relative changes in the variance of Niño 3 SSTAs in the linear model are in fact opposite to that observed in the CM2.1 simulation: the variance is lowest in Epoch H and highest in Epoch L (Table 6.1). In Epoch H, the decreased ENSO variance relative to Epoch M is due to a decrease in the growth rate of the ENSO mode. In Epoch L, the slightly increased variance relative to Epoch M is tied to increased growth rate of the lower order coupled modes. Collectively, our results suggest that tropical Pacific mean state changes are not the primary cause of the extreme ENSO epochs in CM2.1—and instead may be generated by the extreme ENSO behavior during each of these epochs (that is, they are the residual impacts of the ENSO cycles during each epoch), as suggested by Ogata et al. (2013).

Although the LOAM simulations suggest that tropical Pacific mean state changes are not directly responsible for the multi-decadal ENSO variability in CM2.1, that is not to say that the mean state changes do not have an influence on the ENSO variability. Indeed, the simulations with LOAM suggest that the low frequency tropical Pacific mean state changes provide a negative feedback on the stochastically-driven fluctuations in ENSO variability. These results suggest that a two-way feedback mechanism exists between low frequency ENSO variability and tropical Pacific mean state changes in CM2.1: (1) stochastic forcing produces low frequency fluctuations in ENSO variability which give rise to tropical Pacific mean state changes due to the strong non-linear characteristics of the coupled system; (2) these stochastically-driven mean state changes then give rise to negative feedbacks that damp the original ENSO variations. For example, as shown in Ogata et al. (2013), periods of high ENSO variability in CM2.1 produce a decreased zonal SST gradient (Fig. 6.9c), decreased zonal wind stress in the central to western equatorial Pacific (Fig 8c) and thus weaker E-W tilt of the thermocline (Fig 10b). According to the stability analysis in LOAM, these mean state changes act to stabilize the coupled system and thereby weaken the ENSO variability (Table 6.1). Further experiments with LOAM (not shown) in which individual components of the mean state in Epoch H were individually substituted into the Epoch M simulation

indicate that the weaker zonal winds and the thermocline depth changes are the primary mechanisms responsible for the increase in stability of the coupled system.

6.3.4 *Random Noise and Nonlinear Dynamics as Drivers of Multi-Decadal ENSO Variability in CM2.1*

Because the long CM2.1 simulation is unforced, there are essentially only two mechanisms that could be responsible for the large multi-decadal ENSO variability: (1) low frequency changes in the tropical Pacific mean state or (2) stochastic (weather) processes that influence ENSO variability without affecting the tropical Pacific mean state (and therefore the underlying dynamics of ENSO). Our analyses suggest that mean state changes in the tropical Pacific cannot explain the periods of extreme ENSO variability in CM2.1. These results strongly suggest that the large multi-decadal variability in CM2.1 is instead driven by atmospheric noise. Possible mechanisms of the large multi-decadal variability include stochastic forcing acting on the highly nonlinear dynamics present in CM2.1 or low frequency changes in the structure and/or amplitude of noise forcing (either internal or external to the tropical Pacific) acting over any single epoch. While an attempt was made to characterize the noise forcing in the three CM2.1 epochs using a Linear Inverse Model, it was concluded that 40 years of data was not long enough to robustly constrain the dynamics of the coupled system. Thus, the possible role of changes in atmospheric noise forcing has yet to be evaluated.

In support of the conclusion that random noise is responsible for the multi-decadal variability in CM2.1, however, recent work by Wittenberg et al. (2014) demonstrated that by rerunning CM2.1 during the extreme ENSO epochs after applying a small remote SST perturbation to a single grid cell, the extreme variance epochs in in CM2.1 were unpredictable. The impact of nonlinear dynamics on multi-decadal variability in CM2.1 is found by comparing the probability distribution of variance of Niño 3 SSTAs in 40-year intervals from the 2,000-year CM2.1 versus the 2,000-year LOAM simulation run with CM2.1 mean states (Fig.11). The distribution of variance is notably broader in CM2.1 than that in LOAM with CM2.1 mean states (including values that are outside of the range of values found in the linear system), suggesting that the nonlinear dynamics supports a greater frequency and amplitude of high variance periods than that supported

by the linear system. Comparing the empirical PDFs to χ^2 distributions further elucidate the influence of nonlinear dynamics on the distribution of variance. Given a stationary, linear process with well-defined long term variance, the PDF of multi-decadal variance should be well-represented by a χ^2 distribution (Russon et al., 2014). Indeed, the χ^2 distribution is a good fit to the PDF of 40-yr variance of Niño 3 SSTAs in LOAM (Fig. 6.11). That the PDF from CM2.1 deviates substantially from a χ^2 distribution is further evidence that the strong nonlinearities present in CM2.1 serve to broaden the distribution of variance by increasing the amplitude and frequency of high variance epochs.

Our analysis strongly suggests that the periods of large multi-decadal variability in CM2.1 are due to stochastic driving of ENSO that is, in turn, amplified by nonlinear dynamics. It is thus informative to evaluate the sources of nonlinearity in CM2.1. Multiple sources of nonlinearity are present in the coupled ocean-atmosphere system in CM2.1 including a nonlinear relationship between zonal wind speed anomalies and SSTAs in the central Pacific (Fig. 6.12A; Choi et al., 2013) which is the key area for coupling between the atmosphere and ocean that gives rise to the Bjerknes feedback, and a nonlinear relationship between zonal wind stress and wind speed anomalies (Fig. 6.13). These nonlinearities combine to give a relationship between SSTAs and zonal wind stress anomalies (i.e. the relationship that drives the dynamics of the coupled system) that is also highly nonlinear (Fig. 6.14). The nonlinear relationship between SSTAs and surface wind anomalies is primarily due to the nonlinear relationship between SSTAs and zonal wind stress anomalies, which is only partially buffered by the quadratic relationship between wind speed anomalies and zonal wind stress (Fig. 6.12 - Fig. 6.14).

A nonlinear response of the atmosphere to SST anomalies in CM2.1 could be caused by several processes including:

(i) the nonlinear Clausius Clapeyron equation (as saturation vapor pressure is a nonlinear function of temperature, larger positive surface air temperature anomalies forced by positive SSTAs in the central and eastern equatorial Pacific lead to a nonlinear increase in saturation vapor pressure, which produces greater moisture convergence, latent heating and convection, giving rise to a nonlinear increase in westerly wind anomalies);

(ii) changes in the character of the boundary layer (from shallow stratified to deep convective) in association with warm SSTAs; and

(iii) a nonlinear moisture convergence feedback (the efficiency with which anomalous latent heating produces anomalous moisture convergence and convection is strongly a function of the background low-level moisture convergence; Battisti, 1988).

For example, during El Niño events, the warm pool convection region shifts eastward and equatorward, producing a large precipitation response when the edge of the warm pool shifts into the typically dry central equatorial Pacific. However, during La Niña events, the westward shift of the warm pool region produces only a weak precipitation anomaly in the already dry central equatorial Pacific.

Regardless of the source of the strong nonlinear coupling of the atmosphere and ocean in the central Pacific of CM2.1 (that is the coupling between SST anomalies that affect the atmosphere and wind speed anomalies – and therefore wind stress anomalies – that affect the ocean), it is a strong nonlinearity and is causal in producing the non-linear ENSO events in the CM2.1 that are not apparent in nature (cf. the panels in Fig. 6.14), as discussed below.

Separating epochs of high and low ENSO variance in CM2.1 and evaluating the characteristics of the coupled system in each subset of data offers further insight into the role of nonlinearities in producing multi-decadal epochs in which the ENSO variance is vastly different. This separation demonstrates that high variance epochs are populated by extreme ENSO events (cf panels b and c of Fig. 6.12 and Fig 14) and that the skewness in SSTAs and wind stress anomalies (and hence the mean state changes associated with ENSO cycles) is greatest in these high variance and high amplitude ENSO periods (df panels b and c of Fig. 6.15 and 16). In contrast, the low variance epochs are characterized by SSTAs and wind stress anomalies that are far more normally distributed (Fig. 6.15C; Fig. 6.16C) and are characterized by a nearly linear relationship between SSTAs and wind stress anomalies (Fig. 6.14C). From this we conclude that the physics of the coupled ocean-atmosphere system in CM2.1 are fairly linear for small tropical Pacific climate anomalies (i.e. for amplitudes similar to that observed in nature) and that the strongly nonlinear behavior observed in CM2.1 is generated through noise forcing and

state dependent feedbacks that arise under large perturbations in the coupled system. Combined with the determination that the multi-decadal epochs of high ENSO variance in CM2.1 are populated by extreme warm ENSO events but typical cold events, we conclude that the broad distribution of multi-decadal ENSO variability in CM2.1 (Fig. 6.11) is due to these stochastically-driven extreme warm events in the ENSO cycle.

We now seek to address how the nonlinearities present in CM2.1 compare to observations and consider the implications for constraining unforced ENSO variability in nature.

6.3.5 *ENSO in GFDL CM2.1 Versus Observations*

We now explore whether the coupled ocean-atmosphere dynamics present in CM2.1 are representative of the real world is apropos to the interpretation of changes in past, current, and future ENSO variability. Differences in ENSO characteristics between observations and CM2.1 are notable (as in most CGCMs), and include overly large ENSO variance in CM2.1 (Fig. 6.4A,B; Fig. 6.6) and a biased pattern of SST variability, including variability that extends too far west, is too equatorially-confined, and is underestimated in the far equatorial eastern Pacific (Fig. 6.3A,B). Another notable difference between ENSO in observations and CM2.1 can be found in the seasonal cycle of SSTAs, i.e. the phase locking of ENSO to the annual cycle (Fig. 6.7). In observations, ENSO has a robust seasonal cycle, with ENSO events typically peaking at the end of the calendar year (Fig. 6.7A). In contrast, ENSO has little seasonality in CM2.1 and events tend to peak in boreal summer (Fig. 6.7B).

Such ENSO biases are common in GCMs and are likely tied to tropical Pacific mean state biases (Ham et al., 2013). Mean state biases in CM2.1 have been previously documented in Wittenberg et al. (2006) and include a cold SST bias along the equator, a warm bias along the coast of South America, and equatorial easterlies that are too broad zonally and extend too far into the western Pacific. Importantly, the LOAM simulations highlighted in this study clearly demonstrate the sensitivity of ENSO to changes in the tropical Pacific mean state, suggesting that even small mean state biases in GCMs can result in large biases in ENSO variability.

In addition to, or perhaps as a consequence of, these biases in the mean state and variability of the tropical Pacific, the coupled ocean-atmosphere system is substantially more non-linear in CM2.1 than in observations (Fig. 6.12-16). The relationship between Niño 3 SSTAs and CP zonal wind (and wind stress) anomalies – indicative of the Bjerknes feedback that is central to the physics of the ENSO mode (Battisti and Hirst, 1989) –is approximately linear in the observations, while a highly nonlinear relationship is found in CM2.1 (Fig. 6.12; Fig. 6.14). This overly nonlinear behavior in CM2.1 appears to be due to the nonlinear relationship between SSTAs and wind speed anomalies, as the relationship between wind speed and wind stress anomalies is similar between observations and CM2.1 (Fig. 6.13).

Further investigations with the linearized intermediate model, LOAM, demonstrate that the distribution of multi-decadal ENSO variance is highly sensitive to the presence of these ENSO biases. In particular, the width of the distribution of 40-yr variance of Niño 3 SSTAs is highly sensitive to the total variance (Fig. 6.11). Comparing the PDF of variance from the LOAM simulation with observed mean states and total variance tuned to observations versus the LOAM simulations with mean states and total variance from CM2.1 demonstrates the influence of total variance on the spread of the distribution. The range in variance of Niño 3 SSTAs across different 40-yr periods in the linear system with total variance equal to that of CM2.1 is nearly twice that expected from a linear system with realistic variance. The influence of nonlinear dynamics serves to further broaden the distribution of variance (as seen by comparing the PDF from the LOAM simulation with CM2.1 mean states to the PDF from CM2.1 itself).

6.4 SUMMARY

Using a linearized intermediate model of the tropical Pacific to investigate mechanisms of large multi-decadal ENSO variability in the preindustrial control run of GFDL CM2.1, we conclude that tropical Pacific mean state changes are not responsible for the periods of extreme ENSO variability in CM2.1. Instead, the intrinsically-generated tropical Pacific mean state changes are a response to (rather than a driver of) the ENSO modulation, arising from the highly nonlinear behavior of the coupled ocean-atmosphere system in CM2.1. However, simulations with the linearized anomaly model, LOAM,

indicate that the low frequency tropical Pacific mean state changes induced by the nonlinear system likely feed back on ENSO variability, serving to *damp* the ENSO modulation. These results point to a two-way feedback mechanism between ENSO and the mean state of the tropical Pacific in CM2.1, whereby random forcing and nonlinear dynamics produce low frequency changes in ENSO variance that are then counteracted by mean state feedbacks.

We conclude that basic physics of the coupled ocean-atmosphere system in CM2.1 are fairly linear for small tropical Pacific climate anomalies (i.e. amplitudes similar to that observed in nature) and infer that the strongly nonlinear behavior observed in CM2.1 is generated through noise forcing and state dependent feedbacks that arise under large perturbations in the coupled system. This strong nonlinear coupling of the atmosphere and ocean in the central Pacific of CM2.1 is causal in producing the extreme ENSO events in the CM2.1 (that are not apparent in nature) and the high variance epochs.

Finally, we demonstrate that the biases present in the coupled ocean-atmosphere system in CM2.1, in particular, the overly strong nonlinear behavior and ENSO variance that is over twice as large as that in observations, produce large biases in the distribution of multi-decadal variability. In particular, we conclude that the range of multi-decadal ENSO variance in the 2,000 year control run of CM2.1 is nearly twice that expected from a linear system with realistic total variance.

These results have important implications for evaluating ENSO variability as it pertains to past, present, and future climate change. Firstly, taken at face value, the large, unforced, multi-decadal ENSO variability in CM2.1 suggests that very large changes in ENSO variability are needed from multi-decadal and shorter records in order to infer a forced change in ENSO variability (e.g. as provided by coral records). However, our results suggest that the true spectrum of unforced variability of ENSO in nature is likely substantially narrower than that simulated by CM2.1. Secondly, the LOAM simulations presented in this study indicate that ENSO is highly sensitive to tropical Pacific mean state changes. Tropical Pacific mean state changes forced by increased greenhouse gas concentrations are projected to be substantially larger than the relatively small, unforced, mean state changes observed between the epochs of extreme ENSO variance in CM2.1, and, based on the dynamics in LOAM, would thus be expected to result in substantial

changes in ENSO variability. The inferred sensitivity of ENSO to tropical Pacific mean state changes implied from the LOAM simulations also indicate that tropical Pacific mean state *biases* prevalent in GCMs likely have large impacts on the response of ENSO to forcing, underscoring the critical need to resolve deficiencies in simulations of tropical Pacific climate by GCMs before robust projections of future ENSO changes can be made.

Table 6.1. Period and growth rate of the ENSO mode and variance of Niño 3 SSTAs in LOAM run with prescribed mean states from each CM2.1 epoch.

Mean State	Period (yr)	Growth Rate (yr^{-1})	Variance ($°C^2$)
Epoch L	3.2	0.43	1.9
Epoch M	3.0	0.46	1.8
Epoch H	3.0	0.39	1.2

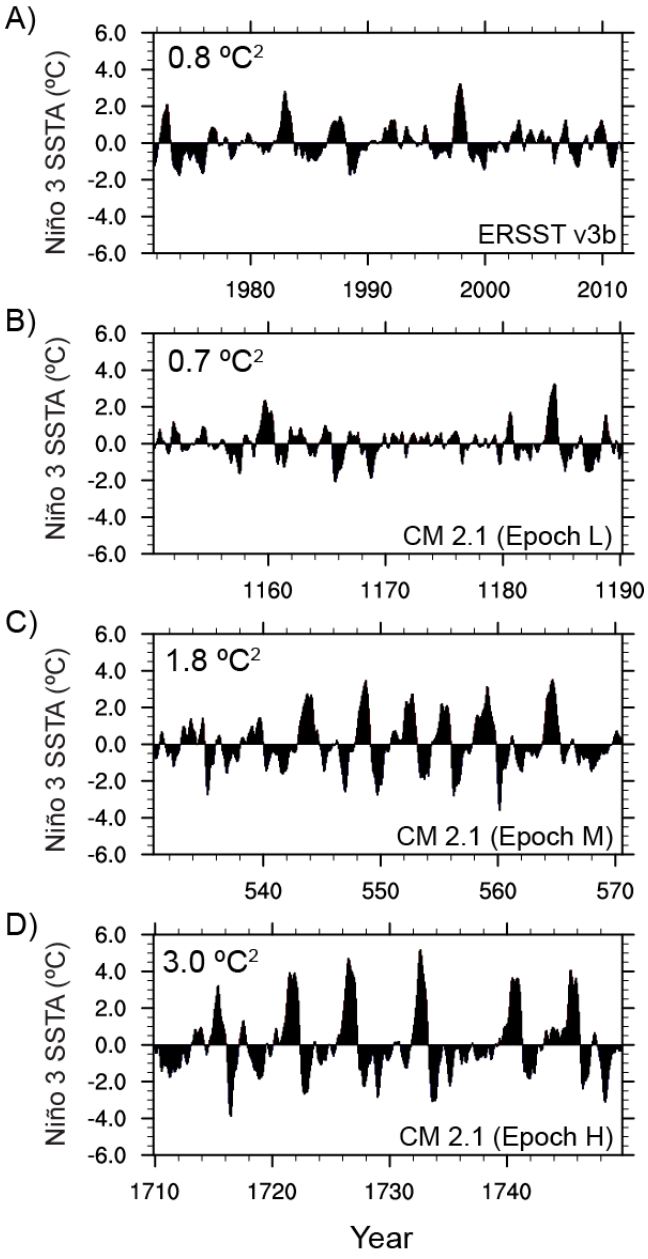

Figure 6.1. Time series of 3-month running mean Niño 3 SSTAs in A) observations (ERSST.v3b, 1971-2010) and CM2.1 epochs B) L, C) M, and D) H.

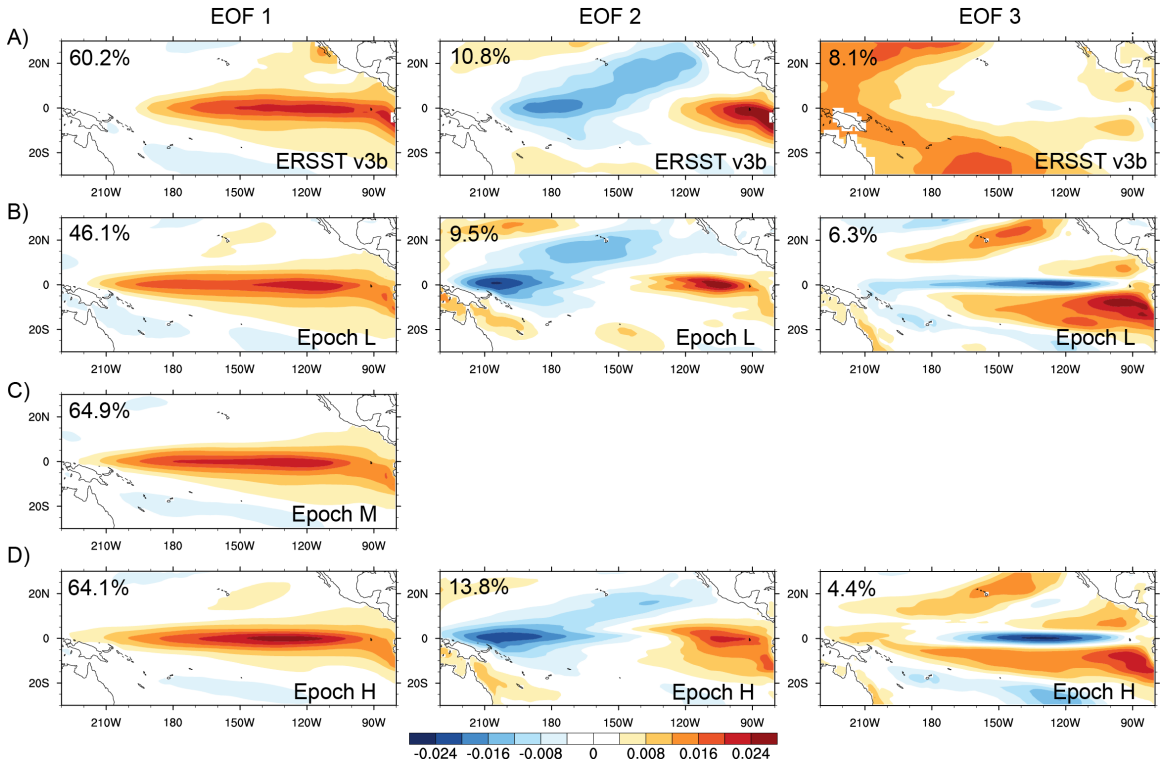

Figure 6.2. Normalized EOF 1-3 of tropical Pacific SSTAs from A) observations (ERSST.v3b, 1971-2010) and CM2.1 epochs B) L, C) M, and D) H. EOF 2 and 3 in Epoch M are omitted as they are not statistically distinguishable, based on the method of North et al. (1982).

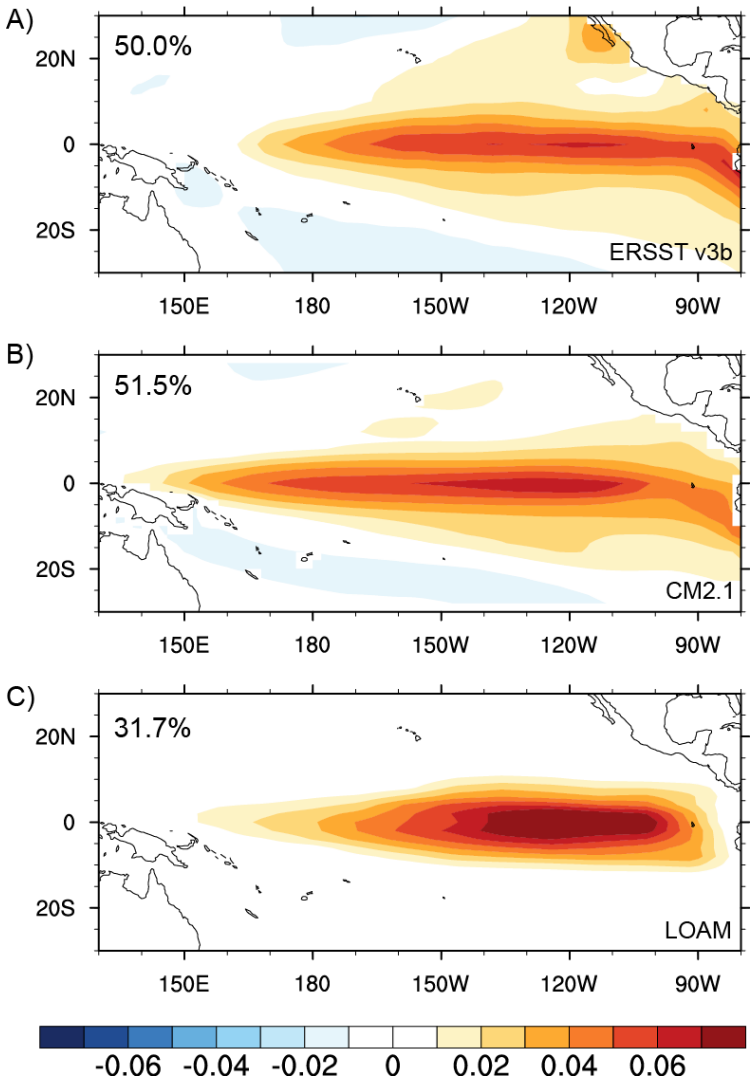

Figure 6.3. Normalized EOF 1 of tropical Pacific SSTAs from A) observations (ERSST.v3b, 1971-2010), B) 200 years of the CM2.1 control-run simulation, and C) 200 years of LOAM run with mean states from CM2.1 (averaged over L, M, H).

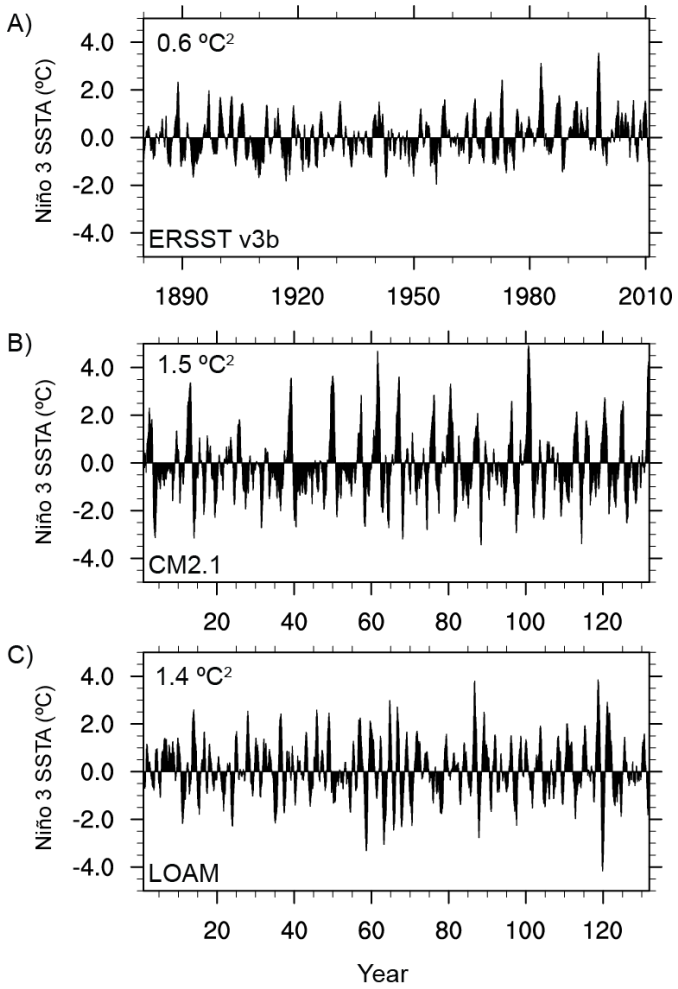

Figure 6.4. 3-month running mean Niño 3 SSTAs in A) observations (ERSST.v3b, 1880 – 2010), B) 130 years of the 2,000-year control run of CM2.1, and C) 130 years of the 2,000-year LOAM run with mean states from CM2.1 (averaged over L, M, H).

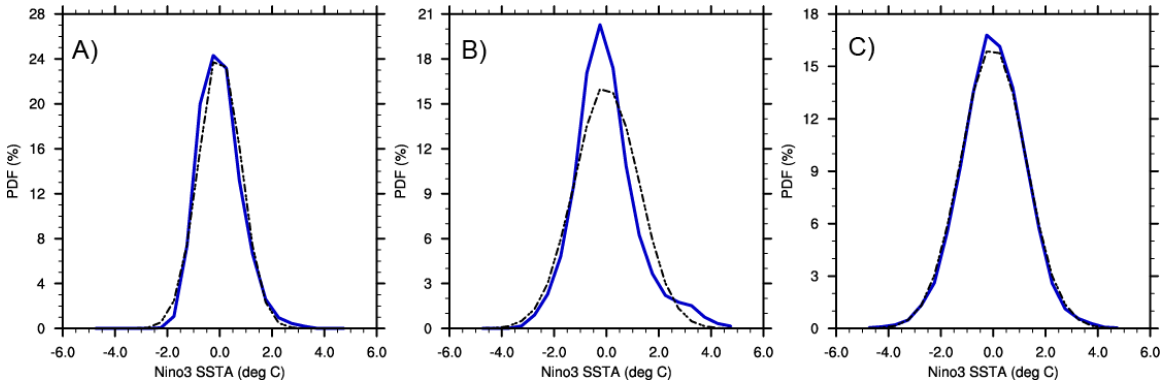

Figure 6.5. Probability distributions of Niño 3 SSTAs in A) detrended observations (NOAA ERSST v3b, 1880 – 2011 AD), B) the 2,000-year CM2.1 control run, C) the 2,000-year LOAM run with mean states from CM2.1 (averaged over L, M, H). Gaussian distributions with the mean and standard deviation estimated from the data are plotted as dashed lines.

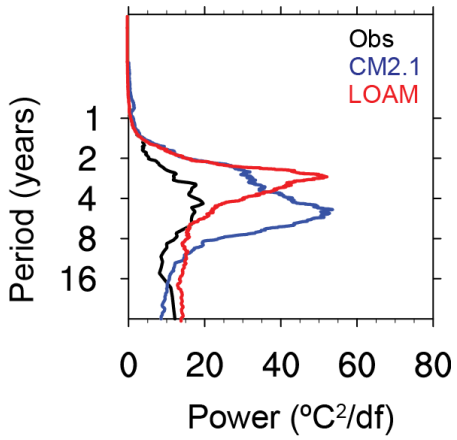

Figure 6.6. Power spectra of 3-month running mean Niño 3 SSTAs in observations (black; ERSST.v3b, 1880 – 2011), the 2,000 year control run of CM2.1 (blue) and the 2,000-year LOAM run with mean states from CM2.1 (red). Spectra have been normalized so that the area under the curve equals the variance of the detrended series; df (=1/N) is the frequency spacing.

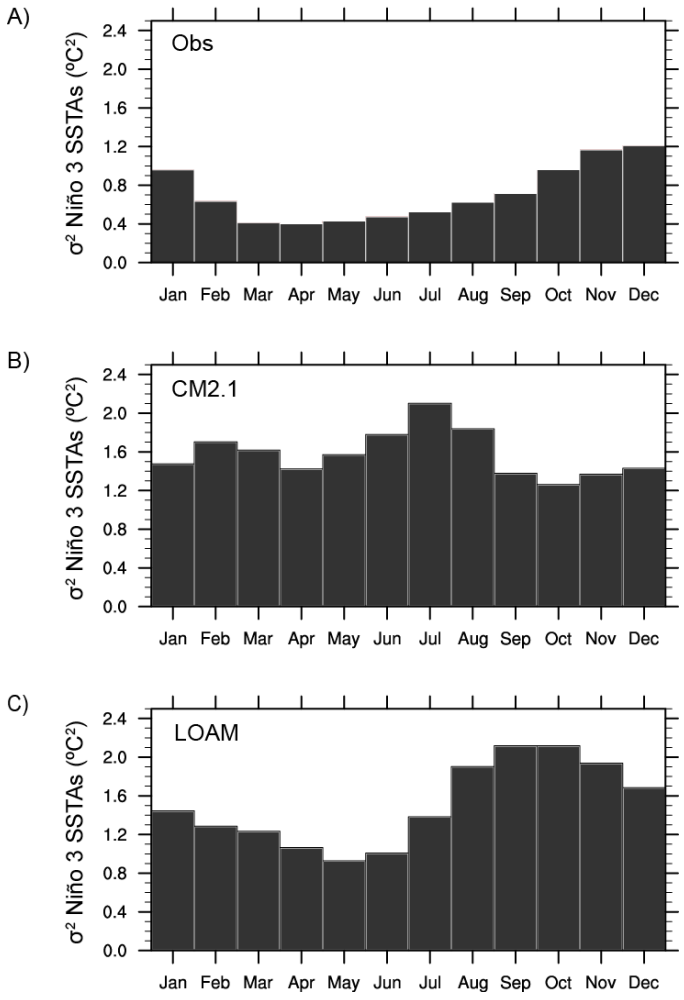

Figure 6.7. Variance of 3-month running mean Niño 3 SSTAs as a function of month in A) observations (ERSST.v3b, 1880-2010), B) the 2,000 year CM2.1 control run, C) the 2,000 year LOAM run with CM2.1 mean states.

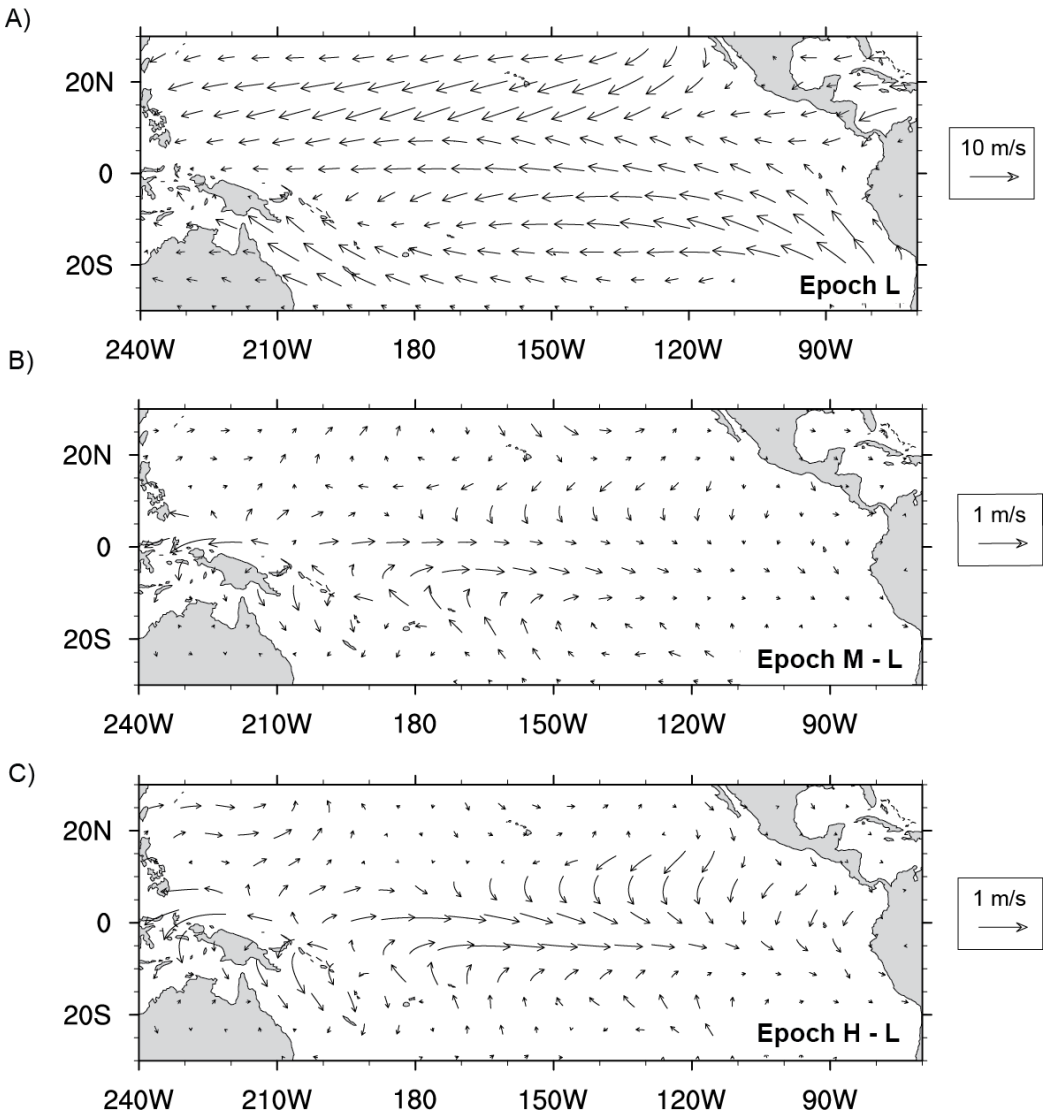

Figure 6.8. A) Annually-averaged tropical Pacific surface winds in CM2.1 Epoch L and differences in mean surface winds between CM2.1 epochs: B) M – L; C) H – L.

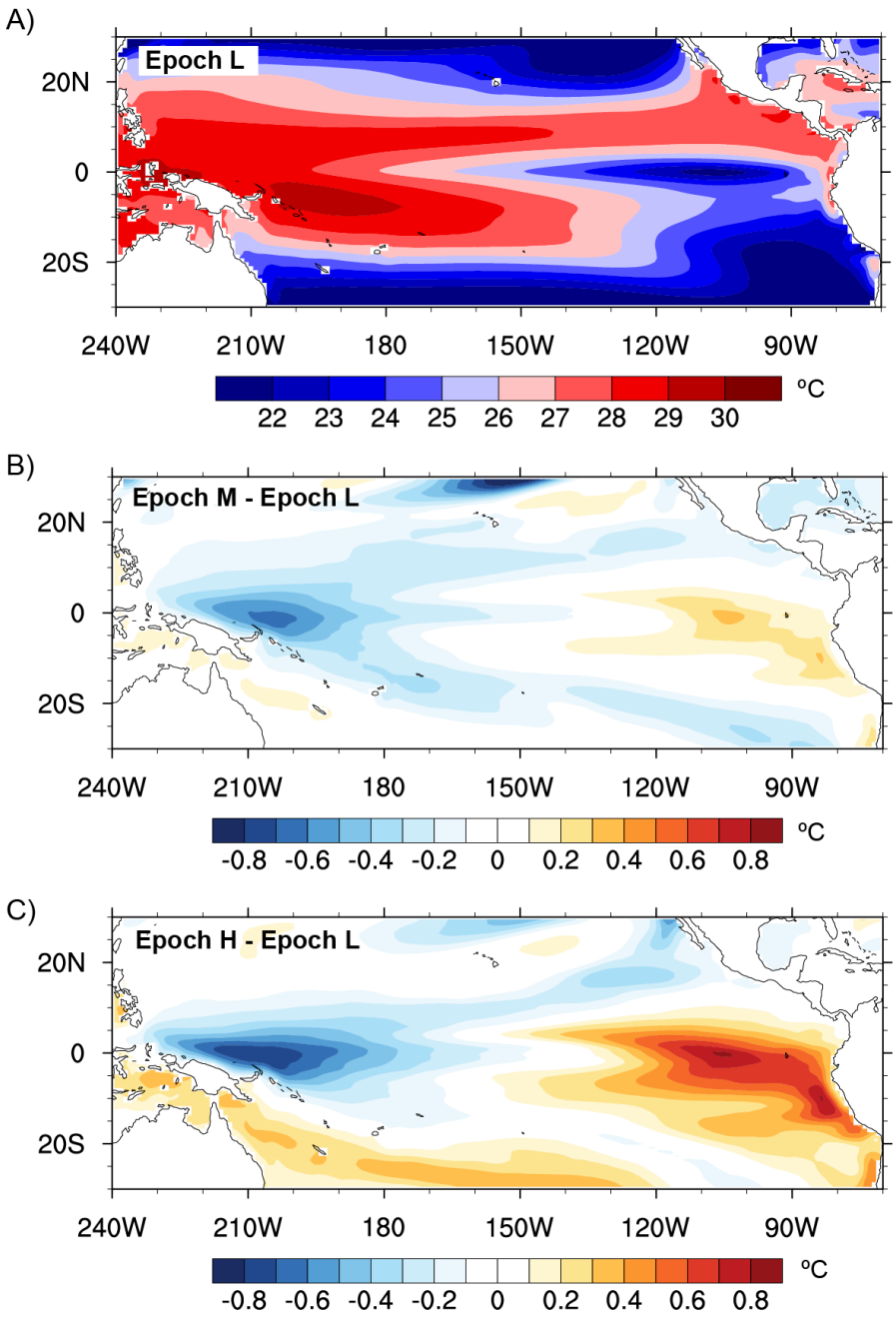

Figure 6.9. A) Annually-averaged tropical Pacific SST in CM2.1 Epoch L (A) and SST difference between epochs B) Epoch M - L (C) Epoch H – L.

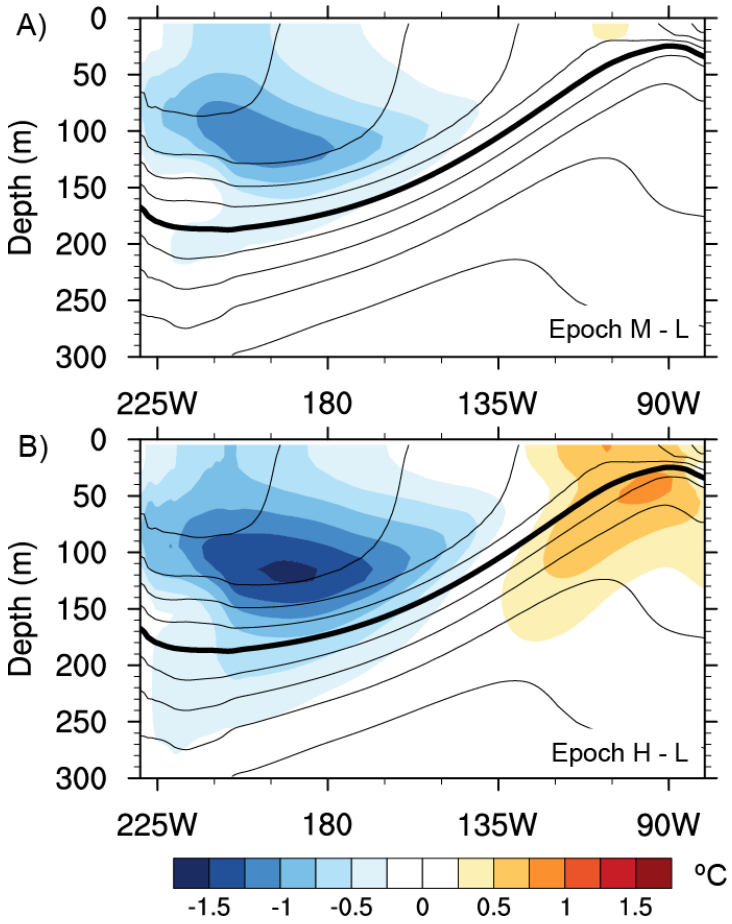

Figure 6.10. Differences in annually-averaged equatorial Pacific upper ocean temperature profiles (colors; averaged between 2S:2N) in CM2.1 epochs: A) M–L and B) H–L. Unfilled contours are the annually-averaged equatorial temperature in Epoch L. The bold contour is the 20°C isotherm.

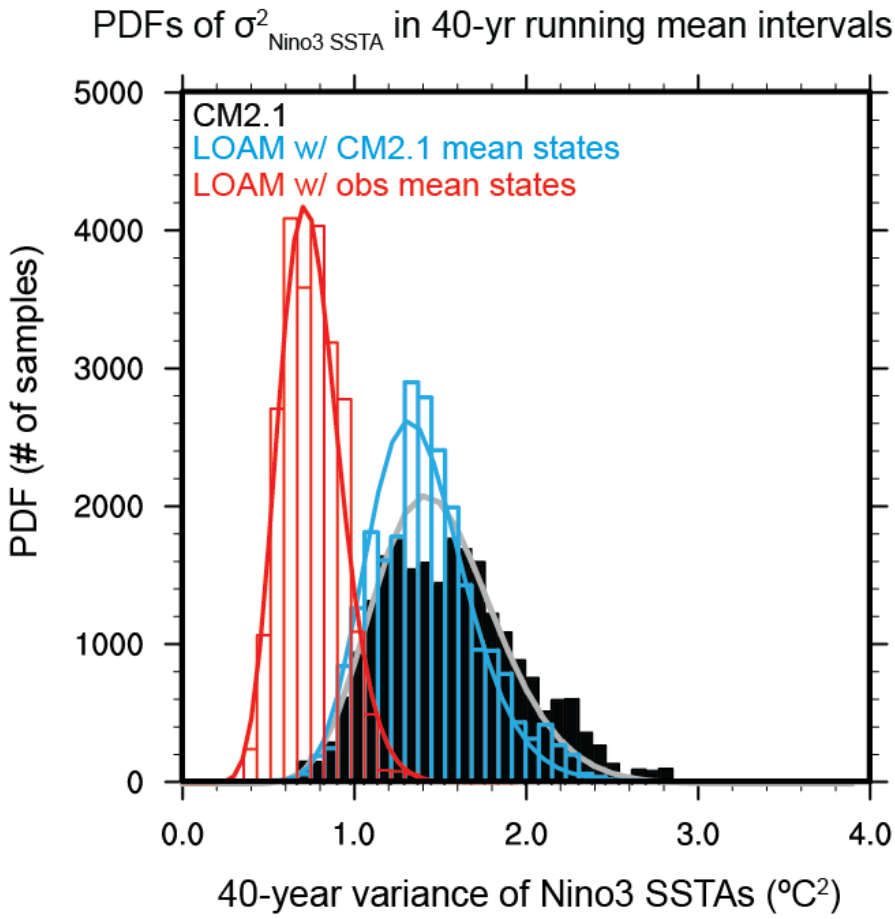

Figure 6.11. Probability distribution functions (PDFs) of 40-year variance of Niño 3 SSTAs (bars) plotted with χ^2 distributions (lines) for the 2,000-year CM2.1 run (black), the 2,000-year LOAM run with CM2.1 mean states (blue) and the 2,000-year LOAM run with observed mean states (red). The χ^2 distributions were calculated based on 40 degrees of freedom and the total variance tuned to match that of the associated PDF.

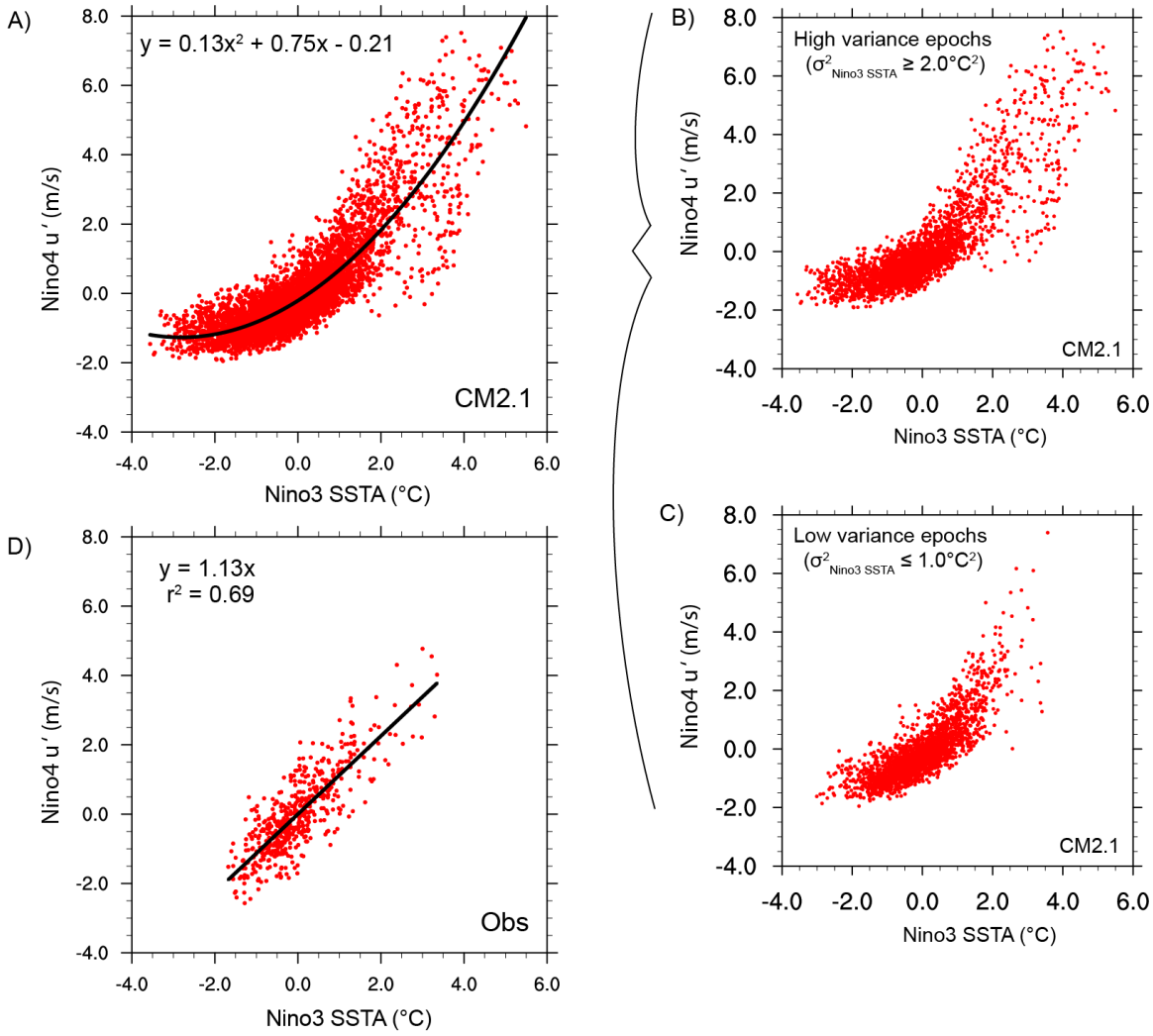

Figure 6.12. Monthly Niño 4 zonal wind anomalies versus Niño 3 SSTAs in A) 500 years of the CM2.1 control simulation; B) a subset of the CM2.1 data from periods in which the 40-year running mean variance of Niño 3 SSTAs ≥ 2.0°C^2; C) a subset of the CM2.1 data from periods in which the 40-year running mean variance of Niño 3 SSTAs ≤ 1.0°C^2; D) observations (1958-2001; ERA40 10 m wind speed and ERSST v3b SST data).

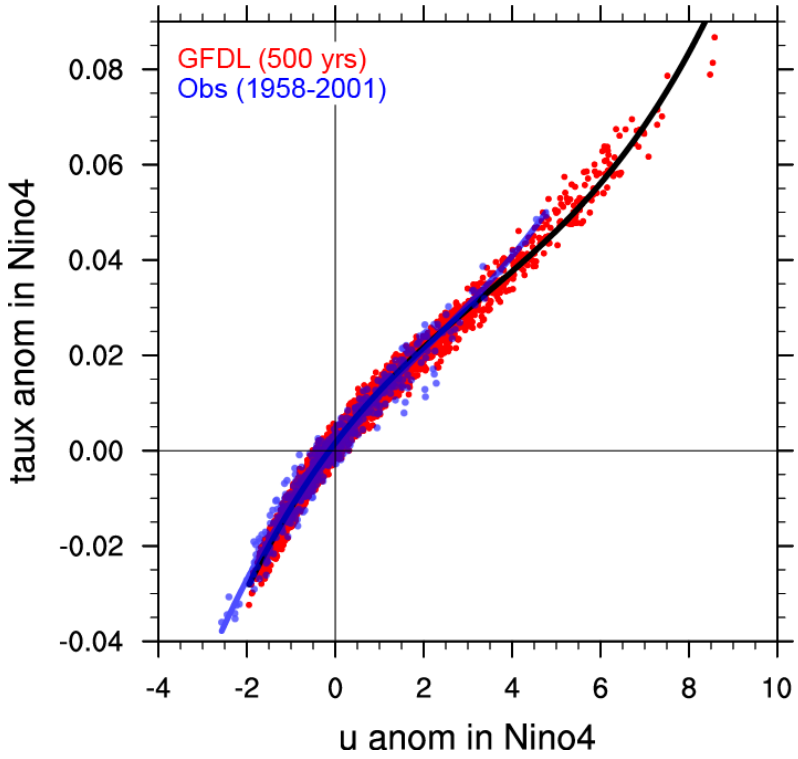

Figure 6.13. Monthly zonal wind stress anomalies versus 10 m zonal wind anomalies in the Niño 4 region in 500 years of the CM2.1 control simulation (red) and observations (blue; 1958-2001; ERA40 10 m wind speed and SODA wind stress data).

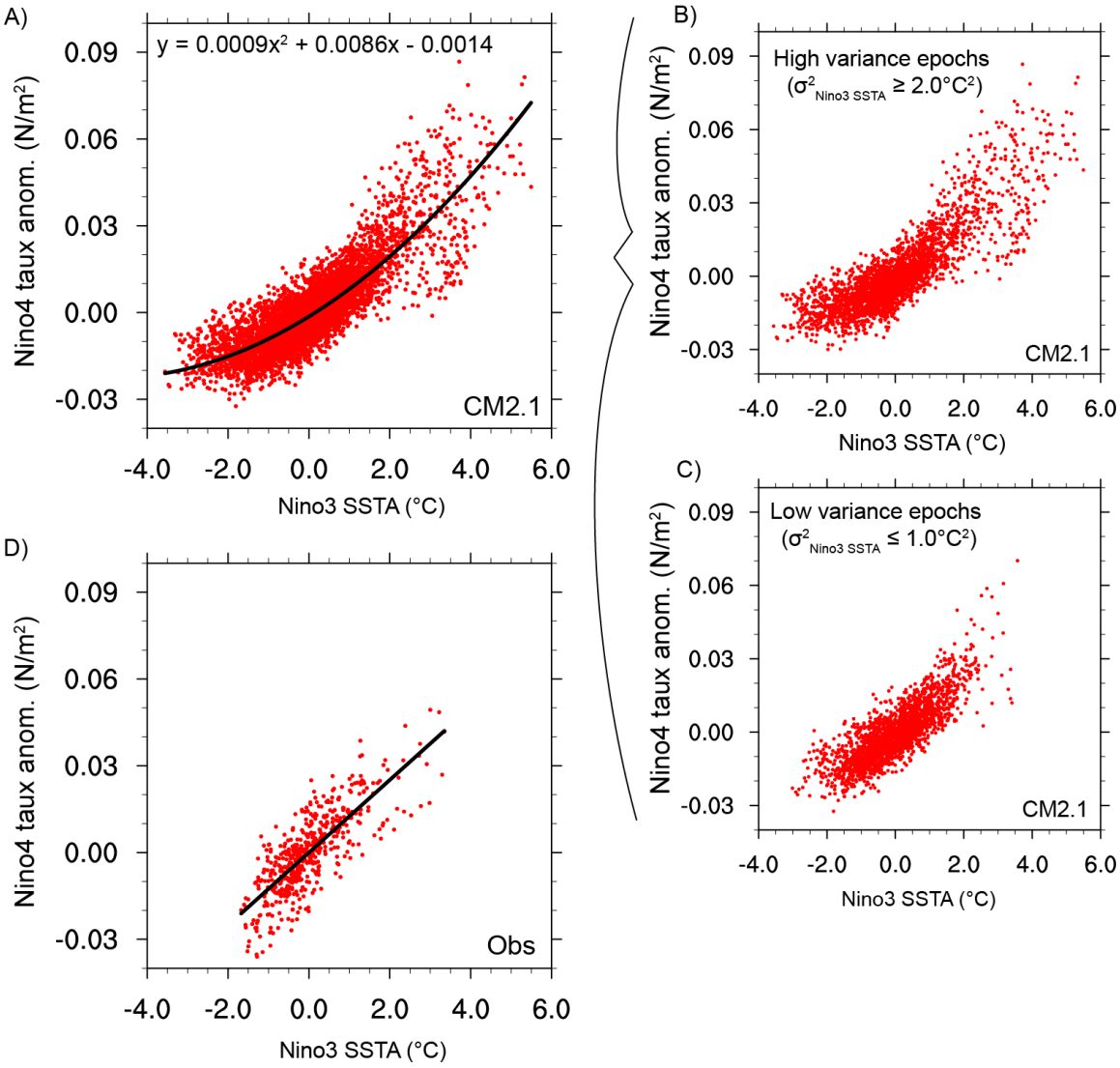

Figure 6.14. Monthly Niño 4 zonal wind stress anomalies versus Niño 3 SSTAs in A) 500 years of the CM2.1 control simulation; B) a subset of the CM2.1 data from periods in which the 40-year running mean variance of Niño 3 SSTAs ≥ 2.0°C^2; C) a subset of the CM2.1 data from periods in which the 40-year running mean variance of Niño 3 SSTAs ≤ 1.0°C^2; D) observations (1958-2001; ERA40 10 m wind speed and ERSST v3b SST data).

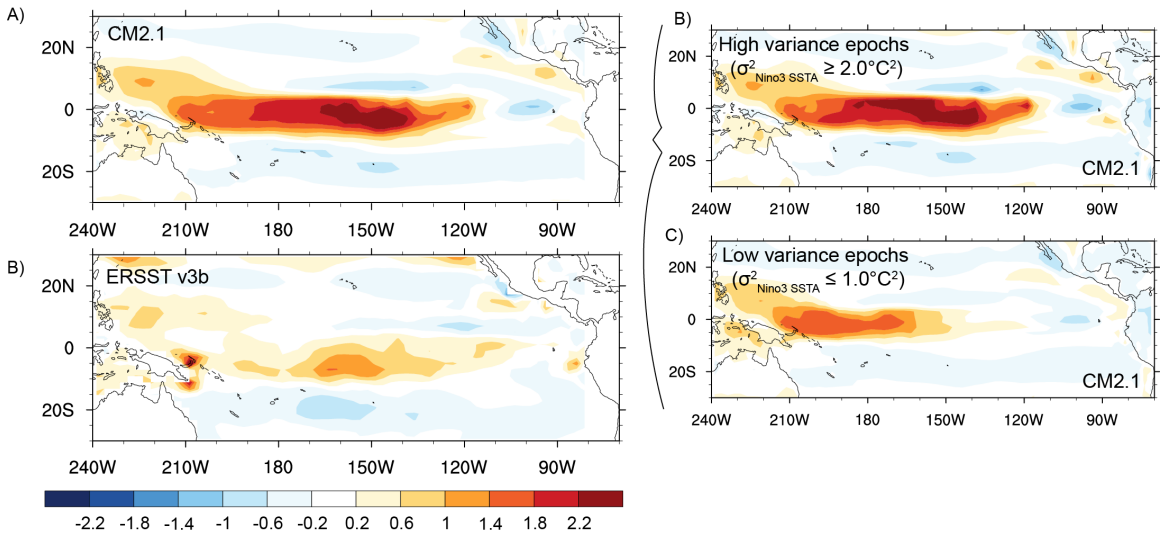

Figure 6.15. Skewness of tropical Pacific zonal wind stress anomalies in A) 500 years of the CM2.1 control simulation; B) a subset of the CM2.1 data from periods in which the 40-year running mean variance of Niño 3 SSTAs ≥ 2.0°C^2; C) a subset of the CM2.1 data from periods in which the 40-year running mean variance of Niño 3 SSTAs ≤ 1.0°C^2; D) observations (SODA, 1958-2007).

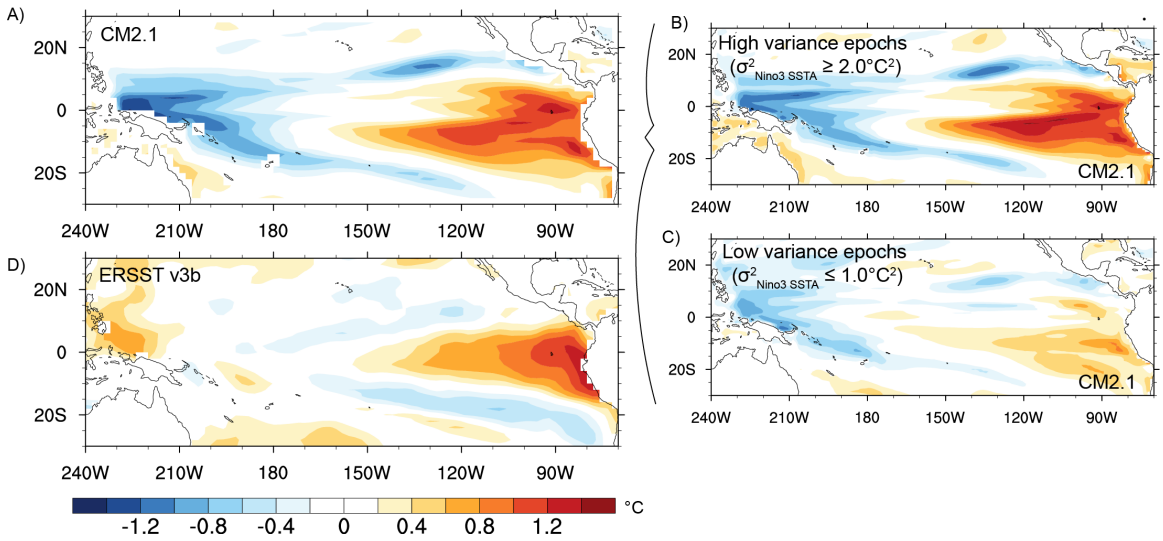

Figure 6.16. Skewness of 3-month running mean tropical Pacific SSTAs in A) 500 years of the CM2.1 control simulation; B) a subset of the CM2.1 data from periods in which the 40-year running mean variance of Niño 3 SSTAs ≥ 2.0°C^2;

C) a subset of the CM2.1 data from periods in which the 40-year running mean variance of Niño 3 SSTAs ≤ 1.0°C^2; D) observations (ERSST.v3b, 1951-2010).

Chapter 7. QUANTIFYING CLIMATE FORCINGS AND FEEDBACKS OVER THE LAST MILLENNIUM IN THE CMIP5/PMIP3 MODELS

(Submitted)

7.1 INTRODUCTION

The temporal evolution and spatial structure of temperature variability over the past millennium serve as important constraints for separating anthropogenic impacts from natural climate variability. Reconstructions point to two major climate epochs during the preindustrial era: the Medieval Warm Period (MWP; ca. 900-1200 AD) and the Little Ice Age (LIA; ca. 1300-1850 AD; e.g. Crowley, 2000; Jones et al., 1998; Lamb, 1965; Mann et al., 2009). Paleoclimate proxy records demonstrate substantial heterogeneity in the timing, amplitude, and spatial extent of the MWP and LIA; these periods are characterized by regionally specific temperature departures from an overall global cooling trend over the last millennium (PAGES 2k Consortium, 2013). Temperature reconstructions across the globe generally indicate a cooling trend beginning ca. 1200-1500 AD and (though interspersed with periods of warmth) continuing to the 19th century, with cooling in North America and the Southern Hemisphere lagging that in the Arctic, Europe and Asia (Fig. 7.1; Cunningham et al., 2013; Kobashi et al., 2011; Larsen et al., 2011; Masse et al., 2008; Ogilvie and Jonsson, 2001; PAGES 2k Consortium, 2013).

Solar, volcanic and orbital forcings combined with atmosphere, ocean and sea-ice feedbacks are thought to have been responsible for the cold conditions during the LIA, while greenhouse gas forcing and internal variability are also thought to have played important roles in global temperature variations over the last millennium (e.g. Bianchi and McCave, 1999; Bond et al., 2001; Briffa et al., 1998; Crowley, 2000; Kaufman et al., 2009; Lean and Rind, 1999; Lehner et al., 2013; Mann et al., 1998; Marcott et al., 2013; Miller et al., 2012; PAGES 2k Consortium, 2013; Palastanga et al., 2011; Schleussner and Feulner, 2013; Schurer et al., 2013; Wanamaker et al., 2012; Zhong et al., 2011). While evidence of LIA cooling has been documented across the globe, substantial spatial and temporal heterogeneity exists in the cooling signal that is likely a

result of a complex array of forcing, feedbacks and internal variability in the climate system (Fernandez-Donado et al., 2013; Kaufman et al., 2009; Lehner et al., 2013). Importantly, the relative contributions of the various forcing and feedback terms to the global and regional cooling signals are still poorly understood. For instance, while some studies have emphasized the role of solar variability on the cooling during the LIA (Bard et al., 2000; Bond et al., 2001; Lean and Rind, 1999; Weber, 2005; Yoshimori et al., 2005), others have suggested that volcanic aerosols and greenhouse gases had a dominant role (Ammann et al., 2007; Briffa et al., 1998; Hegerl et al., 2003; Schurer et al., 2014). Still others have highlighted the importance of orbital variations (Kaufman et al., 2009) and ocean and sea-ice feedbacks (Bianchi and McCave, 1999; Lehner et al., 2013; Miller et al., 2012; Schleussner and Feulner, 2013; Wanamaker et al., 2012).

Here we seek to address this issue by quantifying the relative importance of the various climate forcings and feedbacks to global cooling during the LIA in the last millennium simulations performed as a part of the Coupled Model Intercomparison Project Phase 5 (CMIP5)/Paleoclimate Model Intercomparison Project Phase 3 (PMIP3). These transient climate model simulations are driven by last millennium boundary conditions and enable detailed evaluation of the global energy budget to be evaluated over the last millennium (Braconnot et al., 2012; Schmidt et al., 2012; Taylor et al., 2012). However, decomposing the energy fluxes into contributions from individual forcings and climate feedbacks is nontrivial. One approach to quantifying the response of the climate system to individual forcings involves applying a multiple regression method to proxy-based temperature reconstructions in order to estimate the climatic ”fingerprints” of the forcings (Hegerl et al., 2003). Such climatic fingerprints have also be evaluated from General Circulation Model (GCM) simulations driven with different forcing datasets and the results compared to the fingerprints from proxy-based reconstructions (Schurer et al., 2013). As a part of this analysis, Schurer et al. carried out individually forced model simulations in order to quantify the role of individual forcings on temperature variability over the last millennium. However, such individually forced experiments are computationally expensive with a fully coupled GCM and to date, only a limited number of such simulations have been performed. In this study, we adopt an alternative approach to quantifying the mechanisms of LIA cooling that can be applied to a large number of all-forcing GCM simulations. In this study, we quantify the role of the various forcing and feedback mechanisms to global cooling over the last millennium by decomposing the global energy budget of the last millennium simulations in the

CMIP5/PMIP3 archive through the use of the Approximate Partial Radiative Perturbation (APRP) method and radiative kernels.

7.2 METHODS

7.2.1 *Model Simulations and Forcings*

In this analysis, we use output from transient climate simulations of the last millennium and from unforced 850-1000 year long control simulations with preindustrial boundary conditions from seven different Atmosphere-Ocean General Circulation Models (AOGCMs) in the CMIP5/PMIP3 archive (Braconnot et al., 2012; Taylor et al., 2012). These models are: CCSM4 (Gent et al., 2011; Landrum et al., 2013); GISS-E2-R forcing ensemble members r1i1p121 and r1i1p124 (GISS 121 and GISS 124 hereafter; Schmidt et al., 2006), MPI-ESM-P (MPI hereafter), IPSL-CM5A-LR (IPSL hereafter; Dufresne et al., 2013), CSIRO-Mk3L-1-2 (CSIRO hereafter; Phipps et al., 2012; Rotstayn et al., 2012), and HadCM3 (Collins et al., 2001; Pope et al., 2000; Schurer et al., 2013). These model simulations were chosen based on the availability of data at the time of analysis. MIROC-ESM and FGOALS-s2 simulations were omitted due to long-term drifts in global mean surface air temperature in their preindustrial control simulations. Details of the models, external forcing and references can be found in Table 1, in Masson-Delmotte (2013), and in Flato (2013). Different forcing data sets were imposed in the last millennium simulations of different GCMs, following the protocols of PMIP3 (https://pmip3.lsce.ipsl.fr/wiki/doku.php/pmip3:design:lm:final) as discussed by Schmidt et al. (2012) and outlined in Table 1. The forcings are comprised of (from top to bottom in Fig. 7.2): volcanic aerosols, greenhouse gas (CH_4, CO_2, and N_2O) concentrations, solar radiation associated with changes in orbital configuration and solar output, and (not shown) anthropogenic land-use changes.

a. Volcanic forcing

Reconstructions of volcanic aerosols used in the last millennium simulations (Fig. 7.2A) are derived from either the Gao et al. (2008) (hereafter GRA) data set of sulfate loading, or the Ammann et al. (2007) (hereafter AJS), or Crowley et al. (2008) (hereafter CEA) data sets of aerosol optical depth (AOD), as indicated in Table 1 (Schmidt et al., 2011). The CEA data set is

based on 13 Greenland and Antarctic ice cores and AOD and effective radius are given in 10-day intervals in four equal area latitude bands. The GRA data set is based on 54 ice cores, 32 from Arctic and 22 from Antarctica. Sulfate loading is provided in the GRA data set as a function of month, latitude in 10 bands, and height from 9 to 30 km at 0.5 km resolution. Four models (GISS 121, GISS 124, MPI, HadCM3) prescribed volcanic aerosols in terms of AOD and aerosol effective radius from CEA. CCSM4 prescribed sulfate loading (in Tg) from GRA (Landrum et al., 2013). CSIRO estimated the globally averaged forcing from the CEA data set of AOD and applied the forcing as a total solar irradiance anomaly (Masson-Delmotte, 2013). In IPSL, AOD was prescribed from the AJS data set, but, due to details of the implementation, the aerosol extinction coefficients experienced a slow daily decrease subsequent to being updated at the start of each day (J.-L. Dufresne and M. Khodri, personal communication).

b. Trace gas forcing

Changes in concentration of the principle well mixed GHGs (CO_2, CH_4 and N_2O) over the last millennium (Fig. 7.2D) are related to both natural variations as well as anthropogenic factors in the latter part of the last millennium (Gerber et al., 2003). Reconstructions are derived from high-resolution ice cores in Antarctica and smoothed to retain only decadal-scale and longer variations (Joos and Spahni, 2008). All models use the same set of GHG concentrations, as described in (Schmidt et al., 2011). In addition, one model (MPI) parameterizes ozone variations as a function of changes in solar irradiance based on the results of Shindell et al. (2006).

c. Orbital forcing

Changes in the top of the atmosphere (TOA) insolation during the last millennium were primarily due to changes in precession. From 850 AD to the present, a ca. 20-day shift in perihelion (from Dec. 15^{th} to Jan. 4^{th}) occurred, leading to an increase in insolation in early NH summer relative to the late NH summer (Schmidt et al., 2011). Small decreases in eccentricity and obliquity also contributed to the insolation changes. These changes gave rise to a ca. 3 W/m^2 decrease in insolation in boreal summer (JJA) through the last millennium (Fig. 7.2E).

d. Solar forcing

Changes in total solar irradiance (TSI) are prescribed using either the Vieira et al. (2011) (VSK) or Steinhilber et al. (2009) (SBF) reconstruction as described in Schmidt et al. (2011). In some models, "background" variations of TSI (variations not tied to the solar cycle) are taken from Wang et al. (2005b) (WLS) as indicated in Table 7.1. TSI anomalies from these three products are shown in Fig. 7.2F.

e. Land use forcing

Reconstructions of land use and land cover are available for the last three centuries based on published maps of agricultural areas and for earlier periods based on scaling agricultural activity with population on a per country basis. The resultant data set provides annual maps of cropland, C3 pasture and C4 pasture, which influence the surface albedo, water cycle, surface roughness and soil characteristics (PEA; Pongratz et al., 2008; Schmidt et al., 2011). Although implementation of a given land cover forcing varies across models, all model simulations analyzed in this study either used land cover forcings from PEA, or maintained constant land cover (taken from the preindustrial control runs; Table 7.1).

7.2.2 *Description of the APRP Method*

The Approximate Partial Radiative Perturbation (APRP) method enables changes in top-of-the-atmosphere (TOA) shortwave (SW) energy fluxes to be decomposed into individual radiative forcing and climate feedback terms (Taylor et al., 2007). The APRP method has been used to perform climate feedback analyses in a variety of Last Glacial Maximum, historical, and future climate simulations (e.g. Crucifix, 2006; Hwang et al., 2013; Masson-Delmotte, 2013; Yoshimori et al., 2011). APRP is based on a simple, single layer, shortwave radiative model of the atmosphere, in which the influence of changes in surface albedo, shortwave absorption and scattering on the top of the atmosphere energy budget are diagnosed at every grid cell from all-sky and clear-sky GCM output. APRP analysis relies on the use of a single layer radiative transfer model that is tuned to mimic the radiation code of the GCM. Specifically, three parameters in the single layer model are calculated (the surface albedo, atmospheric scattering coefficient and atmospheric absorption coefficient) to ensure that the surface and top of the atmosphere shortwave fluxes are consistent with those in the GCM. These single layer model

parameters are calculated for two time periods, representing the control and perturbed conditions. These parameters are then individually perturbed in the single layer model by the amount they change between the control and perturbed periods of the GCM simulation and the influence of these changes on the TOA shortwave flux in the single layer model is calculated. In this way, the single layer model enables the effects of changes in surface albedo, atmospheric absorption, atmospheric scattering and clouds to be isolated from one another using a simple and efficient method. Importantly, these calculations allow for an estimate of volcanic forcing to be obtained from the change in shortwave non-cloud scattering (see Section 2.4, below).

This method is similar to the Partial Radiative Perturbation (PRP) method, which is the more accurate method of calculating feedbacks (as it is based on applying a given perturbation of a climate feedback variable to an offline radiation code of the model and determining its feedback strength from the subsequent change in TOA flux). However, whereas the PRP method requires running the GCMs radiation code offline with the various radiation properties individually perturbed, APRP calculations are far less computationally expensive and require far less data from the full GCM simulations (only monthly clear-sky and full-sky radiative flux fields at the surface and TOA are needed). In addition, comparison between full PRP and APRP analyses of global warming and Last Glacial Maximum simulations with two GCMs demonstrated that the differences between them were typically only a few percent (Taylor et al., 2007). Further details of the APRP method can be found in Taylor et al. (2007).

7.2.3 *Description of the Radiative Kernel Method*

Due to the sensitivity of the radiation balance to the vertical distribution of atmospheric water vapor, temperature, and clouds, the simple, single-layer atmosphere model used in the SW APRP calculations is generally not appropriate for LW feedback analysis (Yoshimori et al., 2011). We must thus adopt a different method for decomposing TOA LW fluxes from the last millennium simulations. Under the radiative kernel technique of Soden et al. (2008), climate feedbacks are quantified based on the TOA radiative response to a small change in the climate feedback variable. Climate feedbacks are represented as the product of two terms: the first is the radiative kernel, which is a weighting term that describes the TOA flux perturbation due a standard change in a particular climate feedback variable (e.g. specific humidity), the second is the change in that climate feedback variable in the full GCM simulation. The kernels used in this analysis are from

Shell et al. (2008) based on the CAM3 offline radiative transfer model with a CAM3 present day climate base state. Available kernels include a surface albedo kernel, LW water vapor kernel, LW surface skin temperature kernel, and LW atmospheric temperature kernel, and LW CO2 kernel. For each feedback there is a clear-sky kernel (for which cloud-free conditions were used in the radiative transfer calculations) and an all-sky kernel (which includes the effects of clouds in the radiative transfer calculations). Due to strong non-linearities, cloud feedbacks cannot be evaluated directly from a radiative kernel but instead are calculated by adjusting the cloud radiative forcing to account for cloud masking effects (using the difference between the all-sky and clear-sky kernels) as outlined in Soden et al. (2008). Studies have shown that radiative kernels are dependent on the forcing and background climate state, but are highly similar when calculated from different models under a given base state (Soden et al., 2008; Vial et al., 2013; Yoshimori et al., 2011). Comparison between full PRP, APRP, and radiative kernel methods in Last Glacial Maximum and 2xCO2 simulations with an atmospheric GCM coupled to a slab ocean model suggest that differences between PRP and radiative kernel feedbacks tend to be slightly larger than those between PRP and APRP feedbacks (Yoshimori et al., 2011).

7.2.4 *Calculation of Forcings and Feedbacks Using APRP and Radiative Kernel Methods*

As described in Section 2.3, quantification of the forcing and feedbacks in the CMIP5/PMIP3 last millennium simulations was estimated using the above APRP method to decompose changes in the global shortwave (SW) TOA energy budget and using the radiative kernel method to decompose changes in the global LW TOA energy budget (Shell et al., 2008; Soden and Held, 2006; Soden et al., 2008). The response of the TOA global energy budget to a radiative forcing can be described as follows:

$$\Delta \mathrm{R}_{imbal} = \Delta \mathrm{F} + \Delta \mathrm{R}_{resp} \qquad (7.1)$$

where ΔF represents the radiative forcing, ΔR_resp represents the TOA energy fluxes due to climate feedbacks (i.e. the climate response), and ΔR_imbal represents the remaining imbalance in the Earths TOA energy budget. All TOA energy fluxes are defined as positive downward and surface fluxes are defined as positive upward. The change in the net TOA energy budget can be decomposed into the change in absorbed shortwave ($\Delta \mathrm{R}_{SW}$) and the change in outgoing LW ($-\Delta R_{LW}$):

$$\Delta R_{imbal} = \Delta R_{SW} + \Delta R_{LW} \tag{7.2}$$

a) The shortwave energy budget

The SW energy budget at the TOA can be described as:

$$R_{SW} = \mathrm{S}_0(1 - A) \tag{7.3}$$

where S_0 is the solar constant (in W/m^2) and A is the planetary albedo. Following a perturbation, the new SW budget is:

$$(R_{SW} + \Delta R_{SW}) = (\mathrm{S}_0 + \Delta\mathrm{S})(1 - (A + \Delta A) \tag{7.4}$$

Hence, the change in TOA SW ($\Delta \mathrm{R}_{SW}$) is then:

$$\Delta R_{SW} = \Delta\mathrm{S}(1 - A) - \mathrm{S}_0\Delta A - \Delta\mathrm{S}\Delta A \tag{7.5}$$

where $\Delta F_{solar} = \Delta\mathrm{S}(1 - A)$ is the change in solar forcing (due to either a change in orbital configuration or in solar output), $\Delta R_A = \mathrm{S}_0\Delta A$ is the change in TOA SW due to a change in planetary albedo, and ΔSΔA is the residual. Solar forcing was further decomposed into changes in solar output and changes orbital configuration using equations from Berger (1978). The change in planetary albedo is:

$$\Delta\mathrm{A} = \Delta\mathrm{A}_{\alpha} + \Delta\mathrm{A}_{cloud} + \Delta\mathrm{A}_{clear,scatter} + \Delta\mathrm{A}_{clear,abs} + \Delta\mathrm{A}_{resid} \tag{7.6}$$

The terms on the RHS are changes in the planetary albedo due to the SW climate forcings and feedbacks; they are estimated by the Approximate Partial Radiation Perturbation (APRP) method of Taylor et al. (2007), and $\Delta\mathrm{A}_{resid}$ is the residual. We interpret the change in clear sky scattering to be forcing by volcanic aerosols:

$$\Delta\mathrm{F}_{volc} = \Delta\mathrm{S}_0\Delta A_{clear,scatter} \tag{7.7}$$

and the remaining shortwave feedback ΔR_{SW} terms to be:

$$\Delta R_{SW} = \begin{cases} -\mathrm{S}_0\Delta\mathrm{A}_{\alpha} & surface\ albedo\ feedback\ \Delta\mathrm{R}_{\alpha} \\ -\mathrm{S}_0\Delta\mathrm{A}_{cloud} & SW\ cloud\ feedback\ \Delta\mathrm{R}_{cloud} \\ -\mathrm{S}_0\Delta\mathrm{A}_{clear,abs} & SW\ absorption\ by\ water\ vapor\ \Delta\mathrm{R}_{q} \end{cases} \tag{7.8}$$

Atmospheric clear sky absorption is primarily driven by changes in the absorption of incoming SW radiation by atmospheric water vapor, so this term is therefore interpreted as the SW water

vapor feedback (implicit in this assumption is that the change in SW absorption due to volcanic aerosols is small relative to that due to water vapor changes).

Plugging in Eq. 7.6, 7.7, and 7.8 into Eq. 7.5, we find the changes in shortwave at the top of the atmosphere in terms of forcings and feedbacks:

$$\Delta R_{SW} = \Delta \mathrm{F}_{solar} + \Delta \mathrm{F}_{volc} + \Delta \mathrm{R}_{SW,cloud} + \Delta \mathrm{R}_{SW,q} + \Delta \mathrm{R}_{\alpha} + \varepsilon_{SW} \ , \qquad (7.9)$$

where SW forcings = $\Delta \mathrm{F}_{solar} + \Delta \mathrm{F}_{volc}$, SW feedback = $\Delta \mathrm{R}_{SW,cloud} + \Delta \mathrm{R}_{SW,q} + \Delta \mathrm{R}_{\alpha}$, and

$$\varepsilon_{SW} = -S_0 \Delta A_{resid} - \Delta S \Delta A$$

is the SW residual, which provides a measure of the accuracy of the APRP approximation to the SW TOA fluxes.

b) The longwave energy budget

The change in the TOA longwave radiation is:

$$\Delta R_{LW} = \Delta \mathrm{F}_{GHG} + \Delta \mathrm{R}_{Planck} + \Delta \mathrm{R}_{LW,cloud} + \Delta \mathrm{R}_{LW,q} + \Delta \mathrm{R}_{lapse\,rate} + \varepsilon_{LW} \ , \quad (7.10)$$

where $\Delta \mathrm{F}_{GHG}$ is the forcing due to the change in the concentration of greenhouse gases (calculated using the formulas from Myhre et al. (1998), and $\Delta \mathrm{R}_{Planck} + \Delta \mathrm{R}_{cloud} + \Delta \mathrm{R}_{LW,q} + \Delta \mathrm{R}_{lapse\,rate}$ is the sum of the Planck, cloud, water vapor and lapse rate feedbacks and ε_{LW} is the longwave residual.

c) The total TOA energy budget

Inserting Eq. 7.9 and 7.10 into the total TOA energy budget equation (Eq. 7.1), we find

$$\Delta \mathrm{F} + \Delta \mathrm{R}_{resp} = \Delta \mathrm{R}_{imbal} = \Delta \mathrm{R}_{SW} + \Delta \mathrm{R}_{LW} \qquad (7.11)$$

where ΔF is the sum of the forcings,

$$\Delta F = \Delta \mathrm{F}_{solar} + \Delta \mathrm{F}_{volc} + \Delta \mathrm{F}_{GHG} \ , \qquad (7.12)$$

$\Delta \mathrm{R}_{resp}$ is the sum of the shortwave and longwave feedbacks:

$$\Delta R_{resp} = \Delta \mathrm{R}_{SW,cloud} + \Delta \mathrm{R}_{SW,q} + \Delta \mathrm{R}_{\alpha} + \Delta \mathrm{R}_{Planck} + \Delta \mathrm{R}_{LW,cloud} + \Delta \mathrm{R}_{LW,q} + \Delta \mathrm{R}_{lapse\,rate} + \varepsilon_{SW} + \varepsilon_{LW} \qquad (7.13)$$

and $\Delta \mathrm{R}_{imbal}$ is the energy imbalance if the system is not yet in equilibrium. Note that, given the magnitude and spatial distribution of the surface albedo changes in comparison to land cover

changes (Pongratz et al., 2008; Schmidt et al., 2011) we neglect the contribution of land use changes to global forcing.

Assuming the change in the global average surface air temperature ($\Delta\overline{T_{as}}$) is small, we can expand the climate response in terms of a Taylor series:

$$\Delta R_j = \frac{dR_j}{d\overline{T_{as}}}\,\Delta\overline{T_{as}} + \mathcal{O}((\Delta\overline{T_{as}})^2) \approx \frac{\partial R_j}{\partial x_j}\frac{dx_j}{d\overline{T_{as}}}\Delta\overline{T_{as}} \equiv \lambda_j \times \Delta\overline{T_{as}} \quad , \tag{7.14}$$

where x_j is a state variable. The shortwave changes due to climate feedbacks are obtained by the Approximate Partial Radiation Perturbation (APRP) method of Taylor et al. (2007), while the longwave changes due to due to climate feedbacks are obtained using radiative kernels (Soden and Held, 2006). Note that cloud feedbacks cannot be calculated directly from radiative kernels because of strong nonlinearities that arise from cloud masking. Following Soden et al. (2008), we adjusted the cloud radiative effect by correcting for non-cloud feedbacks (where the clear-sky GHG forcing was calculated as: $\Delta F^{cs}{}_{GHG} = 1.16 * \Delta \mathrm{F}_{GHG}$).

d) Contributions to the change in surface air temperature

Inserting Eq. 7.14 into Eq. 7.11 we find the temperature response in terms of the forcings and feedbacks (as in Feldl and Roe, 2013; Vial et al., 2013):

$$\lambda_{Planck}\Delta\overline{T_{as}} + \sum_{j\neq Planck}\lambda_j \times \Delta\overline{T_{as}} = -\Delta F + \Delta R_{imb} - \varepsilon_{SW} - \varepsilon_{LW} \quad , \tag{7.15}$$

where λ_{Planck} is the climate sensitivity in absence of feedbacks. Equivalently

$$\Delta\overline{T_{as}} = -\frac{\Delta F}{\lambda_{Planck}} - \sum_{j\neq Planck}\frac{\lambda_j}{\lambda_{Planck}} \times \Delta\overline{T_{as}} + \Delta R_{imb}/\lambda_{Planck} - (\varepsilon_{SW} - \varepsilon_{LW})/\lambda_{Planck} \tag{7.16}$$

where λ_j are the climate feedback factors ($[\lambda_j]$ = W m^{-2} K^{-1}).

Finally, we can equate each term in Eq. 7.16 as a contribution to the global average temperature change $\Delta\overline{T_{as}}$:

$$\Delta\overline{T_{as}} = \Delta\overline{T}_{forcing} + \Delta\overline{T}_{feedbacks} + \Delta\overline{T}_{atm+ocn\,uptake} + \Delta\overline{T}_{\varepsilon} \tag{7.17}$$

In addition to the forcing and feedbacks, we report the fraction f of the total global cooling $\Delta\overline{T_{as}}$ due to individual forcings and feedbacks:

$$f = \frac{\Delta\overline{T_x}}{\sum\Delta\overline{T_x}} \times 100 \ . \tag{7.18}$$

Only negative (cooling) $\Delta\overline{T_x}$ are included in calculating f. Feedbacks and global cooling contributions were not calculated for the HadCM3 and CSIRO last millennium simulations

because relative humidity data were not available for HadCM3 and the implementation of volcanic forcing as a TSI perturbation in CSIRO precluded separation of the SW forcings and feedbacks.

7.3 RESULTS

7.3.1 *Temperature Trends Over the Last millennium in the CMIP5/PMIP3 Models*

The globally averaged surface temperature anomaly through the last millennium and preindustrial control simulations is shown in Fig. 7.2C (where annually averaged data were smoothed with a Gaussian filter; $\sigma = 3$ years). Relative to the period from 850-1200 AD, all CMIP5/PMIP3 simulations generally demonstrate colder global temperatures ca. 1250-1850 AD. Compared to the preindustrial control simulations from the same models, the last millennium simulations demonstrate global temperature anomalies outside the range of natural variability during volcanically active periods ca. 1230-1300, 1450, 1600-1750, and 1800-1840 AD. Average Northern Hemisphere (NH) temperature anomalies in the multi-model mean agree well with proxy-derived NH temperature reconstructions with cold periods through the 13th, mid-15th, 17th-18th and early 19th centuries (Fig. 7.3; Frank et al., 2010). That temperature anomalies associated with large volcanic events tend to be substantially larger in the models than in the reconstructions may be related to issues with tree ring-based temperature reconstructions (e.g. anomalous tree growth immediately following large volcanic events; Mann et al., 2012), to uncertainties in the volcanic reconstructions (Sigl et al., 2014) and/or to the models' tendency to overestimate the impact of large volcanic events, e.g. due to the linear scaling that is typically applied between stratospheric sulfate loading and AOD (based on the Pinatubo eruption; Timmreck et al., 2009).

To quantify the contribution of radiative forcings and climate feedbacks to global cooling over the last millennium, we compare the energy budget in the LIA (hereafter defined as 1600-1850 AD) to that in the MWP (950-1200 AD). We extend our analysis to examine the cause of the cold periods ca. 1400-1650 AD and 1200-1450 AD (relative to the same MWP warm period) in Chapter 7.3.4.

While the LIA is characterized by centennial-scale global temperature minima in all CMIP5/PMIP3 models, there are marked differences in the amplitude and spatial pattern of the

surface temperature anomalies (relative to the MWP) across the models (Fig. 7.4). The regional temperature differences are reflected in changes in sea ice concentration (Fig. 7.5); in the Arctic, sea ice concentration increases in all models, whereas Antarctic sea ice concentration increases in some models (CCSM4, CSIRO, HadCM3) and decreases in others (GISS121 and GISS124). Sources of these inter-model differences are discussed in Chapter 7.3.3.

7.3.2 *Attribution of LIA Cooling*

Climate forcing during the last millennium is comprised of contributions from changes in solar output, orbital configuration, stratospheric sulfate aerosols associated with large volcanic eruptions, changes in trace gases and changes in land use through its impact on surface albedo and evapotranspiration (Table 7.1; Bony et al., 2006; Schmidt et al., 2011). Given the magnitude and spatial distribution of the surface albedo changes seen during all three cold periods, land use changes are not important contributors to the forcing of these cold periods. The forcings are shown in Fig. 7.6 and the global cooling contribution from each of these forcings is shown in Fig. 7.7 and Table 7.2.

A TOA energy budget analysis of the CMIP5/PMIP3 last millennium simulations indicates that volcanic forcing was the primary driver of LIA cooling in the models. Volcanic forcing accounted for 77% of the total forcing on average (ranging from 50-84% or −0.07 to −0.32 Wm^{-2}, across models; Fig. 7.6). This forcing directly contributed to 31% (on average) of the global cooling during the LIA (Fig. 7.7; Table 7.2). In comparison, solar and GHG forcing were substantially weaker, comprising an average of 10% and 13% of the total forcing and 4% and 5% of the global cooling, respectively. Globally averaged solar forcing was driven by changes in solar output over the last millennium as changes in orbital parameters imparted insignificant forcing (Fig. 7.6). However it is important to note that the insignificance of the direct orbital forcing term when globally and annual averaged does not necessarily imply that orbital forcing played an insignificant role in global cooling during the LIA. Orbital forcing (which has a rich seasonal and latitudinal structure) likely triggered global climate feedbacks. For instance, precessional forcing imposed a ca. 3 Wm^{-2} decrease in insolation in boreal summer (JJA) at 65ºN through the last millennium (Fig. 7.2E) which may have contributed to non-negligible surface albedo and water vapor feedbacks through colder temperatures and sea ice growth in the Arctic.

A number of positive climate feedbacks reinforce the radiative forcing during the LIA. The global cooling contribution from each of these feedbacks is shown in Fig. 7.7 while the global TOA energy fluxes are shown in Fig. 7.9. (As mentioned above, it is important to note that under the current analysis framework, these feedbacks cannot be ascribed to any particular type of forcing; forcings that had negligible direct contributions to LIA cooling (e.g. orbital forcing) may have been responsible for non-negligible climate feedbacks.) The largest positive feedback is the LW water vapor feedback, which is responsible for 20%, on average, of the global cooling (Table 7.2). The LW water vapor feedback occurs in response to the decreased atmospheric water vapor concentration; the saturation vapor pressure decreases as the atmosphere cools as given by the Clausius-Clapeyron equation. In addition, the SW water vapor feedback represents a lesser but globally important positive feedback in all of the models (contributing 9%, on average, to the global cooling), consistent with decreased absorption of incoming SW radiation by atmospheric water vapor during the LIA.

In global warming simulations, the positive water vapor feedback is due to both the vertically uniform atmospheric warming as well as the vertical redistribution of water vapor (as robust decreases in tropical lapse rate from enhanced warming aloft lead to an upward shift in the water vapor distribution). In the CMIP5 4xCO2 simulations, the large positive water vapor feedback is partially offset by a negative lapse rate feedback. In contrast, the CMIP5/PMIP3 last millennium simulations demonstrate water vapor and lapse rate feedbacks that reinforce one another. The positive lapse rate feedback arises due to greater cooling near the surface than aloft poleward of ca. 30−40º latitude (Fig. 7.10) and contributes 7% on average to the global cooling (Fig. 7.7; Table 7.2). A positive lapse rate feedback has also been observed in Last Glacial Maximum simulations with a slab ocean model under the addition of ice sheet and orbital forcings (Yoshimori et al., 2011), suggesting that the positive (versus negative) lapse rate feedback may be a function of the SW (versus LW) forcings. Combined, the water vapor and lapse rate feedbacks are responsible for 36%, on average, of the global cooling during the LIA. Thus, while the total (SW + LW) water vapor feedback (1.20 ± 0.19 $Wm^{-2}K^{-1}$; Fig. 7.8) is substantially less than that reported from the CMIP5 4xCO2 simulations, the combined water vapor and lapse rate feedback in the LIA (relative to the MCA; 1.47 ± 0.10 $Wm^{-2}K^{-1}$) is larger than that observed in the future climate simulations (1.26 ± 0.07 $Wm^{-2}K^{-1}$) (Masson-Delmotte, 2013). The combined LIA water vapor and lapse rate feedback is closer to that observed in Last

Glacial Maximum simulations compared to the pre-industrial climate (1.39 ± 0.09 $Wm^{-2}K^{-1}$)(Masson-Delmotte, 2013). Yoshimori et al. (2011) argue that the combined water vapor and lapse rate feedbacks are strongly dependent on the background climate state, giving rise to the dependence of climate sensitivity on the background climate state.

Second to the LW water vapor feedback, the next largest global feedback is the surface albedo feedback (0.59 ± $Wm^{-2}K^{-1}$), which is responsible for 14% of the global cooling on average (Fig. 7.7; Table 7.2). The surface albedo feedback arises primarily from increases in high latitude sea ice during the LIA in CCSM4 and MPI. In HadCM3, GISS121 and GISS124 this feedback is equally or predominately due to increased surface albedo over Eurasia and North America (presumably from increased snow cover; data not shown). This surface albedo feedback is generally larger than that found from the CMIP5 4xCO2 simulations (0.33 ± 0.14 $Wm^{-2}K^{-1}$)(Masson-Delmotte, 2013), as well as that from Last Glacial Maximum simulations (0.41 ± 0.18 $Wm^{-2}K^{-1}$)(Crucifix, 2006; Masson-Delmotte, 2013; Yoshimori et al., 2011). Possible sources of the larger surface albedo feedback in the LIA relative to the future climate and Last Glacial Maximum simulations include the disparate forcings and the disparate background climate states. We propose that volcanic forcing played a large role in the strength of the surface albedo feedback during the LIA. Fig. 7.9 shows that the surface albedo feedback has a weak but significant positive correlation ($R^2 = 0.28$, $p < 0.01$) to the strength of the volcanic forcing in the last millennium simulations. The correlation is most pronounced during the 1200-1450 AD period ($R^2 = 0.85$, $p < 0.01$), which is the LIA interval characterized by the largest volcanic events of the last millennium and the largest average volcanic forcing as a fraction of the total forcing.

Not unexpectedly, clouds have a varied response among models, most notably in the SW cloud feedback. The LW cloud feedback (0.27 ± 0.17 $Wm^{-2}K^{-1}$) is positive in all models, and is broadly consistent with that found in the CMIP5 4xCO2 simulations (0.22 ± 0.18 $Wm^{-2}K^{-1}$)(Masson-Delmotte, 2013) and generally higher than that found in the Last Glacial Maximum simulations (0.08 ± 0.10 $Wm^{-2}K^{-1}$)(Masson-Delmotte, 2013). The positive LW cloud feedback is likely due to lower cloud tops in the colder LIA atmosphere. The LW cloud feedback contributes 6%, on average, to the global cooling. The SW cloud feedback (−0.20 ± 0.47 $Wm^{-2}K^{-1}$) is more variable among models, which is a well-documented feature across future and paleo climate simulations (e.g. Masson-Delmotte, 2013; Vial et al., 2013). In all last millennium

simulations aside from IPSL, the SW cloud feedback is a negative feedback during the LIA and generally arises from decreased cloud fraction in the tropics and high latitudes. The positive SW cloud feedback in IPSL is the dominant positive feedback and arises from increased cloud fraction in the midlatitudes, particularly in the SH (data not shown). A strong correlation between SW cloud feedback and low-cloud fidelity has been found in future climate simulations. The SW cloud feedback is strongly positively correlated to the SW cloud radiative effect present in the control simulations, with a larger positive SW cloud feedback present in models with higher control low cloud cover (Lacagnina et al., 2014). This relationship suggests that the large inter-model spread in the SW cloud feedback may be indicative of a large inter-model spread in low cloud amount in the last millennium control simulations.

Combined, these feedbacks are responsible for an average of 60% of the global cooling during the LIA. The water vapor, lapse rate, surface albedo, and cloud feedback parameters sum to 2.18 ± 0.33 $Wm^{-2}K^{-1}$, similar to the combined feedback parameter from the 4xCO2 simulations (2.19 ± 0.35 Wm−2K−1; Masson-Delmotte, 2013). The larger surface albedo and water vapor/lapse rate feedbacks in the LIA, relative to the future climate simulations, are more than offset by the lower average SW cloud feedback. For the Last Glacial Maximum climate, the summed feedback parameter (1.87 ± 0.21 $Wm^{-2}K^{-1}$)(Masson-Delmotte, 2013) is slightly less than that found in the LIA and 4xCO2 simulations. Yoshimori et al. (2011) demonstrate that the lower climate feedback parameter in the Last Glacial Maximum relative to future climate simulations is primarily due to a lower SW cloud feedback. Here we find that lower surface albedo and LW cloud feedbacks are primarily responsible for the lower combined feedback parameter during the Last Glacial Maximum relative to the LIA.

Finally, we note that the SW residual term is negligible (less than 1% of the total SW feedback parameter) while the LW residual term amounts to 0.00 to −0.59 $Wm^{-2}K^{-1}$, or 0-23% of the total LW feedback parameter. While this residual may indicate the presence of nonlinear LW feedbacks, it may also reflect LW absorption by volcanic aerosols, which has been neglected in this analysis. However, the average total residual (19%) is similar to that reported from the CMIP5 4xCO2 simulations (23%; Vial et al., 2013).

7.3.3 *Sources of Inter-Model Differences in LIA Climate Change*

While the LIA is characterized by global cooling relative to the MWP in all models, the amplitude of the cooling differs by more than a factor of 2 among models (Fig. 7.7). Factors that may be responsible for the inter-model spread in global mean temperature change include differing climate forcings, differing climate feedbacks and differing efficiencies with which they transfer heat into the ocean. However, as ocean heat uptake during the LIA is small in all the models (as demonstrated by small changes in surface energy fluxes in Fig. 7.9), the TOA radiative forcings and feedbacks are primarily responsible for the inter-model spread in global cooling during the LIA. Among radiative forcings, differences in volcanic forcing drive the inter-model spread in total forcing (Fig. 7.6). Differences in volcanic forcing across models could be due to differences in the forcing data set used (therefore reflecting uncertainty in the volcanic aerosol reconstructions) as well as due to differences in the treatment of volcanic aerosols in the models. The CEA data set of AOD and effective radius indicates substantially lower AOD anomalies during large volcanic events (Fig. 7.2A) but a larger increase in the number of volcanic events during the LIA relative to the MCA. The use of different forcing data sets is responsible for a substantial portion of the inter-model spread in volcanic forcing during the LIA (e.g. compare the volcanic forcing in CCSM4 to GISS/MPI/HadCM3 in Fig. 7.6). The weaker volcanic forcing in IPSL in comparison to the other models is particularly notable, however, it is unclear to what degree this is due to the forcing data set used (AJS) versus the implementation of the forcing (see Methods). Another substantial contribution to the inter-model spread arises from the differing treatment of volcanic aerosols among models that use the same volcanic reconstruction. For instance, volcanic forcing in CSIRO (which prescribes volcanic forcing based on the CEA data set, imposed as a globally-averaged perturbation to TSI) is up to 50% lower than that in GISS/MPI/HadCM3 (which prescribe latitudenally-varying AOD and effective radius; Fig. 7.6). In contrast to the other models, CCSM4 has an atmospheric chemistry scheme that models the transport, processing and radiative properties of the volcanic aerosols from the aerosol loading provided in GRA).

In addition to differences in radiative forcing among models, differences in the strength of climate feedbacks add to the inter-model spread in LIA cooling. The total effective feedback parameter differs by a factor of 2 across models (ranging from -0.98 to -2.05 $Wm^{-2}K^{-1}$; Fig. 7.8). The Planck response varies little among models, as expected (-3.41 ±0.05 $Wm^{-2}K^{-1}$). The largest

spread in climate feedbacks among models occurs in the SW cloud feedback (-0.20 ±0.47 $Wm^{-2}K^{-1}$) and the lapse rate feedback (0.27 ±0.25 $Wm^{-2}K^{-1}$). The large spread in the SW cloud feedback is a common feature in GCM simulations (Crucifix, 2006; Soden and Held, 2006; Vial et al., 2013). The large spread in the lapse rate feedback is likely in part due to the varied response of high latitude sea ice among models (Fig. 7.5; Fig. 7.10).

7.3.4 *Sensitivity of Results to Definition of LIA*

The processes (forcings and feedbacks) that are responsible for the cold conditions during the periods 1200-1450 AD and 1400-1650 AD are qualitatively similar to those responsible for the cold conditions in the LIA (i.e. from 1600-1850 AD). During all three periods, volcanic forcing is the dominant forcing, with a multi-model mean of 82%, 54% and 77% of the total forcing during the 1200-1450 AD, 1400-1650 AD and 1600-1850 AD periods, respectively (Fig. 7.6). The 1600-1850 AD period is characterized by the largest total forcing (-0.30 W/m^2 in the multi-model mean). In contrast, the 1400-1650 AD period has the weakest total forcing (-0.19 W/m^2), but it features the strongest relative contribution from solar forcing (30%; Fig. 7.9), as it contains the Spörer Minimum. While greenhouse gas forcing makes a notable contribution to the total forcing in 1600-1850 AD (13%) and 1400-1650 AD (16%) it is weak in 1200-1450 AD (3%).

In addition to substantial differences in total forcing across the three cold epochs, there are substantial differences in the mean effective climate feedback across the epochs – ranging from -1.42 to -1.97 $Wm^{-2}K^{-1}$. Differences in the effective climate sensitivity arise primarily due to differences in the SW cloud feedback and the net LW feedback. Ocean heat uptake is small across all three periods, as demonstrated by changes in global mean surface energy fluxes of less than ±0.05 Wm^{-2}.

7.4 SUMMARY

The CMIP5/PMIP3 last millennium simulations feature extended periods of cold conditions across the globe during the period ca. 1200 -1850 AD; temperature anomalies averaged over the NH generally agree well with proxy based temperature reconstructions. Analysis of the global TOA energy budget during the last millennium using APRP and radiative kernel techniques indicates that volcanic forcing is primarily responsible for the cold conditions in the CMIP5/PMIP3 models. Volcanic forcing contributes an average of 82%, 54% and 77% of the

total forcing in the multi-model mean for the cold epochs in 1200-1450 AD, 1400-1650 AD and 1600-1850 AD, respectively. Forcing contributions due to changes in insolation (15%, 30%, 10%) and greenhouse gas concentrations (3%, 16%, 13%) are substantially smaller than the volcanic forcing.

A feedback analysis of the 1600-1850 AD period demonstrates that the dominant climate feedbacks that reinforce the global cooling include the water vapor and lapse rate feedbacks, which combined are responsible for 36% of the LIA cooling in the models; the positive LW and SW water vapor feedbacks are a consequence of the decrease in water vapor concentration associated with the vertically-integrated cooling while the positive lapse rate feedback arises due to greater cooling near the surface than aloft poleward of ca. 30-40º latitude. While lapse rate changes provide a negative feedback in simulations of greenhouse gas forcing, a positive lapse rate feedback has also been observed in Last Glacial Maximum simulations. The combined water vapor and lapse rate feedback present in the last millennium simulations is larger than that from future climate simulations but similar to that from Last Glacial Maximum simulations. In contrast, the surface albedo feedback is generally larger than that found in either the future climate or Last Glacial Maximum simulations. Indeed, the surface albedo feedback is the dominant positive SW feedback in the last millennium simulations, responsible for 14% of the global cooling on average, and arises from sea ice growth and increased snow cover during the LIA. The positive correlation between the strength of the surface albedo feedback and the magnitude of volcanic forcing in the last millennium simulations suggests that volcanic forcing may be responsible for the larger surface albedo feedback during the LIA (relative to the future climate and Last Glacial Maximum simulations). LW cloud feedback provides an additional 6% of the global cooling on average and is consistent with lower cloud tops in the colder LIA atmosphere.

There are several points to consider when interpreting the results of the CMIP5/PMIP3 last millennium simulations in light of the paleoclimate record. Firstly, large uncertainties exist in the characterization of volcanic forcing that may not be adequately represented in the last millennium simulations. Large uncertainties exist in reconstructions of aerosol concentration, AOD and aerosol effective radius as a function of time, latitude and height, all of which exert important controls on the climate system. These uncertainties are compounded by the CMIP5 models' poor representation of the dynamical response of the atmosphere to volcanic eruptions

(Driscoll et al., 2012). Further, large uncertainties remain concerning the magnitude of changes in insolation over the last millennium. In particular, one TSI reconstruction suggests that changes in insolation during the LIA were an order of magnitude larger than those used in the CMIP5/PMIP3 last millennium simulations (Schmidt et al., 2012; Shapiro et al., 2011). This uncertainty, in conjunction with the fact that only one of the CMIP5/PMIP3 last millennium runs included solar-driven ozone variations (Shindell et al., 2006) leaves open the possibility that solar forcing may have played a larger role in LIA cooling than suggested by these model simulations.

Table 7.1. Description of CMIP5/PMIP3 models and their forcings used in this analysis.

Model	Ensemble	(lon x lat x vert levels)		Forcings				
		Atm Resolution	Ocean Resolution	Solar	Volcanic	Ozone	Land use	Orbital variations
CCSM4	r1i1p1	288 x 192 x L26	320 x 384 x L60	VSK	GRA (sulfate loading)	PI Control	PEA	Internally calc.
GISS 121	r1i1p121	144 x 90 x L40	288 x 180 x L32	SBF	CEA (AOD)	PI Control	PEA	Internally calc.
GISS 124	r1i1p124	144 x 90 x L40	288 x 180 x L32	VSK + WLS back	CEA (AOD)	PI Control	PEA	Internally calc.
MPI	r1i1p1	196 x 98 x L47	256 x 220 x L40	VSK + WLS back	CEA (AOD)	Regression	PEA	Internally calc.
IPSL	r1i1p1	96 x 95 x L39	182 x 149 x L31	VSK + WLS back	AJS (AOD)	PI Control	PI Control	Internally calc.
CSIRO	r1i1p1	64 x 56 x L18	128 x 112 x L21	SBF	CEA (TSI anomaly)	PI Control	PI Control	Internally calc.
HadCM3	r1i1p1	96 x 73 x L19	288 x 144 x L20	SBF + WLS back	CEA (AOD)	PI Control	PEA	Internally calc.

Table 7.2. Global Cooling Contributions (1600-1850 AD minus 950-1200 AD)

Model	Volcanic forcing (°C)	Solar forcing (°C)	GHG forcing (°C)	Sfc albedo fdbk (°C)	SW cloud fdbk (°C)	SW q fdbk (°C)	Lapse rate fdbk (°C)	LW q fdbk (°C)	LW cloud fdbk (°C)
CCSM4	-0.07 (23%)	-0.01 (2%)	-0.01 (3%)	-0.06 (20%)	0.01	-0.03 (8%)	-0.06 (18%)	-0.05 (17%)	-0.02 (8%)
MPI	-0.09 (39%)	-0.01 (4%)	-0.01 (5%)	-0.03 (13%)	0.03	-0.03 (12%)	0.00 (0%)	-0.04 (20%)	-0.02 (7%)
GISS121	-0.09 (39%)	-0.01 (4%)	-0.01 (4%)	-0.03 (13%)	0.02	-0.02 (7%)	-0.01 (4%)	-0.05 (20%)	-0.02 (9%)
GISS124	-0.10 (40%)	-0.01 (4%)	-0.01 (4%)	-0.03 (13%)	0.02	-0.02 (7%)	-0.01 (5%)	-0.04 (18%)	-0.02 (8%)
IPSL	-0.02 (14%)	-0.01 (7%)	-0.01 (7%)	-0.02 (11%)	-0.03 (21%)	-0.01 (8%)	-0.01 (7%)	-0.04 (25%)	-0.00 (0%)
Mean	-0.07 (31%)	-0.01 (4%)	-0.01 (5%)	-0.03 (14%)	0.01	-0.02 (9%)	-0.02 (7%)	-0.05 (20%)	-0.02 (6%)

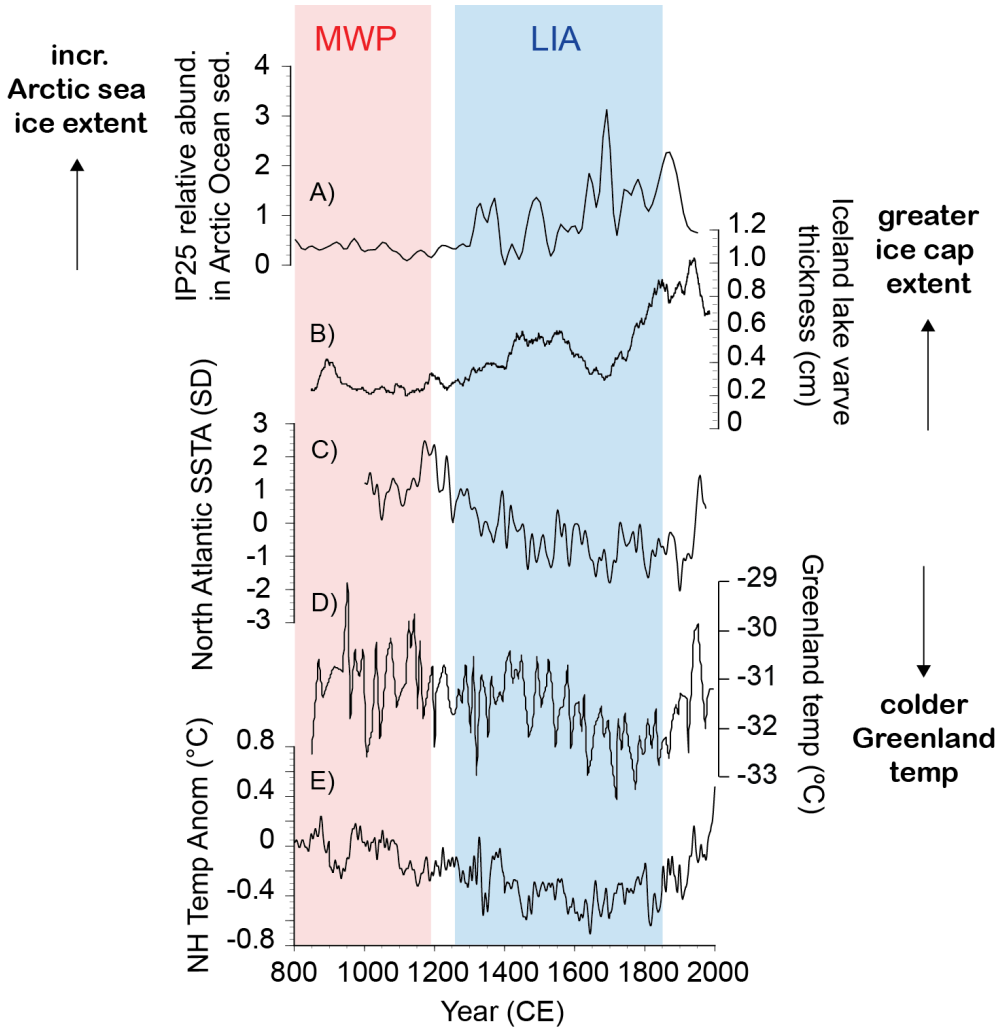

Figure 7.1. Proxy records of climate change over the past millennium. A) Arctic sea ice changes based on the relative abundance of IP25, a biomarker produced by sea ice algae, in a sediment core from the north coast of Iceland (Masse et al., 2008); B) ice cap extent in central Iceland from Hvítárvatn Lake sediment varve thickness (Larsen et al., 2011); C) multi-proxy NE Atlantic SST composite (Cunningham et al., 2013); D) Greenland temperature reconstruction (Kobashi et al., 2011); E) NH temperature anomalies based on a multi-proxy network and the climate field reconstruction method (Mann et al., 2009).

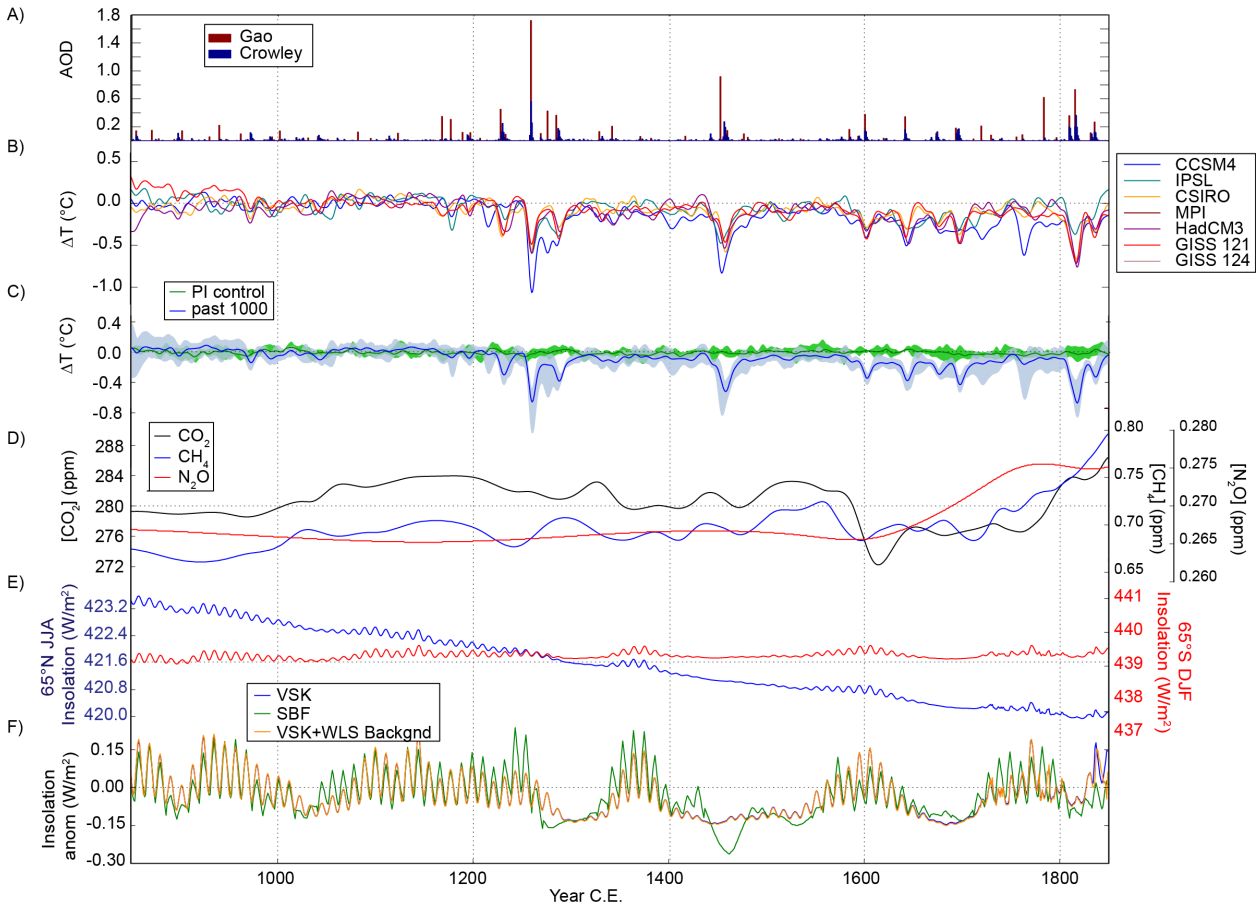

Figure 7.2. Climate forcings and global surface air temperature through the last millennium in the CMIP5 models: A) Aerosol optical depth from the Crowley et al. (2000) data set (blue bars) and estimated from the Gao et al. (2008) data set (red bars) by dividing sulfate loading by 150 Tg (Stothers, 1984). B) Globally averaged surface air temperature anomaly (relative to 950-1200 AD) in each last millennium simulation. C) Globally averaged surface air temperature anomaly for the multi-model ensemble mean of the last millennium simulations (blue) and the control simulations (green) where solid lines represent the multi-model mean and shading represents ±1σ. Temperature anomalies are calculated relative to years 100-350 in each data set and annually averaged data were smoothed with a Gaussian filter with σ = 3 years. D) Concentration of CO_2, CH_4, and N_2O. E) Changes in insolation at 65°N in JJA (blue) and 65°S in DJF (red). F) Globally averaged insolation anomalies (relative to 950-1200 AD) for the solar forcing data sets outlined in Table 7.1.

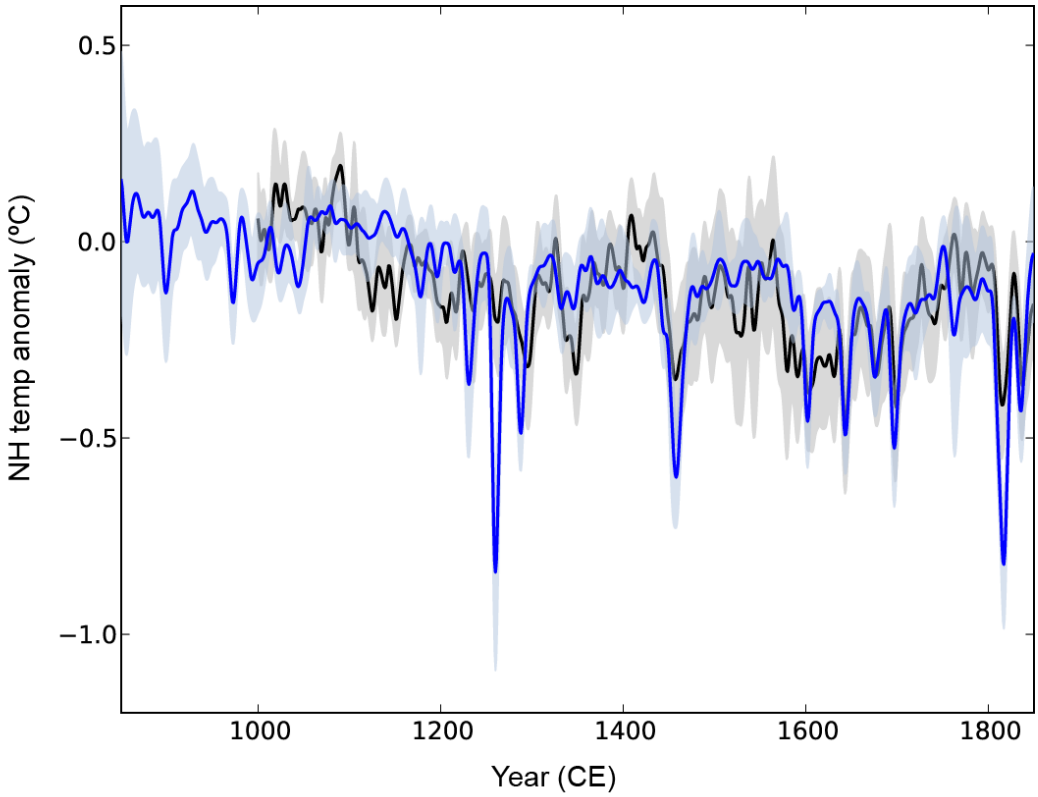

Figure 7.3. Mean NH temp anomaly from CMIP5/PMIP3 models (blue) and from 521 proxy-based ensemble estimates (black; Frank et al. 2010; based on 9 different large-scale NH temperature reconstructions spanning the last millennium, recalibrated to annual NH temperatures over all possible decadal intervals > 40 years during the 19th-20th centuries in order to consider uncertainty in the individual records as well as in the slope and intercept of the calibration). Temperature anomalies are calculated relative to the MCA (950-1200 CE) and annually averaged data were smoothed with a Gaussian filter with $\sigma = 3$ yrs. Solid lines represent the multi-model/multi-reconstruction mean and shading represents $\pm 1\sigma$.

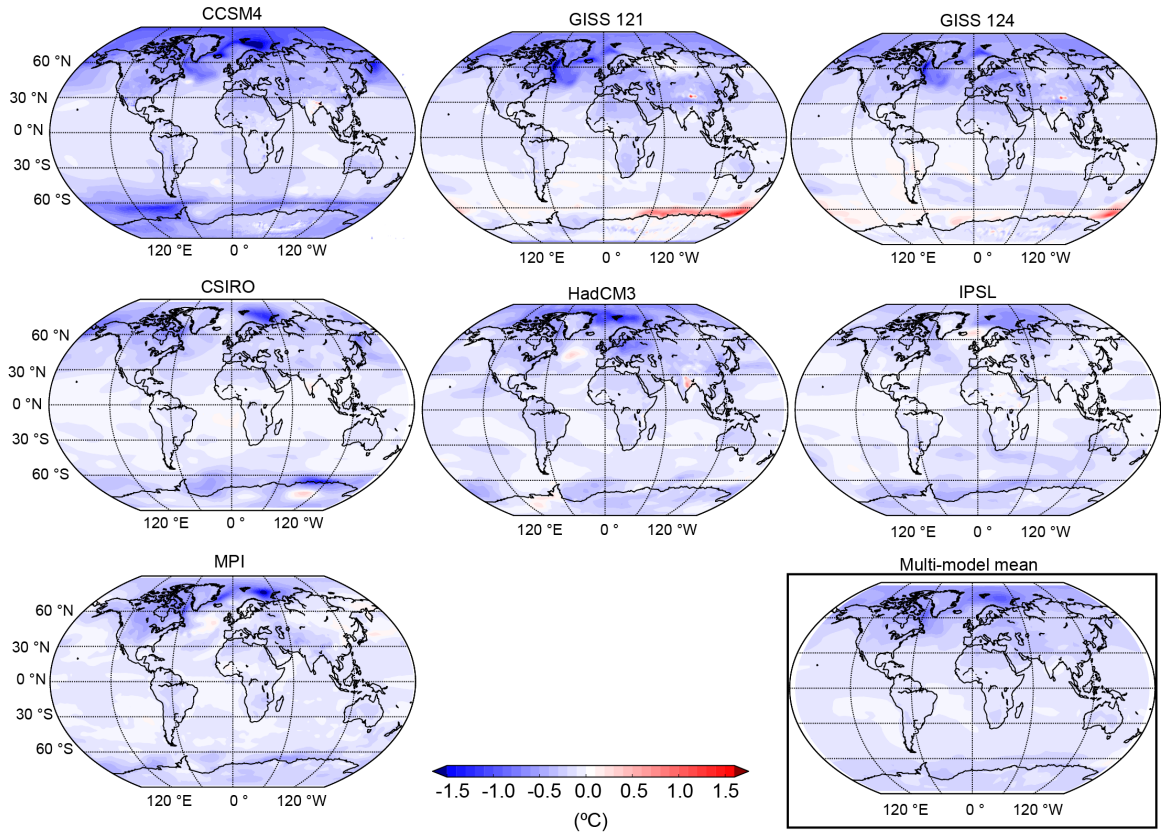

Figure 7.4. LIA (1600 – 1850 AD) minus MWP (950-1200 AD) surface air temperature changes in the CMIP5/PMIP3 simulations.

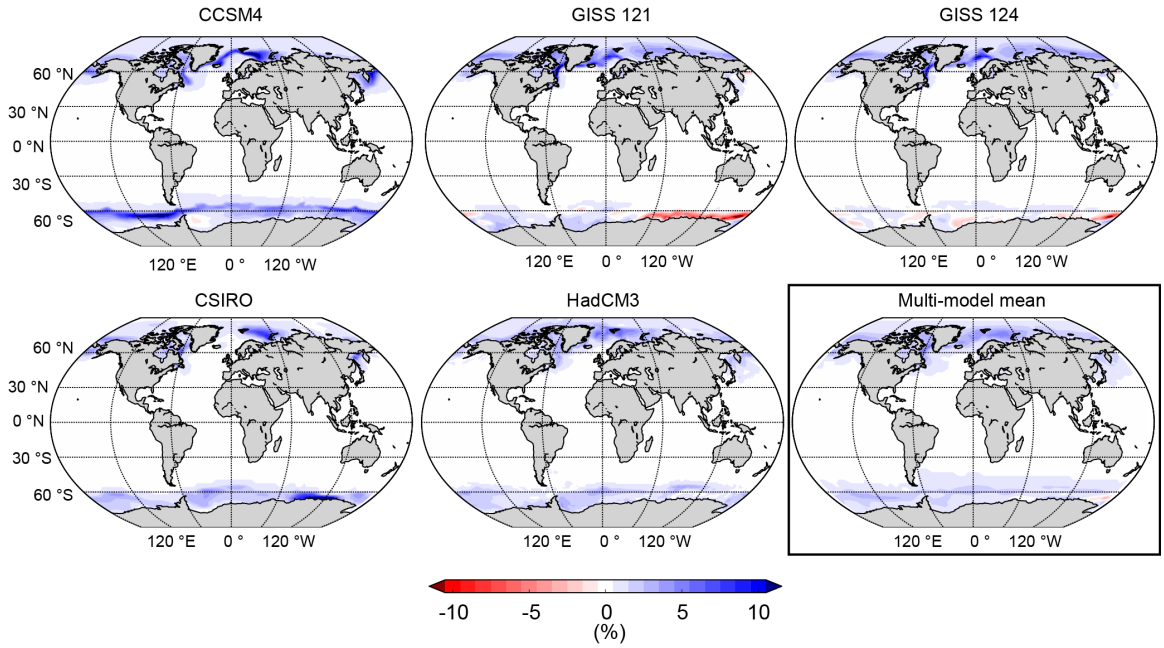

Figure 7.5. LIA (1600 – 1850 AD) minus MWP (950-1200 AD) sea ice concentration changes in the CMIP5/PMIP3 simulations.

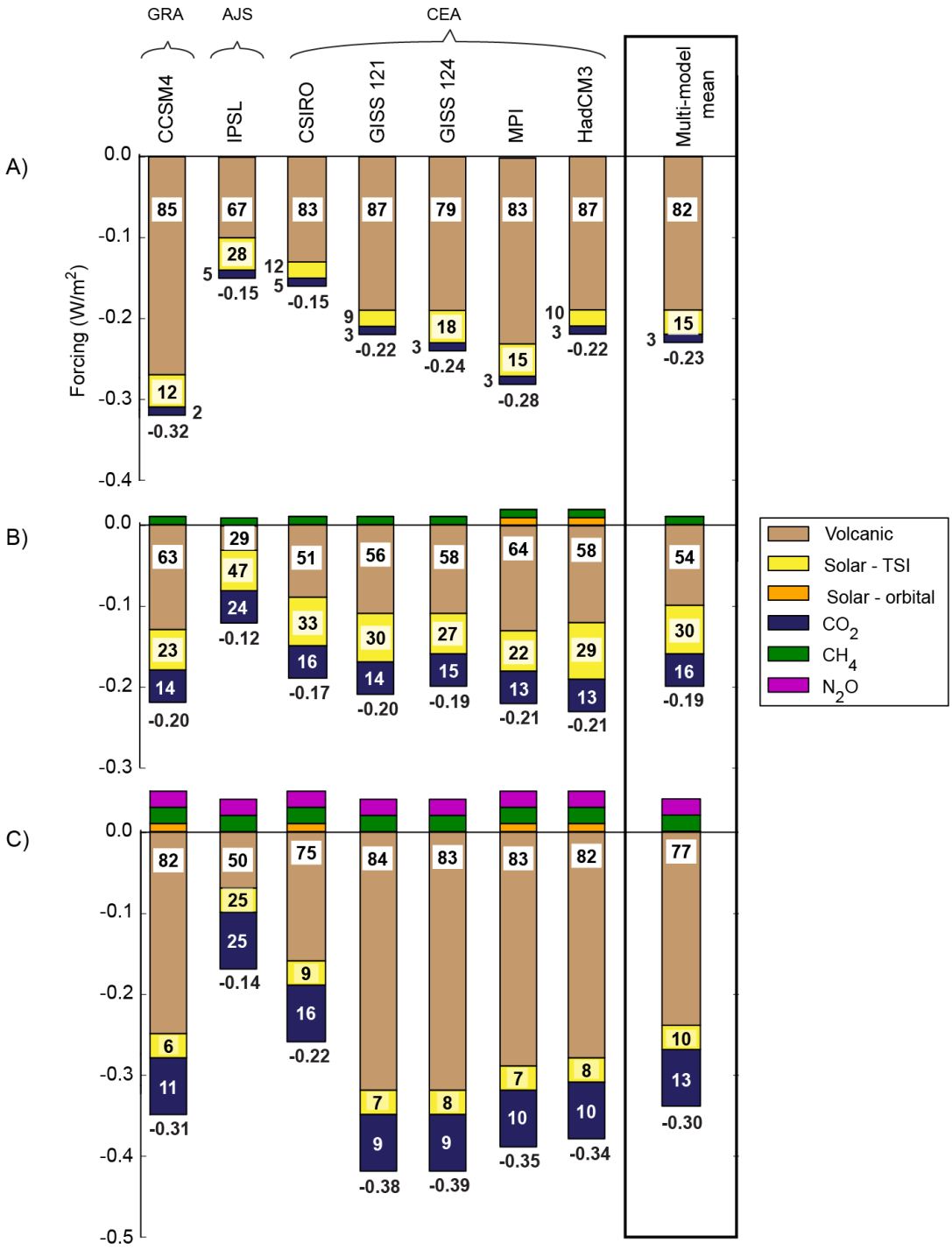

Figure 7.6. Decomposition of radiative forcings in the CMIP5/PMIP3 last millennium simulations into contributions from volcanic aerosols, solar output, orbital configuration and the well-mixed GHGs for the period from: A) 1200-1450 CE, B) 1400-1650 CE and C) 1600-1850 CE, relative to the MCA (950-1200 CE). Percentages in the brown, yellow, and blue boxes represent fractional contributions to total forcing from volcanic, total

solar (orbital and TSI), and total GHG (CO2, CH4, and N2O) forcings, respectively. Values below the bars represent total forcing in W/m^2. GRA, AJS, and CEA (at the top of the figure) indicate the volcanic forcing data set used.

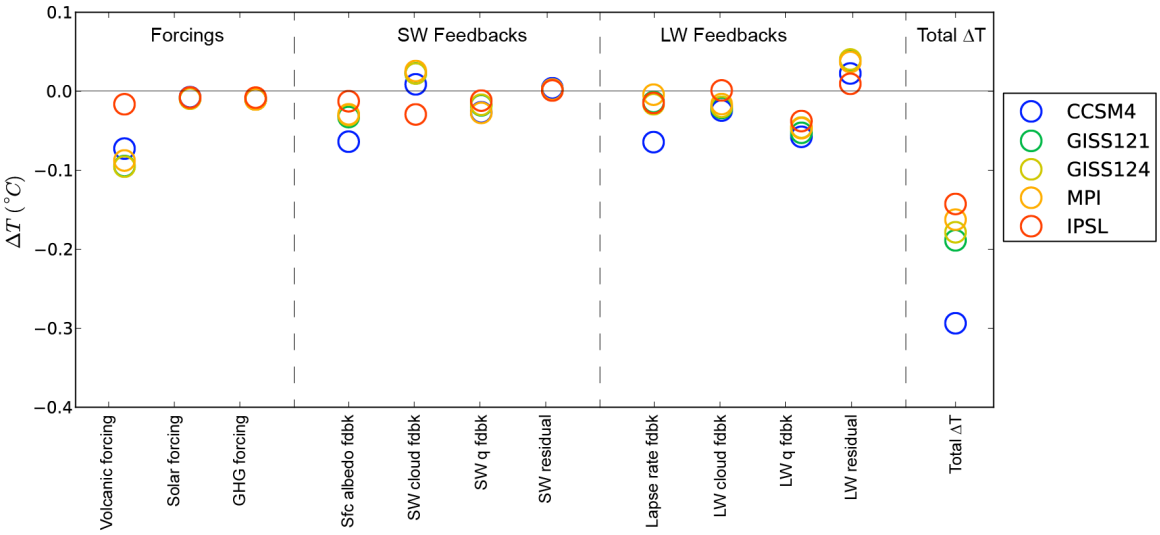

Figure 7.7. Global cooling contributions due to volcanic, solar and GHG forcings and the SW and LW feedbacks compared to the total globally averaged temperature change between the LIA (1600 – 1850 AD) and MWP (950-1200 AD). The difference between the total cooling and the sum of the forcings and feedbacks is the Planck response. Global cooling contributions were not calculated for the HadCM3 and CSIRO last millennium simulations because relative humidity data were not available for HadCM3 (see text for details).

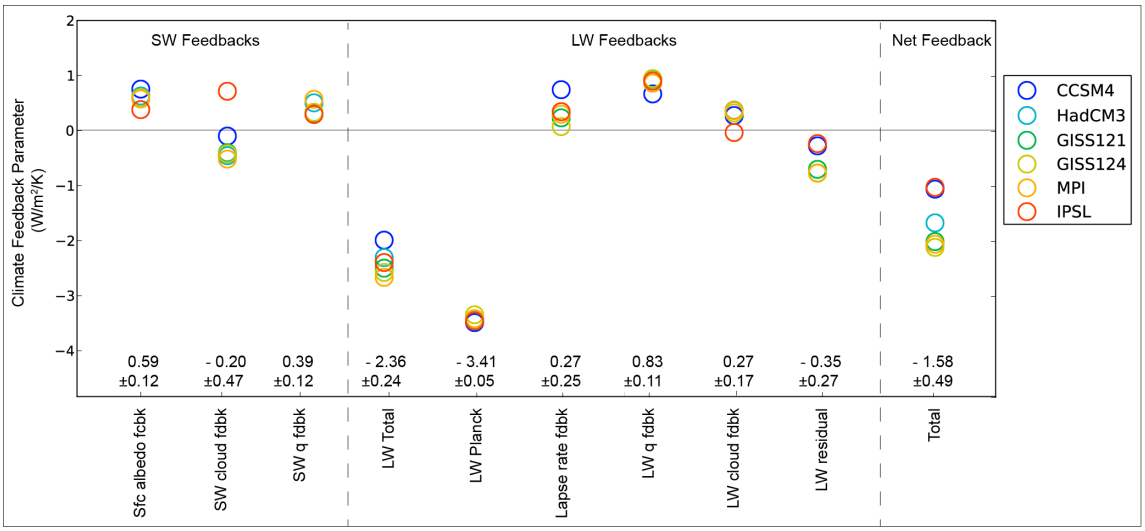

Figure 7.8. LIA climate feedback parameters calculated from the CMIP5/PMIP3 simulations for the SW (surface albedo, SW cloud, SW absorption, SW residual), LW (total LW, Planck response, lapse rate, LW water vapor and LW cloud, LW residual) and total feedbacks. Decomposition of feedbacks was not performed for the HadCM3 and CSIRO last millennium simulations (see text for details).

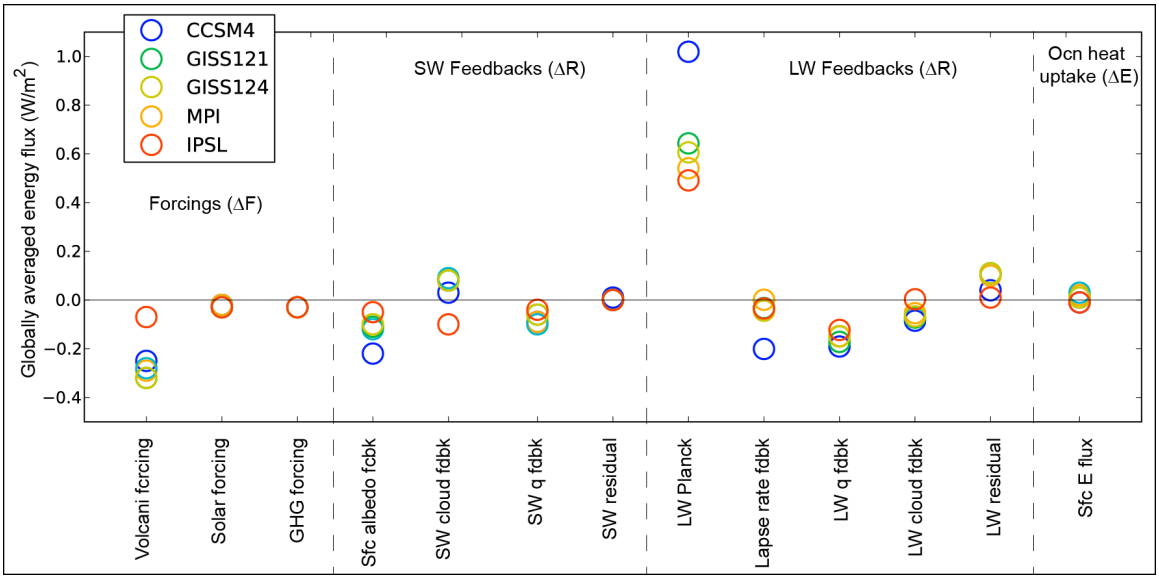

Figure 7.9. LIA (1600-18050 AD) minus MWP (950-1200 AD) globally averaged TOA energy flux changes due to forcings (volcanic, solar, greenhouse gas), SW feedbacks (surface albedo, SW cloud, SW absorption, SW residual), LW feedbacks (Planck, lapse rate, LW water vapor, LW cloud, LW residual) and globally averaged surface energy flux

(ΔE_{sfc}). Decomposition of feedbacks was not performed for the HadCM3 and CSIRO last millennium simulations (see text for details).

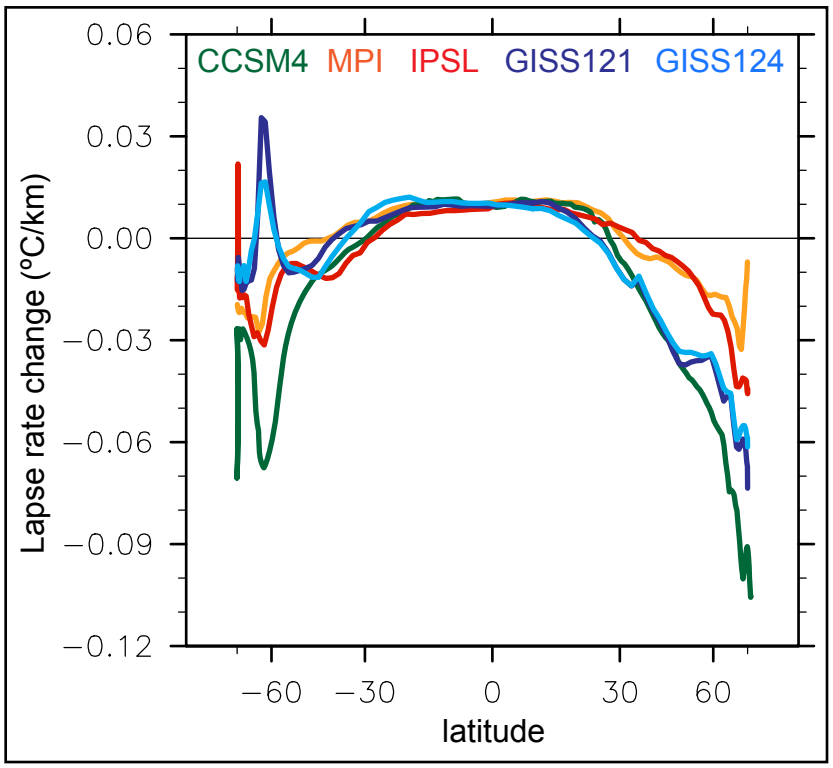

Figure 7.10. LIA (1600-1850 AD) minus MWP (950-1200 AD) changes in tropospheric lapse rate (calculated as a pressure-weighted average between 1000-200 mbar).

Chapter 8. POSSIBLE MECHANISMS OF A SOUTHWARD SHIFTED ITCZ DURING THE LITTLE ICE AGE

8.1 INTRODUCTION

Global compilations of paleoclimate reconstructions underscore the complexity of changes in the climate system over the last millennium (e.g. PAGES 2k Consortium, 2013). These records generally paint a picture of widespread cooling across much of the globe from ca. 1250-1850 AD, albeit with variable magnitude, timing, and duration (Cunningham et al., 2013; Kobashi et al., 2011; Masse et al., 2008; Neukom et al., 2014; PAGES 2k Consortium, 2013). Surface temperature reconstructions suggest that average Northern Hemisphere (NH) temperatures cooled by ca. 0.5 °C between ca. 800-1000 AD and 1400-1850 AD (Hegerl et al., 2007; Mann et al., 2009; Marcott et al., 2013; Moberg et al., 2005), with cooling of up to 1.0-1.5°C in central Greenland (Kobashi et al., 2011). Sea ice reconstructions from the Arctic further suggest that Arctic sea ice was more extensive ca. 1300-1850 AD (Masse et al., 2008; Rasmussen and Thomsen, 2014). While sufficiently long and highly resolved proxy records are sparser in the SH, recent multiproxy reconstructions have pointed to somewhat weaker hemispheric scale cooling in the SH (Neukom et al., 2014).

In the tropics, a number of paleohydroclimate records provide evidence for substantial changes in tropical rainfall patterns over the last millennium. Oxygen isotope records from cave deposits in India and China, tree ring records from Southeast Asia, and relative abundances of foraminifera in marine sediment from the Arabian Sea generally suggest that summer monsoon rainfall in these regions weakened and extreme droughts prevailed during the LIA, ca. 650-250 yr BP (1300-1700 AD; Anderson et al., 2002; Buckley et al., 2010; Sinha et al., 2011; Wang et al., 2005a; Zhang et al., 2008). These rainfall changes are thought to have played a role in societal changes and contributed to the collapse of several major civilizations in India, China and Southeast Asia during this time (Buckley et al., 2010; Sinha et al., 2011; Zhang et al., 2008). While fewer proxy records exist from maritime regions, evidence from the northern tropical Pacific (based on microbiological and hydrogen isotopic records from lake sediments) and the western Atlantic (based on titanium concentrations in the Cariaco Basin) suggest that arid

conditions prevailed ca. 550-150 yr BP (1400-1800 AD; Haug et al., 2001; Sachs et al., 2009). South of the equator, increased rainfall in the Indo-Pacific Warm Pool is inferred ca. 600-100 yr BP (1350-1850 AD), based on oxygen isotopes of foraminifera (Newton et al., 2006). In addition, the El Junco Lake biomarker records (presented in Chapter 3) suggest that climatological rainfall in the eastern equatorial Pacific was increased ca. 700-500 yr BP (1250-1450 AD). Finally, proxy records from Peru and Brazil suggest that the South American summer monsoon intensified beginning ca. 1300 – 1500 AD and continued through 1800 AD, based on oxygen isotopes in cave deposits, authigenic calcite in lake sediments, and tropical glacier records (Vuille et al., 2012). Taken together, these tropical hydroclimate reconstructions provide evidence for a widespread (though not necessarily synchronous) southward shift of tropical precipitation during the LIA (Fig. 8.1).

It is well known from theory, observations and climate model simulations that shifts in the zonal average position of the ITCZ are strongly anti-correlated to changes in atmospheric heat transport across the equator (Donohoe et al., 2013; Frierson and Hwang, 2012; Kang et al., 2008). The ITCZ is the rising branch of the Hadley circulation, which is the primary driver of meridional atmospheric energy transport in the tropics. Vertically-integrated moist static energy flux occurs in the direction of the upper (poleward) branch of the Hadley cell (since the Hadley cell is a thermally direct circulation) while net moisture flux occurs in the direction of the lower (equatorward) branch of the cell (since humidity decreases with altitude). Because of this relationship, a hemispherically asymmetric change in net atmospheric heating causes the Hadley circulation to shift meridionally in order to bring the atmospheric energy balance back into equilibrium. It does so by shifting the position of the ITCZ. This relationship holds even when the heating occurs far from the tropics (Kang et al., 2009).

We perform a preliminary investigation of the possible mechanisms of a southward shifted ITCZ during the LIA, utilizing the last millennium simulations in the Coupled Model Intercomparison Project Phase 5 (CMIP5)/Paleoclimate Intercomparison Project Phase 3 (PMIP3). We evaluate the hypothesis that a southward shift of the ITCZ occurs during the LIA in the last millennium simulations due to anomalous northward cross-equatorial energy transport by the atmosphere (e.g. greater atmospheric cooling in the NH than the SH). For the purposes of this study, we characterize a meridional shift of the zonally averaged ITCZ by a change in tropical precipitation asymmetry (i.e. the area-integrated precipitation from 0-20° latitude in the

NH minus the SH). Following the methods outlined in Chapter 7, we employed the Approximate Partial Radiative Perturbation (APRP) method to quantify the hemispheric asymmetry of the shortwave forcings and feedbacks during the LIA. Seven model simulations were included in our analysis from six models run with different sets of forcings, which include solar, orbital, volcanic, and greenhouse gas forcings. We refer the reader to Chapter 7 for a detailed description of the models, their forcings, and a description of the Approximate Partial Radiation Perturbation Method (APRP) used in this analysis.

8.2 RESULTS

8.2.1 *Simulated Changes in Cross-Equatorial Atmospheric Heat Transport and Tropical Precipitation During the LIA*

As demonstrated in Chapter 7, global cooling is observed in all CMIP5/PMIP3 last millennium simulations from ca. 1200-1850 AD relative to the first 350 years of the simulations with substantial multi-decadal to centennial-scale temperature variability and pronounced minima corresponding with volcanically active periods (Fig. 7.2). As in Chapter 7, we define the LIA as the time period from 1600-1850 AD and compare conditions during this time to the MWP, which we define as 950-1200 AD. (These time periods are chosen as they generally represent the minimum and maximum, respectively, in globally averaged temperature in the simulations). While LIA cooling is observed in all models, large differences in both the amplitude and spatial pattern of the cooling are observed among models (Fig. 7.4). These differences are particularly pronounced when comparing the interhemispheric differences. For instance, while high latitude cooling is pronounced in both the northern hemisphere (NH) and southern hemisphere (SH) in CCSM4, the GISS simulations demonstrate substantial warming in the Antarctic. These hemispheric differences are reflected in sea ice changes - while Artic sea ice extent increases in all model simulations, Antarctic sea ice extent decreases in the two GISS simulations (Fig. 8.2). Surface albedo increases over northern Eurasia, presumably due to increased snow cover, are also pronounced in all simulations except IPSL and CSIRO (data not shown). Through their role in the atmospheric energy budget, these hemispheric asymmetries in sea ice and snow cover are likely to have important implications for changes in tropical precipitation.

The change in the global cross-equatorial atmospheric heat transport and associated change in tropical precipitation asymmetry between the LIA and the MWP is shown in Fig. 8.3 for all seven model simulations analyzed. Anomalous northward cross-equatorial atmospheric heat transport occurs during the LIA in six out of the seven simulations, which shifts the ITCZ southward in those models. In one model, IPSL, anomalous southward atmospheric heat transport occurs that shifts the ITCZ northward. While a southward shift in tropical precipitation occurs in all but one simulation, the changes in precipitation asymmetry are small (representing a ca. -15% to +10% change in precipitation asymmetry across models). To put the magnitude of these changes into context, the multi-model mean change in tropical precipitation asymmetry in the last millennium simulations (10 mm/yr) is approximately half that associated with the Sahel drought of the 1950s-1980s as simulated by the CMIP5/PMIP3 ensemble mean (20 mm/yr; Hwang et al., 2013). The mean change in the tropical precipitation centroid (defined as the median of zonal average precipitation from 20ºS to 20ºN) is -0.03º in the last millennium simulations (data not shown), which is ca. 15% as large as the -0.2º multi-model mean from the PMIP2 Last Glacial Maximum simulations (Donohoe et al., 2013).

The southward shift in tropical precipitation is manifested in the different model simulations in largely disparate ways. However, some common features emerge, as shown in Fig. 8.4 (the multi-model mean precipitation anomaly where stippled regions show where 6 out 7 of the simulations agree on the sign of the change). Robust precipitation changes across the simulations include decreased precipitation in the northern branch of the Pacific ITCZ, the far Western Pacific Warm Pool and parts of Asia, as well as increased precipitation in the equatorial Atlantic, near the eastward extent of the South Pacific Convergence Zone and in the tropical North Pacific. Comparing the simulated precipitation changes with the paleohydroclimate reconstructions from Fig. 8.1, we see some evidence of agreement, including decreased precipitation in parts of India and Asia as well as under the northern branch of the ITCZ in the central tropical Pacific (Fig. 8.4). While the changes in precipitation result in a decreased zonal mean NH-SH precipitation asymmetry, it is unclear to what extent this precipitation asymmetry is purely due to thermodynamic scaling principles (i.e. a wet-get-drier, dry-get-wetter scenario associated with global cooling) and to what extent it is tied to circulation changes in the atmosphere. We are currently pursuing these lines of inquiry.

8.2.2 *Attribution of Cross-Equatorial Atmospheric Heat Fluxes During the LIA*

Possible sources of asymmetric atmospheric cooling during the LIA include asymmetry in the climate forcings (e.g. the volcanic forcing), symmetric forcing (due to the seasonal cycle in planetary albedo), and asymmetry in the climate feedbacks, including those associated with changes in surface albedo and clouds. In addition, asymmetry in the surface energy fluxes (e.g. through a change in the Atlantic Meridional Overturning Circulation) could lead to asymmetric atmospheric cooling.

In order to evaluate which mechanisms give rise to the anomalous northward cross-equatorial atmospheric energy transport during the LIA in the last millennium simulations, we applied the APRP method outlined in Chapter 7. The net shortwave (SW) energy fluxes at the surface and top of the atmosphere (TOA) were quantified and decomposed into contributions from climate forcings and feedbacks. In contrast to the approach used in Chapter 7, here we perform the analysis separately for each hemisphere. Changes in the hemispheric asymmetry of the SW energy fluxes are shown in Fig. 8.5 and 8.6. Energy fluxes are reported as NH minus SH, where negative terms indicate more NH cooling and positive terms indicate more SH cooling. Clear-sky radiation data for CSIRO was not available at the time of analysis, thus this simulation was omitted from the analyses.

In all models simulations, net (downward) TOA SW fluxes decreased more in the NH than the SH during the LIA (Fig. 8.5), although in the IPSL simulation this asymmetry is very small. The asymmetry in the SW fluxes is opposed by the LW fluxes- i.e. outgoing longwave radiation (OLR) decreases more in the NH than the SH. To first order, this can be explained by the Planck response, in which the asymmetry in OLR is tied to the greater cooling of the NH versus SH (which is expected due to the greater distribution of landmass in the NH, which because of its lower heat capacity, cools faster than the ocean). When the changes in the net vertical surface fluxes are added to those at the TOA, we see that the NH atmosphere loses heat with respect to the SH in all but one of the models (IPSL) as depicted in Fig. 8.3. These changes are consistent with the anomalous northward cross-equatorial energy transport observed in six of the model simulations.

Decomposition of the changes in net TOA SW into contributions from changes in total solar irradiance (TSI), volcanic forcing, SW cloud feedback and surface albedo feedback from the APRP method is shown in Fig. 8.6. In all models, solar forcing contributes very little to

asymmetry in the TOA SW fluxes. In contrast, volcanic forcing contributes to greater cooling in the NH in all model simulations– in MPI and CCSM4 this term dominates the asymmetry of the TOA SW energy fluxes, while in IPSL this term is very small. The asymmetry of the volcanic forcing is greatest in CCSM4, which is the only model to use the volcanic forcing data set from Gao et al. (2008), which has a substantially larger aerosol loading in the NH than SH during the LIA (data not shown). This is in contrast to the Crowley (2000) data set used by the GISS, MPI, and HadCM3 models, in which the symmetry is much weaker. The IPSL simulation prescribed volcanic forcing from Ammann et al. (2007), however, due to details of the implementation, slow daily decreases in the extinction values of the volcanic aerosols occurred (J.-L. Dufresne and M. Khodri, personal communication). These issues may have led to the weak asymmetry in both the forcing and feedbacks in this model.

Climate feedbacks also contribute to the asymmetry in the TOA SW fluxes. In all models except IPSL, the surface albedo feedback contributes to greater cooling of the atmosphere in the NH, thereby reinforcing the asymmetry provided by volcanic forcing. This result is consistent with the fact that most models demonstrate a greater increase in snow and/or sea ice cover in the NH than SH during the LIA (Fig. 8.2, Fig. 7.5). This surface albedo feedback is the dominant contributor to the asymmetry in the net TOA SW flux in three out of the six simulations (GISS 121, GISS 124 and HadCM3). The asymmetry in the surface albedo feedback is largest in the GISS simulations, which also demonstrate the largest asymmetry in sea ice response. In HadCM3, the hemispheric asymmetry in surface albedo is largely driven by changes in snow cover (data not shown).

Unsurprisingly, there is no consistency among models on the sign of the asymmetry in the SW cloud feedback. This term is weak in all simulations except CCSM4 and GISS124, in which the SW cloud feedback opposes the hemispheric asymmetry induced by the volcanic forcing and surface albedo feedback. In the IPSL simulation, all components of the net TOA SW flux demonstrate weak asymmetry; the small anomalous southward cross-equatorial heat transport shown in Fig. 8.3 is driven by the weak asymmetry in the net surface fluxes (Fig. 8.5).

Taken together, these results indicate that the simulated anomalous northward cross-equatorial heat transport in the atmosphere during the LIA (associated with the southward shift in tropical precipitation) occurs primarily due to the volcanic forcing and the snow and sea ice feedbacks.

8.3 SUMMARY

Tropical hydroclimate records provide evidence for a widespread southward shift of tropical precipitation during the LIA. We perform a preliminary investigation of the possible mechanisms of a southward shift of the ITCZ during the LIA, utilizing the last millennium runs in the CMIP5/PMIP3 archive. In general agreement with tropical paleohydroclimate reconstructions, a southward shift of the zonally averaged ITCZ occurs during the LIA (1600-1850 AD) with respect to the MWP (950-1200 AD) in six out of seven last millennium simulations analyzed. This southward shift of the ITCZ was tied to anomalous northward atmospheric energy transport across the equator during the LIA. Through the use of the APRP method to decompose the changes in TOA SW fluxes into contributions from the individual climate forcings and feedbacks, we determined that greater cooling of the NH (with respect to the SH) during the LIA was driven by asymmetric volcanic forcing (i.e. greater loading of volcanic aerosols in the NH), as well as from the asymmetry in the snow/sea ice response (i.e. greater snow and sea ice response in northern Eurasia and the Arctic than the SH). However, because the asymmetric SW fluxes are opposed by changes in OLR, the changes in cross-equatorial atmospheric heat transport, and thus the associated shifts of the zonally averaged ITCZ, are modest.

Future work will involve investigating the spatial structure of the tropical precipitation features and evaluating to what extent the changes in zonally averaged tropical precipitation asymmetry can be explained through thermodynamic scaling principles versus changes in atmospheric circulation. However, our results indicate that the robust simulation of past tropical hydroclimate changes critically hinges on robust reconstructions of the distribution of volcanic aerosols as well as on processes that determine changes in snow and sea ice extent.

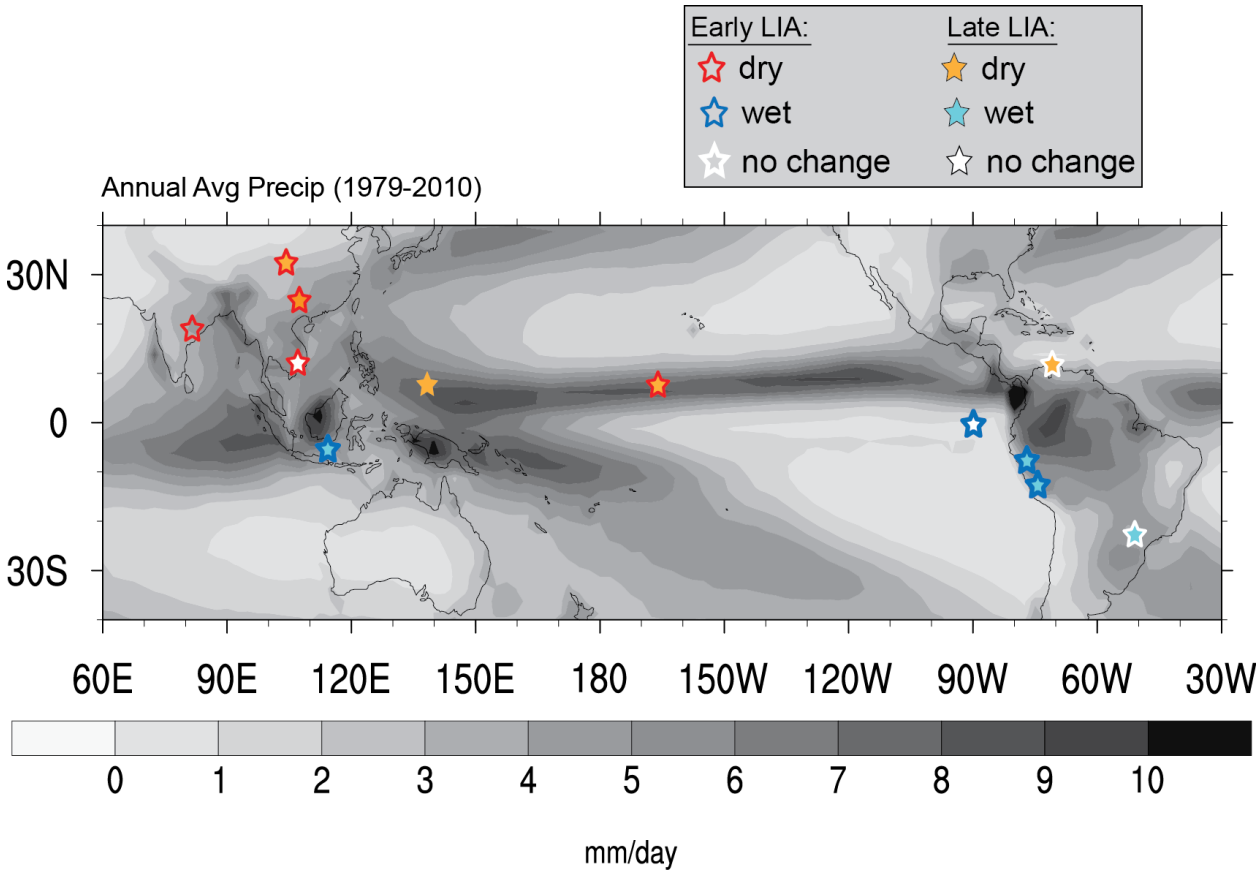

Figure 8.1. Summary of paleohydroclimate reconstructions of the early LIA (1250-1500 AD) and late LIA (1500-1850 AD) relative to the MWP (950-1200 AD; or to the last 100 years if MWP data is not available). Paleo records are from (Haug et al., 2001), (Wang et al., 2005a), Newton et al. (2006), Zhang et al. (2008), Sachs et al. (2009), Sinha et al. (2011), Vuille et al. (2012), Atwood and Sachs (2014), and references therein. Modern mean annual rainfall (grey shading) is from the GPCP Version 2.2 Combined Precipitation Data Set (http://www.esrl.noaa.gov) for the period 1979-2010 AD.

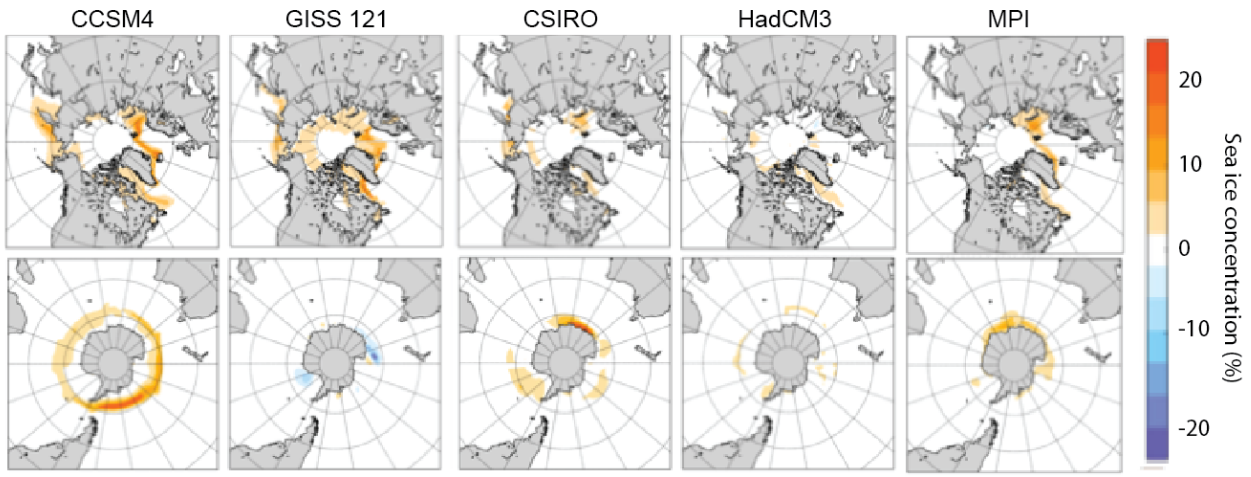

Figure 8.2. Change in sea ice area concentration during the LIA (1600-1850 AD) relative to the MWP (950-1200 AD).

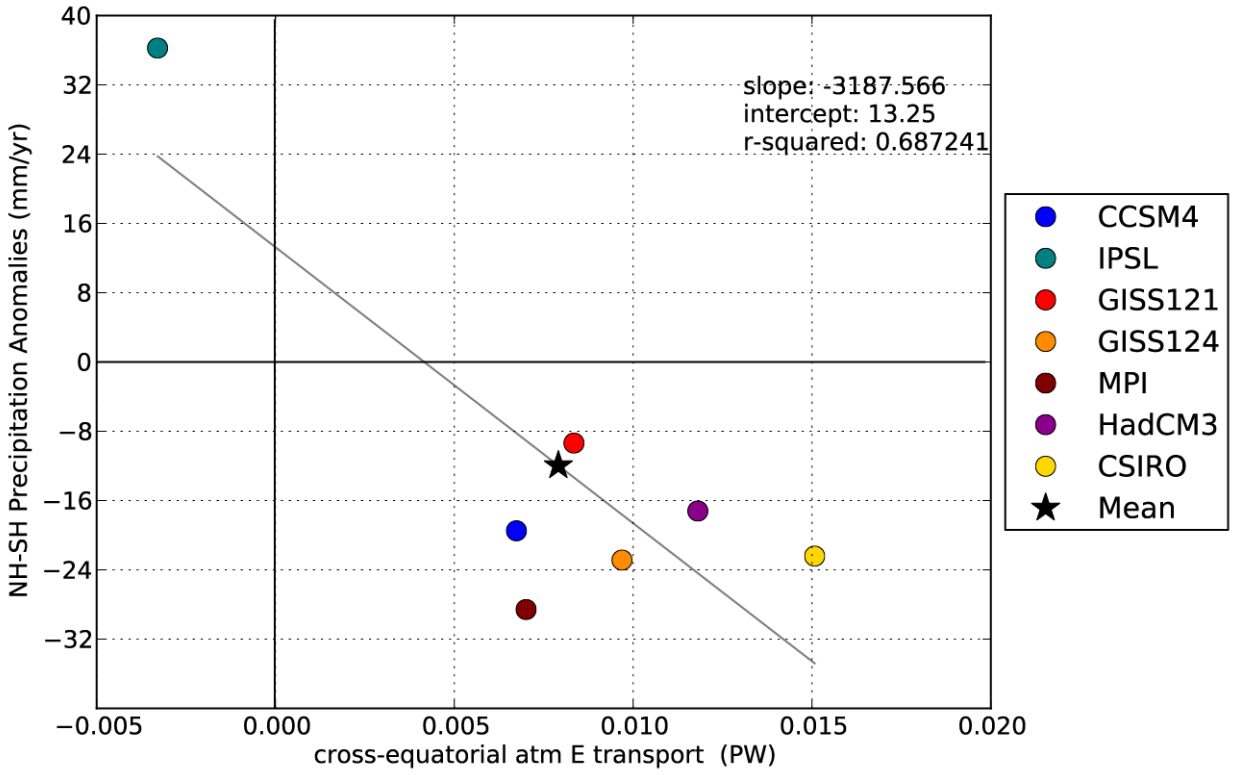

Figure 8.3. Change in zonal mean tropical precipitation asymmetry in the LIA (1600-1850 AD) relative to the MWP (950-1200 AD) versus the change in cross-equatorial atmospheric energy transport in the last millennium simulations.

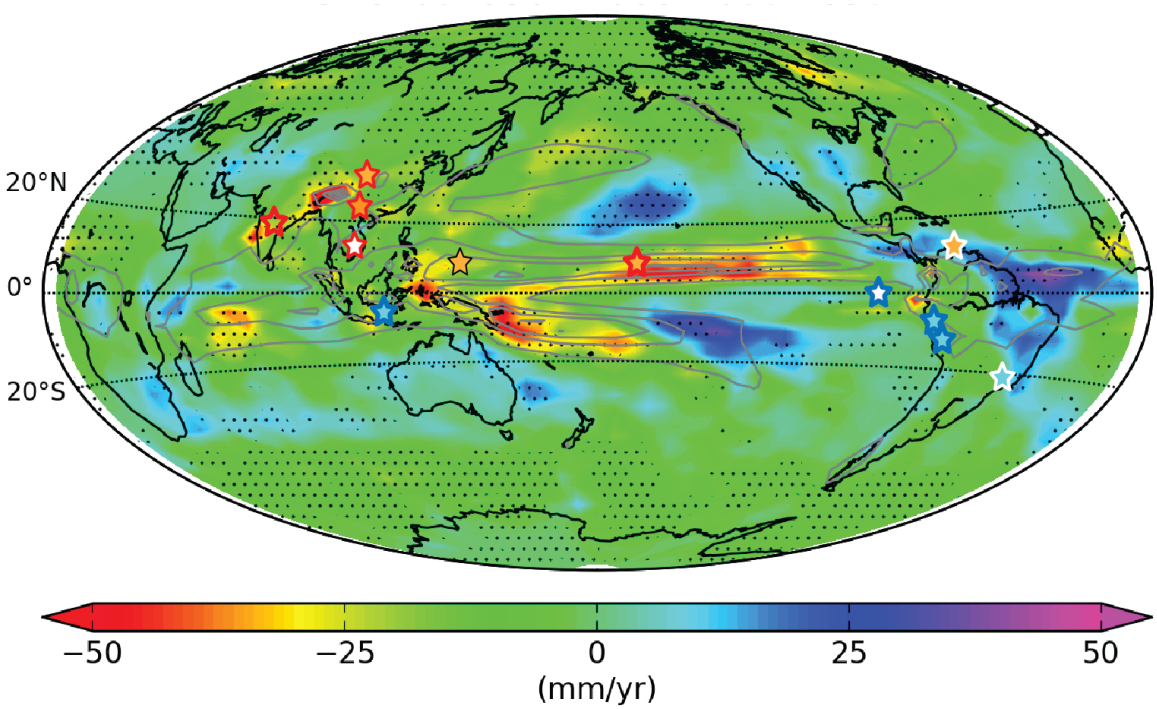

Figure 8.4. Multi-model mean change in precipitation during the LIA (1600-1850 AD) relative to the MWP (950-1200 AD) (colors) overlaid on contours of mean annual precipitation over the MWP. The stars indicate the paleohydroclimate records shown in Fig. 8.1.

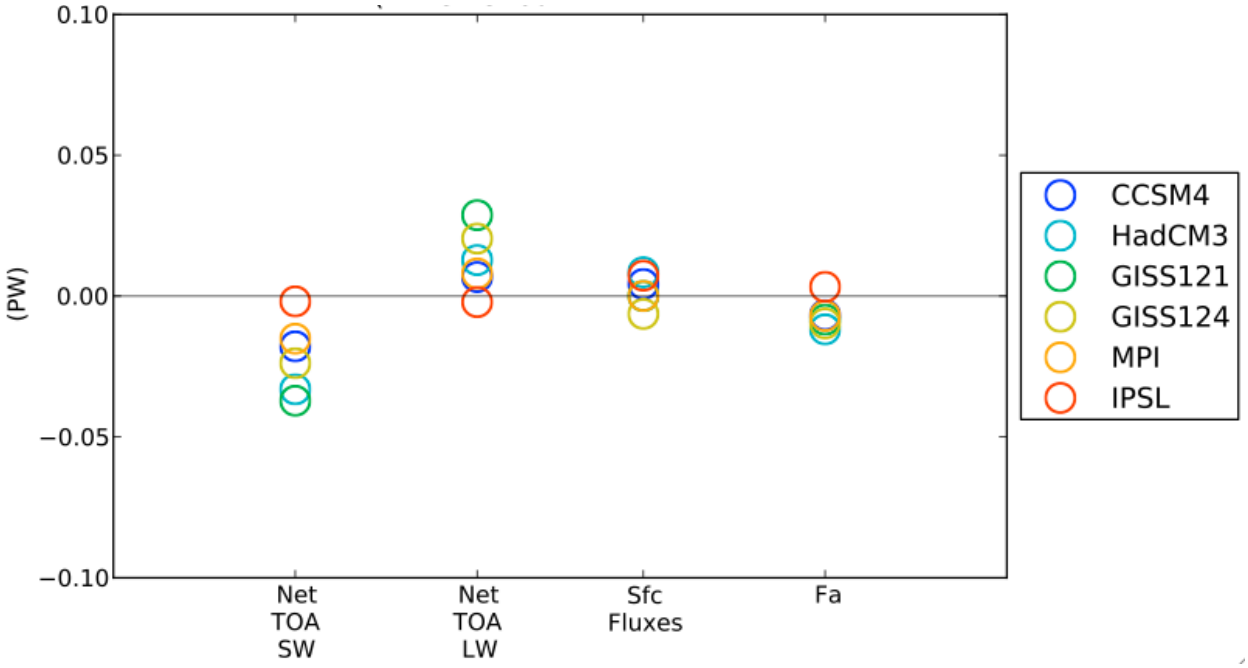

Figure 8.5. Difference in NH minus SH vertical energy flux in the atmosphere during the LIA (1600-1850 AD) relative to the MWP (950-1200 AD) due to contributions from: TOA SW, TOA LW, surface fluxes and their sum, F_a (the net change in the vertical atmospheric energy flux). Negative values indicate a decrease of vertical energy fluxes into the atmosphere in the NH with respect to the SH.

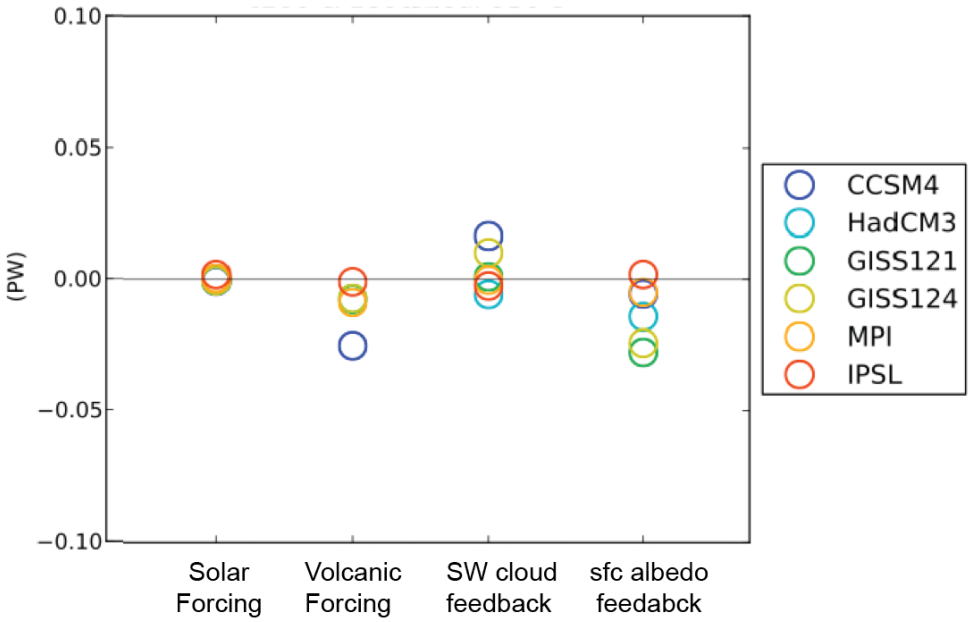

Figure 8.6. Difference in NH minus SH vertical energy fluxes in the atmosphere during the LIA (1600-1850 AD) relative to the MWP (950-1200 AD) due to contributions from: solar forcing, volcanic forcing, SW cloud feedback and surface albedo feedback.

Chapter 9. CONCLUSIONS

In Chapters 2-4, we presented a new set of hydroclimate reconstructions from the eastern equatorial Pacific that spans the last 9100 years. Past changes in (total) climatological rainfall and rainfall associated with El Niño events were reconstructed from the Galápagos Islands using the sedimentary distribution, accumulation rate, and hydrogen isotope composition of four lipid biomarkers in the sediment of El Junco Lake, San Cristóbal Island. In Chapter 2 we presented an idealized isotope hydrology model of El Junco Lake in to facilitate the interpretation of these rainfall reconstructions. In addition, we compared the biomarker records to meteorological rainfall data over the modern period and demonstrated that the comparisons broadly support our interpretation of the proxy records. We propose that these reconstructions offer valuable insight into past tropical Pacific climate change, due to their location in the heart of the eastern equatorial Pacific where the local hydroclimate is highly sensitive to both El Niño events and to movements of the eastern Pacific ITCZ.

In Chapter 3, we extended these biomarker records to span the last 9100 years and compared the rainfall reconstructions to other tropical hydroclimate reconstructions in the region. Multi-decadal to millennial scale oscillations of (total) climatological rainfall and rainfall associated with El Niño events are inferred from the eastern equatorial Pacific over the Holocene. Most of the large (total) climatological rainfall changes that occurred at El Junco Lake during the Holocene were opposed by changes in climatological rainfall associated with El Niño events, from which we infer that the changes in total climatological rainfall were driven by non-El Niño processes, such as meridional displacements of the eastern Pacific ITCZ.

Many of the pronounced changes in total mean annual rainfall inferred from the El Junco Lake biomarker records have counterparts in hydroclimate reconstructions from central-eastern Brazil and coincide with periods of notable tropical hydroclimate and high latitude climate changes. The driest conditions of the Holocene are inferred at El Junco Lake ca. 1200-950 yr BP (750 AD-1000 AD), at a time when widespread aridity was recorded in tropical hydroclimate records that span Mesoamerica, South America and Saharan Africa. Anomalously wet conditions at El Junco Lake and central-eastern Brazil ca. 8500-8000, 5500-5000, and 4000 yr BP appear to have broadly coincided with widespread northern tropical aridity, suggesting that tropical rainfall patterns may have been shifted southward during these intervals, possibly in association with

high latitude climate changes. In contrast to continental monsoon records, the El Junco Lake biomarker records do not provide support for monotonic trends in ENSO variability or the position of the ITCZ in the eastern equatorial Pacific in response to precessional forcing through the Holocene.

Chapter 4 focused on the period of anomalously high total climatological rainfall and reduced El Niño rainfall inferred at El Junco Lake around the time of the "8.2 ka event". By comparing the El Junco Lake rainfall reconstructions to other regional hydroclimate reconstructions and implementing a simple set of idealized simulations with a linearized ocean-atmosphere model of the tropical Pacific (LOAM), we propose that a possible mechanism of the rainfall changes at El Junco Lake was the following: the large meltwater pulse to the North Atlantic ca. 8300 yr BP produced a global southward shift of tropical rainfall, including a southward shift of the ITCZ in the eastern Pacific, that gave rise to reduced ENSO variability through associated tropical Pacific mean state changes that increased the stability of the coupled ocean-atmosphere system..

In Chapter 5, we further evaluated the relationship between North Atlantic freshwater forcing, tropical Pacific mean state changes, and ENSO variability using simulations with a fully coupled global climate model, CESM, in tandem with LOAM. Simulations were performed in which a large freshwater perturbation was applied to the North Atlantic and the response of the mean state and variability of the tropical Pacific were evaluated. In support of the El Junco Lake hydroclimate reconstructions, the CESM simulations demonstrate a southward shift of the Pacific ITCZ and reduced ENSO variability in response to North Atlantic freshwater forcing. Simulations with LOAM indicate that the reduced ENSO variability is caused by subsurface warming in the tropical Pacific (driven by increased equatorial wind stress through changes in the wind stress curl) and wind-driven surface cooling, both of which decrease the coupling between the tropical Pacific atmosphere and ocean.

In Chapter 6, we investigated the source of large, low frequency, unforced changes in ENSO variability in a General Circulation Model (GFDL CM2.1). Using the intermediate complexity model from Chapters 4 and 5, we evaluated whether the low frequency variability in CM2.1 could be explained by mean state changes in the tropical Pacific. The results suggest that a two-way feedback operates between ENSO and the mean state of the tropical Pacific in CM2.1, whereby random forcing and nonlinear dynamics produce low frequency changes in ENSO

variance that are then counteracted by mean state feedbacks. We further demonstrated that the overly strong nonlinear behavior in the model produces large biases in the distribution of multi-decadal variability. We concluded that the range of multi-decadal ENSO variance in the 2,000 year control run of CM2.1 is nearly twice that expected from a linear system with realistic variance.

Finally, in Chapter 7 and Chapter 8 we evaluated the mechanisms of global cooling and tropical hydroclimate changes during the Little Ice Age (LIA). In Chapter 7, we quantified the contributions of the various climate forcings and feedbacks to global cooling during the LIA in the CMIP5/PMIP3 last millennium simulations. We found that volcanic forcing comprised 77% of the total forcing for the period 1600-1850 AD (relative to 950-1200 AD). A feedback analysis demonstrated that the dominant climate feedbacks were the water vapor and lapse rate feedbacks, which combined were responsible for 36% of the LIA cooling in the models. In addition, the surface albedo feedback (through sea ice growth and increased snow cover) was the dominant positive shortwave feedback, responsible for 14% of the LIA cooling on average.

In Chapter 8 we perform a preliminary analysis of the changes in tropical precipitation in the CMIP5/PMIP3 last millennium simulations in order to evaluate potential mechanisms of a southward shifted of the ITCZ, as has been inferred from a number of tropical hydroclimate records. We demonstrated that a weak southward shift in zonally averaged tropical precipitation occurs in 6 of the 7 model simulations analyzed that is associated with anomalous northward atmospheric energy transport across the equator during the LIA. We demonstrated that greater cooling of the NH (with respect to the SH) during the LIA is driven in the model simulations by greater loading of volcanic aerosols in the NH, as well as from the asymmetry in the snow and sea ice response. Future work will involve investigating the spatial structure of the tropical precipitation changes and evaluating the relative influence of thermodynamic versus atmospheric circulation changes on the changes in zonally averaged tropical precipitation.

BIBLIOGRAPHY

Alexander, M.A., Blade, I., Newman, M., Lanzante, J.R., Lau, N.C., Scott, J.D., 2002. The atmospheric bridge: The influence of ENSO teleconnections on air-sea interaction over the global oceans. Journal of Climate 15, 2205-2231.

Alley, R.B., Mayewski, P.A., Sowers, T., Stuiver, M., Taylor, K.C., Clark, P.U., 1997. Holocene climatic instability: A prominent, widespread event 8200 yr ago. Geology 25, 483-486.

Ammann, C.M., Joos, F., Schimel, D.S., Otto-Bliesner, B.L., Tomas, R.A., 2007. Solar influence on climate during the past millennium: Results from transient simulations with the NCAR Climate System Model. Proceedings of the National Academy of Sciences of the United States of America 104, 3713-3718.

An, S.I., Kug, J.S., Ham, Y.G., Kang, I.S., 2008. Successive modulation of ENSO to the future greenhouse warming. Journal of Climate 21, 3-21.

Anchukaitis, K.J., Tierney, J.E., 2013. Identifying coherent spatiotemporal modes in time-uncertain proxy paleoclimate records. Climate Dynamics 41, 1291-1306.

Anderson, D.M., Overpeck, J.T., Gupta, A.K., 2002. Increase in the Asian southwest monsoon during the past four centuries. Science 297, 596-599.

Apaestegui, J., Cruz, F.W., Sifeddine, A., Vuille, M., Espinoza, J.C., Guyot, J.L., Khodri, M., Strikis, N., Santos, R.V., Cheng, H., Edwards, L., Carvalho, E., Santini, W., 2014. Hydroclimate variability of the northwestern Amazon Basin near the Andean foothills of Peru related to the South American Monsoon System during the last 1600 years. Climate of the Past 10, 1967-1981.

Ashok, K., Behera, S.K., Rao, S.A., Weng, H., Yamagata, T., 2007. El Niño Modoki and its possible teleconnection. Journal of Geophysical Research 112, C11007.

Atwood, A.R., Sachs, J.P., 2012. Purification of dinosterol from complex mixtures of sedimentary lipids for hydrogen isotope analysis. Organic Geochemistry 48, 37-46.

Atwood, A.R., Sachs, J.P., 2014. Separating ITCZ- and ENSO-related rainfall changes in the Galápagos over the last 3 kyr using D/H ratios of multiple lipid biomarkers. Earth and Planetary Science Letters 404, 408-419.

Atwood, A.R., Volkman, J.K., Sachs, J.P., 2014. Characterization of unusual sterols and long chain diols, triols, keto-ols and n-alkenols in El Junco Lake, Galapagos. Organic Geochemistry 66, 80-89.

Barber, D.C., Dyke, A., Hillaire-Marcel, C., Jennings, A.E., Andrews, J.T., Kerwin, M.W., Bilodeau, G., McNeely, R., Southon, J., Morehead, M.D., Gagnon, J.M., 1999. Forcing of the cold event of 8,200 years ago by catastrophic drainage of Laurentide lakes. Nature 400, 344-348.

Bard, E., Raisbeck, G., Yiou, F., Jouzel, J., 2000. Solar irradiance during the last 1200 years based on cosmogenic nuclides. Tellus Series B-Chemical and Physical Meteorology 52, 985-992.

Battisti, D.S., 1988. Dynamics and thermodynamics of a warming event in a coupled tropical atmosphere-ocean model. Journal of the Atmospheric Sciences 45, 2889-2919.

Battisti, D.S., Hirst, A.C., 1989. Interannual variability in a tropical atmosphere ocean model-influence of the basic state, ocean geometry and nonlinearity. Journal of the Atmospheric Sciences 46, 1687-1712.

Bellenger, H., Guilyardi, E., Leloup, J., Lengaigne, M., Vialard, J., 2014. ENSO representation in climate models: from CMIP3 to CMIP5. Climate Dynamics 42, 1999-2018.

Berger, A.L., 1978. Long-term variations of daily insolation and Quaternary climatic changes. Journal of the Atmospheric Sciences 35, 2362-2367.

Bhattacharya, T., Byrne, R., Bohnel, H., Wogau, K., Kienelc, U., Ingram, B.L., Zimmerman, S., 2015. Cultural implications of late Holocene climate change in the Cuenca Oriental, Mexico. Proceedings of the National Academy of Sciences of the United States of America 112, 1693-1698.

Bianchi, G.G., McCave, I.N., 1999. Holocene periodicity in North Atlantic climate and deep-ocean flow south of Iceland. Nature 397, 515-517.

Bird, B.W., Abbott, M.B., Rodbell, D.T., Vuille, M., 2011a. Holocene tropical South American hydroclimate revealed from a decadally resolved lake sediment delta O-18 record. Earth and Planetary Science Letters 310, 192-202.

Bird, B.W., Abbott, M.B., Vuille, M., Rodbell, D.T., Stansell, N.D., Rosenmeier, M.F., 2011b. A 2,300-year-long annually resolved record of the South American summer monsoon from the Peruvian Andes. Proceedings of the National Academy of Sciences of the United States of America 108, 8583-8588.

Blunier, T., Chappellaz, J., Schwander, J., Stauffer, B., Raynaud, D., 1995. Variations in atmospheric methane concentration during the Holocene epoch. Nature 374, 46-49.

Bond, G., Kromer, B., Beer, J., Muscheler, R., Evans, M.N., Showers, W., Hoffmann, S., Lotti-Bond, R., Hajdas, I., Bonani, G., 2001. Persistent solar influence on north Atlantic climate during the Holocene. Science 294, 2130-2136.

Bony, S., Colman, R., Kattsov, V.M., Allan, R.P., Bretherton, C.S., Dufresne, J.-L., Hall, A., Hallegatte, S., Holland, M.M., Ingram, W., Randall, D.A., Soden, B.J., Tselioudis, G., Webb, M.J., 2006. How well do we understand and evaluate climate change feedback processes? Journal of Climate 19, 3445-3482.

Booth, R.K., Jackson, S.T., Forman, S.L., Kutzbach, J.E., Bettis, E.A., Kreig, J., Wright, D.K., 2005. A severe centennial-scale drought in mid-continental North America 4200 years ago and apparent global linkages. Holocene 15, 321-328.

Braconnot, P., Harrison, S.P., Kageyama, M., Bartlein, P.J., Masson-Delmotte, V., Abe-Ouchi, A., Otto-Bliesner, B., Zhao, Y., 2012. Evaluation of climate models using palaeoclimatic data. Nature Climate Change 2, 417-424.

Briffa, K.R., Jones, P.D., Schweingruber, F.H., Osborn, T.J., 1998. Influence of volcanic eruptions on Northern Hemisphere summer temperature over the past 600 years. Nature 393, 450-455.

Bronk Ramsey, C., 2009. Bayesian analysis of radiocarbon dates. Radiocarbon 51, 337-360.

Buckley, B.M., Anchukaitis, K.J., Penny, D., Fletcher, R., Cook, E.R., Sano, M., Le, C.N., Wichienkeeo, A., Ton, T.M., Truong, M.H., 2010. Climate as a contributing factor in the demise of Angkor, Cambodia. Proceedings of the National Academy of Sciences of the United States of America 107, 6748-6752.

Cai, W.J., Borlace, S., Lengaigne, M., van Rensch, P., Collins, M., Vecchi, G., Timmermann, A., Santoso, A., McPhaden, M.J., Wu, L.X., England, M.H., Wang, G.J., Guilyardi, E., Jin, F.F., 2014. Increasing frequency of extreme El Nino events due to greenhouse warming. Nature Climate Change 4, 111-116.

Cane, M.A., 1998. Climate change - A role for the tropical Pacific. Science 282, 59-+.

Carton, J.A., Chepurin, G., Cao, X.H., 2000a. A Simple Ocean Data Assimilation analysis of the global upper ocean 1950-95. Part II: Results. Journal of Physical Oceanography 30, 311-326.

Carton, J.A., Chepurin, G., Cao, X.H., Giese, B., 2000b. A Simple Ocean Data Assimilation analysis of the global upper ocean 1950-95. Part I: Methodology. Journal of Physical Oceanography 30, 294-309.

Chalie, F., Gasse, F., 2002. Late Glacial-Holocene diatom record of water chemistry and lake level change from the tropical East African Rift Lake Abiyata (Ethiopia). Palaeogeography Palaeoclimatology Palaeoecology 187, 259-283.

Chappellaz, J., Blunier, T., Raynaud, D., Barnola, J.M., Schwander, J., Stauffer, B., 1993. Synchronous changes in atmospheric CH4 and Greenland climate between 40 kyr and 8 kyr BP. Nature 366, 443-445.

Cheng, H., Fleitmann, D., Edwards, R.L., Wang, X.F., Cruz, F.W., Auler, A.S., Mangini, A., Wang, Y.J., Kong, X.G., Burns, S.J., Matter, A., 2009. Timing and structure of the 8.2 kyr BP event inferred from delta O-18 records of stalagmites from China, Oman, and Brazil. Geology 37, 1007-1010.

Chiang, J.C.H., 2009. The Tropics in Paleoclimate. Annual Review of Earth and Planetary Sciences 37, 263-297.

Chiang, J.C.H., Bitz, C.M., 2005. Influence of high latitude ice cover on the marine Intertropical Convergence Zone. Climate Dynamics 25, 477-496.

Choi, K.Y., Vecchi, G.A., Wittenberg, A.T., 2013. ENSO Transition, Duration, and Amplitude Asymmetries: Role of the Nonlinear Wind Stress Coupling in a Conceptual Model. Journal of Climate 26, 9462-9476.

Clarke, A.J., Van Gorder, S., Colantuono, G., 2007. Wind stress curl and ENSO discharge/recharge in the equatorial Pacific. Journal of Physical Oceanography 37, 1077-1091.

Clement, A.C., Seager, R., Cane, M.A., Zebiak, S.E., 1996. An ocean dynamical thermostat. Journal of Climate 9, 2190-2196.

Cobb, K.M., Charles, C.D., Cheng, H., Edwards, R.L., 2003. El Nino/Southern Oscillation and tropical Pacific climate during the last millennium. Nature 424, 271-276.

Cobb, K.M., Westphal, N., Sayani, H.R., Watson, J.T., Di Lorenzo, E., Cheng, H., Edwards, R.L., Charles, C.D., 2013. Highly Variable El Nino-Southern Oscillation Throughout the Holocene. Science 339, 67-70.

Colinvaux, P.A., 1968. Reconnaissance and chemistry of lakes and bogs of Galápagos Islands. Nature 219, 590-594.

Collins, M., An, S.I., Cai, W.J., Ganachaud, A., Guilyardi, E., Jin, F.F., Jochum, M., Lengaigne, M., Power, S., Timmermann, A., Vecchi, G., Wittenberg, A., 2010. The impact of global warming on the tropical Pacific ocean and El Nino. Nature Geoscience 3, 391-397.

Collins, M., Tett, S.F.B., Cooper, C., 2001. The internal climate variability of HadCM3, a version of the Hadley Centre coupled model withou flux adjustments. Climate Dynamics 17, 61-81.

Conroy, J.L., Overpeck, J.T., Cole, J.E., Shanahan, T.M., Steinitz-Kannan, M., 2008. Holocene changes in eastern tropical Pacific climate inferred from a Galapagos lake sediment record. Quat. Sci. Rev. 27, 1166-1180.

Cosford, J., Qing, H.R., Eglington, B., Mattey, D., Yuan, D.X., Zhang, M.L., Cheng, H., 2008. East Asian monsoon variability since the Mid-Holocene recorded in a high-resolution, absolute-dated aragonite speleothem from eastern China. Earth and Planetary Science Letters 275, 296-307.

Cózar, A., Bruno, M., Bergamino, N., Ubeda, B., Bracchini, L., Dattilo, A.M., Loiselle, S.A., 2012. Basin-scale control on the phytoplankton biomass in Lake Victoria, Africa. PLOS ONE 7, e29962.

Craig, H., 1961. Isotopic variations in meteoric waters. Science 133, 1702-&.

Crowley, T.J., 2000. Causes of climate change over the past 1000 years. Science 289, 270-277.

Crowley, T.J., Zielinski, G., Vinther, B., Udisti, R., Kreutz, K., Cole-Dai, J., Castellano, E., 2008. Volcanism and the Little Ice Age. PAGES Newsletter 16, 22-23.

Crucifix, M., 2006. Does the Last Glacial Maximum constrain climate sensitivity? Geophysical Research Letters 33, L18701.

Cunningham, L.K., Austin, W.E.N., Knudsen, K.L., Eiriksson, J., Scourse, J.D., Wanamaker, A.D., Butler, P.G., Cage, A.G., Richter, T., Husum, K., Hald, M., Andersson, C., Zorita, E., Linderholm, H.W., Gunnarson, B.E., Sicre, M.A., Sejrup, H.P., Jiang, H., Wilson, R.J.S., 2013. Reconstructions of surface ocean conditions from the northeast Atlantic and Nordic seas during the last millennium. Holocene 23, 921-935.

Curtis, J.H., Hodell, D.A., Brenner, M., 1996. Climate variability on the Yucatan Peninsula (Mexico) during the past 3500 years, and implications for Maya Cultural Evolution. Quaternary Research 46, 37-47.

Daley, T.J., Thomas, E.R., Holmes, J.A., Street-Perrott, F.A., Chapman, M.R., Tindall, J.C., Valdes, P.J., Loader, N.J., Marshall, J.D., Wolff, E.W., Hopley, P.J., Atkinson, T., Barber, K.E., Fisher, E.H., Robertson, I., Hughes, P.D.M., Roberts, C.N., 2011. The 8200 yr BP cold event in stable isotope records from the North Atlantic region. Global and Planetary Change 79, 288-302.

Dansgaard, W., 1964. Stable isotopes in precipitation. Tellus 16, 436-468.

de Szoeke, S.P., Fairall, C.W., Wolfe, D.E., Bariteau, L., Zuidema, P., 2010. Surface Flux Observations on the Southeastern Tropical Pacific Ocean and Attribution of SST Errors in Coupled Ocean-Atmosphere Models. Journal of Climate 23, 4152-4174.

Delworth, T.L., Broccoli, A.J., Rosati, A., Stouffer, R.J., Balaji, V., Beesley, J.A., Cooke, W.F., Dixon, K.W., Dunne, J., Dunne, K.A., Durachta, J.W., Findell, K.L., Ginoux, P., Gnanadesikan, A., Gordon, C.T., Griffies, S.M., Gudgel, R., Harrison, M.J., Held, I.M., Hemler, R.S., Horowitz, L.W., Klein, S.A., Knutson, T.R., Kushner, P.J., Langenhorst, A.R., Lee, H.C., Lin, S.J., Lu, J., Malyshev, S.L., Milly, P.C.D., Ramaswamy, V., Russell, J., Schwarzkopf, M.D., Shevliakova, E., Sirutis, J.J., Spelman, M.J., Stern, W.F., Winton, M., Wittenberg, A.T., Wyman, B., Zeng, F., Zhang, R., 2006. GFDL's CM2 global coupled climate models. Part I: Formulation and simulation characteristics. Journal of Climate 19, 643-674.

deMenocal, P., Ortiz, J., Guilderson, T., Adkins, J., Sarnthein, M., Baker, L., Yarusinsky, M., 2000. Abrupt onset and termination of the African Humid Period: rapid climate responses to gradual insolation forcing. Quat. Sci. Rev. 19, 347-361.

Deser, C., Phillips, A.S., Tomas, R.A., Okumura, Y.M., Alexander, M.A., Capotondi, A., Scott, J.D., Kwon, Y.O., Ohba, M., 2012. ENSO and Pacific Decadal Variability in the Community Climate System Model Version 4. Journal of Climate 25, 2622-2651.

Dewitte, R., 2000. Sensitivity of an intermediate ocean-atmosphere coupled model of the tropical Pacific to its oceanic vertical structure. Journal of Climate 13, 2363-2388.

Diaz, H.F., Trigo, R., Hughes, M.K., Mann, M.E., Xoplaki, E., Barriopedro, D., 2011. Spatial and temporal characteristics of climate in Medieval times revisited. Bulletin of the American Meteorological Society 92, 1487-1500.

DiNezio, P.N., Kirtman, B.P., Clement, A.C., Lee, S.K., Vecchi, G.A., Wittenberg, A., 2012. Mean Climate Controls on the Simulated Response of ENSO to Increasing Greenhouse Gases. Journal of Climate 25, 7399-7420.

Domingues, R.B., Anselmo, T.P., Barbosa, A.B., Sommer, U., Galvao, H.M., 2011. Nutrient limitation of phytoplankton growth in the freshwater tidal zone of a turbid, Mediterranean estuary. Estuarine, Coastal and Shelf Science 91, 282-297.

Donders, T.H., Wagner-Cremer, F., Visscher, H., 2008. Integration of proxy data and model scenarios for the mid-Holocene onset of modern ENSO variability. Quat. Sci. Rev. 27, 571-579.

Dong, B., Sutton, R.T., 2007. Enhancement of ENSO variability by a weakened Atlantic thermohaline circulation in a coupled GCM. Journal of Climate 20, 4920-4939.

Donohoe, A., Marshall, J., Ferreira, D., McGee, D., 2013. The Relationship between ITCZ Location and Cross-Equatorial Atmospheric Heat Transport: From the Seasonal Cycle to the Last Glacial Maximum. Journal of Climate 26, 3597-3618.

Driscoll, S., Bozzo, A., Gray, L.J., Robock, A., Stenchikov, G., 2012. Coupled Model Intercomparison Project 5 (CMIP5) simulations of climate following volcanic eruptions. Journal of Geophysical Research-Atmospheres 117, D17105.

Dufresne, J.L., Foujols, M.A., Denvil, S., Caubel, A., Marti, O., Aumont, O., Balkanski, Y., Bekki, S., Bellenger, H., Benshila, R., Bony, S., Bopp, L., Braconnot, P., Brockmann, P.,

Cadule, P., Cheruy, F., Codron, F., Cozic, A., Cugnet, D., de Noblet, N., Duvel, J.P., Ethe, C., Fairhead, L., Fichefet, T., Flavoni, S., Friedlingstein, P., Grandpeix, J.Y., Guez, L., Guilyardi, E., Hauglustaine, D., Hourdin, F., Idelkadi, A., Ghattas, J., Joussaume, S., Kageyama, M., Krinner, G., Labetoulle, S., Lahellec, A., Lefebvre, M.P., Lefevre, F., Levy, C., Li, Z.X., Lloyd, J., Lott, F., Madec, G., Mancip, M., Marchand, M., Masson, S., Meurdesoif, Y., Mignot, J., Musat, I., Parouty, S., Polcher, J., Rio, C., Schulz, M., Swingedouw, D., Szopa, S., Talandier, C., Terray, P., Viovy, N., Vuichard, N., 2013. Climate change projections using the IPSL-CM5 Earth System Model: from CMIP3 to CMIP5. Climate Dynamics 40, 2123-2165.

Ellison, C.R.W., Chapman, M.R., Hall, I.R., 2006. Surface and deep ocean interactions during the cold climate event 8200 years ago. Science 312, 1929-1932.

Emile-Geay, J., Cobb, K.M., Mann, M.E., Wittenberg, A.T., 2013. Estimating Central Equatorial Pacific SST Variability over the Past Millennium. Part II: Reconstructions and Implications. Journal of Climate 26, 2329-2352.

Englebrecht, A.C., Sachs, J.P., 2005. Determination of sediment provenance at drift sites using hydrogen isotopes and unsaturation ratios in alkenones. Geochimica Et Cosmochimica Acta 69, 4253-4265.

Fedorov, A.V., Philander, S.G., 2001. A stability analysis of tropical ocean-atmosphere interactions: Bridging measurements and theory for El Nino. Journal of Climate 14, 3086-3101.

Feldl, N., Roe, G.H., 2013. Four perspectives on climate feedbacks. Geophysical Research Letters 40, 4007-4011.

Feng, S., Oglesby, R.J., Rowe, C.M., Loope, D.B., Hu, Q., 2008. Atlantic and Pacific SST influences on Medieval drought in North America simulated by the Community Atmospheric Model. Journal of Geophysical Research-Atmospheres 113.

Fernandez-Donado, L., Gonzalez-Rouco, J.F., Raible, C.C., Ammann, C.M., Barriopedro, D., Garcia-Bustamante, E., Jungclaus, J.H., Lorenz, S.J., Luterbacher, J., Phipps, S.J., Servonnat, J., Swingedouw, D., Tett, S.F.B., Wagner, S., Yiou, P., Zorita, E., 2013. Large-scale temperature response to external forcing in simulations and reconstructions of the last millennium. Climate of the Past 9, 393-421.

Ferreira, A.M., Miranda, A., Caetano, M., Baas, M., Vale, C., Sinninghe Damsté, J.S., 2001. Formation of mid-chain alkane keto-ols by post-depositional oxidation of mid-chain diols in Mediterranean sapropels. Organic Geochemistry Organic Geochemistry 32, 271-276.

Ferrington, L.C., Pehofer, H.E., 1996. Instar distribution and biomass of Chironomidae larvae in Lago El Junco, Isla San Cristobal, the Galápagos. Hydrobiologia 318, 123-133.

Flato, G., J. Marotzke, B. Abiodun, P. Braconnot, S.C. Chou, W. Collins, P. Cox, F. Driouech, S. Emori, V. Eyring, C. Forest, P. Gleckler, E. Guilyardi, C. Jakob, V. Kattsov, C. Reason and M. Rummukainen, 2013. Evaluation of Climate Models. In: Climate Change 2013: The Physical Science Basis. Contribution of Working Group I to the Fifth Assess- ment Report of the Intergovernmental Panel on Climate Change [Stocker, T.F., D. Qin, G.-K. Plattner, M. Tignor, S.K. Allen, J. Boschung, A. Nauels, Y. Xia, V. Bex and P.M. Midgley (eds.)]. Cambridge University Press, Cambridge, United Kingdom and New York, NY, USA.

Fleitmann, D., Burns, S.J., Mangini, A., Mudelsee, M., Kramers, J., Villa, I., Neff, U., Al-Subbary, A.A., Buettner, A., Hippler, D., Matter, A., 2007. Holocene ITCZ and Indian monsoon dynamics recorded in stalagmites from Oman and Yemen (Socotra). Quat. Sci. Rev. 26, 170-188.

Fleitmann, D., Burns, S.J., Mudelsee, M., Neff, U., Kramers, J., Mangini, A., Matter, A., 2003. Holocene forcing of the Indian monsoon recorded in a stalagmite from Southern Oman. Science 300, 1737-1739.

Frank, D.C., Esper, J., Raible, C.C., Buentgen, U., Trouet, V., Stocker, B., Joos, F., 2010. Ensemble reconstruction constraints on the global carbon cycle sensitivity to climate. Nature 463, 527-532.

Frierson, D.M.W., Hwang, Y.T., 2012. Extratropical Influence on ITCZ Shifts in Slab Ocean Simulations of Global Warming. Journal of Climate 25, 720-733.

Galanti, E., Tziperman, E., Harrison, M., Rosati, A., Giering, R., Sirkes, Z., 2002. The equatorial thermocline outcroppin - A seasonal control on the tropical Pacific Ocean-atmosphere instability strength. Journal of Climate 15, 2721-2739.

Gao, C., Robock, A., Ammann, C., 2008. Volcanic forcing of climate over the past 1500 years: An improved ice core-based index for climate models. Journal of Geophysical Research-Atmospheres 113, D231111.

Gasse, F., 2000. Hydrological changes in the African tropics since the Last Glacial Maximum. Quat. Sci. Rev. 19, 189-211.

Gent, P.R., Danabasoglu, G., Donner, L.J., Holland, M.M., Hunke, E.C., Jayne, S.R., Lawrence, D.M., Neale, R.B., Rasch, P.J., Vertenstein, M., Worley, P.H., Yang, Z.-L., Zhang, M., 2011. The Community Climate System Model Version 4. Journal of Climate 24, 4973-4991.

Gerber, S., Joos, F., Brugger, P., Stocker, T.F., Mann, M.E., Sitch, S., Scholze, M., 2003. Constraining temperature variations over the last millennium by comparing simulated and observed atmospheric CO2. Climate Dynamics 20, 281-299.

Gibbs, H.L., Latta, S.C., Gibbs, J.P., 1987. Effects of the 1982-83 El Niño on Blue-Footed and Masked Booby populations on Isla Daphne Major, Galápagos. Condor 89, 440-442.

Graham, N.E., Ammann, C.M., Fleitmann, D., Cobb, K.M., Luterbacher, J., 2011. Support for global climate reorganization during the "Medieval Climate Anomaly". Climate Dynamics 37, 1217-1245.

Guilyardi, E., Bellenger, H., Collins, M., Ferrett, S., Cai, W., Wittenberg, A., 2012a. A first look at ENSO in CMIP5. Clivar Exchanges 58, 29-32.

Guilyardi, E., Cai, W.J., Collins, M., Fedorov, A., Jin, F.F., Kumar, A., Sun, D.Z., Wittenberg, A., 2012b. New strategies for evaluating ENSO processes in climate models. Bulletin of the American Meteorological Society 93, 235-238.

Guilyardi, E., Wittenberg, A., Fedorov, A., Collins, M., Wang, C., Capotondi, A., van Oldenborgh, J., Stockdale, T., 2009. Understanding El Nino in Ocean-Atmosphere General Circulation Models. Bulletin of the American Meteorological Society 90, 325-340.

Gupta, A.K., Das, M., Anderson, D.M., 2005. Solar influence on the Indian summer monsoon during the Holocene. Geophysical Research Letters 32.

Ham, Y.G., Kug, J.S., Kim, D., Kim, Y.H., Kim, D.H., 2013. What controls phase-locking of ENSO to boreal winter in coupled GCMs? Climate Dynamics 40, 1551-1568.

Haug, G.H., Gunther, D., Peterson, L.C., Sigman, D.M., Hughen, K.A., Aeschlimann, B., 2003. Climate and the collapse of Maya civilization. Science 299, 1731-1735.

Haug, G.H., Hughen, K.A., Sigman, D.M., Peterson, L.C., Rohl, U., 2001. Southward migration of the intertropical convergence zone through the Holocene. Science 293, 1304-1308.

Hegerl, G.C., Crowley, T.J., Allen, M., Hyde, W.T., Pollack, H.N., Smerdon, J., Zorita, E., 2007. Detection of human influence on a new, validated 1500-year temperature reconstruction. Journal of Climate 20, 650-666.

Hegerl, G.C., Crowley, T.J., Baum, S.K., Kim, K.Y., Hyde, W.T., 2003. Detection of volcanic, solar and greenhouse gas signals in paleo-reconstructions of Northern Hemispheric temperature. Geophysical Research Letters 30.

Hirst, A.C., 1986. Unstable and damped equatorial modes in simple coupled ocean-atmosphere models. Journal of the Atmospheric Sciences 43, 606-630.

Hodell, D.A., Brenner, M., Curtis, J.H., 2005. Terminal Classic drought in the northern Maya lowlands inferred from multiple sediment cores in Lake Chichancanab (Mexico). Quat. Sci. Rev. 24, 1413-1427.

Hodell, D.A., Brenner, M., Curtis, J.H., Guilderson, T., 2001. Solar forcing of drought frequency in the Maya lowlands. Science 292, 1367-1370.

Hoffman, J.S., Carlson, A.E., Winsor, K., Klinkhammer, G.P., LeGrande, A.N., Andrews, J.T., Strasser, J.C., 2012. Linking the 8.2 ka event and its freshwater forcing in the Labrador Sea. Geophysical Research Letters 39.

Hong, Y.T., Hong, B., Lin, Q.H., Zhu, Y.X., Shibata, Y., Hirota, M., Uchida, M., Leng, X.T., Jiang, H.B., Xu, H., Wang, H., Yi, L., 2003. Correlation between Indian Ocean summer monsoon and North Atlantic climate during the Holocene. Earth and Planetary Science Letters 211, 371-380.

Horita, J., Rozanski, K., Cohen, S., 2008. Isotope effects in the evaporation of water: a status report of the Craig-Gordon model. Isotopes in Environmental and Health Studies 44, 23-49.

Huang, Y.S., Shuman, B., Wang, Y., Webb, T., 2004. Hydrogen isotope ratios of individual lipids in lake sediments as novel tracers of climatic and environmental change: a surface sediment test. Journal of Paleolimnology 31, 363-375.

Hughen, K.A., Overpeck, J.T., Peterson, L.C., Trumbore, S., 1996. Rapid climate changes in the tropical Atlantic region during the last deglaciation. Nature 380, 51-54.

Huszar, V., Kruk, C., Caraco, N., 2003. Steady-state assemblages of phytoplankton in four temperate lakes (NE USA). Hydrobiologia 502, 97-109.

Huszar, V.L.D., Caraco, N.F., 1998. The relationship between phytoplankton composition and physical-chemical variables: a comparison of taxonomic and morphological-functional descriptors in six temperate lakes. Freshw. Biol. 40, 679-696.

Hwang, Y.T., Frierson, D.M.W., Kang, S.M., 2013. Anthropogenic sulfate aerosol and the southward shift of tropical precipitation in the late 20th century. Geophysical Research Letters 40, 1-6.

Itambi, A.C., Von Dobeneck, T., Adegbie, A.T., 2010. Millennial-scale precipitation changes over Central Africa during the late Quaternary and Holocene: evidence in sediments from the Gulf of Guinea. Journal of Quaternary Science 25, 267-279.

Jones, P.D., Briffa, K.R., Barnett, T.P., Tett, S.F.B., 1998. High-resolution palaeoclimatic records for the last millennium: interpretation, integration and comparison with General Circulation Model control-run temperatures. Holocene 8, 455-471.

Joos, F., Spahni, R., 2008. Rates of change in natural and anthropogenic radiative forcing over the past 20,000 years. Proceedings of the National Academy of Sciences of the United States of America 105, 1425-1430.

Kalnay, E., Kanamitsu, M., Kistler, R., Collins, W., Deaven, D., Gandin, L., Iredell, M., Saha, S., White, G., Woollen, J., Zhu, Y., Chelliah, M., Ebisuzaki, W., Higgins, W., Janowiak, J., Mo, K.C., Ropelewski, C., Wang, J., Leetmaa, A., Reynolds, R., Jenne, R., Joseph, D., 1996. The NCEP/NCAR 40-year reanalysis project. Bulletin of the American Meteorological Society 77, 437-471.

Kang, S.M., Frierson, D.M.W., Held, I.M., 2009. The Tropical Response to Extratropical Thermal Forcing in an Idealized GCM: The Importance of Radiative Feedbacks and Convective Parameterization. Journal of the Atmospheric Sciences 66, 2812-2827.

Kang, S.M., Held, I.M., Frierson, D.M.W., Zhao, M., 2008. The response of the ITCZ to extratropical thermal forcing: Idealized slab-ocean experiments with a GCM. Journal of Climate 21, 3521-3532.

Karamperidou, C., Cane, M.A., Lall, U., Wittenberg, A.T., 2014. Intrinsic modulation of ENSO predictability viewed through a local Lyapunov lens. Climate Dynamics 42, 253-270.

Kaufman, D.S., Schneider, D.P., McKay, N.P., Ammann, C.M., Bradley, R.S., Briffa, K.R., Miller, G.H., Otto-Bliesner, B.L., Overpeck, J.T., Vinther, B.M., Arctic Lakes 2k Project Members, 2009. Recent Warming Reverses Long-Term Arctic Cooling. Science 325, 1236-1239.

Kebede, E., Belay, A., 1994. Species composition and phytoplankton biomass in a tropical African lake (Lake Awassa, Ethiopia). Hydrobiologia 288, 13-32.

Keigwin, L.D., 1996. The Little Ice Age and Medieval warm period in the Sargasso Sea. Science 274, 1504-1508.

Kleiven, H.F., Kissel, C., Laj, C., Ninnemann, U.S., Richter, T.O., Cortijo, E., 2008. Reduced North Atlantic Deep Water coeval with the glacial Lake Agassiz freshwater outburst. Science 319, 60-64.

Kobashi, T., Kawamura, K., Severinghaus, J.P., Barnola, J.-M., Nakaegawa, T., Vinther, B.M., Johnsen, S.J., Box, J.E., 2011. High variability of Greenland surface temperature over the past 4000 years estimated from trapped air in an ice core. Geophysical Research Letters 38.

Kobashi, T., Severinghaus, J.P., Brook, E.J., Barnola, J.M., Grachev, A.M., 2007. Precise timing and characterization of abrupt climate change 8200 years ago from air trapped in polar ice. Quat. Sci. Rev. 26, 1212-1222.

Koutavas, A., Demenocal, P.B., Olive, G.C., Lynch-Stieglitz, J., 2006. Mid-Holocene El Nino-Southern Oscillation (ENSO) attenuation revealed by individual foraminifera in eastern tropical Pacific sediments. Geology 34, 993-996.

Koutavas, A., Joanides, S., 2012. El Nino-Southern Oscillation extrema in the Holocene and Last Glacial Maximum. Paleoceanography 27.

Lacagnina, C., Selten, F., Siebesma, A.P., 2014. Impact of changes in the formulation of cloud-related processes on model biases and climate feedbacks. Journal of Advances in Modeling Earth Systems 6, 1224-1243.

Lachniet, M.S., Asmerom, Y., Burns, S.J., Patterson, W.P., Polyak, V.J., Seltzer, G.O., 2004. Tropical response to the 8200 yr BP cold event? Speleothem isotopes indicate a weakened early Holocene monsoon in Costa Rica. Geology 32, 957-960.

Lamb, H.H., 1965. The early medieval warm epoch and its sequal. Palaeogeography Palaeoclimatology Palaeoecology 1, 13-37.

Landrum, L., Otto-Bliesner, B.L., Wahl, E.R., Conley, A., Lawrence, P.J., Rosenbloom, N., Teng, H., 2013. Last Millennium Climate and Its Variability in CCSM4. Journal of Climate 26, 1085-1111.

Larsen, D.J., Miller, G.H., Geirsdottir, A., Thordarson, T., 2011. A 3000-year varved record of glacier activity and climate change from the proglacial lake Hvitarvatn, Iceland. Quat. Sci. Rev. 30, 2715-2731.

Lea, D.W., Pak, D.K., Peterson, L.C., Hughen, K.A., 2003. Synchroneity of tropical and high-latitude Atlantic temperatures over the last glacial termination. Science 301, 1361-1364.

Lean, J., Rind, D., 1999. Evaluating sun-climate relationships since the Little Ice Age. Journal of Atmospheric and Solar-Terrestrial Physics 61, 25-36.

LeGrande, A.N., Schmidt, G.A., Shindell, D.T., Field, C.V., Miller, R.L., Koch, D.M., Faluvegi, G., Hoffmann, G., 2006. Consistent simulations of multiple proxy responses to an abrupt climate change event. Proceedings of the National Academy of Sciences of the United States of America 103, 837-842.

Lehner, F., Born, A., Raible, C.C., Stocker, T.F., 2013. Amplified Inception of European Little Ice Age by Sea Ice-Ocean-Atmosphere Feedbacks. Journal of Climate 26, 7586-7602.

Leuenberger, M.C., Lang, C., Schwander, J., 1999. Delta(15)N measurements as a calibration tool for the paleothermometer and gas-ice age differences: A case study for the 8200 BP event on GRIP ice. Journal of Geophysical Research-Atmospheres 104, 22163-22170.

Lewis, C.F.M., Miller, A.A.L., Levac, E., Piper, D.J.W., Sonnichsen, G.V., 2012. Lake Agassiz outburst age and routing by Labrador Current and the 8.2 cal ka cold event. Quaternary International 260, 83-97.

Lewis Jr., W.M., 1983. Temperature, heat, and mixing in Lake Valencia, Venezuela. . Limnology and Oceanography 28, 273-286.

Li, J.L.F., Lee, W.L., Waliser, D.E., Stachnik, J.P., Fetzer, E., Wong, S., Yue, Q., 2014. Characterizing tropical Pacific water vapor and radiative biases in CMIP5 GCMs: Observation-based analyses and a snow and radiation interaction sensitivity experiment. Journal of Geophysical Research-Atmospheres 119, 10981-10995.

Lin, J.L., Qian, T.T., Shinoda, T., 2014. Stratocumulus Clouds in Southeastern Pacific Simulated by Eight CMIP5-CFMIP Global Climate Models. Journal of Climate 27, 3000-3022.

Liu, F.G., Feng, Z.D., 2012. A dramatic climatic transition at ~4000 cal. yr BP and its cultural responses in Chinese cultural domains. Holocene 22, 1181-1197.

Liu, Z.Y., Zhu, J., Rosenthal, Y., Zhang, X., Otto-Bliesner, B.L., Timmermann, A., Smith, R.S., Lohmann, G., Zheng, W.P., Timm, O.E., 2014. The Holocene temperature conundrum. Proceedings of the National Academy of Sciences of the United States of America 111, E3501-E3505.

Loulergue, L., Schilt, A., Spahni, R., Masson-Delmotte, V., Blunier, T., Lemieux, B., Barnola, J.M., Raynaud, D., Stocker, T.F., Chappellaz, J., 2008. Orbital and millennial-scale features of atmospheric CH4 over the past 800,000 years. Nature 453, 383-386.

Magny, M., Haas, J.N., 2004. A major widespread climatic change around 5300 cal. yr BP at the time of the Alpine Iceman. Journal of Quaternary Science 19, 423-430.

Magyari, E., Buczko, K., Jakab, G., Braun, M., Pal, Z., Karatson, D., Pap, I., 2009. Palaeolimnology of the last crater lake in the Eastern Carpathian Mountains: a multiproxy study of Holocene hydrological changes. Hydrobiologia 631, 29-63.

Majoube, M., 1971. Fractionnement en oxygen 18 et en deuterium entre l'eau et sa vapeur. Journal de Chemise et de Physique 68, 1423-1436.

Mann, M.E., Bradley, R.S., Hughes, M.K., 1998. Global-scale temperature patterns and climate forcing over the past six centuries. Nature 392, 779-787.

Mann, M.E., Fuentes, J.D., Rutherford, S., 2012. Underestimation of volcanic cooling in tree-ring-based reconstructions of hemispheric temperatures. Nature Geoscience 5, 202-205.

Mann, M.E., Zhang, Z.H., Rutherford, S., Bradley, R.S., Hughes, M.K., Shindell, D., Ammann, C., Faluvegi, G., Ni, F.B., 2009. Global Signatures and Dynamical Origins of the Little Ice Age and Medieval Climate Anomaly. Science 326, 1256-1260.

Manny, B.A., Johnson, W.C., Wetzel, R.G., 1994. Nutrient additions by waterfowl to lakes and reservoirs- predicting their effects on productivity and water quality. Hydrobiologia 279, 121-132.

Marcott, S.A., Shakun, J.D., 2015. Holocene climate change and its context for the future. PAGES Magazine Workshop Report 23, 28.

Marcott, S.A., Shakun, J.D., Clark, P.U., Mix, A.C., 2013. A Reconstruction of Regional and Global Temperature for the Past 11,300 Years. Science 339, 1198-1201.

Marion, L., Clergeau, P., Brient, L., Bertru, G., 1994. The importance of avian-contributed nitrogen (N) and phosphorus (P) to Lake Grand-Lieu, France. Hydrobiologia 279, 133-147.

Masse, G., Rowland, S.J., Sicre, M.A., Jacob, J., Jansen, E., Belt, S.T., 2008. Abrupt climate changes for Iceland during the last millennium: Evidence from high resolution sea ice reconstructions. Earth and Planetary Science Letters 269, 564-568.

Masson-Delmotte, V., M. Schulz, A. Abe-Ouchi, J. Beer, A. Ganopolski, J.F. González Rouco, E. Jansen, K. Lambeck, J. Luterbacher, T. Naish, T. Osborn, B. Otto-Bliesner, T. Quinn, R. Ramesh, M. Rojas, X. Shao and A. Timmermann, 2013. Information from Paleoclimate Archives. In: Climate Change 2013: The Physical Science Basis. Contribution of Working Group I to the Fifth Assessment Report of the Intergovernmental Panel on Climate Change [Stocker, T.F., D. Qin, G.-K. Plattner, M. Tignor, S.K. Allen, J. Boschung, A. Nauels, Y. Xia, V. Bex and P.M. Midgley (eds.)] Cambridge University Press, Cambridge, United Kingdom and New York, NY, USA.

Mayewski, P.A., Maasch, K.A., 2006. Recent warming inconsistent with natural association between temperature and atmospheric circulation over the last 2000 years. Climate of the Past Discussions 2, 327-355.

Mayewski, P.A., Rohling, E.E., Stager, J.C., Karlen, W., Maasch, K.A., Meeker, L.D., Meyerson, E.A., Gasse, F., van Kreveld, S., Holmgren, K., Lee-Thorp, J., Rosqvist, G., Rack, F., Staubwasser, M., Schneider, R.R., Steig, E.J., 2004. Holocene climate variability. Quaternary Research 62, 243-255.

Méjanelle, L., Sanchez-Gargallo, A., Bentaleb, I., Grimalt, J.O., 2003. Long chain *n*-alkyl diols, hydroxy ketones and sterols in a marine eustigmatophyte, *Nannochloropsis gaditana*, and in *Brachionus plicatilis* feeding on the algae. Organic Geochemistry 34, 527-538.

Metzger, P., Berkaloff, C., Casadevall, E., Coute, A., 1985. Alkadiene- and botryoccocene-producing races of wild strains of Botryococcus braunii. Phytochemistry 24, 2305-2312.

Mignot, J., Frankignoul, C., 2005. The variability of the Atlantic meridional overturning circulation, the North Atlantic Oscillation, and the El Nino-Southern Oscillation in the Bergen Climate Model. Journal of Climate 18, 2361-2375.

Miller, G.H., Geirsdottir, A., Zhong, Y.F., Larsen, D.J., Otto-Bliesner, B.L., Holland, M.M., Bailey, D.A., Refsnider, K.A., Lehman, S.J., Southon, J.R., Anderson, C., Bjornsson, H., Thordarson, T., 2012. Abrupt onset of the Little Ice Age triggered by volcanism and sustained by sea-ice/ocean feedbacks. Geophysical Research Letters 39, 5.

Mitsch, W.J., Nahlik, A., Wolski, P., Bernal, B., Zhang, L., Ramberg, L., 2010. Tropical wetlands: seasonal hydrologic pulsing, carbon sequestration, and methane emissions. Wetlands Ecology and Management 18, 573-586.

Moberg, A., Sonechkin, D.M., Holmgren, K., Datsenko, N.M., Karlen, W., 2005. Highly variable Northern Hemisphere temperatures reconstructed from low- and high-resolution proxy data. Nature 433, 613-617.

Morrill, C., Anderson, D.M., Bauer, B.A., Buckner, R., Gille, E.P., Gross, W.S., Hartman, M., Shah, A., 2013. Proxy benchmarks for intercomparison of 8.2 ka simulations. Climate of the Past 9, 423-432.

Morrill, C., Jacobsen, R.M., 2005. How widespread were climate anomalies 8200 years ago? Geophysical Research Letters 32.

Moy, C.M., Seltzer, G.O., Rodbell, D.T., Anderson, D.M., 2002. Variability of El Nino/Southern Oscillation activity at millennial timescales during the Holocene epoch. Nature 420, 162-165.

Murphy, B.F., Ye, H., Delage, F., 2015. Impacts of variations in the strength and structure of El Nino events on Pacific rainfall in CMIP5 models. Climate Dynamics 44, 3171-3186.

Myhre, G., Highwood, E.J., Shine, K.P., Stordal, F., 1998. New estimates of radiative forcing due to well mixed greenhouse gases. Geophysical Research Letters 25, 2715-2718.

Ndebele-Murisa, M.R., Musil, C.F., Raitt, L., 2010. A review of phytoplankton dynamics in tropical African lakes. . South African Journal of Science 106, 13-18.

Neukom, R., Gergis, J., Karoly, D.J., Wanner, H., Curran, M., Elbert, J., Gonzalez-Rouco, F., Linsley, B.K., Moy, A.D., Mundo, I., Raible, C.C., Steig, E.J., van Ommen, T., Vance, T., Villalba, R., Zinke, J., Frank, D., 2014. Inter-hemispheric temperature variability over the past millennium. Nature Climate Change 4, 362-367.

Newton, A., Thunell, R., Stott, L., 2006. Climate and hydrographic variability in the Indo-Pacific Warm Pool during the last millennium. Geophysical Research Letters 33, L19710.

North, G.R., Bell, T.L., Cahalan, R.F., Moeng, F.J., 1982. Sampling errors in the estimation of empirical orthogonal functions. Monthly Weather Review 110, 699-706.

Novello, V.F., Cruz, F.W., Karmann, I., Burns, S.J., Stirkis, N.M., Vuille, M., Cheng, H., Edwards, R.L., Santos, R.V., Frigo, E., Barreto, E.A.S., 2012. Multidecadal climate variability in Brazil's Nordeste during the last 3000 years based on speleothem isotope records. Geophysical Research Letters 39.

O'Brien, S.R., Mayewski, P.A., Meeker, L.D., Meese, D.A., Twickler, M.S., Whitlow, S.I., 1995. Complexity of Holocene climate as reconstructed from a Greenland ice core. Science 270, 1962-1964.

O'Reilly, C.M., Alin, S.R., Plisnier, P.-D., Cohen, A.S., McKee, B.A., 2003. Climate change decreases aquatic ecosystem productivity of Lake Tanganyika, Africa. . Nature 424, 766-768.

Ogata, T., Xie, S.P., Wittenberg, A., Sun, D.Z., 2013. Interdecadal Amplitude Modulation of El Nino-Southern Oscillation and Its Impact on Tropical Pacific Decadal Variability. Journal of Climate 26, 7280-7297.

Ogilvie, A.E.J., Jonsson, T., 2001. "Little Ice Age" research: A perspective from Iceland. Climatic Change 48, 9-52.

Oppo, D.W., McManus, J.F., Cullen, J.L., 2003. Palaeo-oceanography: Deepwater variability in the Holocene epoch. Nature 422, 277-278.

Otto-Bliesner, B.L., Brady, E.C., 2010. The sensitivity of the climate response to the magnitude and location of freshwater forcing: last glacial maximum experiments. Quat. Sci. Rev. 29, 56-73.

PAGES 2k Consortium, 2013. Continental-scale temperature variability during the past two millennia. Nature Geoscience 6, 339-346.

Pahnke, K., Sachs, J.P., Keigwin, L., Timmermann, A., Xie, S.P., 2007. Eastern tropical Pacific hydrologic changes during the past 27,000 years from D/H ratios in alkenones. Paleoceanography 22.

Paillard, D., Labeyrie, L., Yiou, P., 1996. Macintosh Program Performs Time-Series Analysis. Eos Transactions, American Geophysical Union 77, 379.

Palastanga, V., van der Schrier, G., Weber, S.L., Kleinen, T., Briffa, K.R., Osborn, T.J., 2011. Atmosphere and ocean dynamics: contributors to the European Little Ice Age? Climate Dynamics 36, 973-987.

Partin, J.W., Cobb, K.M., Adkins, J.F., Clark, B., Fernandez, D.P., 2007. Millennial-scale trends in west Pacific warm pool hydrology since the Last Glacial Maximum. Nature 449, 452-U453.

Pausata, F.S.R., Battisti, D.S., Nisancioglu, K.H., Bitz, C.M., 2011. Chinese stalagmite delta O-18 controlled by changes in the Indian monsoon during a simulated Heinrich event. Nature Geoscience 4, 474-480.

Penland, C., Sardeshmukh, P.D., 1995. The optimal growth of tropical sea surface temperature anomalies. Journal of Climate 8, 1999-2024.

Phipps, S.J., Rotstayn, L.D., Gordon, H.B., Roberts, J.L., Hirst, A.C., Budd, W.F., 2012. The CSIRO Mk3L climate system model version 1.0-Part 2: Response to external forcings. Geoscientific Model Development 5, 649-682.

Pinilla, G.A., 2006. Vertical distribution of phytoplankton in a clear water lake of Colombian Amazon (Lake Boa, Middle Caqueta). Hydrobiologia 568, 79-90.

Pongratz, J., Reick, C., Raddatz, T., Claussen, M., 2008. A reconstruction of global agricultural areas and land cover for the last millennium. Global Biogeochemical Cycles 22, GB3018.

Pope, V.D., Gallani, M.L., Rowntree, P.R., Stratton, R.A., 2000. The impact of new physical parametrizations in the Hadley Centre climate model: HadAM3. Climate Dynamics 16, 123-146.

Prigent, C., Matthews, E., Aires, F., Rossow, W.B., 2001. Remote sensing of global wetland dynamics with multiple satellite data sets. Geophysical Research Letters 28, 4631-4634.

Pryet, A., Dominguez, C., Tomai, P.F., Chaumont, C., d'Ozouville, N., Villacis, M., Violette, S., 2012. Quantification of cloud water interception along the windward slope of Santa Cruz Island, Galápagos (Ecuador). Agricultural and Forest Meteorology 161, 94-106.

Rasmussen, T.L., Thomsen, E., 2014. Brine formation in relation to climate changes and ice retreat during the last 15,000 years in Storfjorden, Svalbard, 76-78 degrees N. Paleoceanography 29, 911-929.

Rasmusson, E.M., Carpenter, T.H., 1982. Variations in tropical sea surface temperature and surface wind fields associated with the Southern Oscillation/El Nino. Monthly Weather Review 110, 354-384.

Reichler, T., Kim, J., 2008. Uncertainties in the climate mean state of global observations, reanalyses, and the GFDL climate model. Journal of Geophysical Research-Atmospheres 113.

Riedinger, M.A., Steinitz-Kannan, M., Last, W.M., Brenner, M., 2002. A similar to 6100 C-14 yr record of El Nino activity from the Galapagos Islands. Journal of Paleolimnology 27, 1-7.

Risi, C., Bony, S., Vimeux, F., 2008. Influence of convective processes on the isotopic composition (delta O-18 and delta D) of precipitation and water vapor in the tropics: 2. Physical interpretation of the amount effect. Journal of Geophysical Research-Atmospheres 113.

Roberts, W., 2007. An Investigation into the Causes for the Reduction in the Variability of the El Niño-Southern Oscillation in the Early Holocene in a Global Climate Model. University of Washington, Seattle, WA, p. pp 145.

Roberts, W.H.G., Battisti, D.S., 2011. A new tool for evaluating the physics of coupled atmosphere-ocean variability in nature and in general circulation models. Climate Dynamics 36, 907-923.

Roberts, W.H.G., Battisti, D.S., Tudhope, A.W., 2014. ENSO in the Mid-Holocene according to CSM and HadCM3. Journal of Climate 27, 1223-1242.

Rohling, E.J., Palike, H., 2005. Centennial-scale climate cooling with a sudden cold event around 8,200 years ago. Nature 434, 975-979.

Rotstayn, L.D., Jeffrey, S.J., Collier, M.A., Dravitzki, S.M., Hirst, A.C., Syktus, J.I., Wong, K.K., 2012. Aerosol- and greenhouse gas-induced changes in summer rainfall and circulation in the Australasian region: a study using single-forcing climate simulations. Atmospheric Chemistry and Physics 12, 6377-6404.

Russell, J., Talbot, M.R., Haskell, B.J., 2003. Mid-holocene climate change in Lake Bosumtwi, Ghana. Quaternary Research 60, 133-141.

Russon, T., Tudhope, A.W., Hegerl, G.C., Schurer, A., Collins, M., 2014. Assessing the Significance of Changes in ENSO Amplitude Using Variance Metrics. Journal of Climate 27, 4911-4922.

Sachs, J.P., Sachse, D., Smittenberg, R.H., Zhang, Z.H., Battisti, D.S., Golubic, S., 2009. Southward movement of the Pacific intertropical convergence zone AD 1400-1850. Nature Geoscience 2, 519-525.

Sachs, J.P., Schwab, V.F., 2011. Hydrogen isotopes in dinosterol from the Chesapeake Bay estuary. . Geochimica et Cosmochimica Acta 75, 444-459.

Sachse, D., Billault, I., Bowen, G.J., Chikaraishi, Y., Dawson, T.E., Feakins, S.J., Freeman, K.H., Magill, C.R., McInerney, F.A., van der Meer, M.T.J., Polissar, P., Robins, R.J., Sachs, J.P., Schmidt, H.L., Sessions, A.L., White, J.W.C., West, J.B., Kahmen, A., 2012. Molecular paleohydrology: Interpreting the hydrogen- isotopic composition of lipid biomarkers from photosynthesizing organisms. Annual Review of Earth and Planetary Sciences 40, 221-249.

Sachse, D., Radke, J., Gleixner, G., 2004. Hydrogen isotope ratios of recent lacustrine sedimentary n-alkanes record modern climate variability. Geochimica Et Cosmochimica Acta 68, 4877-4889.

Sauer, P.E., Eglinton, T.I., Hayes, J.M., Schimmelmann, A., Sessions, A.L., 2001. Compound-specific D/H ratios of lipid biomarkers from sediments as a proxy for environmental and climatic conditions. Geochimica et Cosmochimica Acta 65, 213-222.

Schleussner, C.F., Feulner, G., 2013. A volcanically triggered regime shift in the subpolar North Atlantic Ocean as a possible origin of the Little Ice Age. Climate of the Past 9, 1321-1330.

Schmidt, G.A., Jungclaus, J.H., Ammann, C.M., Bard, E., Braconnot, P., Crowley, T.J., Delaygue, G., Joos, F., Krivova, N.A., Muscheler, R., Otto-Bliesner, B.L., Pongratz, J., Shindell, D.T., Solanki, S.K., Steinhilber, F., Vieira, L.E.A., 2011. Climate forcing reconstructions for use in PMIP simulations of the last millennium (v1.0). Geoscientific Model Development 4, 33-45.

Schmidt, G.A., Jungclaus, J.H., Ammann, C.M., Bard, E., Braconnot, P., Crowley, T.J., Delaygue, G., Joos, F., Krivova, N.A., Muscheler, R., Otto-Bliesner, B.L., Pongratz, J., Shindell, D.T., Solanki, S.K., Steinhilber, F., Vieira, L.E.A., 2012. Climate forcing reconstructions for use in PMIP simulations of the Last Millennium (v1.1). Geoscientific Model Development 5, 185-191.

Schmidt, G.A., Ruedy, R., Hansen, J.E., Aleinov, I., Bell, N., Bauer, M., Bauer, S., Cairns, B., Canuto, V., Cheng, Y., Del Genio, A., Faluvegi, G., Friend, A.D., Hall, T.M., Hu, Y., Kelley, M., Kiang, N.Y., Koch, D., Lacis, A.A., Lerner, J., Lo, K.K., Miller, R.L., Nazarenko, L., Oinas, V., Perlwitz, J., Perlwitz, J., Rind, D., Romanou, A., Russell, G.L., Sato, M., Shindell, D.T., Stone, P.H., Sun, S., Tausnev, N., Thresher, D., Yao, M.-S., 2006. Present-Day Atmospheric Simulations Using GISS ModelE: Comparison to In Situ, Satellite, and Reanalysis Data. Journal of Climate 19, 153-192.

Schmittner, A., Clement, A.C., 2002. Sensitivity of the thermohaline circulation to tropical and high latitude freshwater forcing during the last glacial-interglacial cycle. Paleoceanography 17.

Schouten, S., Ossebaar, J., Schreiber, K., Kienhuis, M.V.M., Langer, G., Benthien, A., Bijma, J., 2006. The effect of temperature, salinity and growth rate on the stable hydrogen isotopic composition of long chain alkenones produced by Emiliania huxleyi and Gephyrocapsa oceanica. Biogeosciences 3, 113-119.

Schurer, A.P., Hegerl, G.C., Mann, M.E., Tett, S.F.B., Phipps, S.J., 2013. Separating Forced from Chaotic Climate Variability over the Past Millennium. Journal of Climate 26, 6954-6973.

Schurer, A.P., Tett, S.F.B., Hegerl, G.C., 2014. Small influence of solar variability on climate over the past millennium. Nature Geoscience 7, 104-108.

Seager, R., Graham, N., Herweijer, C., Gordon, A.L., Kushnir, Y., Cook, E., 2007. Blueprints for Medieval hydroclimate. Quat. Sci. Rev. 26, 2322-2336.

Shanahan, T.M., Overpeck, J.T., Anchukaitis, K.J., Beck, J.W., Cole, J.E., Dettman, D.L., Peck, J.A., Scholz, C.A., King, J.W., 2009. Atlantic Forcing of Persistent Drought in West Africa. Science 324, 377-380.

Shanahan, T.M., Overpeck, J.T., Wheeler, C.W., Beek, J.W., Pigati, J.S., Talbot, M.R., Scholz, C.A., Peck, J., King, J.W., 2006. Paleoclimatic variations in West Africa from a record of late Pleistocene and Holocene lake level stands of Lake Bosumtwi, Ghana. Palaeogeography Palaeoclimatology Palaeoecology 242, 287-302.

Shapiro, A.I., Schmutz, W., Rozanov, E., Schoell, M., Haberreiter, M., Shapiro, A.V., Nyeki, S., 2011. A new approach to the long-term reconstruction of the solar irradiance leads to large historical solar forcing. Astronomy & Astrophysics 529, A67.

Shell, K.M., Kiehl, J.T., Shields, C.A., 2008. Using the radiative kernel technique to calculate climate feedbacks in NCAR's Community Atmospheric Model. Journal of Climate 21, 2269-2282.

Shindell, D.T., Faluvegi, G., Miller, R.L., Schmidt, G.A., Hansen, J.E., Sun, S., 2006. Solar and anthropogenic forcing of tropical hydrology. Geophysical Research Letters 33, L24706.

Sigl, M., McConnell, J.R., Toohey, M., Curran, M., Das, S.B., Edwards, R., Isaksson, E., Kawamura, K., Kipfstuhl, S., Krueger, K., Layman, L., Maselli, O.J., Motizuki, Y., Motoyama, H., Pasteris, D.R., Severi, M., 2014. Insights from Antarctica on volcanic forcing during the Common Era. Nature Climate Change 4, 693-697.

Sinha, A., Stott, L., Berkelhammer, M., Cheng, H., Edwards, R.L., Buckley, B., Aldenderfer, M., Mudelsee, M., 2011. A global context for megadroughts in monsoon Asia during the past millennium. Quat. Sci. Rev. 30, 47-62.

Smittenberg, R.H., Baas, M., Schouten, S., Damste, J.S.S., 2005. The demise of the alga Botryococcus braunii from a Norwegian fjord was due to early eutrophication. Holocene 15, 133-140.

Smittenberg, R.H., Saenger, C., Dawson, M.N., Sachs, J.P., 2011. Compound-specific D/H ratios of the marine lakes of Palau as proxies for West Pacific Warm Pool hydrologic variability. Quat. Sci. Rev. 30, 921-933.

Smol, J.P., Birks, J.B., Last, W.M., 2001. Tracking environmental change using lake sediments. Vol. 3. Terrestrial, Algal and Siliceous Indicators. Kluwer Academic Publishers, London.

Soden, B.J., Held, I.M., 2006. An assessment of climate feedbacks in coupled ocean-atmosphere models. Journal of Climate 19, 3354-3360.

Soden, B.J., Held, I.M., Colman, R., Shell, K.M., Kiehl, J.T., Shields, C.A., 2008. Quantifying climate feedbacks using radiative kernels. Journal of Climate 21, 3504-3520.

Souza, M.B.G., Barros, C.F.A., Barbosa, F., Hajnal, E., Padisak, J., 2008. Role of atelomixis in replacement of phytoplankton assemblages in Dom Helvécio Lake, South-East Brazil. . Hydrobiologia 607, 211-224.

Staubwasser, M., Sirocko, F., Grootes, P.M., Segl, M., 2003. Climate change at the 4.2 ka BP termination of the Indus valley civilization and Holocene south Asian monsoon variability. Geophysical Research Letters 30.

Stein, K., Schneider, N., Timmermann, A., Jin, F.F., 2010. Seasonal Synchronization of ENSO Events in a Linear Stochastic Model. Journal of Climate 23, 5629-5643.

Steinhilber, F., Beer, J., Froehlich, C., 2009. Total solar irradiance during the Holocene. Geophysical Research Letters 36, L19704.

Stothers, R.B., 1984. The great Tambora eruption in 1815 and its aftermath. Science 224, 1191-1198.

Street-Perrott, F.A., Holmes, J.A., Waller, M.P., Allen, M.J., Barber, N.G.H., Fothergill, P.A., Harkness, D.D., Ivanovich, M., Kroon, D., Perrott, R.A., 2000. Drought and dust

deposition in the West African Sahel: A 5500-year record from Kajemarum Oasis, northeastern Nigeria. Holocene 10, 293-302.

Strikis, N.M., Cruz, F.W., Cheng, H., Karmann, I., Edwards, R.L., Vuille, M., Wang, X.F., de Paula, M.S., Novello, V.F., Auler, A.S., 2011. Abrupt variations in South American monsoon rainfall during the Holocene based on a speleothem record from central-eastern Brazil. Geology 39, 1075-1078.

Stuiver, M., Grootes, P.M., 2000. GISP2 oxygen isotope ratios. Quaternary Research 53, 277-283.

Sun, D.Z., 2003. Possible effect of an increase in the warm-pool SST on the magnitude of El Nino warming. Journal of Climate 16, 185-205.

Taylor, K.E., Crucifix, M., Braconnot, P., Hewitt, C.D., Doutriaux, C., Broccoli, A.J., Mitchell, J.F.B., Webb, M.J., 2007. Estimating shortwave radiative forcing and response in climate models. Journal of Climate 20, 2530-2543.

Taylor, K.E., Stouffer, R.J., Meehl, G.A., 2012. An overview of CMIP5 and the experiment design. Bulletin of the American Meteorological Society 93, 485-498.

Teller, J.T., Leverington, D.W., Mann, J.D., 2002. Freshwater outbursts to the oceans from glacial Lake Agassiz and their role in climate change during the last deglaciation. Quat. Sci. Rev. 21, 879-887.

Thomas, E.R., Wolff, E.W., Mulvaney, R., Steffensen, J.P., Johnsen, S.J., Arrowsmith, C., White, J.W.C., Vaughn, B., Popp, T., 2007. The 8.2 ka event from Greenland ice cores. Quat. Sci. Rev. 26, 70-81.

Thompson, C.J., 1998. Initial conditions for optimal growth in a coupled ocean-atmosphere model of ENSO. Journal of the Atmospheric Sciences 55, 537-557.

Thompson, C.J., Battisti, D.S., 2000. A linear stochastic dynamical model of ENSO. Part I: Model development. Journal of Climate 13, 2818-2832.

Thompson, C.J., Battisti, D.S., 2001. A linear stochastic dynamical model of ENSO. Part II: Analysis. Journal of Climate 14, 445-466.

Thompson, L.G., Mosley-Thompson, E., Davis, M.E., Henderson, K.A., Brecher, H.H., Zagorodnov, V.S., Mashiotta, T.A., Lin, P.N., Mikhalenko, V.N., Hardy, D.R., Beer, J., 2002. Kilimanjaro ice core records: Evidence of Holocene climate change in tropical Africa. Science 298, 589-593.

Timmermann, A., Okumura, Y., An, S.I., Clement, A., Dong, B., Guilyardi, E., Hu, A., Jungclaus, J.H., Renold, M., Stocker, T.F., Stouffer, R.J., Sutton, R., Xie, S.P., Yin, J., 2007. The influence of a weakening of the Atlantic meridional overturning circulation on ENSO. Journal of Climate 20, 4899-4919.

Timmreck, C., Lorenz, S.J., Crowley, T.J., Kinne, S., Raddatz, T.J., Thomas, M.A., Jungclaus, J.H., 2009. Limited temperature response to the very large AD 1258 volcanic eruption. Geophysical Research Letters 36, L21708.

Trenberth, K.E., Branstator, G.W., Karoly, D., Kumar, A., Lau, N.C., Ropelewski, C., 1998. Progress during TOGA in understanding and modeling global teleconnections associated

with tropical sea surface temperatures. Journal of Geophysical Research-Oceans 103, 14291-14324.

Trenberth, K.E., Caron, J.M., Stepaniak, D.P., Worley, S., 2002. Evolution of El Nino-Southern Oscillation and global atmospheric surface temperatures. Journal of Geophysical Research-Atmospheres 107.

Trigueros, J.M., Ansotegui, A., Orive, E., 2000. Remarks on morphology and ecology of recurrent dinoflagellate species in the estuary of Urdaibai (northern Spain). Bot. Marina 43, 93-103.

Trueman, M., d'Ozouville, N., 2010. Characterizing the Galápagos terrestrial climate in the face of global climate change. Galápagos Research 67, 26-37.

Tudhope, A.W., Chilcott, C.P., McCulloch, M.T., Cook, E.R., Chappell, J., Ellam, R.M., Lea, D.W., Lough, J.M., Shimmield, G.B., 2001. Variability in the El Nino - Southern oscillation through a glacial-interglacial cycle. Science 291, 1511-1517.

Tzedakis, P.C., Palike, H., Roucoux, K.H., de Abreu, L., 2009. Atmospheric methane, southern European vegetation and low-mid latitude links on orbital and millennial timescales. Earth and Planetary Science Letters 277, 307-317.

Tziperman, E., Cane, M.A., Zebiak, S.E., Xue, Y., Blumenthal, B., 1998. Locking of El Nino's peak time to the end of the calendar year in the delayed oscillator picture of ENSO. Journal of Climate 11, 2191-2199.

Umaña-Villalobos, G., 2001. Limnology of Botos Lake, a tropical crater lake in Costa Rica. Revista De Biologia Tropical 49, 1-10.

van der Meer, M.T.J., Sangiorgi, F., Baas, M., Brinkhuis, H., Damste, J.S.S., Schouten, S., 2008. Molecular isotopic and dinoflagellate evidence for Late Holocene freshening of the Black Sea. Earth and Planetary Science Letters 267, 426-434.

van Oldenborgh, G.J., Philip, S.Y., Collins, M., 2005. El Nino in a changing climate: a multi-model study. Ocean Science 1, 81-95.

Vecchi, G.A., Wittenberg, A.T., 2010. El Nino and our future climate: where do we stand? Wiley Interdisciplinary Reviews-Climate Change 1, 260-270.

Vial, J., Dufresne, J.-L., Bony, S., 2013. On the interpretation of inter-model spread in CMIP5 climate sensitivity estimates. Climate Dynamics 41, 3339-3362.

Vieira, L.E.A., Solanki, S.K., Krivova, N.A., Usoskin, I., 2011. Evolution of the solar irradiance during the Holocene. Astronomy & Astrophysics 531, A6.

Viner-Mozzini, Y., Zohary, T., Gasith, A., 2003. Dinoflagellate bloom development and collapse in Lake Kinneret: a sediment trap study. Journal of Plankton Research 25, 591-602.

Volkman, J.K., Barrett, S.M., Blackburn, S.I., 1999. Eustigmatophyte microalgae are potential sources of C_{29} sterols, C_{22}-C_{28} *n*-alcohols and C_{28}-C_{32} *n*-alkyl diols in freshwater environments. Organic Geochemistry 30, 307-318.

Volkman, J.K., Barrett, S.M., Dunstan, G.A., Jeffrey, S.W., 1992. C_{30}-C_{32} alkyl diols and unsaturated alcohols in microalgae of the class Eustigmatophyceae. Organic Geochemistry 18, 131-138.

Vuille, M., Burns, S.J., Taylor, B.L., Cruz, F.W., Bird, B.W., Abbott, M.B., Kanner, L.C., Cheng, H., Novello, V.F., 2012. A review of the South American monsoon history as recorded in stable isotopic proxies over the past two millennia. Climate of the Past 8, 1309-1321.

Wanamaker, A.D., Butler, P.G., Scourse, J.D., Heinemeier, J., Eiriksson, J., Knudsen, K.L., Richardson, C.A., 2012. Surface changes in the North Atlantic meridional overturning circulation during the last millennium. Nature Communications 3, 7.

Wang, Y.J., Cheng, H., Edwards, R.L., He, Y.Q., Kong, X.G., An, Z.S., Wu, J.Y., Kelly, M.J., Dykoski, C.A., Li, X.D., 2005a. The Holocene Asian monsoon: Links to solar changes and North Atlantic climate. Science 308, 854-857.

Wang, Y.M., Lean, J.L., Sheeley, N.R., 2005b. Modeling the sun's magnetic field and irradiance since 1713. Astrophysical Journal 625, 522-538.

Wanner, H., Butikofer, J., 2008. Holocene Bond cycles: real or imaginary? Geografie 113, 338-350.

Watanabe, M., Kug, J.S., Jin, F.F., Collins, M., Ohba, M., Wittenberg, A.T., 2012. Uncertainty in the ENSO amplitude change from the past to the future. Geophysical Research Letters 39.

Weber, S.L., 2005. A timescale analysis of the Northern Hemisphere temperature response to volcanic and solar forcing. Climate of the Past 1, 9-17.

Winder, M., Hunter, D.A., 2008. Temporal organization of phytoplankton communities linked to physical forcing. Oecologia 156, 179-192.

Wittenberg, A.T., 2009. Are historical records sufficient to constrain ENSO simulations? Geophysical Research Letters 36.

Wittenberg, A.T., Rosati, A., Delworth, T.L., Vecchi, G.A., Zeng, F.R., 2014. ENSO Modulation: Is It Decadally Predictable? Journal of Climate 27, 2667-2681.

Wittenberg, A.T., Rosati, A., Lau, N.C., Ploshay, J.J., 2006. GFDL's CM2 global coupled climate models. Part III: Tropical pacific climate and ENSO. Journal of Climate 19, 698-722.

Wolhowe, M.D., Prahl, F.G., Probert, I., Maldonado, M., 2009. Growth phase dependent hydrogen isotopic fractionation in alkenone-producing haptophytes. . Biogeosciences 6, 1681-1694.

Wurtzel, J.B., Black, D.E., Thunell, R.C., Peterson, L.C., Tappa, E.J., Rahman, S., 2013. Mechanisms of southern Caribbean SST variability over the last two millennia. Geophysical Research Letters 40, 5954-5958.

Yang, H., Huang, Y.S., 2003. Preservation of lipid hydrogen isotope ratios in Miocene lacustrine sediments and plant fossils at Clarkia, northern Idaho, USA. Organic Geochemistry 34, 413-423.

Yoshimori, M., Hargreaves, J.C., Annan, J.D., Yokohata, T., Abe-Ouchi, A., 2011. Dependency of Feedbacks on Forcing and Climate State in Physics Parameter Ensembles. Journal of Climate 24, 6440-6455.

Yoshimori, M., Stocker, T.F., Raible, C.C., Renold, M., 2005. Externally forced and internal variability in ensemble climate simulations of the Maunder Minimum. Journal of Climate 18, 4253-4270.

Yuan, X.J., 2004. ENSO-related impacts on Antarctic sea ice: a synthesis of phenomenon and mechanisms. Antarctic Science 16, 415-425.

Zebiak, S.E., Cane, M.A., 1987. A model El Nino-Southern Oscillation. Monthly Weather Review 115, 2262-2278.

Zhang, P.Z., Cheng, H., Edwards, R.L., Chen, F.H., Wang, Y.J., Yang, X.L., Liu, J., Tan, M., Wang, X.F., Liu, J.H., An, C.L., Dai, Z.B., Zhou, J., Zhang, D.Z., Jia, J.H., Jin, L.Y., Johnson, K.R., 2008. A Test of Climate, Sun, and Culture Relationships from an 1810-Year Chinese Cave Record. Science 322, 940-942.

Zhang, R., Delworth, T.L., 2005. Simulated tropical response to a substantial weakening of the Atlantic thermohaline circulation. Journal of Climate 18, 1853-1860.

Zhang, Z., Sachs, J.P., Marchetti, A., 2009. Hydrogen isotope fractionation in freshwater and marine algae: II. Temperature and nitrogen limited growth rate effects. . Organic Geochemistry 40, 428-439.

Zhang, Z.H., Leduc, G., Sachs, J.P., 2014. El Nino evolution during the Holocene revealed by a biomarker rain gauge in the Galapagos Islands. Earth and Planetary Science Letters 404, 420-434.

Zhang, Z.H., Metzger, P., Sachs, J.P., 2007. Biomarker evidence for the co-occurrence of three races (A, B and L) of *Botryococcus braunii* in El Junco Lake, Galápagos. Organic Geochemistry 38, 1459-1478.

Zhang, Z.H., Sachs, J.P., 2007. Hydrogen isotope fractionation in freshwater algae: I. Variations among lipids and species. Organic Geochemistry 38, 582-608.

Zhong, Y., Miller, G.H., Otto-Bliesner, B.L., Holland, M.M., Bailey, D.A., Schneider, D.P., Geirsdottir, A., 2011. Centennial-scale climate change from decadally-paced explosive volcanism: a coupled sea ice-ocean mechanism. Climate Dynamics 37, 2373-2387.

APPENDIX A

FIELD METHODS

Multiple overlapping sediment cores down to 372 cm depth were collected in September 2004 from 6 m water-depth using a Nesje piston corer (9 cm dia.) and an adapted Livingston-type corer (7 cm dia.) designed to recover the undisturbed sediment-water interface. Unconsolidated near-surface sediment was sectioned at 1 cm intervals on-site and was stored frozen prior to analysis. Whole cores were transported to J. Overpeck's lab at the University of Arizona where they were split, imaged, and placed on a common depth scale. The resulting composite sediment sequence was subsampled in 0.5 or 1 cm increments at 5 cm intervals.

AGE MODEL

Age model uncertainty was calculated following the method of Anchukaitis and Tierney (2013), in which a Monte Carlo approach was used to iteratively resample the probability distributions of the dated samples 10,000 times to create an ensemble of age models. The probability distributions of the ^{210}Pb-dated samples were taken to be Gaussian functions while those of the ^{14}C-dated samples were taken from OxCal 4.2 calibrations (Bronk Ramsey, 2009), using the ShCal04 curve. Age uncertainty bounds are taken to be the 68% confidence interval from the ensemble. This age error ranged from a few years in the upper layers of the sediment to 150 years in the deepest layers.

LIPID EXTRACTION AND PURIFICATION

Sediments were freeze-dried and heneicosanol (n-C_{21} alcohol) was added as a recovery standard prior to accelerated solvent extraction (Dionex ASE 200) using three cycles of dichloromethane (DCM) and methanol (MeOH) (9:1) at 100 °C and 1500 psi. The total lipid extract (TLE) was evaporated under a gentle N_2 stream using a Turbo-vap system (Caliper, Hopkinton, MA, USA). Neutral and polar lipids were separated from sediment extracts on aminopropyl SPE cartridges (Burdick & Jackson, 500 mg/4 mL) with DCM and isopropyl alcohol (IPA) (3:1 v/v), followed by 4% acetic acid (HOAc) in diethyl ether (Et_2O). The neutral fraction was applied to a column

of 5% water-deactivated Si gel and separated into hydrocarbon, wax ester, sterol/alcohol, and polar fractions with hexane, 10% ethyl acetate (EtOAc) in hexane, DCM, and MeOH, respectively.

Dinosterol was purified from the sterol/alcohol fractions via normal phase (NP)- and reverse phase (RP)- high performance liquid chromatography (HPLC) based on the methods presented in Atwood and Sachs (2012). An Agilent 1100 HPLC with an integrated autoinjector, quaternary pump, and fraction collector was coupled to an Agilent 1100 LC/MSD SL mass spectrometer with a multimode source that was operated in positive atmospheric pressure chemical ionization (APCI+) mode. A HPLC pump (Waters 510) delivered additional solvent (iso-octane for NP-HPLC and MeOH for RP-HPLC) at 0.3 mL/min to the mass spectrometer for optimal ionization efficiency.

During NP-HPLC, sterol/alcohol fractions were dissolved in 100 μL of 15% DCM in hexane for injection. Dinosterol was eluted from a Prevail Cyano column (250 mm x 4.6 mm x 5 μm) with a mobile phase of 15% DCM in hexane at a flow rate of 1.5 mL/min. During RP-HPLC, sterol/alcohol fractions were dissolved in 25 μL of DCM/MeOH (2:1) and injected onto an Agilent ZORBAX Eclipse XDB-C_{18} analytical column (250 mm x 4.6 mm x 5 μm) with a mobile phase of 5% H_2O in MeOH at 1.5 mL/min.

Mass spectra were acquired in selected ion monitoring (SIM)/scan mode. Dinosterol (MW = 428) was identified by the m/z 411 signal that results from the loss of water and addition of a hydrogen atom $(M - 18 + H)^+$. Fractions were collected in 1 min intervals and 3–4 were typically combined based on m/z 411 peak retention times in order to quantitatively recover the analyte.

BIOMARKER IDENTIFICAITON/QUANTIFICATION

Dinosterol and C_{30} keto-ols were identified via gas chromatography- mass spectrometry (GC-MS). A known amount of 5α-cholestane was added to samples as a quantification standard prior to injection. One aliquot of each sterol/alcohol fraction of the sediment samples was silylated for identification purposes while a second aliquot was acetylated for quantification and isotope analysis. Silylated samples were derivatized with 10 μL pyridine and 20 μL bis(trimethylsilyl)trifluoroacetamide (BSTFA) and heated at 60 °C for 1 hr. Acetylated samples were derivatized with 20 μL pyridine and 20 μL acetic anhydride at 70 °C for 30 min.

GC-MS acquisitions were performed on an Agilent 6890N GC coupled to an Agilent 5975 Mass Selective Detector with either a non-polar Agilent DB-5ms capillary column (60 m x 0.32 mm x 0.25 μm) or a mid-polarity Varian VF-17ms column. Samples were dissolved in toluene and injected in a split/splitless inlet operated in splitless mode at 300 °C. The oven was ramped from 60–150 °C at 15 °C/min, then to 320 °C at 6 °C/min, before holding at 320 °C for 28 min. The He carrier gas was held at 1.5 mL/min.

Ratios of C_{30} ω16-keto-1-ol to C_{30} ω20-keto-1-ol were quantified in sterol/alcohol fractions of sediment samples from GC-MS acquisitions in full scan mode. The relative proportion of keto-ol isomers was estimated from integration of the MS signal produced by fragment ions resulting from cleavage of the C-C bond adjacent to the mid-chain OTMS group.

Dinosterol was quantified in the sterol/alcohol fractions prior to HPLC purification via GC-MS in SIM mode using dinosterol and heneicosanol calibration standards. Following HPLC purification, the dinosterol samples were acetylated and analyzed on a Gas Chromatograph - Flame Ionization Detector (GC-FID) for purity assessment and quantification prior to isotope analysis. A known amount of 5α-cholestane was added to the samples as quantification standard. GC-FID analyses were performed on an Agilent 6890N GC-FID with an Agilent DB-5ms column (60 m x 0.32 mm x 0.25 μm). Samples were injected into a PTV inlet at 70 °C that ramped to 450 °C over a period of 5 min. The oven was held at 60 °C for 3 min before ramping from 60–220 °C at a rate of 20 °C/min, then from 220–325 °C at a rate of 2 °C/min under a constant flow of He at 2.5 mL/min.

C_{34} botryococcene concentration data are published in Zhang et al. (2014). Identification and quantification methods of C_{34} botryococcene can be found in Zhang and Sachs (2007) and Zhang et al. (2014).

δD MEASUREMENTS

Hydrogen isotope measurements of dinosterol were performed on a Finnigan Delta V Plus Isotope Ratio Mass Spectrometer (IRMS) coupled to a Thermo Trace GC Ultra with a Varian VF-17ms FactorFour capillary column (60 m x 0.32 mm x 0.25 μm) and a pyrolysis reactor according to the methods described in Atwood and Sachs (2012). Samples were injected into a split/splitless inlet in splitless mode at 310 °C. The oven temperature was ramped from 100 °C to

220 °C at a rate of 20 °C/min, then at 2 °C /min up to 325 °C where it was held for 17 min. The carrier gas, He, was held constant at 2.6 mL/min. The pyroloysis reactor was maintained at 1400 °C. Isotope values, expressed as δD values, were calculated in Isodat software relative to VSMOW using a co-injection standard containing *n*-C_{32}, *n*-C_{40}, and *n*-C_{44} of known δD values (obtained from A. Schimmelmann, Indiana University, Bloomington, IN, USA). The measured isotope values of dinosterol were corrected for the addition of hydrogen atoms (of known δD value) that occurred during acetylation. Triplicate analyses were typically performed on each sample and mean values and standard deviations reported. Instrument performance was evaluated using H_2 reference gas and a prepared standard of *n*-alkanes of known δD values. C_{34} botryococcene δD data are published in Zhang et al. (2014) wherein details of the measurements can be found.

STATISTICS

The significance of correlations between biomarker concentration and δD values was determined using a two-tailed Student t-test and a 95% confidence interval. The number of degrees of freedom was determined by dividing the length of the time series by the decorrelation time, where the decorrelation time was calculated from the most recent 2,000 years of data (when the sampling resolution was highest) using the statistical software, AnalySeries (Paillard et al., 1996).

APPENDIX B

DESCRIPTION OF HYDROLOGIC MODEL OF EL JUNCO LAKE

We constructed an idealized isotope hydrology model of El Junco Lake in order to simulate the hydrologic response of the lake to a change in climate. The model lake has a hydrologic balance that is governed by precipitation, evaporation, seepage, and overflow. The area of the lake is represented as an ellipse and the bottom slope as a 2nd degree polynomial fit to a major radius of 160 m, minor radius of 145 m, and depth of 6 m. The lake catchment was prescribed as 0.08 km^2. The geometry of the lake in the modern simulation approximates El Junco Lake in surface area (0.03 km^2) and depth (6 m). An overflow channel located 2 m above the modern lake level was included in the model. Monthly rainfall in the modern simulation were based on historical data from the Bellavista weather station for the period 1987–1999 provided by the Charles Darwin Research Station (http://www.darwinfoundation.org; Trueman and d'Ozouville, 2010). Monthly rainfall during El Niño events was determined by averaging monthly rainfall during moderate-to-strong El Niño events in the historical record (Niño 3.4 SSTAs ≥ 1.0 °C; http://www.cpc.ncep.noaa.gov). To simulate the average seasonal cycle in the modern climate, during non-El Niño conditions the rainfall was prescribed to be 2.6 mm/day for 5 months of the year (the wet season) and 1.6 mm/day for 7 months of the year (the dry season). Rainfall during El Niño events was set to 8.9 mm/day for 1.5 years and the frequency of strong El Niño events was set to one every 13 years. The evaporation rate was prescribed as 2.3 mm/day (based on estimates made by Conroy, 2008). In order to maintain a mean lake level of ~ 6 m in the modern simulation given the observation-based estimates of P and E, a constant seepage rate of 2.5×10^3 m^3/mo was added to the model.

To simulate the hydrologic response of the lake to a range of climate conditions, the wet season rainfall and El Niño rainfall were varied from 1.6–7.0 mm/day (in increments of 0.2 mm/day) and 1.6–17.0 mm/day (in increments of 0.3 mm/day), respectively. Wet season rainfall of 1.6 mm/day represents monthly rainfall throughout the year being equal to dry season rainfall (i.e. *garúa*), while wet season rainfall of 7.0 mm/day would be consistent with the mean annual position of ITCZ being shifted ca. 4º south of its modern position (estimated from GPCP

precipitation data; http://www.esrl.noaa.gov). The rainfall rate during El Niño events ranged from the dry season rainfall rate (effectively eliminating El Niño events) to nearly doubling the amount of El Niño-related rainfall observed in the modern climate. The dry season rainfall and the evaporation rate were kept constant.

DESCRIPTION OF ISOTOPE MODEL

The isotope mass balance of a lake whose surface inflow and groundwater are assumed negligible is given by:

$$\frac{\partial}{\partial t}(V_L \cdot \delta D_L) = P \cdot \delta D_P \cdot A_{catch} - E \cdot \delta D_E \cdot A_L - O \cdot \delta D_O - S \cdot \delta D_S \qquad \text{(A.1)}$$

where V_L represents lake volume, P and E precipitation rate and evaporation rate, respectively, A_L lake area, A_{catch} area of the lake catchment, O outflow, S seepage, and δD_L, δD_P, δD_E, and δD_O the hydrogen isotopic composition of the lake, precipitation, evaporation, and outflow, respectively. δD_O and δD_S are assumed to be in equilibrium with δD_L. δD_P is calculated from the precipitation rate using the empirical relationship between climatological monthly precipitation and δD of precipitation observed at tropical island stations from the Global Network of Isotopes in Precipitation (GNIP) database (http://www-naweb.iaea.org/napc/ih/IHS_resources_gnip.html; Bony, 2008):

$$\delta D_P = -3.9*P + 6.6 \qquad \text{(A.2)}$$

where P is given in units of mm/day. δDE is calculated using the Craig-Gordon model as described in Horita et al. (2008):

$$\delta D_E = \frac{\alpha_{V/L} \cdot \delta D_L - h \cdot \delta D_A - (\varepsilon* + \varepsilon_K)}{(1-h)+10^{-3}\varepsilon_K} \qquad \text{(A.3)}$$

$$\varepsilon_K = 12.5(1-h) \qquad \text{(A.4)}$$

$$\varepsilon* = (1-\alpha_{V/L})10^3 \qquad \text{(A.5)}$$

where $\alpha_{V/L}$ is the equilibrium vapor-liquid fractionation factor ($\alpha_{V/L} < 1$), h is the relative humidity calculated relative to the observed mean air temperature of 22.5 °C, δD_A is the isotopic composition of atmospheric water vapor, and ε_K represents the total kinetic isotope effect. Air temperature and relative humidity estimates were calculated from the Bellavista station data for the period 1987–1999 (http://www.darwinfoundation.org). Mean relative humidity was kept

constant at 90% in the model runs. A value of 0.9241 was used for $\alpha_{V/L}$ based on (Majoube, 1971) and assuming the lake temperature to be in equilibrium with the air temperature. δD_A was calculated based on the assumption that the precipitation was in isotopic equilibrium with the local atmospheric water vapor (Horita et al., 2008). The initial δD_L was set to 7.7‰ (based on lake water samples taken in Sept. 2004).

Each model simulation (with a uniquely prescribed set of El Niño and ITCZ rainfall values) was run for 130 years with a 1-month time step. To evaluate the hydrologic response of the lake to the varying climate conditions, changes in lake δD were compared to the prescribed changes in El Niño and ITCZ rainfall.

Modeled Lake Responses to ITCZ- and El Niño Rainfall Changes

Analysis of the model simulations with imposed changes in El Niño and ITCZ rainfall indicate that changes in mean lake δD scale linearly with the prescribed changes in total mean annual rainfall ($\Delta\overline{P_T}$; Fig. 2.11A). In addition, changes in mean lake δD during El Niño events scale linearly with the prescribed changes in mean monthly El Niño rainfall (ΔP^*_E; Fig. 2.11B). Finally Fig. 2.11C demonstrates that, in our simple hydrologic model of El Junco Lake, mean lake δD during non-El Niño conditions generally scales linearly with non-El Niño (i.e. ITCZ) mean annual rainfall ($\Delta\overline{P_R}$), therefore suggesting that if the alternative interpretation of dinosterol δD were to be adopted (as outlined in Chapter 2.3.1, that dinosterol δD reflects the lake δD during non-El Niño conditions), this proxy could be used directly as a proxy for changes in residual (i.e. non-El Niño) climatological rainfall. As noted in Chapter 2.3.1, this alternative interpretation of the dinosterol δD data would be appropriate if the dinoflagellates only grew under non-El Niño conditions in the lake. However, we choose to adopt the more conservative approach outlined in Chapter 2.3.4.

As a final demonstration of the theory behind the El Junco Lake rainfall indices, three representative simulations of the lake model are shown in Fig. 2.10. The first simulation (Fig. 2.10A) depicts the transient lake response to modern climate conditions. The second simulation (Fig. 2.10B) depicts the lake response to a 40% reduction in rainfall during El Niño events and a 120% increase in wet season rainfall (consistent with the mean annual position of the ITCZ shifted south by ca. 2° latitude in this region, as estimated from GPCP precipitation data

(http://www.esrl.noaa.gov). Given our assumptions concerning the growth conditions of the dinoflagellate and B. braunii, the decrease in mean lake δD would be recorded by a decrease in dinosterol δD. However, the decreased mean annual El Niño rainfall would produce a decrease in the sedimentary accumulation rate of botryococcene. The decreased monthly mean El Niño rainfall produces an increase in lake δD during El Niño events, which would be recorded by botryococcene δD. Consequently, the combination of decreased dinosterol δD and decreased botryococcene accumulation rate would be inferred as an increase in ($\Delta\overline{P_R}$), consistent with the prescribed conditions of increased ITCZ rainfall.

The final simulation (Fig. 9C) depicts the lake response to a 20% increase in rainfall during El Niño events and an elimination of the wet season (i.e. perpetual dry season) rainfall, simulating a climate in which the ITCZ is permanently north of El Junco Lake. The increase in El Niño rainfall results in a decrease in lake δD during El Niño events while the decrease in ITCZ rainfall results in a modest increase in mean lake δD. Such conditions would be recorded by increased dinosterol δD, increased botryococcene accumulation rates, and decreased botryococcene δD. The combination of increased dinosterol δD and increased botryococcene accumulation rate would be inferred as a decrease in ($\Delta\overline{P_R}$), consistent with the prescribed conditions of decreased ITCZ rainfall.

APPENDIX C

CHANGING HYDROLOGIC CONDITIONS IN EL JUNCO LAKE FROM KETO-OLS

A reconstruction of mean lake level changes of El Junco Lake was developed based on the ratio of sedimentary keto-ol isomers derived from algae and ferns. C_{30} ω16-keto-1-ol (structure III in Fig. S1), produced by algae of the class Eustigmatophyceae (Méjanelle et al., 2003; Volkman et al., 1999; Volkman et al., 1992), and C_{30} ω20-keto-1-ol (structure V in Fig. S1), produced by the tree fern *Cyathea weatherbyana* (Atwood et al., 2014), comprise some of the most abundant keto-ols in El Junco Lake sediment. Because keto-ol production has also been found to occur through diagenetic alteration of diols (Ferreira et al., 2001), sources of the corresponding diols were also investigated. Similarly to their keto-ols counterparts, C_{30} 1,ω16-diols (structure IV in Fig. S1) have been reported in algae of the class Eustigmatophyceae (Méjanelle et al., 2003; Volkman et al., 1999; Volkman et al., 1992) C_{30} 1,ω20-diols (structure VI in Fig. S1) are produced by *Azolla microphylla,* an aquatic fern that populates the shoreline of El Junco Lake.

Because C_{30} 1,ω20-diols and keto-ols are produced by terrestrial and shoreline ferns, while C_{30} 1,ω16-diols and keto-ols are produced by aquatic algae, it is expected that as the lake level increases, the input of C_{30} ω20-keto-1-ol relative to C_{30} ω16-keto-1-ol would decrease owing to two effects. Firstly, as the radius of the lake increases, the ratio of its surface area to its circumference increases as approximately r/2 ($\pi r^2/2\pi r$). Secondly, as the lake level increases, the catchment area (from the crater rim to the edge of the lake) decreases. Both of these effects should result in greater production of organic matter from aquatic organisms relative to terrestrial and shoreline vegetation during higher lake stands. Thus, we propose that the ratio of C_{30} ω16-keto-1-ol/ω20-keto-1-ol serves as an indicator of El Junco Lake level, where greater abundances of the 1,ω16 isomer relative to 1,ω20 isomer indicate higher lake levels.

The ratio of C_{30} ω16-keto-1-ol/ω20-keto-1-ol is anti-correlated to the dinosterol δD values over the last 3 kyr ($r = -0.54$, $p < 0.05$; Fig. 6C,D), in support of our interpretation of dinosterol δD as a proxy of mean rainfall changes. However, large differences in dinosterol δD and keto-ol records exist in the upper 5 cm of sediment. We hypothesize that these differences are due to a

lower degree of diagenetic transformation of diols to keto-ols in the surface sediment relative to deeper sediment. The idea is supported by the fact that the upper 5 cm sediment contain relatively high C_{30} 1,ω16-diol/ω16-keto-1-ol ratios as compared to deeper sediment (data not shown). Because only trace amounts of C_{30} 1,ω20-diol exist throughout the sediment record (including in the upper layers), incomplete diagenetic transformation of C_{30} 1,ω16-diol to C_{30} ω16-keto-1-ol in the surface sediment would result in low C_{30} ω16-keto-1-ol/ω20-keto-1-ol ratios in the upper sediment layers, as observed.

We place more weight on the dinosterol δD record than on the keto-ol record as a record of mean rainfall changes, for several reasons. Firstly, changes in the ratio of the characteristic ions of keto-ol isomers on a GC-MS does not have a 1:1 relationship with changes in the ratio of the concentration of the isomers. Unfortunately, the co-elution of keto-ol isomers precluded improved quantification. Secondly, the keto-ol proxy assumes that the concentration of algal biomass remained constant with changes in lake levels, which is likely to be an imperfect assumption. Additional uncertainties in the keto-ol record include environmental variables other than the hydrologic conditions of the lake influencing their relative input to the sediment and changes in the diagenetic alteration of these compounds under varying depositional conditions. Despite these limitations, the ratio of C_{30} ω16-keto-1-ol/ω20-keto-1-ol provides an independent record of past hydrologic conditions of El Junco Lake that supports many of the prominent trends in the dinosterol δD record and thus strengthens the paleoclimate interpretations of the biomarker records.

VITA

Alyssa Regine Atwood was born in Eureka, California and graduated from U.C. Berkeley with a B.A. in Physics and Atmospheric Science in 2006. In addition to science, she loves the outdoors and thoroughly enjoyed her time in Seattle during her PhD program, exploring the natural wonders of the Pacific Northwest.